nanomaterials

MDPI

Article

Tuning Particle Sizes and Active Sites of Ni/CeO_2 Catalysts and Their Influence on Maleic Anhydride Hydrogenation

Qiuming Zhang, Xin Liao, Shaobo Liu, Hao Wang *, Yin Zhang * and Yongxiang Zhao *

Engineering Research Center of Ministry of Education for Fine Chemicals,
School of Chemistry and Chemical Engineering, Shanxi University, Taiyuan 030006, China;
matthwwe@163.com (Q.Z.); lx2006294034@126.com (X.L.); lovog@163.com (S.L.)
* Correspondence: haowang@sxu.edu.cn (H.W.); sxuzhy@sxu.edu.cn (Y.Z.); yxzhao@sxu.edu.cn (Y.Z.)

Abstract: Supported metal catalysts are widely used in industrial processes, and the particle size of the active metal plays a key role in determining the catalytic activity. Herein, CeO_2-supported Ni catalysts with different Ni loading and particle size were prepared by the impregnation method, and the hydrogenation performance of maleic anhydride (MA) over the Ni/CeO_2 catalysts was investigated deeply. It was found that changes in Ni loading causes changes in metal particle size and active sites, which significantly affected the conversion and selectivity of MAH reaction. The conversion of MA reached the maximum at about 17.5 Ni loading compared with other contents of Ni loading because of its proper particle size and active sites. In addition, the effects of Ni grain size, surface oxygen vacancy, and Ni–CeO_2 interaction on MAH were investigated in detail, and the possible mechanism for MAH over Ni/CeO_2 catalysts was deduced. This work greatly deepens the fundamental understanding of Ni loading and size regimes over Ni/CeO_2 catalysts for the hydrogenation of MA and provides a theoretical and experimental basis for the preparation of high-activity catalysts for MAH.

Keywords: hydrogenation; particle size; maleic anhydride; Ni loading; CeO_2

Citation: Zhang, Q.; Liao, X.; Liu, S.; Wang, H.; Zhang, Y.; Zhao, Y. Tuning Particle Sizes and Active Sites of Ni/CeO_2 Catalysts and Their Influence on Maleic Anhydride Hydrogenation. *Nanomaterials* **2022**, *12*, 2156. https://doi.org/10.3390/nano12132156

Academic Editor: Maria Filipa Ribeiro

Received: 27 May 2022
Accepted: 17 June 2022
Published: 23 June 2022

Publisher's Note: MDPI stays neutral with regard to jurisdictional claims in published maps and institutional affiliations.

1. Introduction

Maleic anhydride (MA) is an important C4 fundamental material in the chemical industry that can be obtained by oxidation of coking benzene, butane, or biomass platform compounds. MA is a multifunctional and five-membered ring compound composed of one C=C, double C=O bonds, and one C–O–C functional group. A series of high-value-added fine chemicals such as succinic anhydride (SA), γ-butyrolactone (GBL), and tetrahydrofuran (THF) can be synthesized by maleic anhydride hydrogenation (MAH). These solvents and intermediates are widely used in the military, textile, pharmaceutical, and food industries [1–3]. The hydrogenation of MA involves C=C and C=O hydrogenation, and the investigation of hydrogenation mechanism for C=C and C=O bonds has been a hot topic. Until now, the catalysts used in the MAH have mainly been supported Ni-based catalysts, and the supports have mainly been metal or nonmetal oxides such as Al_2O_3, SiO_2, TiO_2, and CeO_2 [4–7].

For supported catalysts, the type of active metals, the acid and base properties of the surface, defect sites, and metal–support interactions have important effects on the adsorption and activation forms, hydrogenation path, and product selectivity of MAH. Among these factors, the particle size of the active metal plays a crucial role in the catalytic performance of catalysts [8–10]. The geometrical structure, electronic structure, and dispersion of metal particles change dynamically with changes in particle size, and these changes lead to variation in the active sites on the catalyst surface, which significantly affects the catalytic activity of the catalyst [11–14]. Zhao et al. [15] discovered that for the Ni/SiO_2 catalytic system, when Ni species were fine clusters, the product GBL was obtained from the hydrogenation of MA because of the strong interaction between Ni and the support. However, succinic anhydride (SA) was obtained when the Ni species was in a crystalline

state and had weak interaction with the support. Li et al. [16] found that the selectivity of MAH was closely related to the grain size of the active metal, Ni. For a Ni/HY–Al_2O_3 catalyst, smaller sizes of Ni nanoparticles were favorable for the formation of SA, while as the Ni loading amount increased, the particle size of Ni and the selectivity of GBL increased. Meyer et al. [17] observed that NiO had a stronger interaction with the support when the Ni loading was lower (less than 8 wt%) and that the Ni nanoparticles were conducive to the generation of SA. However, when the Ni loading was gradually increased, NiO particles tended to aggregate on the surface of the support, which reduced the interaction between NiO and the support until more GBL products were finally obtained. Bertone et al. [3] found that compared with a Ni/SiO_2 catalyst, a Ni/SiO_2–Al_2O_3 catalyst had smaller grain size of Ni on the surface and showed higher GBL selectivity. They speculated that the Lewis acid on the surface of the SiO_2–Al_2O_3 support promoted the formation of GBL. Ma et al. [18] prepared Pd/CeO_2 catalysts with different Pd particle sizes on a CeO_2 carrier and found that the CeO_2-supported Pd single atomic catalyst showed the best activity for CO oxidation reaction. In addition, in recent works [4,19,20], we synthesized a series of Ni/CeO_2 catalysts under different conditions and investigated deeply the important role of CeO_2 in MA hydrogenation. These works will be very helpful for investigating the effect of the particle size and active sites of metal on MAH. On the basis of regulating the particle size and active sites of metal on CeO_2 support, they provided a new opportunity to comprehensively understand the interaction between the active metal and support and systematically study the change in the active sites of catalysts in heterogeneous catalysis.

Based on the above discussion, in this paper, Ni-supported catalysts with different Ni loading were prepared by the impregnation method using CeO_2 as support, and the hydrogenation performance of the catalysts was investigated carefully. It was found that changes in Ni loading caused changes in the metal particle size and active sites, which significantly affected the conversion and selectivity of MAH reaction. In this work, the effects of Ni grain size, dispersion, surface oxygen vacancy, and Ni–CeO_2 interaction on the hydrogenation of MA were investigated in detail, and the synthesis process of metal-supported catalysts was optimized. This paper provides a theoretical and experimental basis for the preparation of MAH catalysts with higher activity and selectivity.

2. Experimental Section

2.1. Catalysts Preparation

The chemicals, including $Ce(NO_3)_3{\cdot}6H_2O$, $Ni(NO_3)_2{\cdot}6H_2O$, and NaOH, were purchased from the Sinopharm Chemical Reagent Co., Ltd. (Shanghai, China) and used without any purification. A CeO_2 support was prepared by the sol–gel method. First, 5.00 g $Ce(NO_3)_3{\cdot}6H_2O$ was dissolved into 20 mL distilled water, and then, 6.56 g citric acid (CA) was added and stirred. After the cerium salt and citric acid were completely dissolved, the solution was heated in a water bath at 80 °C until the dry sol was formed. After drying at 120 °C for 8 h in the oven, the dry sol formed a spongy material. It was then moved to a muffle oven and calcined at 500 °C for 3 h to finally obtain the CeO_2 support. xNi/CeO_2 (x: mass content of Ni) catalysts with different loading contents were prepared by citric acid assisted over-volume impregnation method. For the 5Ni/CeO_2 catalyst, 0.505 g $Ni(NO_3)_2{\cdot}6H_2O$ was dissolved in a mixture of 10 mL ethanol and deionized water (volume ratio 1:1), followed by 2.00 g solid CeO_2 and 0.139 g citric acid (mole ratio 1:1). After stirring at room temperature for 30 min, the mixture was placed in a water bath at 80 °C to volatilize the solvent. After the solvent was completely volatilized, the sample was transferred to a drying oven at 120 °C for 8 h. The obtained samples were calcinated at 450 °C for 3 h (heating rate of 3 °C/min) and then reduced for 3 h at 350 °C with H_2 at a flow rate of 50 mL/min to prepare the catalyst, which was used for subsequent characterization and evaluation. According to different content of Ni, the catalysts were labeled as 5Ni/CeO_2, 10Ni/CeO_2, 15Ni/CeO_2, 17.5Ni/CeO_2, 20Ni/CeO_2, and 30Ni/CeO_2.

2.2. Catalyst Characterizations and Tests

X-ray diffraction (XRD) was performed using a Bruker D8 Advanced X-ray diffractometer (Billerica, MA, USA). The instrument used Cu Kα1 radiation (λ = 0.15418 nm) as an X-ray source and was supplied with a Ni filter and Vantec detector. The scanning range was 10~80°, and the scanning rate was 30°/min. The average crystallite size was calculated by the Scherrer formula, D = Kλ/βcosθ, where K is Scherrer's constant (0.89). The characterizations of H_2-TPR (hydrogen temperature programed reduction) and H_2-TPD (hydrogen temperature programmed desorption) were determined using a Micromeritics AutoChem II 2950 chemisorption apparatus. Raman spectroscopy (Raman) was performed on a Raman spectrometer with a laser wavelength of 532 nm (HORIBA, Tokyo, Japan). X-ray photoelectron spectroscopy (XPS) was recorded using a SCIENTIFIC ESCALAB 250 X-ray photoelectron spectrometer (Thermo Company, Waltham, MA, USA) with a standard Al-Kα (h = 1486.6 eV). The spectra were calibrated according to standard C 1s (284.6 eV).

The catalytic performance of the catalyst was evaluated in a 100 mL stainless steel autoclave. First, 0.1 g catalyst was added together with 4.9 g MA and 40 mL THF into the reactor. The N_2 was passed through to replace the air in the reactor 5 times, and then H_2 was passed through 5 times to replace N_2. Then, the reaction system was heated to 210 °C with stirring at 500 rpm, and the pressure was kept at 5.0 MPa. The product was analyzed using an Agilent 7890A gas chromatograph. To verify precise separation of each component in the products, the programmed temperature was selected. The primary temperature of the oven was increased to 120 °C from 100 °C at a ramp of 5 °C min^{-1}, and the temperatures of the detector and injector were 190 °C and 260 °C, respectively. The conversion and selectivity of MA to the product were calculated according to the following equations [20]:

$$X_{MA}\ (\%) = \frac{C_{GBL} + C_{SA}}{C_{GBL} + C_{SA} + C_{MA}} \times 100\%$$

$$S_{SA}\ (\%) = \frac{C_{SA}}{C_{SA} + C_{GBL}} \times 100\%$$

where C_{MA}, C_{SA}, and C_{GBL} represent the percent content of the reactant and the two products in the reaction, respectively, and X_{MA} and S_{SA} represent the conversion of MA and selectivity of SA.

3. Results and Discussion

3.1. Catalyst Characterization

Figure 1 shows the XRD patterns of xNiO/CeO_2 samples with different Ni contents. As shown in Figure 1A, after metal Ni loading, the CeO_2 support still maintained the crystal structure of fluorite cubic phase (JCPDS File 34-0394), similarly to pure CeO_2 [21]. The enlarged pattern (shown in Figure 1B) revealed that the diffraction peaks of the CeO_2 (111) crystal plane in xNiO/CeO_2 samples moved to a higher angle, indicating that the crystal cell parameters of CeO_2 shrank after Ni loading. This may have been due to the Ni^{2+}, with its smaller ionic radius (R = 0.72 nm), replacing Ce^{4+} (R = 0.81 nm) in the CeO_2 lattice, which resulted in reductions in the cell parameters of CeO_2 [22]. The average crystal sizes of NiO and CeO_2 in the xNiO/CeO_2 samples were calculated by the Scherrer formula, and the results are listed in Table 1. Compared with pure CeO_2 support, the grain size of CeO_2 increased after Ni loading, which may have been caused by sintering during the thermal calcination or the lattice distortion of CeO_2 caused by Ni species [23].

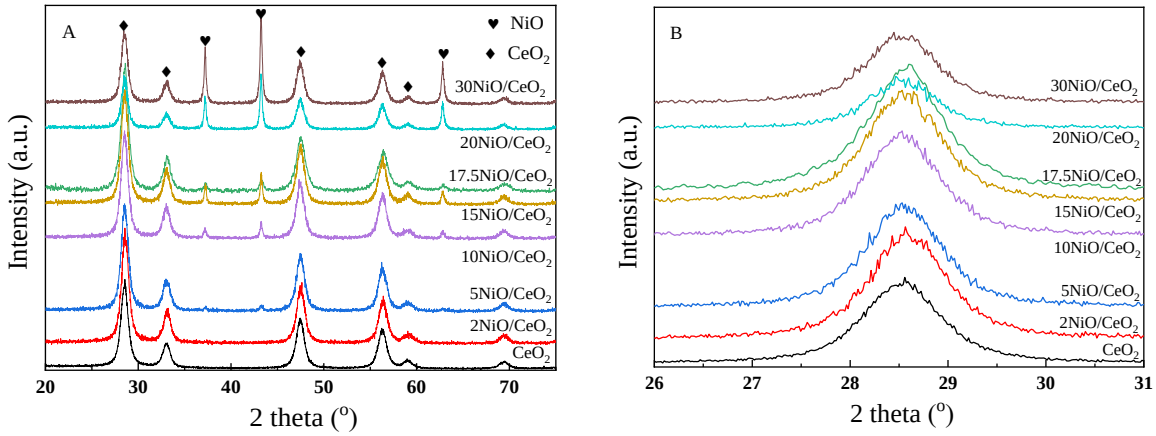

Figure 1. (**A**) XRD patterns of calcined xNiO/CeO_2 samples; (**B**) the enlarged pattern at the range of 26–31°.

Table 1. The surface areas (S_{BET}), Ni loading, and average crystallite sizes of CeO_2, NiO, and metallic Ni in the reduced catalysts.

Sample	D(CeO_2) (nm)	Surface Area (m^2/g)	Ni Loading (wt%)	D(NiO) (nm)	D(Ni) (nm)
CeO_2	11.6	35.6	-	-	-
5Ni/CeO_2	13.4	35.8	4.8	10.1	-
10Ni/CeO_2	13.8	37.5	10.2	21.6	10.7
15Ni/CeO_2	13.3	34.2	15.3	24.7	15.2
17.5Ni/CeO_2	13.8	32.1	17.2	28.2	17.5
20Ni/CeO_2	13.7	28.4	20.5	30.5	18.9
30Ni/CeO_2	13.1	22.2	29.1	35.1	36.6

As shown in Figure 1A, the XRD diffraction peaks at 37.0°, 43.0°, and 62.9° corresponded to the characteristic diffraction peaks of NiO's (111), (200), and (220) crystal planes (JCPDS 47-1049), respectively. As Ni loading increased, the intensity of the NiO diffraction peak gradually increased, indicating that NiO particles aggregated on the surface of the catalyst and the grain size gradually grew. The particle sizes of NiO are also listed in Table 1, revealing that as Ni loading increased, the particle size of NiO increased from about 10.1 nm to 35.1 nm. The change in NiO grain size led to a change in the interaction between NiO and CeO_2, which may have affected the reduction behavior of NiO and the structural difference of the catalyst surface.

Figure 2 shows the XRD patterns of xNi/CeO_2 catalysts after reduction at 350 °C. As shown in Figure 2, the CeO_2 support maintained a fluorite cubic structure after reduction, and the characteristic peak of NiO disappeared, while the characteristic diffraction peak of the Ni (111) plane appeared at 44.6° (JCPDS 01-1258), indicating that NiO was reduced to metallic Ni. However, for the 5Ni/CeO_2 catalyst, the diffraction peak of the metal Ni was not observed, which may have been due to the high dispersion of amorphous Ni species on the catalyst surface or the smaller particle size of Ni (<4 nm). The crystal sizes of Ni in xNi/CeO_2 catalysts with different loading content were calculated by the Scherrer formula and are listed in Table 1. As the Ni loading content increased, the metal Ni aggregates on the surface of the catalyst increased, and the average grain size increased gradually from about 10.7 nm to 36.6 nm.

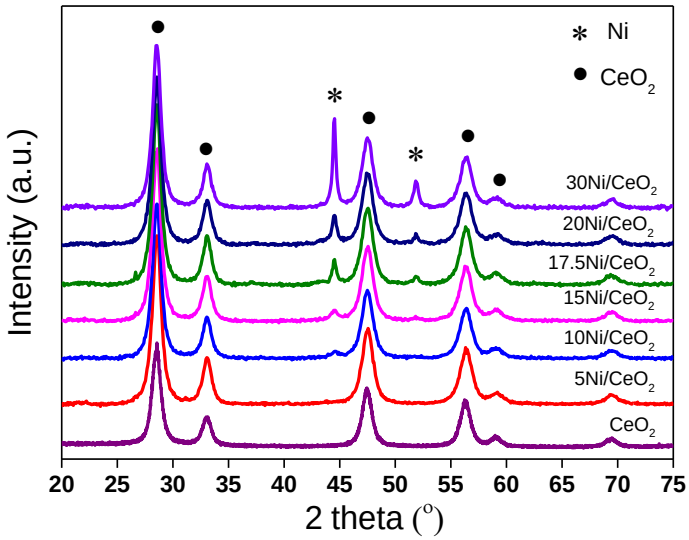

Figure 2. The XRD patterns of reduced xNi/CeO_2 catalysts.

Figure 3 shows the H_2-TPR spectrum of xNiO/CeO_2 samples. The peaks of H_2 consumption, named α, β, γ, and δ, were well fitted through a Gauss-type function for these samples. The α peak showed lower intensity and a broader shape at about 150 °C, which was attributed to the reduction of oxygen species adsorbed on the surface of CeO_2 [24,25]. It has been reported that parts of Ni^{2+} species could enter the CeO_2 lattice to replace Ce^{4+}, which resulted in the distortion of CeO_2 lattice and produced oxygen vacancies to balance charges [24]. Raman results also confirmed that the loaded NiO species promoted the formation of oxygen vacancies on the CeO_2 surface (Figure 4A). These oxygen vacancies could adsorb some small oxygen-containing molecules and generate reactive oxygen species, which can easily react with hydrogen [25]. The sharp β peak of H_2 consumption at about 200 °C could be attributed to the H_2 depletion caused by the dissociation and adsorption of H_2 onto the oxygen vacancies or the Ni–Ce interface and the formation of OH groups on the surface. A similar result was found in Ni–Ce solid solution [26]. As shown in Figure 3, as Ni loading increased, the β peak gradually moves towards higher temperatures, and the peak intensity decreased, indicating that the increase in Ni content inhibited the dissociation and adsorption of H_2 on the oxygen vacancies or the Ni–Ce interface, which may have been caused by the excessive Ni species masking the oxygen vacancies on the surface.

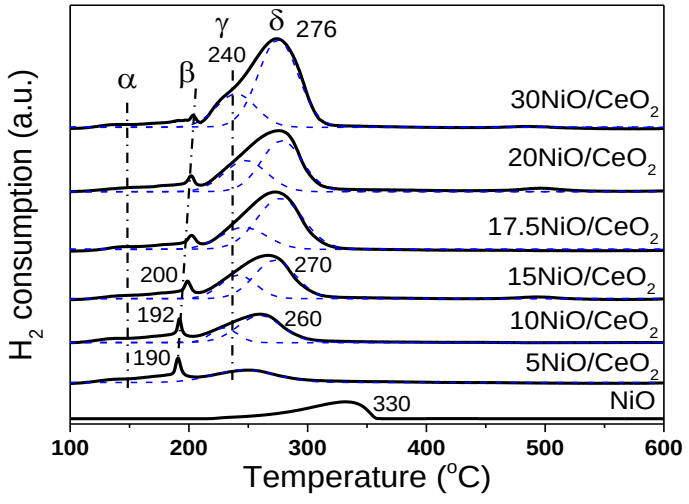

Figure 3. H_2-TPR profiles of xNiO/CeO_2 precursors.

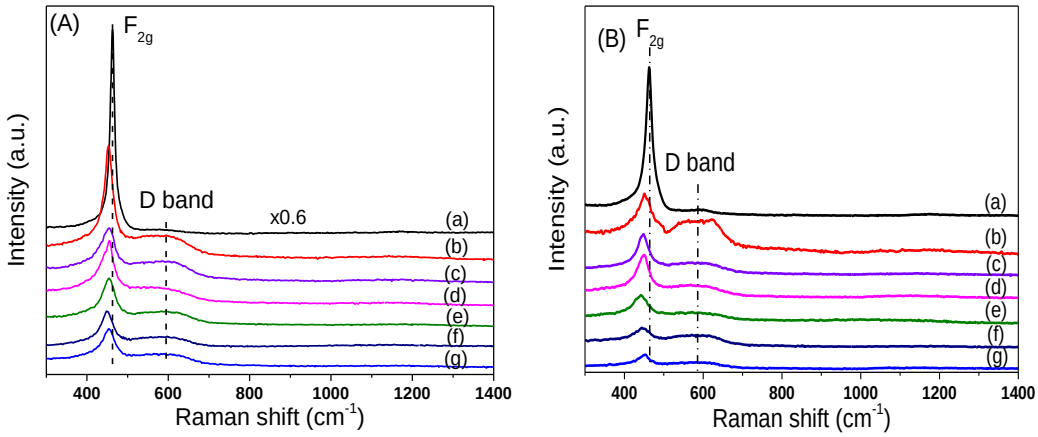

Figure 4. Raman spectra (**A**) xNiO/CeO_2 precursors and (**B**) reduced xNi/CeO_2 catalysts (a) CeO_2, (b) 5Ni/CeO_2, (c) 10Ni/CeO_2, (d) 15Ni/CeO_2, (e) 17.5Ni/CeO_2, (f) 20Ni/CeO_2, (g) 30Ni/CeO_2.

In general, the reduction of NiO species occurs in the temperature range of 200–300 °C. The asymmetric reduction peaks of NiO were deconvolved into two peaks for H_2 consumption, which are labeled γ and δ, respectively. The γ peak at 240 °C was attributed to the reduction of highly dispersed NiO species closely linked to the CeO_2 support. The stronger metal–support interaction promoted the reduction of NiO at lower temperatures [21]. The δ peak at high temperature (about 275 °C) was ascribed to the reduction of bulk NiO species aggregated on the CeO_2 surface. From Figure 3, the reduction temperature of NiO species on the CeO_2 surface was lower than that of bulk NiO. This was mainly because loaded NiO, with smaller size and larger surface area, could more easily contact with H_2, which resulted in the lower reduction temperature. Moreover, oxygen vacancies and preferential reduced Ni species on the surface of CeO_2 support (at 240 °C) promoted the dissociation and activation of H_2, and the overflow of H atoms to NiO with large particle size was favorable to the reduction of NiO at low temperature. It should be noted that as Ni loading increased, the δ peak moved towards high temperatures. A possible reason for this is that the activation and migration of H_2 may have been inhibited because of the increase in NiO particle size and the decrease in oxygen vacancy, thus retarding the reduction of NiO at low temperatures.

In order to study the effect of Ni loading on the surface structure of CeO_2, Raman characterizations for xNiO/CeO_2 samples were conducted, and the results are shown in Figure 4. The Raman peak intensity of CeO_2 in the figure was 0.6 times that of the original peak intensity in order to facilitate comparison of results. For CeO_2 support, a strong Raman vibration peak was observed at 466 cm^{-1}, corresponding to the F2g vibration mode for the Ce–O bond in the cubic fluorite structure of CeO_2 [27]. After the loading of NiO on the surface of CeO_2, the F2g peak intensity of CeO_2 decreased, the peak shape widened, and the peak position moved towards low wavelengths. This was because the strong interaction between NiO and CeO_2 led to lattice distortion of CeO_2, which reduced the symmetry of the Ce–O bond [25]. Besides the F2g vibration peak, the Raman vibration peak at 600 cm^{-1} was attributed to the vibration (D band) caused by defect sites on the CeO_2 surface [25]. Compared with that of the pure CeO2 support, the peak intensity of the D band of the xNiO/CeO_2 sample increased significantly, indicating that the existence of NiO promoted the formation of oxygen vacancies on the CeO_2 surface. However, the vibration peak of NiO at 520 cm^{-1} could not be observed and may be covered by the F2g vibration peak of CeO_2 [26]. Raman spectrum results for the xNiO/CeO_2 catalyst after reduction are shown in Figure 4B. Similarly to the xNiO/CeO_2 precursor, two Raman characteristic peaks were observed at 466 cm^{-1} and 600 cm^{-1}, corresponding to the F2g vibration of Ce–O bond for cubic fluorite CeO_2 and the D-band vibration induced by surface defects, respectively [25].

Figure 5 shows the variation trend of the I_D/I_{F2g} ratio with Ni content before and after reduction, which reflects the influence of Ni loading on the oxygen vacancy concentration on the catalyst surface [20]. As shown in Figure 5, the oxygen vacancy concentrations of all $xNiO/CeO_2$ samples loaded with Ni were higher than that of the CeO_2 support without Ni, which indicates that the addition of Ni was beneficial to the formation of oxygen vacancies on the surface of CeO_2. Among these NiO/CeO_2 samples, the I_D/I_{F2g} ratio of the $5NiO/CeO_2$ sample is the highest, and then the I_D/I_{F2g} ratio decreased gradually as the Ni content increased, which means that the oxygen vacancy decreased as the Ni content increased. A possible reason for this is that the aggregation of NiO and the growth in particle size on the surface of CeO_2 weakened the interaction of NiO and CeO_2 and covered part of the oxygen vacancies on the surface, which resulted in a decrease in oxygen vacancies.

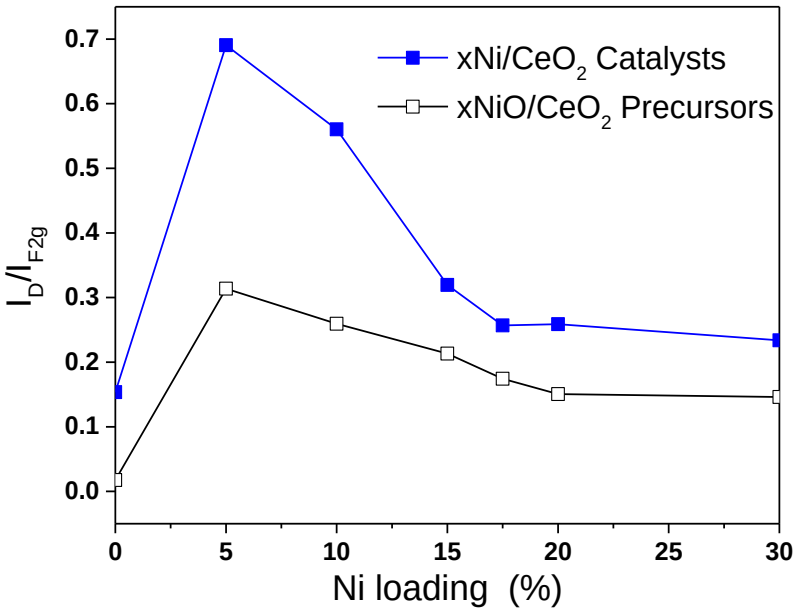

Figure 5. I_D/I_{F2g} ratios for the $xNiO/CeO_2$ precursors and reduced xNi/CeO_2 catalysts.

As shown in Figure 5, compared with the $xNiO/CeO_2$ samples, the I_D/I_{F2g} ratios for the xNi/CeO_2 catalysts increased significantly after reduction, indicating that the oxygen vacancy concentrations on the surface of the xNi/CeO_2 catalysts increased obviously after H_2 reduction. The oxygen vacancy increments of $5Ni/CeO_2$ and $10Ni/CeO_2$ were significantly larger than those of other catalysts with higher Ni loading, which suggests that lower Ni content was beneficial to the formation of oxygen vacancies on the surface of the catalyst. When the loaded content of Ni was low, Ni species and CeO_2 were in close contact and interacted strongly each other, which could have promoted the reduction of the CeO_2 surface and facilitated the formation of oxygen vacancies on the surface. However, as Ni loading increased, the active Ni species began to aggregate and cover the surface of CeO_2, which weakened the Ni–CeO_2 interaction and inhibited the reduction of CeO_2 surface.

In order to further study the effect of Ni content on the surface species of Ni/CeO_2, five samples of CeO_2, $5Ni/CeO_2$, $10Ni/CeO_2$, $17.5Ni/CeO_2$, and $30Ni/CeO_2$ were characterized by the XPS technique. Figure 6A shows the Ce 3d XPS spectra of the catalyst. The peak of Ce is deconvolved into five groups of characteristic peaks according to the literature [28,29]. The three characteristic peaks labeled u and v, u" and v", and u"' and v"' belong to the XPS peaks of $3d_{1/2}$ and $3d_{5/2}$ of Ce^{4+} 3d, while the two characteristic peaks of u' and v' and u_0 and v_0 belong to the $3d_{1/2}$ and $3d_{5/2}$ of Ce^{3+} 3d. Compared with pure CeO_2, the XPS peak of Ce^{4+} in the $5Ni/CeO_2$ catalyst moved slightly towards the high-energy direction, indicating that the strong interaction between Ni and CeO_2 changed the electronic configuration of Ce on the surface. Similar phenomena were observed in

Pt/CeO_2 and Cu/CeO_2 catalysts, and the peak shift of Ce^{4+} should be caused by electron transfer from metal to CeO_2 [30,31]. According to the XPS peaks of Ce^{3+} and Ce^{4+}, the concentration of Ce^{3+} on the catalyst surface was estimated, and the results are listed in Table 2. Per Table 2, the amount of Ce^{3+} on the surface of the $5Ni/CeO_2$ catalyst was the highest among these samples. As the Ni loading amount increased, the amount of Ce^{3+} on the surface gradually decreased and was even lower than that of pure CeO_2 after reduction for $17.5Ni/CeO_2$ and $30Ni/CeO_2$. This may have been caused by excessive Ni covering the Ce^{3+} on the surface of the catalyst.

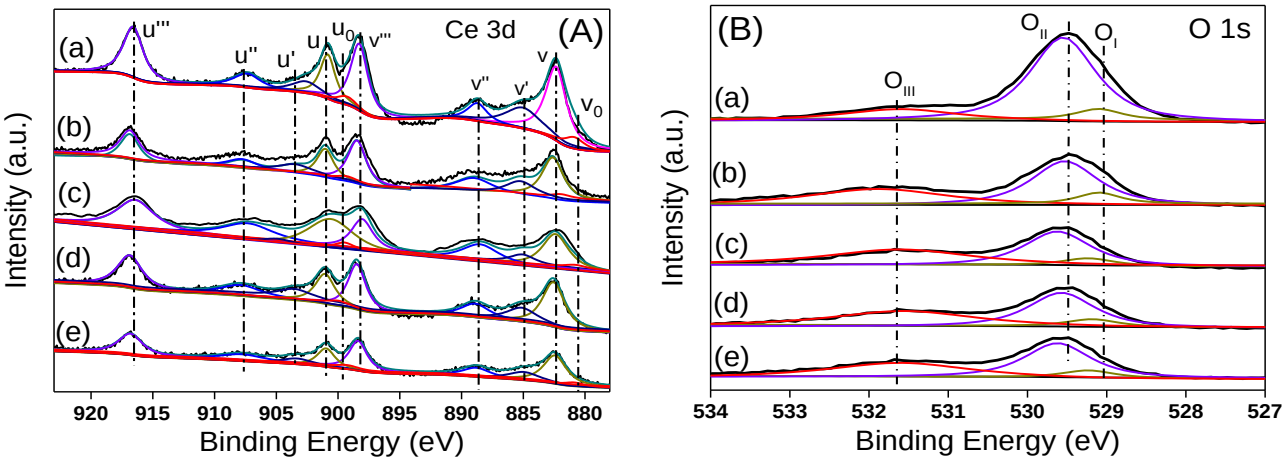

Figure 6. The (**A**) Ce 3d and (**B**) O 1s core-level XPS spectra of the xNi/CeO_2 catalysts (a) CeO_2, (b) $5Ni/CeO_2$, (c) $10Ni/CeO_2$, (d) $17.5Ni/CeO_2$, and (e) $30Ni/CeO_2$.

Table 2. The quantitative analysis of XPS for reduced xNi/CeO_2 catalysts.

Sample	$Ce^{3+}/(Ce^{3+} + Ce^{4+})$	$O_{III}/(O_I + O_{II} + O_{III})$	Ni^0:Ni^{2+}:Ni^{3+}
CeO_2	0.162	0.2066	-
$5Ni/CeO_2$	0.178	0.414	0.18:0.57:0.25
$10Ni/CeO_2$	0.164	0.374	0.25:0.56:0.19
$17.5Ni/CeO_2$	0.146	0.364	0.34:0.45:0.20
$30Ni/CeO_2$	0.139	0.334	0.43:0.39:0.18

Figure 6B shows the O 1s XPS spectra of the reduced xNi/CeO_2 catalysts. After deconvolution, three groups of XPS peaks of O were observed, representing three types of O species. O_I and O_{II} represented O species with different coordination in the CeO_2 lattice, and O_{III} represented oxygen species adsorbed at defect sites on the catalyst surface. The O_I peak at 528.8 eV was the oxygen species coordinated with Ce^{3+} in the CeO_2 lattice, while the O_{II} peak with slightly higher binding energy (529.4 eV) represented the oxygen species coordinated with Ce^{4+} [32]. The concentration of oxygen vacancies on the surface of the catalyst can be estimated by the ratio $O_{III}/(O_I + O_{II} + O_{III})$, and the results are listed in Table 2. Per Table 2, as the Ni content increased, the concentration of oxygen vacancies gradually decreased but was higher than that of the pure CeO_2, indicating that the introduction of Ni promotes the formation of oxygen vacancies on CeO_2 surface, which was consistent with the Raman results.

Figure 7 shows the XPS peaks of Ni $2_{p3/2}$ for all catalysts. In addition to the satellite shake-up peak of Ni at about 861.0 eV, three fitting peaks represented three kinds of Ni species with different chemical states, namely α, β, and γ, which were assigned to Ni^0 (~852.4 eV), Ni^{2+} (~854.7 eV), and Ni^{3+} (~856.8 eV), respectively. Three kinds of Ni species coexisted on the surface of the Ni/CeO_2 catalysts. According to previous research [30,33,34], highly dispersed Ni clusters can interact with CeO_2 support to generate

the Ni–O–Ce structure, in which case the outer electrons of Ni would transfer to the 4f orbital of Ce through the Ni–O–Ce bond, which would result in the formation of Ni^{2+} or $Ni^{\delta+}$. Ni^{3+} ions should come from Ni species that enter into the CeO_2 lattice and form a $Ni_xCe_{1-x}O_{2-y}$ solid solution with CeO_2 [35]. According to the peak area of different Ni species, the proportionate relationship among different Ni species was estimated, and the results are listed in Table 2. From Table 2, as Ni loading increased, the content of Ni^0 gradually increased, while the content of Ni^{2+} gradually decreased. This was due to the fact that when the content of loaded Ni was low, the Ni particles with smaller size were highly dispersed on the surface of the catalyst and had stronger interaction with CeO_2 support, which made the outer electrons of Ni easily transfer to CeO_2, thus forming more Ni^{2+}. However, the increase in Ni loading led to the growth of the Ni particle size, which weakened the electron induction effect of CeO_2 on Ni and led to the decrease in Ni^{2+} content. In addition, the relative content of Ni^{3+} was relatively low for all xNi/CeO_2 catalysts, which means that only a small amount of Ni formed a $Ni_xCe_{1-x}O_{2-y}$ solid solution with the CeO_2 support because of the limitation of the loading method (the impregnation method).

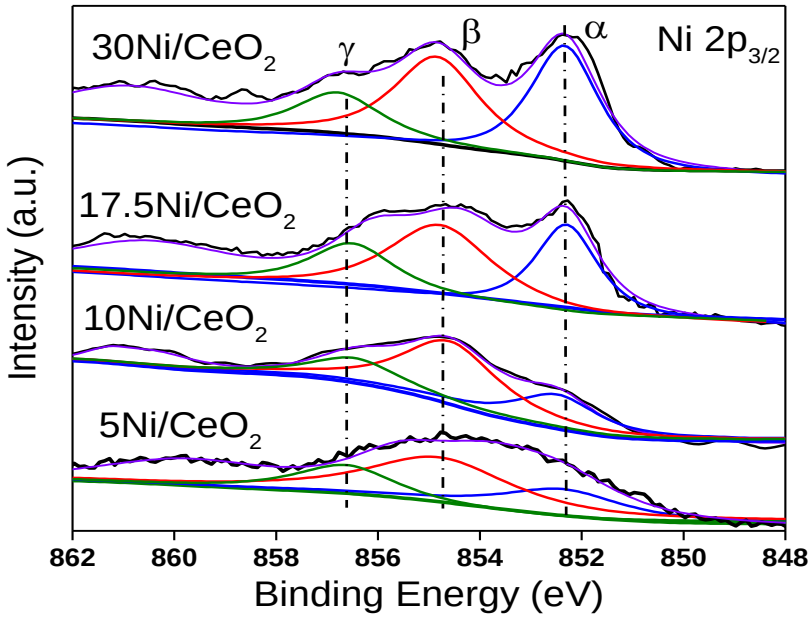

Figure 7. The Ni $2p_{3/2}$ core-level XPS spectra of the xNi/CeO_2 catalysts.

The H_2-TPD characterization results of the CeO_2 support and each catalyst are listed in Figure 8. As shown in Figure 8A, the CeO_2 support had the ability to activate and adsorb H_2 before and after reduction at 350 °C, and the oxygen vacancies had a great influence on the form of existence for the adsorption of H_2 [36]. In order to further study the hydrogen species on CeO_2 surface, H_2-TPD combined with a mass spectrometer (MS) was used to detect the desorbed H_2 species. Figure 9A shows that H_2 was desorbed in the form of H_2O in the range of 150–400 °C on the surface of unreduced CeO_2 (labelled CeO_2), indicating that the adsorption of H_2 on the surface was irreversible, and OH groups were generated on the surface of the support. In contrast, as shown in Figure 9B, on the surface of reduced CeO_2 (labelled CeO_2-350), the adsorbed atomic H was desorbed from the CeO_2 surface in the form of H_2 at about 80 °C, meaning that the oxygen vacancies on the surface of reduced CeO_2 were favorable for the reversible adsorption of H_2, which was consistent with literature reports [37].

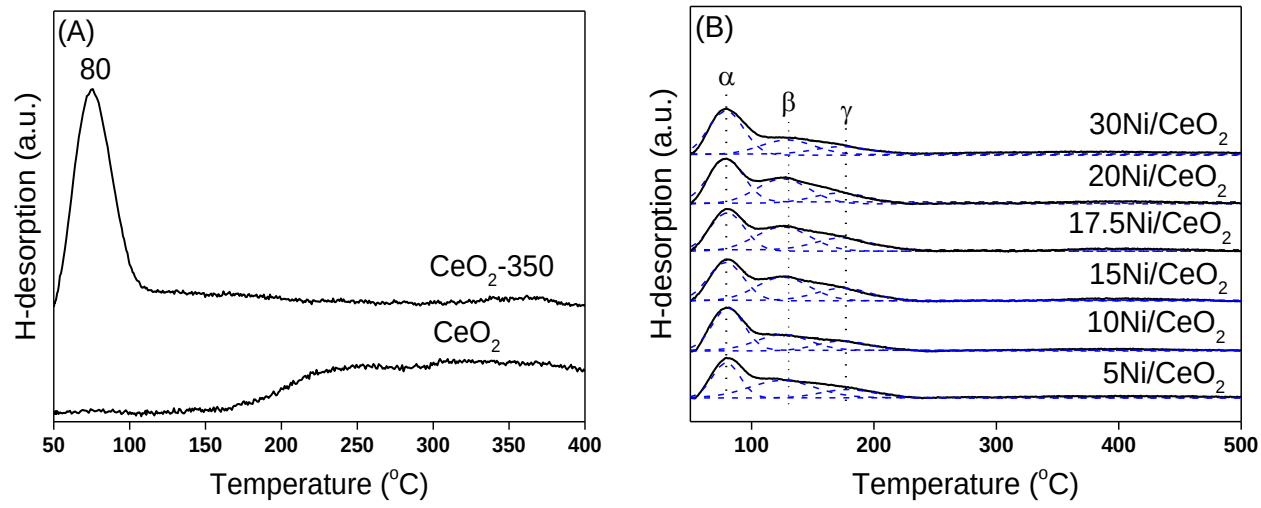

Figure 8. H_2-TPD profiles of (**A**) the unreduced CeO_2 and reduced CeO_2 support (CeO_2-350) and (**B**) xNi/CeO_2 catalysts.

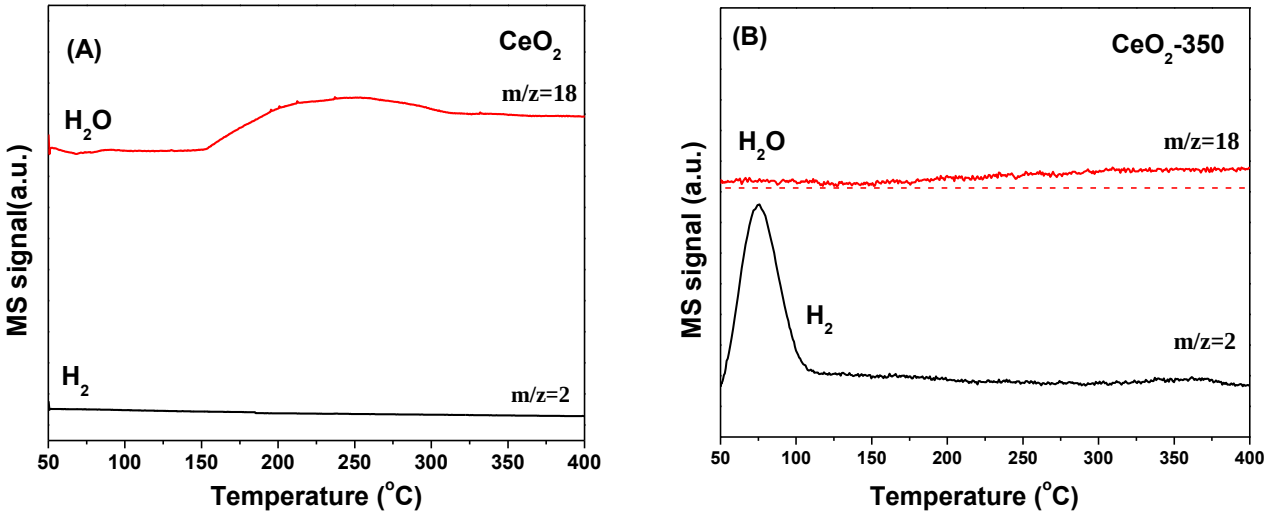

Figure 9. H_2-TPD-MS profiles of (**A**) unreduced CeO_2 (CeO_2) and (**B**) reduced CeO_2 (CeO_2-350) samples.

As shown in Figure 8B, xNi/CeO_2 catalysts with different Ni loadings had similar H_2-TPD spectra. The desorption peak was fitted into three desorption peaks by the Gaussian method. The desorption peak (α peak) at about 80 °C was similar to the H_2 desorption peak of CeO_2 after reduction and was attributed to the desorption of H_2 from the support surface. The desorption peaks β and γ were attributed to the desorption of H_2 adsorbed on different Ni species. The β peak could be assigned to the H_2 desorption of Ni species at the Ni–CeO_2 interface. The strong interaction between Ni and CeO_2 support weakened the binding ability of Ni species to H_2 and then lowered the energy barrier of H_2 desorption. The desorption peak γ (at 178 °C) was assigned to the desorption of hydrogen species adsorbed on the surface of Ni in bulk phase, which was similar to the H_2 desorption on the Ni surface in Ni/Al_2O_3 and Ni/SiO_2 systems and indicated that the support had little influence on the H_2 adsorption capacity on Ni species here [38]. It can be concluded that different Ni species on the xNi/CeO_2 surface had different adsorption and activation abilities for H_2.

Based on H_2-TPD results, H_2 adsorption volumes at different active sites were estimated and correlated with Ni loading. Figure 10A shows that compared with reduced CeO_2, the H_2 adsorption capacity of xNi/CeO_2 catalysts greatly increased, confirming that

Ni was the center of adsorption and activation of H_2. For all xNi/CeO_2 catalysts, as the Ni loading increased, the amount of adsorbed H_2 on the catalyst first increased and then decreased gradually. A possible reason for this is that as the Ni loading increased, the Ni particles aggregated on the surface of CeO_2, and the grain size became larger, which may have reduced the number of active sites for H_2 adsorption. Figure 10B shows that the peak area of α desorption for 5Ni/CeO_2 was the largest among the samples. The peak area of the other samples decreased as the Ni loading increased, which indicates that the 5Ni/CeO_2 catalyst possessed the highest concentration of oxygen vacancies for H_2 adsorption. According to Raman and XPS results, excessive Ni was not conducive to the formation of oxygen vacancies on the surface and inhibited the ability of oxygen vacancies to activate hydrogen [39]. In addition, as the Ni loading increased, the peak areas of β and γ increased gradually in the beginning and then decreased obviously after 17.5Ni/CeO_2. The results showed that a proper amount of Ni loading was helpful to increase the number of active sites on the support surface, while an excessive amount of Ni loading may have led to the aggregation and growth of Ni species, which could reduce the surface area of Ni particles and the number of active sites on the surface.

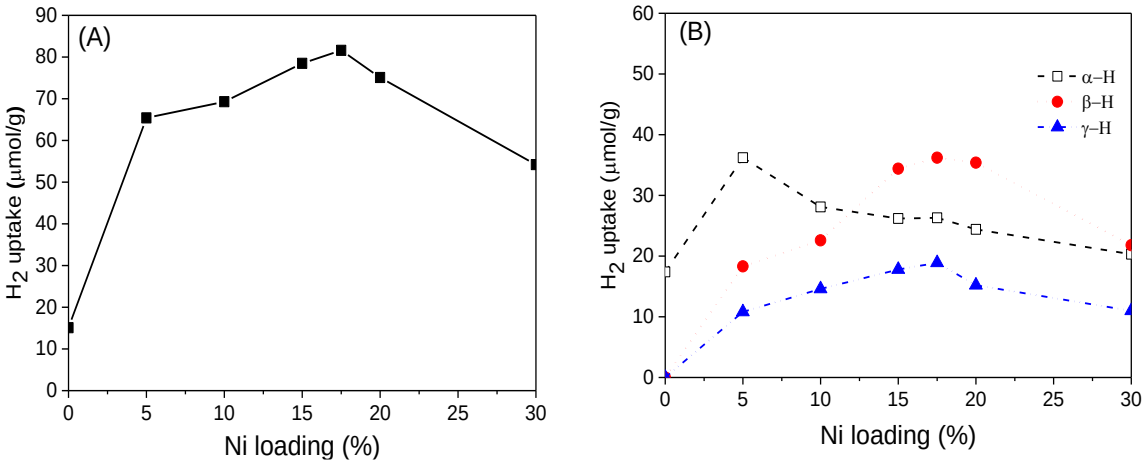

Figure 10. The total (**A**) and site-defined (**B**) hydrogen uptake on the xNi/CeO_2 catalyst.

3.2. Catalytic Performance

Figure 11 shows the conversion curves of maleic anhydride (MA) over xNi/CeO_2 catalysts and reduced CeO_2 support at 210 °C and 5 MPa. After a reaction time of 1 h, the conversion of MA for all xNi/CeO_2 catalysts was close to 100%, and the main product was succinic anhydride (SA), indicating that all xNi/CeO_2 catalysts showed high hydrogenation activity for the C=C bond. It is noteworthy that the reduced CeO_2 carrier also had a certain ability of MAH and that the conversion of MA was about 30% after 1 h under the same conditions. When Ni species were loaded on the surface of CeO_2, the activity of MA hydrogenation increased sharply, indicating that Ni was the main active site for the MAH reaction. For all xNi/CeO_2 catalysts, in the initial time, the catalytic activity for MAH increased gradually as Ni content increased until 17.5 wt%, and then the conversion of MA decreased slightly until 1 h.

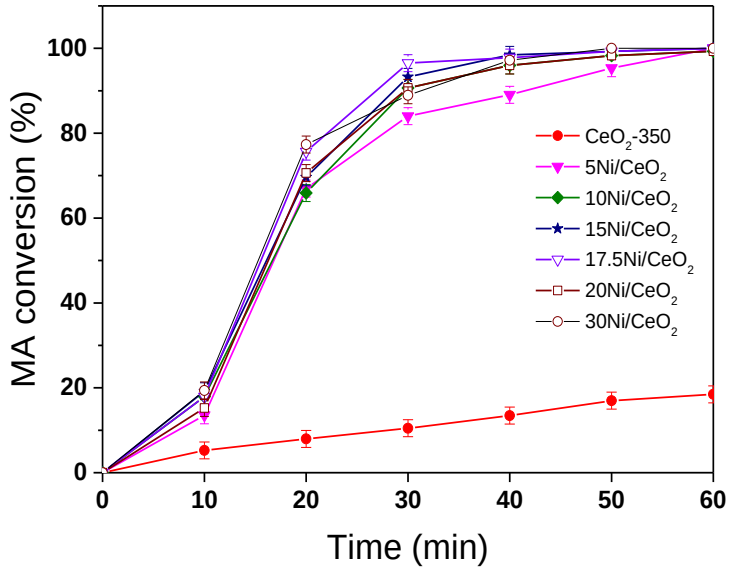

Figure 11. The conversion of MA on reduced the xNi/CeO_2 catalysts.

In order to further investigate the C=C hydrogenation performance of xNi/CeO_2 catalysts, the turnover frequency values for MA to SA ($TOF_{MA\rightarrow SA}$) over the active Ni were calculated and correlated with the oxygen vacancies, Ni species, and Ni loading content. As shown in Figure 12, the $TOF_{MA\rightarrow SA}$ of the xNi/CeO_2 catalysts decreased as the Ni content increased, which was consistent with the change trend of oxygen vacancies on the surface, indicating that the oxygen vacancies of the catalyst also played an important role in the C=C hydrogenation of MA. According to H_2-TPR and H_2-TPD results, oxygen vacancies not only improved the dissociation and adsorption capacity of H_2 on the catalyst but promoted the diffusion of active H on the catalyst surface, providing more active H species for the hydrogenation reaction [37]. Moreover, according to theoretical calculations, oxygen vacancies with rich electron structure can provide electrons to the active metal and enhance the electron-giving ability of the active metal, thus improving the C=C hydrogenation performance of the metal [40]. For the xNi/CeO_2 catalytic system, it can be speculated that the synergistic effect between active metal Ni and oxygen vacancies (Ovac) could have improved the C=C hydrogenation performance of Ni.

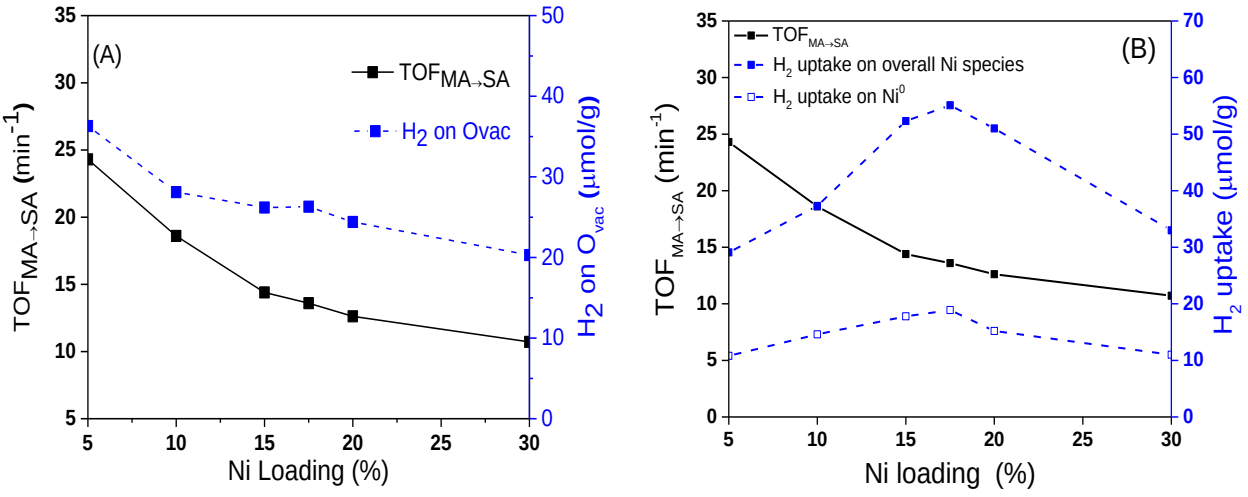

Figure 12. Effect of Ovac (**A**) and surface Ni species (**B**) on the $TOF_{MA\rightarrow SA}$ over the xNi/CeO_2 catalysts.

Figure 13A shows the trend of SA selectivity with reaction time on different catalysts. From Figure 13A and B, the selectivity of SA for all xNi/CeO_2 catalysts was around 100% at the initial reaction time of 40 min and then decreased gradually while the selectivity of γ-butyrolactone (GBL) increased gradually. The selectivity of GBL on the 17.5Ni/CeO_2 catalyst was the highest (about 35.7%) after 8 h compared with the other xNi/CeO_2 catalysts. In addition, the selectivity of SA on the CeO_2 support remained at 100% within 8 h of the reaction, indicating that the CeO_2 support had almost no hydrogenation activity for the C=O bond. The above results identify that the metal Ni was the active center for the hydrogenation of SA to GBL and that the content of Ni loading significantly affected the C=O hydrogenation over the catalyst. As for the stability of the xNi/CeO_2 catalysts, it should be noted that all samples showed good stability in the hydrogenation process. After a reaction time of 1 h, the conversion of MA for all xNi/CeO_2 catalysts was close to 100%, and the catalysts kept their high catalytic performance. Furthermore, after five cycles of use, all the catalysts kept their high activity and selectivity, and there was no obvious decrease in either. In addition, the stability of the 17.5Ni/CeO_2 catalyst had no obvious change compared with other catalysts in the MAH process.

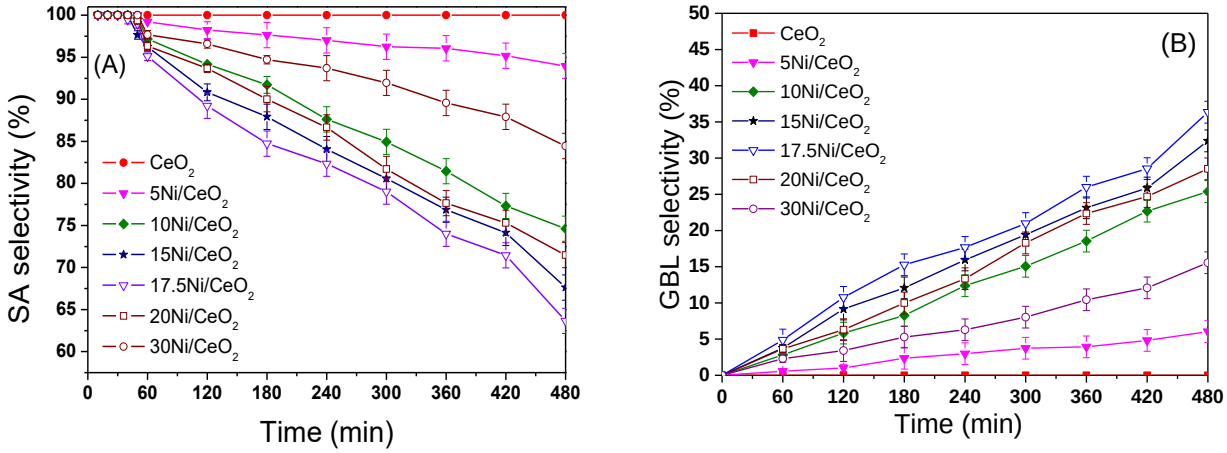

Figure 13. The selectivity of SA (**A**) and GBL (**B**) on reduced the xNi/CeO_2 catalysts.

It has been reported that the metal Ni with certain grain size is the active center of hydrogenation of SA to GBL. Meyer et al. [17] studied the effect of Ni loading on the hydrogenation of MA and found that Ni/SiO_2–Al_2O_3 catalyst had hydrogenation activity for C=O only when Ni loading was more than 8 wt%. They concluded that a certain size of Ni grain was the active center for the hydrogenation of SA to GBL. In this work, the selectivity of GBL also showed a strong dependence on the particle size of Ni. However, when the particle size of Ni exceeded a certain amount (17.5 nm), the hydrogenation activity of C=O started to decrease. For example, though the average sizes of Ni particles on the 20Ni/CeO_2 (18.9 nm) and 30Ni/CeO_2 catalysts (36.6 nm) were larger than that of the 17.5Ni/CeO_2 catalyst (17.5 nm), the selectivities of GBL were lower than that of 17.5Ni/CeO_2 (as shown in Figure 13B).

In order to understand deeply the influence of catalysts on the hydrogenation activity of C=O, the values of $TOF_{SA\rightarrow GBL}$ over different catalysts were calculated. As shown in Figure 14, as the Ni loading increased, the value of $TOF_{SA\rightarrow GBL}$ gradually increased. When the content of Ni was 17.5 wt%, the value of $TOF_{SA\rightarrow GBL}$ reached the maximum. It then rapidly decreased as the Ni loading increased further. At the same time, the H_2 concentration adsorbed on Ovac decreased monotonously as the Ni loading increased. The volcanic curve for $TOF_{SA\rightarrow GBL}$ showed that the hydrogenation of SA to GBL was structure sensitive, which is quite different from the trend of $TOF_{MA\rightarrow SA}$ in Figure 12A.

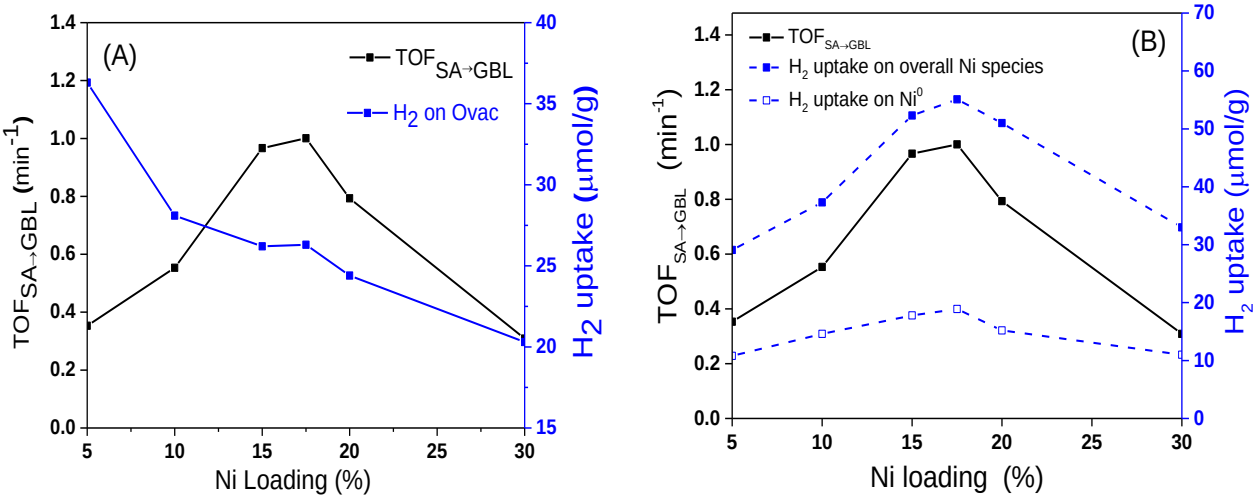

Figure 14. Effect of Ovac (**A**) and surface Ni species (**B**) on the $TOF_{SA\rightarrow GBL}$ over the xNi/CeO_2 catalysts.

According to previous research [41–43], for reducible supports, such as TiO_2 and CeO_2, the metal–support interface is considered to be the active site of C=O adsorption activation. It was found that the C=O functional groups could be adsorbed and polarized at the interfaces of Pt–TiOx and Ni–TiOx and that the catalytic activity of hydrogenation for crotonaldehyde to crotonyl alcohol was significantly improved [41]. Because of strong interaction with the carrier, the electronic configuration for most of the metal particles at the interface was in an ionic state (such as Ni^{2+} at the interface of Ni–TiO_2). These ionic metal particles could play the role of a Lewis acid and participate in the adsorption and activation of C=O functional groups [42]. In addition, in the hydrogenation reaction of citral, a small amount of Ni^{2+} at the Ni–TiO_2 interface promoted the adsorption and activation of C=O in the citral molecule and finally improved the selectivity of the hydrogenation of citral to citric alcohol [41,43].

As shown in Figure 14B, the change trend of $TOF_{SA\rightarrow GBL}$ was consistent with the change in the total amount of H_2 adsorbed on the active sites of interface Ni and bulk Ni, which indicates that both the interfacial Ni and bulk Ni^0 could catalyze the hydrogenation reaction of the C=O bond. According to the characterization results of H_2-TPR, H_2-TPD, and XPS, the Ni species at the interface showed a valence state of $Ni^{\delta+}$ because of the strong interaction with the CeO_2 support [34]. Therefore, it can be inferred that $Ni^{\delta+}$ at the interface could also promote the adsorption of C=O on the catalyst surface as the Lewis acid site. Based on the catalytic effect of metal Ni on the adsorption and activation of C atoms in C=O and subsequent C–O bond breaking [33], we propose the possible mechanism of the $Ni^{\delta+}$–Ni^0 synergistic effect on the hydrogenation reaction of C=O. As shown in Figure 15, first, the metal Ni^0 adsorbs and activates C atoms in the C=O functional group, and $Ni^{\delta+}$ at the interface acts as a Lewis acid to synergistically activate O atoms. Second, the synergistic effect of $Ni^{\delta+}$ and Ni^0 promotes the adsorption and activation of C=O, and the activated C=O group reacts with highly active hydrogen atoms on the surface of metal Ni, which results in the C=O bond hydrogenation and subsequent C–O fracture. According to this mechanism, if the particle size of Ni becomes larger, the distance between the top Ni^0 and the bottom $Ni^{\delta+}$ increases, which weakens the synergistic activation for C=O by $Ni^{\delta+}$–Ni^0. This constitutes a good explanation for the phenomenon in which the selectivity of GBL decreased as the average particle size of Ni increased beyond 17.5 nm.

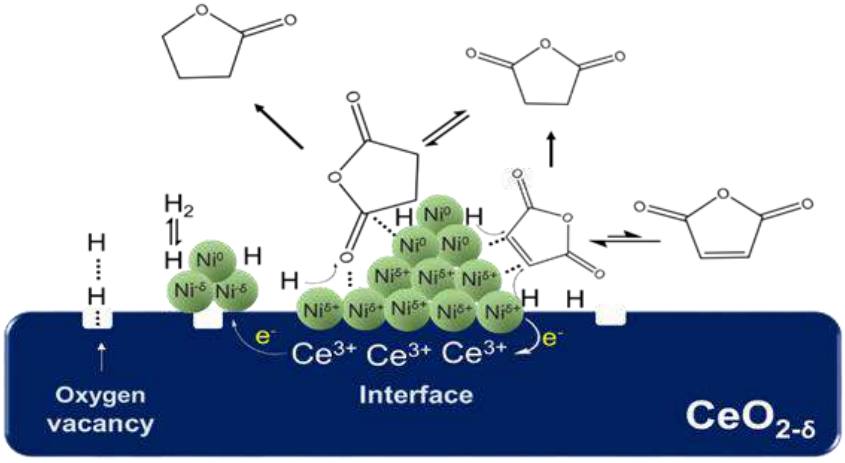

Figure 15. The synergy of $Ni^{\delta+}$–Ni^0 in C=O hydrogenolysis over Ni/CeO_2 catalyst.

4. Conclusions

In this work, Ni/CeO_2 catalysts were synthesized by the impregnation method, and a series of xNi/CeO_2 catalysts with different particle sizes and active sites were successfully prepared by changing the Ni loading. The effects of particle size and active sites of Ni/CeO_2 on the hydrogenation of MA were systematically studied. It was found that the catalytic activity of the xNi/CeO_2 catalysts was size dependent for MAH and that the metal Ni was the active center for the catalytic hydrogenation of C=C from MA to SA and of C=O from SA to GBL. In the beginning of the reaction, the hydrogenation activity of the catalyst increased as the Ni loading increased until $17.5Ni/CeO_2$ and then decreased gradually as the Ni loading increased further. The oxygen vacancies on the surface of Ni/CeO_2 could promote the adsorption and activation of H_2, and the synergistic effect of active metal Ni and oxygen vacancies could improve the hydrogenation of the C=C bond. The synergistic effect of $Ni^{\delta+}$ species obtained from the strong electronic attraction of the CeO_2 support and Ni^0 promoted the adsorption and activation of C=O in MAH. The current results confirmed that the particle size and catalytic ability of Ni/CeO_2 catalysts could be modulated through changing the Ni loading on the CeO_2 support. This work not only provides a deep understanding of MA hydrogenation over Ni/CeO_2 catalysts but highlights the potential of size-dependent catalysts in heterogeneous catalysis.

Author Contributions: Conceptualization, H.W., Y.Z. (Yin Zhang) and Y.Z. (Yongxiang Zhao); methodology, Q.Z.; formal analysis, S.L.; writing—original draft preparation, Q.Z. and X.L.; writing—review and editing, H.W. and Y.Z. (Yin Zhang); supervision, Y.Z. (Yongxiang Zhao); funding acquisition, Y.Z. (Yongxiang Zhao). All authors have read and agreed to the published version of the manuscript.

Funding: This research was funded by the National Natural Science Foundation (U1710221, 21303097, 22075167) and the Shanxi Province International Science and Technology Cooperation Program Project (201803D421074).

Institutional Review Board Statement: Not applicable.

Informed Consent Statement: Not applicable.

Data Availability Statement: Data presented in this article are available at request from the corresponding author.

Conflicts of Interest: The authors declare no conflict of interest.

References

1. Meyer, C.I.; Regenhardt, S.A.; Marchi, A.J.; Garetto, T.F. Gas phase hydrogenation of maleic anhydride at low pressure over silica-supported cobalt and nickel catalysts. *Appl. Catal. A* **2012**, *417–418*, 59–65. [CrossRef]
2. Papageorgiou, G.Z.; Grigoriadou, I.; Andriotis, E.; Bikiaris, D.N.; Panayiotou, C. Miscibility and Properties of New Poly(propylene succinate)/Poly(4-vinylphenol) Blends. *Ind. Eng. Chem. Res.* **2013**, *52*, 11948–11955. [CrossRef]
3. Bertone, M.E.; Meyer, C.I.; Regenhardt, S.A.; Sebastian, V.; Garetto, T.F.; Marchi, A.J. Highly selective conversion of maleic anhydride to γ-butyrolactone over Ni-supported catalysts prepared by precipitation–deposition method. *Appl. Catal. A Gen.* **2015**, *503*, 135–146. [CrossRef]
4. Liao, X.; Zhang, Y.; Hill, M.; Xia, X.; Zhao, Y.; Jiang, Z. Highly efficient Ni/CeO_2 catalyst for the liquid phase hydrogenation of maleic anhydride. *Appl. Catal. A* **2014**, *488*, 256–264. [CrossRef]
5. Gao, C.G.; Zhao, Y.X.; Zhang, Y.; Liu, D.S. Synthesis characterization and catalytic evaluation of $Ni/ZrO_2/SiO_2$ aerogels catalysts. *J. Sol.-Gel. Sci. Technol.* **2007**, *44*, 145–151. [CrossRef]
6. Yang, Y.P.; Zhang, Y.; Gao, C.G.; Zhao, Y.X. Selective Hydrogenation of Maleic Anhydride to γ-Butyrolactone over TiOx (x < 2) Surface-Modified Ni/TiO_2-SiO_2 in Liquid Phase. *Chin. J. Catal.* **2011**, *32*, 1768–1774.
7. Englisch, M.; Jentys, A.; Lercher, J.A. Structure Sensitivity of the Hydrogenation of Crotonaldehyde over Pt/SiO_2 and Pt/TiO_2. *J. Catal.* **1997**, *166*, 25–35. [CrossRef]
8. Che, M.; Bennett, C.O. The influence of particle size on the catalytic properties of supported metals. *Adv. Catal.* **1989**, *36*, 55–172.
9. Nørskov, J.K.; Bligaard, T.; Hvolbæk, B.; Abild-Pedersen, F.; Chorkendorff, I.; Christensen, C.H. The nature of the active site in heterogeneous metal catalysis. *Chem. Soc. Rev.* **2008**, *37*, 2163. [CrossRef]
10. Wang, H.; Lu, J. A review on particle size effect in metal-catalyzed heterogeneous reactions. *Chin. J. Chem.* **2019**, *38*, 1422–1444. [CrossRef]
11. Breejen, J.P.; Radstake, P.B.; Bezemer, G.L.; Bitter, J.H.; Frøseth, V.; Holmen, A.; de Jong, K.P. On the origin of the cobalt particle size effects in Fischer-Tropsch catalysis. *J. Am. Chem. Soc.* **2009**, *131*, 7197–7203. [CrossRef] [PubMed]
12. Chen, S.; Luo, L.; Jiang, Z.; Huang, W. Size-dependent reaction pathways of lowtemperature CO oxidation on Au/CeO_2 catalysts. *ACS Catal.* **2015**, *5*, 1653–1662. [CrossRef]
13. Li, J.; Chen, W.; Zhao, H.; Zheng, X.; Wu, L.; Pan, H.; Zhu, J.; Chen, Y.; Lu, J. Sizedependent catalytic activity over carbon-supported palladium nanoparticles in dehydrogenation of formic acid. *J. Catal.* **2017**, *352*, 371–381. [CrossRef]
14. Zhang, X.; Gu, Q.; Ma, Y.; Guan, Q.; Jin, R.; Wang, H.; Yang, B.; Lu, J. Support-induced unusual size dependence of Pd catalysts in chemoselective hydrogenation of para-chloronitrobenzene. *J. Catal.* **2021**, *400*, 173–183. [CrossRef]
15. Zhao, Y.X.; Qin, X.Q.; Wu, Z.G.; Xu, L.P.; Liu, D.S. Comparison of selective hydrogenation of maleic anhydride over NiO-SiO_2, NiO-Al_2O_3 and NiO-Al_2O_3-SiO_2 catalysts. *J. Fuel Chem. Technol.* **2003**, *31*, 263–266.
16. Li, J.; Tian, W.; Shi, L. Hydrogenation of Maleic Anhydride to Succinic Anhydride over Ni/HY-Al_2O_3. *Ind. Eng. Chem. Res.* **2010**, *49*, 11837–11840. [CrossRef]
17. Meyer, C.I.; Regenhardt, S.A.; Bertone, M.E. Gas-Phase Maleic Anhydride Hydrogenation Over Ni/SiO_2–Al_2O_3 Catalysts: Effect of Metal Loading. *Catal. Lett.* **2013**, *143*, 1067–1073. [CrossRef]
18. Ma, K.X.; Liao, W.Q.; Shi, W.; Xu, F.K.; Zhou, Y.; Tang, C.; Lu, J.Q.; Shen, W.J.; Zhang, Z.H. Ceria-supported Pd catalysts with different size regimes ranging from single atoms to nanoparticles for the oxidation of CO. *J. Catal.* **2022**, *407*, 104–114. [CrossRef]
19. Liao, X.; Zhang, Y.; Guo, J.; Zhao, L.; Hill, M.; Jiang, Z.; Zhao, Y. The Catalytic Hydrogenation of Maleic Anhydride on CeO_2-delta-Supported Transition Metal Catalysts. *Catalysts* **2017**, *7*, 272. [CrossRef]
20. Liu, S.B.; Liao, X.; Zhang, Q.M.; Zhang, Y.; Wang, H.; Zhao, Y.X. Crystal-Plane and Shape Influences of Nanoscale $CeO_2$2 on the Activity of Ni/CeO_2 Catalysts for Maleic Anhydride Hydrogenation. *Nanomaterials* **2022**, *12*, 762. [CrossRef]
21. Matte, L.P.; Kilian, A.S.; Luza, L.; Alves, M.C.M.; Morais, J.; Baptista, D.L.; Dupont, J.; Bernardi, F. Influence of the CeO2 Support on the Reduction Properties of Cu/CeO_2 and Ni/CeO_2 Nanoparticles. *J. Phys. Chem. C* **2015**, *119*, 26459–26470. [CrossRef]
22. Deraz, N.M. Effect of NiO content on structural, surface and catalytic characteristics of nano-crystalline NiO/CeO_2 system. *Ceram. Int.* **2012**, *38*, 747–753. [CrossRef]
23. Wang, N.; Qian, W.; Chu, W.; Wei, F. Crystal-plane effect of nanoscale CeO_2 on the catalytic performance of Ni/CeO_2 catalysts for methane dry reforming. *Catal. Sci. Technol.* **2016**, *6*, 3594–3605. [CrossRef]
24. Shan, W. Reduction property and catalytic activity of Ce1-$XNiXO_2$ mixed oxide catalysts for CH_4 oxidation. *Appl. Catal. A* **2003**, *246*, 1–9.
25. Wu, Z.L.; Li, M.J.; Howe, J.; Meyer, H.M.; Overbury, S.H. Probing defect sites on CeO_2 nanocrystals with well-defined surface planes by Raman spectroscopy and O_2 adsorption. *Langmuir* **2010**, *26*, 16595–16606. [PubMed]
26. Barrio, L.; Kubacka, A.; Zhou, G.; Estrella, M.; Arias, A.M.; Hanson, J.C.; García, M.F.; Rodriguez, J.A. Unusual Physical and Chemical Properties of Ni in $Ce_{1-x}NixO_{2-y}$ Oxides: Structural Characterization and Catalytic Activity for the Water Gas Shift Reaction. *J. Phys. Chem. C* **2010**, *114*, 12689–12697. [CrossRef]
27. Spanier, J.E.; Robinson, R.D.; Zhang, F.; Chan, S.W.; Herman, I.P. Size-dependent properties of CeO_{2-y} nanoparticles as studied by Raman scattering. *Phys. Rev. B* **2001**, *64*, 245407. [CrossRef]
28. Burroughs, P.; Hamnett, A.; Orchard, A.F.; Thornton, G. Satellite structure in the X-ray photoelectron spectra of some binary and mixed oxides of lanthanum and cerium. *J. Chem. Soc. Dalton Trans.* **1976**, *17*, 1686–1698. [CrossRef]

29. Nelson, A.E.; Schulz, K.H. Surface chemistry and microstructural analysis of $CexZr_{1-x}O_{2-y}$ model catalyst surfaces. *Appl. Surf. Sci.* **2003**, *210*, 206–221. [CrossRef]
30. Campbell, C.T. Catalyst-support interactions: Electronic perturbations. *Nat. Chem.* **2012**, *4*, 597–598. [CrossRef]
31. Branda, M.M.; Hernández, N.C.; Sanz, J.F.; Illas, F. Density Functional Theory Study of the Interaction of Cu, Ag, and Au Atoms with the Regular CeO_2(111) Surface. *J. Phys. Chem. C* **2010**, *114*, 1934–1941. [CrossRef]
32. Soler, L.; Casanovas, A.; Urrich, A.; Angurell, I.; Llorca, J. CO oxidation and COPrOx over preformed Au nanoparticles supported over nanoshaped CeO_2. *Appl. Catal. B* **2016**, *197*, 47–55. [CrossRef]
33. Carrasco, J.; Rodriguez, J.A.; Lopez-Duran, D.; Liu, Z.Y.; Duchon, T.; Evans, J.; Senanayake, S.D.; Crumlin, E.J.; Matolin, V.; Ganduglia-Pirovano, M.V. In situ and theoretical studies for the dissociation of water on an active Ni/CeO_2 catalyst: Importance of strong metal-support interactions for the cleavage of O-H bonds. *Angew. Chem. Int. Ed.* **2015**, *54*, 3917–3921. [CrossRef]
34. He, L.; Liang, B.L.; Li, L.; Yang, X.F.; Huang, Y.Q.; Wang, A.Q.; Wang, X.D.; Zhang, T. Cerium-Oxide-Modified Nickel as a Non-Noble Metal Catalyst for Selective Decomposition of Hydrous Hydrazine to Hydrogen. *ACS Catal.* **2015**, *5*, 1623–1628. [CrossRef]
35. Tang, K.; Liu, W.; Li, J.; Guo, J.X.; Zhang, J.C.; Wang, S.P.; Niu, S.L.; Yang, Y.Z. The Effect of Exposed Facets of Ceria to the Nickel Species in Nickel-Ceria Catalysts and Their Performance in a NO+CO Reaction. *ACS Appl. Mater. Interfaces* **2015**, *7*, 26839–26849. [CrossRef]
36. Chen, B.H.; Ma, Y.S.; Ding, L.B.; Xu, L.S.; Wu, Z.F.; Yuan, Q.; Huang, W.X. Reactivity of Hydroxyls and Water on a CeO_2(111) Thin Film Surface: The Role of Oxygen Vacancy. *J. Phys. Chem. C* **2013**, *117*, 5800–5810. [CrossRef]
37. Wu, X.P.; Gong, X.Q.; Lu, G. Role of oxygen vacancies in the surface evolution of H at CeO_2(111): A charge modification effect. *Phys. Chem. Chem. Phys.* **2015**, *17*, 3544–3549. [CrossRef]
38. Znak, L.; Zieliński, J. Effects of support on hydrogen adsorption/desorption on nickel. *Appl. Catal. A Gen.* **2008**, *334*, 268–276. [CrossRef]
39. Hahn, K.R.; Seitsonen, A.P.; Iannuzzi, M.; Hutter, J. Functionalization of CeO_2(111) by Deposition of Small Ni Clusters: Effects on CO_2 Adsorption and O Vacancy Formation. *ChemCatChem* **2015**, *7*, 625–634. [CrossRef]
40. Zhang, S.; Li, J.; Xia, Z.; Wu, C.; Zhang, Z.; Ma, Y.; Qu, Y. Towards highly active Pd/CeO_2 for alkene hydrogenation by tuning Pd dispersion and surface properties of the catalysts. *Nanoscale* **2017**, *9*, 3140–3149. [CrossRef]
41. Dandekar, A.; Vannice, M.A. Crotonaldehyde Hydrogenation on Pt/TiO_2 and Ni/TiO_2 SMSI Catalysts. *J. Catal.* **1999**, *183*, 344–354. [CrossRef]
42. Rodriguez, J.A.; Grinter, D.C.; Liu, Z.Y.; Palomino, R.M.; Senanayake, S.D. Ceria-based model catalysts: Fundamental studies on the importance of the metal-ceria interface in CO oxidation, the water-gas shift, CO_2 hydrogenation, and methane and alcohol reforming. *Chem. Soc. Rev.* **2017**, *46*, 1824–1841. [PubMed]
43. Prakash, M.G.; Mahalakshmy, R.; Krishnamurthy, K.R.; Viswanathan, B. Selective hydrogenation of cinnamaldehyde on nickel nanoparticles supported on titania: Role of catalyst preparation methods. *Catal. Sci. Technol.* **2015**, *5*, 3313–3321. [CrossRef]

nanomaterials

MDPI

Article

Crystal-Plane and Shape Influences of Nanoscale CeO_2 on the Activity of Ni/CeO_2 Catalysts for Maleic Anhydride Hydrogenation

Shaobo Liu, Xin Liao, Qiuming Zhang, Yin Zhang *, Hao Wang * and Yongxiang Zhao *

Engineering Research Center of Ministry of Education for Fine Chemicals, School of Chemistry and Chemical Engineering, Shanxi University, Taiyuan 030006, China; lovog@163.com (S.L.); lx2006294034@126.com (X.L.); matthwwe@163.com (Q.Z.)

* Correspondence: sxuzhy@sxu.edu.cn (Y.Z.); haowang@sxu.edu.cn (H.W.); yxzhao@sxu.edu.cn (Y.Z.)

Abstract: Through use of the hydrothermal technique, various shaped CeO_2 supports, such as nanocubes (CeO_2-C), nanorods (CeO_2-R), and nanoparticles (CeO_2-P), were synthesized and employed for supporting Ni species as catalysts for a maleic anhydride hydrogenation (MAH) reaction. The achievements of this characterization illustrate that Ni atoms are capable of being incorporated into crystal lattices and can occupy the vacant sites on the CeO_2 surface, which leads to an enhancement of oxygen vacancies. The results of the MAH reaction show that the morphology and shape of CeO_2 play an important role in the catalytic performance of the MAH reaction. The catalyst for the rod-like CeO_2-R obtains a higher catalytic activity than the other two catalysts. It can be concluded that the higher catalytic performances of rod-like CeO_2-R sample should be attributed to the higher dispersion of Ni particles, stronger support-metal interaction, more oxygen vacancies, and the lattice oxygen mobility. The research on the performances of morphology-dependent Ni/CeO_2 catalysts as well as the relative reaction strategy of MAH will be remarkably advantageous for developing novel catalysts for MA hydrogenation.

Keywords: maleic anhydride; crystal-plane; oxygen vacancies; hydrogenation; Ni/CeO_2

Citation: Liu, S.; Liao, X.; Zhang, Q.; Zhang, Y.; Wang, H.; Zhao, Y. Crystal-Plane and Shape Influences of Nanoscale CeO_2 on the Activity of Ni/CeO_2 Catalysts for Maleic Anhydride Hydrogenation. *Nanomaterials* **2022**, *12*, 762. https://doi.org/10.3390/nano12050762

Academic Editors: Simon Freakley and Alberto Villa

Received: 22 January 2022
Accepted: 21 February 2022
Published: 24 February 2022

1. Introduction

As high value-added solvents and intermediates, γ-butyrolactone (GBL), tetrahydrofuran (THF), and succinic anhydride (SA) are broadly employed in diverse industries including pesticides, machinery, military, plastics, and batteries. These fine chemicals can be prepared by means of catalytic hydrogenation of maleic anhydride (MA), which is a fundamental material that can be produced using butane in the petrochemical industry, using benzene from coal chemical's primary product, and using 5-hydroxymethyl-furfaldehyde or furfaldehyde oxidation from biomass platform compounds [1–4]. In general, the procedure of maleic anhydride hydrogenation (MAH) comprises two sorts of hydrogenation procedures, namely the catalytic hydrogenation of C=C and C=O. These two hydrogenation procedures include similar reaction conditions (pressure and temperature) and can generate a mixture of various fine chemicals [5,6]. Therefore, the novel catalysts with remarkable catalytic activity and selectivity are highly desirable in order to reduce the contamination and further purification costs for synthesizing high-quality fine chemicals.

As a fundamental support material, ceria is capable of promoting the catalytic performances of catalysts by increasing the dispersion of the active metal particles and enhancing the support-metal interactions [7,8]. Furthermore, ceria is known as an oxygen buffer because of a fast and reversible transition between Ce^{4+} and Ce^{3+}, which can provide various peculiar chemical and physical features. Hence, in a diverse range of catalytic reactions, including methane reforming, CO oxidation, NO catalytic reduction, and water-gas shift, ceria is extensively employed as an active catalyst or support material [9–13].

In our recent works [4,14], series Ni/CeO_2 catalysts were synthesized and implemented for in-depth understanding of the important role of CeO_2 in MA hydrogenation. By means of comparative research on support selection, the association of oxygen vacancies, Ni-CeO_2 interaction, interface of M-CeO_2 with the catalytic behaviors were thoroughly studied.

Very recently, a broad range of investigations has discovered that the feature of exposed lattice face has a notable impact on the catalytic behavior of CeO_2. Moreover, morphology-dependent CeO_2 has been deeply explored as a catalyst [15–23] and support [24–33] in various reactions, for instance in acetylene semi-hydrogenation, WGS reaction, and CO oxidation. Thus, the catalytic behaviors of CeO_2-supported catalysts could be optimized and improved through modification of CeO_2 morphology. Riley et al. [34] reported DFT calculation results on CeO_2 (111) surface with oxygen vacancies and proposed the doping of ceria by Ni as a means of creating oxygen vacancies and enhancing the catalytic performance of the hydrogenation of acetylene. Vilé et al. [35] discovered that the cubic CeO_2 was mostly exposed to (100) planes, while the particles of polyhedral CeO_2 were mostly exposed to (111) planes, and the particles of polyhedral CeO_2 demonstrated more considerable catalytic activity compared to the particles of cubic CeO_2 in the C_2H_2 semi-hydrogenation reaction. Moreover, the exposed (110) plane of rod-like CeO_2 illustrated more desirable catalytic performances in selective hydrogenation of nitroaromatic hydrocarbons [36]. Si and coworkers [24] prepared cubic, rod, and polyhedral shaped crystals of CeO_2 with the aid of precipitation and deposition approaches. Subsequently, the preparation of Au/CeO_2 catalysts was conducted by employing the synthesized CeO_2 as support and implemented to WGS reaction. The following trend exhibits the catalytic activities of the three considered catalysts in the WGS reactions: rod-shaped Au/CeO_2 > polyhedral $Au/CeO_2 \gg$ cubic Au/CeO_2. These investigations revealed that the exposed surface of CeO_2 represented a substantial impact on the catalytic behaviors of the active metals since the dispersion of metals on the surfaces of the supports and the strong interaction of metal–support were regarded to be the key factors for the alterations in the physicochemical characteristics of the catalyst. As a result, the Ni/CeO_2 catalyst possesses a remarkable catalytic activity in the hydrogenating process of maleic anhydride, and the morphology of CeO_2 support also has an important effect on the chemical features and catalytic behavior of the catalyst, although researchers' understanding of this aspect is limited.

In this study, based on the above discussions, three kinds of ceria, namely cube-like, rod-like, and particle-like, were prepared. By employing the impregnation technique, Ni species were dispersed on the surface of the particles of CeO_2. The fundamental purpose of the current research is to study the potential effects of the CeO_2 nano-crystal shape on the MAH reaction. It is revealed that the crystal plane and morphology of the CeO_2-support show an apparent effect on the selectivity and conversion of MAH reaction. The catalyst supported over rod-like CeO_2 obtains a substantially higher catalytic activity than the other two catalysts. The present research provides a deep understanding of nature and process of metal/oxide–carrier interactions and elucidates the optimization and synthesis technique of metal-supported catalysts; therefore, contributing to the preparation of MAH catalysts with higher product selectivity and catalytic activity.

2. Experimental Section

2.1. Catalysts Preparation

The utilized chemicals, namely, $Ni(NO_3)_2{\cdot}6H_2O$, $Ce(NO_3)_3{\cdot}6H_2O$, and NaOH were provided by the Sinopharm Chemical Reagent Co., Ltd. (Shanghai, China), and they were analytical grade and used as-purchased without pre-purification. The nanocrystals of CeO_2 with various morphologies were prepared in accordance with Mai et al.'s procedure [17]. In general, the dissolution of 16.88 g NaOH was fulfilled in 30 mL water (6.0 mol/L), and the dissolution of 1.96 g $Ce(NO_3)_3{\cdot}6H_2O$ was performed in 40 mL water (0.05 mol/mL). Subsequently, the solution of NaOH was increased dropwise into the solution of $Ce(NO_3)_3$ under stirring at ambient temperature. The prepared solution was sufficiently stirred for a further 30 min at ambient temperature and then transferred into a 100 mL Teflon bottle,

which was tightly sealed and hydrothermally processed in a stainless-steel autoclave at 180 and 100 °C for 1 day accordingly for synthesizing CeO_2 cubes (demonstrated as CeO_2-C) and rods (demonstrated as CeO_2-R). Following the cooling procedure, the resulting precipitate was collected, washed out with water, and dehydrated in a vacuum for 16 h at 80 °C. Afterwards, in a muffle oven, the obtained yellowish powder was calcined for 3 h at 500 °C for synthesizing the nanocrystals of CeO_2-R and CeO_2-C. In the case of CeO_2 particles (denoted as CeO_2-P), the synthesized process was practically the same as CeO_2-R, except the added concentration of NaOH was about 0.01 mol/L. To prepare the Ni/CeO_2 catalyst, the acquired CeO_2 supports with three morphologies were moistened with corresponding volumes of the $Ni(NO_3)_2 \cdot 6H_2O$ solution for achieving the theoretical Ni-loading of 5 wt%. The hydrated precursor was dehydrated during the night hours at 120 °C and then through calcination in air for 3 h at 450 °C for the production of NiO/CeO_2 powder. Finally, the Ni (5 wt%)/CeO_2 catalysts were achieved by means of reducing the NiO/CeO_2 for 3 h at 350 °C, denoted as 5Ni/CeO_2-R, 5Ni/CeO_2-C, and 5Ni/CeO_2-P, respectively.

2.2. Catalyst Characterizations

The outcomes of X-ray diffraction were provided through the powder diffraction of X-ray implementing a D8 Advance (Bruker, Billerica, MA, USA) (λ = 0.15418 nm, Cu Kα1 radiation) supplied with a Ni filter and Vantec detector. The findings were obtained within the 2θ zone of 10–80° through a scan speed at 3 °/min. The average crystallite size of the selected samples was evaluated by implementing the formula of Scherrer $D = K\lambda/B\cos\theta$, where K is 0.9. The materials morphologies were visualized by employing a Transmission Electron Microscope (TEM) (JEOL, JEM-2010, Tokyo, Japan). By taking advantage of the ultrasonic method, the specimens were dispersed in ethanol. The loading of Ni species of the catalysts was executed with the help of an inductively coupled plasma (ICP) spectroscopy instrument (iCAP 7400 ICP-OES, Thermo Fisher Scientific, Waltham, MA, USA). To characterize the property of a surface, the spectrum of Raman was obtained by using a Raman microscope with a 532 nm laser wavelength (HORIBA, Tokyo, Japan). The pore distribution and specific surface area of the catalysts, supports, and oxide precursors were determined through physisorption of N_2 at −196 °C employing an ASAP-2020 device (Micromeritics, Norcross, GA, USA). The specimens were pre-degassed under vacuum at 250 °C prior to assessment. The specific surface area of the specimen was evaluated according to the Brunauer–Emmett–Teller (BET) method. The distribution of pore-size was assessed by considering the adsorption isotherms employing the Barett–Joyner–Halenda (BJH) approach.

The assessments of H_2-TPR (hydrogen temperature programed reduction) and H_2-TPD (Hydrogen temperature programmed desorption) were conducted on similar device employing the Micromeritics AutoChem II 2950 system supplemented with a thermal conductivity detector. X-ray photoelectron spectra (XPS) were recorded at ambient temperature employing a SCIENTIFIC ESCALAB 250 spectrometer supplemented with a standard Al-Kα (h = 1486.6 eV). By employing the carbon contamination (C1s, 284.6 eV), the calibration of the binding energies was accomplished. To fit XPS peaks, Lorentzian/Gaussian and Shirley functions were implemented together.

2.3. Catalytic Tests

The hydrogenation of MA at liquid was executed on the catalysts of Ni/CeO_2 in a batch reactor at 5 MPa and 180 °C. Prior to MA hydrogenating, through the flow of pure H_2 in a reactor at correspondent temperature, the catalysts were pre-reduced. The 4.9 g MA and 0.1 g reduced catalysts were mixed in a 100 mL autoclave comprising THF solvent; the mixed system was subsequently purged with N_2 for the elimination of air. The reaction system was next heated to 180 °C with stirring at 500 rpm to diminish any possible mass transfer restriction. The pressure of hydrogen was kept at 5.0 MPa during the MAH reaction at the same time. The products of the reaction were scrutinized by employing a gas chromatograph (7890A, Agilent, Palo Alto, CA, USA). To verify precise separation

of each component in the products, the programmed temperature was selected. The primary temperature of the oven was increased to 120 °C from 100 °C at a ramp of 5 °C min^{-1}, and the temperatures of the detector and injector were 190 °C and 260 °C, respectively. The selectivity and conversion of MA to the product were evaluated considering the equations given below:

$$X_{MA}\ (\%) = \frac{C_{GBL} + C_{SA}}{C_{GBL} + C_{SA} + C_{MA}} \times 100\%$$

$$S_{SA}\ (\%) = \frac{C_{SA}}{C_{SA} + C_{GBL}} \times 100\%$$

where C_{MA}, C_{SA}, and C_{GBL} demonstrate the percent content of the reactant and products in the reaction sewage, respectively. S_{SA} and X_{MA} imply the *SA* selectivity and *MA* conversion.

3. Results and Discussion

3.1. Catalyst Characterization

Figure 1 demonstrates the images of HRTEM and TEM for the three nanomaterials studied. Figure 1A shows the images of TEM for the irregular nanoparticles of CeO_2 with a less-uniform length within 10–20 nm. The image of HRTEM in Figure 1D shows the clear (111), (220), (200), and (311) lattice fringes with the interplanar spacing of 0.32, 0.28, 0.20, and 0.16 nm, respectively, meaning that the particles of CeO_2-P are predominantly a hexahedral shape and surrounded by the (111) facet. Figure 1B exhibits the image of TEM for the CeO_2 nanorods, with a less-uniform length within 20–150 nm and a uniform diameter in 10 ± 1.0 nm. Figure 1E illustrates the image of HRTEM for a CeO_2 nanorod incorporated with a fast Fourier transform (FFT) assessment (inset). Considering the FTT assessment, two kinds of lattice fringe directions assigned to (200) and (220) are detected for the nanorods, which possess an interplanar spacing of 0.28 and 0.19 nm on the HRTEM image, respectively.

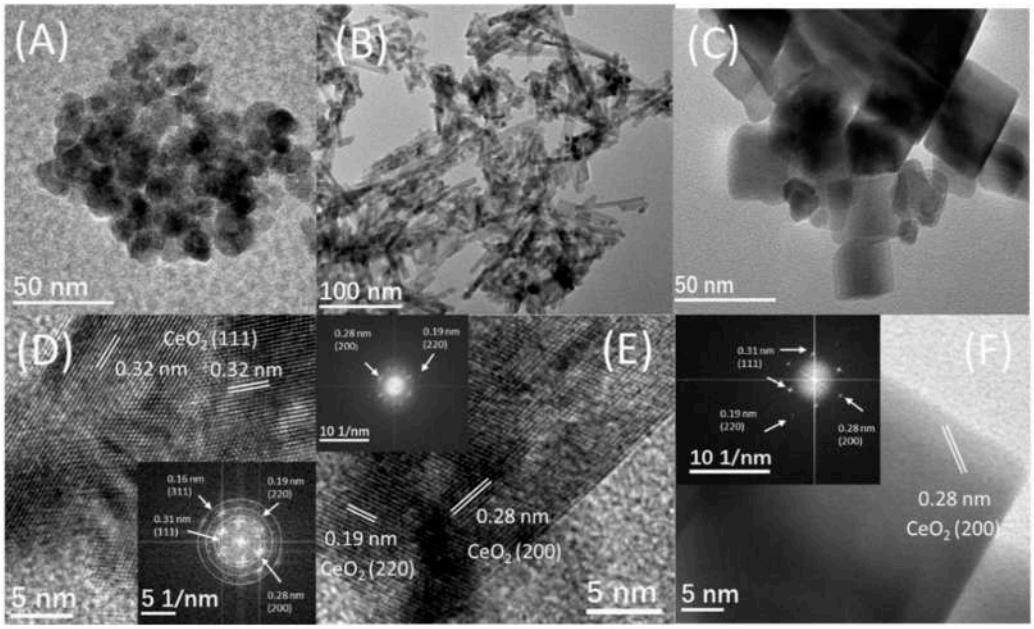

Figure 1. TEM, HRTEM, and FFT images of CeO_2-P (**A**,**D**), CeO_2-R (**B**,**E**), and CeO_2-C (**C**,**F**) supports; inset is a fast Fourier transform (FFT) analysis.

The nanorods demonstrate a 1D growth structure with a preferred growth direction along (220), and are surrounded by (200) planes, which are similar to the CeO_2 nanorods synthesized under similar hydrothermal conditions by Mai and colleagues [17]. It is worth mentioning that the surface of CeO_2 nanorods is rough, which implies the crystals have

lower crystallinity and more defect sites on their surface. The image of TEM for the uniform nanocubes of CeO_2 with the size of 10–50 nm is illustrated in Figure 1C. The image of HRTEM in Figure 1F incorporated with FFT assessment (inset) shows the apparent (220), (200), and (111) lattice fringes with the interplanar spacing of 0.19, 028, and 0.31 nm, respectively, indicating that the nanocubes of CeO_2 are surrounded by the (200) planes.

The images of TEM in Figure 2 show that three various shaped nanomaterials of ceria maintain their intrinsic crystal shapes after the impregnation of Ni and further heat processing. According to the images of HRTEM, it could be observed that the species of Ni with exposed (111) planes are uniformly dispersed on the surface of CeO_2 supports for all samples. The average sizes of Ni nanoparticles in 5Ni/CeO_2-P, 5Ni/CeO_2-R, and 5Ni/CeO_2-C samples are 3.0, 2.0–3.0, and 5.0 nm, respectively. Therefore, most of the counted Ni in the samples are supported on the faces of the nanocrystals of CeO_2 in comparison to their truncated corners and edges.

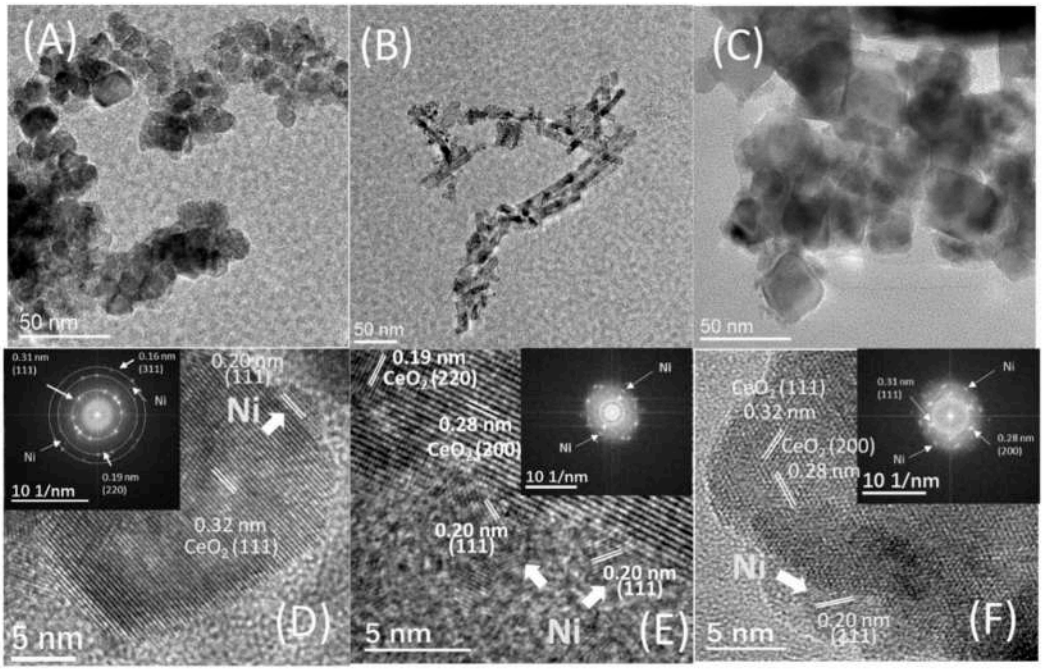

Figure 2. TEM, HRTEM, and FT images of 5Ni/CeO_2-P (**A**,**D**), 5Ni/CeO_2-R (**B**,**E**), and 5Ni/CeO_2-C (**C**,**F**) supports; inset is a fast Fourier transform (FFT) analysis.

The XRD patterns for the as-prepared supports of CeO_2 are shown in Figure 3A. The diffraction peaks related to Bragg for the CeO_2 specimen presented at 28, 33, 47, and 56○ can be described as (111), (200), (220), and (311) planes, which should belong to the fluorite-type structure of ceria with cubic crystalline (Fd3m, JCPDS file 34-0394) [37]. The weaker and wider peaks of diffraction for CeO_2-Rs indicate a lower crystallinity and smaller crystallite size in comparison with the other samples. Owing to the impurity, no other diffraction peaks can be detected.

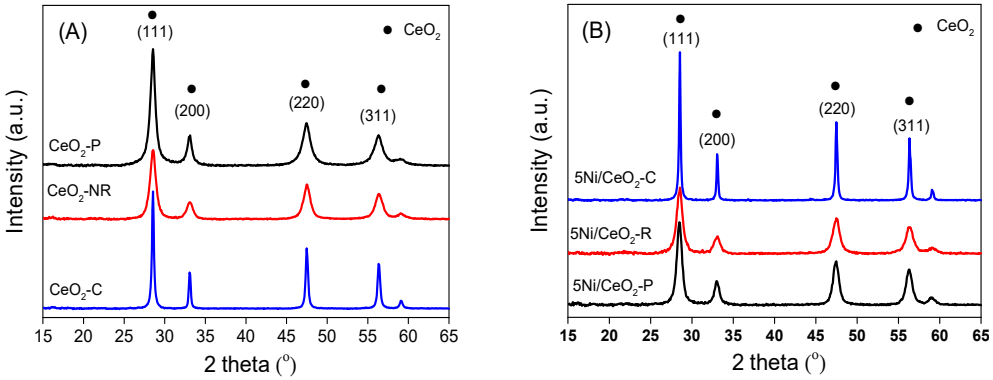

Figure 3. Patterns of XRD for different CeO_2 supports (**A**) and 5Ni/CeO_2 samples (**B**).

Following the introduction of nickel, the ceria remained in the primary face-centered cubic structure and no Ni diffraction peaks appeared (Figure 2B), which reveals that the Ni species anchored on CeO_2 are smaller and highly dispersed, suggesting there is stronger interaction between CeO_2 and Ni. Moreover, in comparison with pure ceria structures, the crystallite size of ceria (D) over Ni/CeO_2 increases (Table 1), which is possibly correlated with the partial sintering during the procedure of thermal calcination. Based on the previous investigation [38], the microstrain (ε) of crystal is an assessment of lattice stress available in the materials due to lattice elongation, distortion, or contraction, which can be determined according to the broadening degree of XRD diffraction peak with pseudo-Voigt method. Thus, the number of inherent defects on the surface of three CeO_2 supports can be qualitatively analyzed by comparing the value of microstrain. As shown in Table 1, the CeO_2-R shows the highest value of microstrain both prior to and following the Ni loading, and the CeO_2-C has the least value of microstrain. This order should be consistent with the reducibility (the oxygen vacancies concentration) for diverse CeO_2 supports. Since there is a close association between the concentration of oxygen vacancies and the lattice strain, it is suggested that the asymmetrical five-coordinate structure of Ni/CeO_2-R with the greatest strain could be unstable, which is desirable for the surface oxygen mobility. In contrast, the stability of the symmetrical eight-coordination structure of Ni/CeO_2-C with the least strain could be considerable [38]. Due to the largest lattice strain and relatively highest concentration of oxygen defects, the 5Ni/CeO_2-R should exhibit superior stability and catalytic activity compared with the other two samples for MA hydrogenation. Moreover, the specific surface areas achieved from the isotherms of N_2 adsorption–desorption are also illustrated in Table 1. It can be detected that the 5Ni/CeO_2-R and CeO_2-R express the greatest S_{BET} values in comparison with the other samples. It should be noted that greater surface area of CeO_2-R is in favor of the Ni dispersion on the support.

Table 1. Physical parameters and structure of CeO_2 supports and 5Ni/CeO_2 catalysts.

Sample	Ni Loading (%)	S_{BET} (m^2/g)	D (CeO_2) (nm)	Microstrains (ε) (%)		
				(111)	(200)	(220)
CeO_2-P	-	60.3	12.8	0.98	0.67	0.58
CeO_2-R	-	80.2	10.6	1.04	0.79	0.62
CeO_2-C	-	20.4	24.5	0.43	0.29	0.26
5Ni/CeO_2-P	5.2	56.6	11.8	1.19	0.77	0.68
5Ni/CeO_2-R	4.7	78.7	11.2	1.24	0.89	0.72
5Ni/CeO_2-C	4.8	18.6	26.8	0.53	0.39	0.28

Note: The amount of metal loading was ascertained through ICP-OES. The specific surface area achieved from the isotherms of N_2 adsorption–desorption. D(CeO_2) represents the crystallite size of CeO_2 phase, evaluated employing the equation of Scherrer to the (111) plane of ceria.

Raman spectroscopy is implemented for exploring the surface structure of the 5Ni/CeO_2 catalysts and CeO_2 supports. As shown in Figure 4A, the strong vibration mode (F2g, ~460 cm^{-1}), because of the symmetrical stretching vibration of Ce-O bonds, predominates the Raman spectrum of CeO_2. In addition to the F2g band, two wide bands at the regions of 1162 cm^{-1} and 590 cm^{-1} are also detected for the 5Ni/CeO_2 and CeO_2 specimens, which could be ascribed to the second order longitudinal optical mode (2LO), and the Frenkel defect-induced modes (D band), respectively [16]. The 2LO and D bonds are relevant to the existence of oxygen vacancies (Ovac) because of the existence of Ce^{3+} ions in the lattice of ceria, and the comparative ratio of intensity for I_D/I_{F2g} reflects the oxygen vacancies concentration in ceria [39]. As shown in Figure 4, the values of I_D/I_{F2g} and $I_D + I_{2LO}/I_{F2g}$ for Ni/CeO_2 and CeO_2 with different morphologies reduces in the following trend: CeO_2-R > CeO_2-P > CeO_2-C. This represents that the amount of oxygen vacancies for the various ceria nanostructures differ as: nanorod > nanoparticle > nanocube.

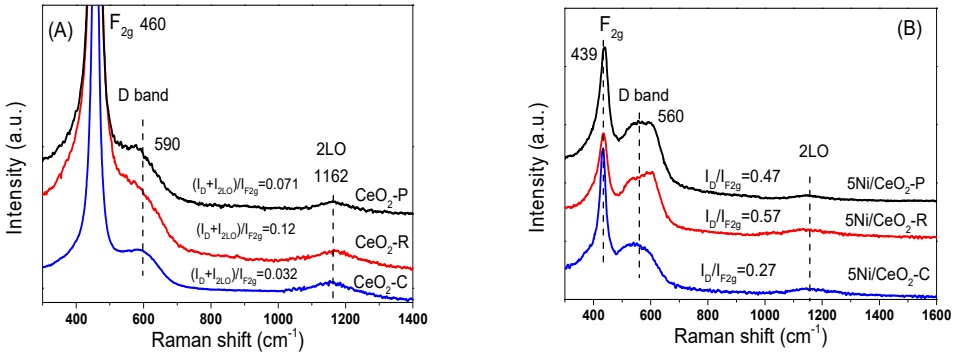

Figure 4. Raman spectra of different CeO_2 support (**A**) and 5Ni/CeO_2 catalysts (**B**).

Following loading the nickel (demonstrated in Figure 4B), the F2g modes red shifted from 460 cm^{-1} to 439 cm^{-1} with peak widening because of the strong interactions between CeO_2 and Ni that resulted in the distortion of the lattice of CeO_2 and generates electron-rich oxygen vacancies to maintain the system charge neutral [16]. In comparison with CeO_2, all the samples of 5Ni/CeO_2 show wider and stronger vibrations in the 2LO modes and D bands, and all of the ratios of intensity enhance sharply. Note that the incorporation of lower-valent cations such as Ni^{2+} in the CeO_2 lattice yields defects as oxygen vacancies and dopant cations: the defect-induced (D) mode includes both the contributions due to oxygen vacancies and to cation substitution in the lattice (D1 and D2 bands, respectively). As shown in Figure 4B, D1and D2 components are clearly seen in the D band profile of Ni/CeO_2-R and Ni/CeO_2-P samples. The increase in (I_D/I_{F2g}) as well as the (I_{D1}/I_{D2}) intensity ratios, can be taken as an indication of a solid solution formation. This finding implies that the loading of Ni species facilitates the creation of oxygen vacancies (Ovac) thanks to metal substitution in the lattice of ceria, which is in a desirable consistency with the XRD achievements. Further, Ni/CeO_2-R exhibits the largest value of I_D/I_{F2g} among three samples, which subsequently reveals that the interactions between ceria rods, and nickel is stronger than other ceria structures. Thus, the morphology of CeO_2 demonstrates an important influence on the synergistic interactions between ceria and nickel.

The H_2-TPR files revealing the reducibility of catalysts are demonstrated in Figure 5. Four peaks of H_2 consumption, namely α, β, γ, and δ are well-fitted through a Gauss-type function for three specimens of Ni/CeO_2. The α and β peaks of H_2 consumption at low temperature of 160 and 200 °C could be attributed to the reduction of the surface adsorbed oxygen species attached to the surface oxygen vacancies and considerably dispersed nanocrystallites of NiO for the catalysts, respectively. As explained before, the oxygen vacancy could be produced through the incorporation of Ni cations with the lattice of CeO_2 and partial substitution of Ce^{4+} or/and Ce^{3+} cations to create solid solution. Moreover, Shan et al. and Li et al. successfully verified that the solid solution of Ni-Ce-O can be produced by

means of the incorporation of the ions of Ni^{2+} into the lattice of CeO_2, leading to oxygen vacancies and easily reduced oxygen species [40,41]. The oxygen vacancies can lead to charge imbalance and lattice distortion that is capable of adsorbing oxygen molecules on the surface of oxide. The adsorbed oxygen molecules are considerably reactive oxygen species and can be reduced easily by H_2 at relatively lower temperatures in the range of 100 to 200 °C as shown in Figure 5.

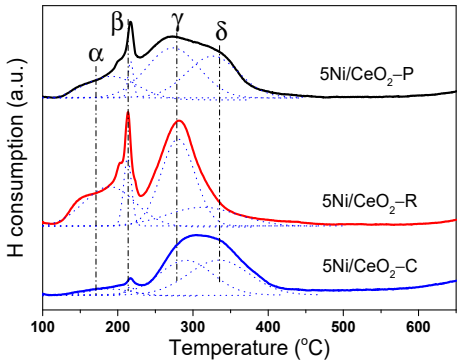

Figure 5. H_2-TPR profiles of three 5Ni/CeO_2 catalysts.

The reduction peak γ could be attributed to the reduction of strongly interactive species of NiO with ceria support. It could be seen that the consumption of H_2 for the γ peak on the Ni/CeO_2-R is superior to that on the Ni/CeO_2-C and Ni/CeO_2-P catalysts, suggesting that a larger amount of strong interactive NiO is available on the surface of CeO_2-R. The interaction of NiO-CeO_2 obeys the following trend: Ni/CeO_2-R > Ni/CeO_2-P > Ni/CeO_2-C. The reduction peak δ exhibited in the profiles of Ni/CeO_2-C and Ni/CeO_2-P is earmarked to the single step reduction of free NiO species, which accumulates on the surface and possesses weakly interaction with ceria support [42]. However, for the Ni/CeO_2-R sample, the reduction behavior of the free NiO almost did not appear in the profile, which should be ascribed to the abundant defect sites on the CeO_2 surface and high dispersion of NiO on the support in accordance with the XRD and Roman analysis. Hence, it can be concluded that the interaction between ceria rods and nickel is stronger in comparison with the other ceria structures. Consequently, the morphology of ceria support has a significant influence on the synergistic interactions between ceria and nickel.

XPS is a powerful tool for characterizing the surface composition of the catalysts and the valance state of the constituent elements, and also exploring the availability of oxygen vacancies. Figure 6A,B show the Ce3d and O1s core level XPS spectra of the reduced catalyst of Ni/CeO_2. As shown in Figure 6A, the XPS spectrum for the Ce3d core level is deconvoluted into 10 Gaussian peaks and tagged according to the deconvolution conducted by Burroughs and colleagues [43]. The detected peaks labelled as U and V, U″ and V″ and U‴ and V‴ relate to $3d_{3/2}$ ($3d_{5/2}$) and are characteristic of the final state of Ce^{4+}3d, whilst U′ and V′ and U_0 and V_0 relate to $3d_{3/2}$ ($3d_{5/2}$) for the final states of Ce^{3+} 3d [4,44]. Thus, the chemical valance of Ce on the surface of the reduced specimens is mostly an oxidation state of Ce^{4+}, and a limited amount of Ce^{3+} co-existed.

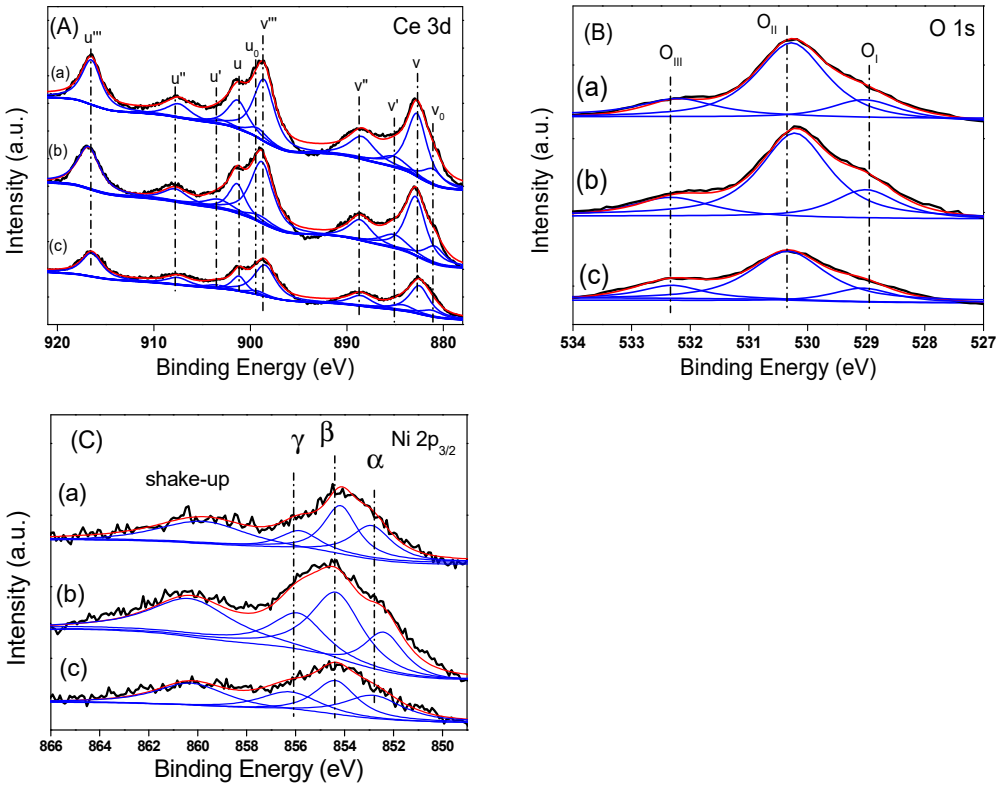

Figure 6. Spectra of XPS for (**A**) Ce 3d, (**B**) O 1s, and (**C**) Ni $2p_{3/2}$ for reduced $5Ni/CeO_2$. Catalysts, (**a**) $5Ni/CeO_2$-P, (**b**) $5Ni/CeO_2$-R, and (**c**) $5Ni/CeO_2$-C. The black line is primary curve, and the red and blue lines are fitted curves.

Furthermore, it is obvious that there is an enhancement in the value of binding energy for the $Ce3d_{5/2}$ component (883.9 eV) in comparison with the pure CeO_2 (882.9 eV). This little shift could be described by the interactions between cerium oxide and nickel, meaning the incorporation of nickel into the cerium surface lattice [25]. Table 2 represents the comparative contributions of Ce^{4+} and Ce^{3+} evaluated by fitting the peaks and the areas under the fitted entities. The ratio of $Ce^{3+}/(Ce^{4+} + Ce^{3+})$ is observed to be dependent on the morphologies and the contents of Ce^{3+} in Ni/CeO_2 decrease in the following trend: Ni/CeO_2-R > Ni/CeO_2-P > Ni/CeO_2-C. In the previous reports [18,28], it has been reported that the existence of oxygen vacancies is capable of promoting the conversion of Ce^{4+} to Ce^{3+}. Hence, considering both the XRD and Raman results, it can be defined through the creation of more surface oxygen vacancies over Ni/CeO_2-R.

Table 2. The quantitative XPS assessment of the $5Ni/CeO_2$ catalysts.

Sample	$Ce^{3+}/(Ce^{4+} + Ce^{3+})$ (%)	$O_I/(O_I + O_{II} + O_{III})$ (%)	$O_{III}/(O_I + O_{II} + O_{III})$ (%)
$5Ni/CeO_2$-P	15.5	18.6	13.5
$5Ni/CeO_2$-R	18.7	20.5	25.4
$5Ni/CeO_2$-C	14.6	12.3	9.4

As shown in Figure 6B, the O1s XPS is fitted into three peaks and summarized in Table 2. The two lesser peaks of energy placed at 528.9 eV and 530.4 eV are assigned to lattice oxygen entities (O^{2-}) binding to Ce^{4+} (O_{II}) and Ce^{3+} (O_I) [45], whilst the peak placed at 532.4 eV (O_{III}) is attributed to the adsorbed oxygen entities (C–O species and water) on the surface of CeO_2 [25]. The adsorption of CO_2 and CO on the reduced state Ce^{3+} sites demonstrate a greater thermal stability compared to that on the sites of Ce^{4+} [46]. Consequently, the adsorbed oxygen is originated from carbonate entities trapped with the aid of oxygen vacancies. The oxygen vacancies content could be achieved from XPS

comparative percentage of adsorbed oxygen. Table 2 represents the XPS findings of the lattice oxygen (O_{II} and O_I) and the adsorbed oxygen (O_{III}). According to Table 2, the ratio of $O_I/(O_I + O_{II} + O_{III})$ of these specimens illustrate the following trend: 5Ni/CeO_2-R > 5Ni/CeO_2-P > 5Ni/CeO_2-C, which is consistent with the trend of the Ce^{3+} content. The great concentration of oxygen species on 5Ni/CeO_2-R is because of its (110) plane with considerable chemical activity, which are active sites for the chemisorption of oxygen from H_2O and CO_2. Moreover, the ratio of $O_{III}/(O_I + O_{II} + O_{III})$ is able to determine this point. Figure 6C shows the Ni2$p_{3/2}$ XPS spectra of reduced 5Ni/CeO_2 catalysts. The Ni2$p_{3/2}$ region is fitted into three peaks firstly by curve fitting using peaks and associated satellites in Figure 6C, and then three peaks are named with α, β, and γ, respectively. According to previous research, the peak α is assigned to Ni^0, and peaks of β and γ refer to Ni^{2+}. It can be seen that both Ni^0 (α~852.7 eV) and Ni^{2+} (β~854.7 eV and γ~856.8 eV) coexist on the surface of Ni/CeO_2 catalysts. Note that the peak area (α) of Ni^0 for Ni/CeO_2-R is larger than other two samples, which means more Ni^{2+} is reduced to Ni^0 over the Ni/CeO_2-R compared with other two samples, indicating that the Ni/CeO_2-R has a higher reducibility of Ni species in this condition.

Hydrogen temperature programmed desorption (H_2-TPD) is an advantageous approach for gaining deep insight in metal-support interaction and hydrogen activation on the catalysts. Figure 7 exhibits the profiles of H_2-TPD for the 5Ni/CeO_2 specimens with three configurations are deconvoluted into three peaks. The α peaks for the catalysts of Ni/CeO_2 emerge in a remarkably similar temperature region (at 80 °C), which are attributed to the desorption of H_2 up-taking surface oxygen vacancies in CeO_2. The γ and β peaks placed in 100–200 °C are because of the desorption of H_2 from the correspondent Ni entities. The β peaks could be assigned to ineffectively adsorbed dissociative H-entities taken up the interface of Ni-CeO_2, which is close to oxygen vacancy on the support [4]. The γ peaks are correlated with the dissociated hydrogen entities attaching to the free particles of Ni. In the higher temperature region, the catalyst of Ni/CeO_2 shows a single wide peak of H_2-TPD emerging at 300 °C and tailing to further than 500 °C. This H_2-TPD peak is because of the H_2 adsorption in the subsurface layers of Ni or/and to the spillover of H_2 [47].

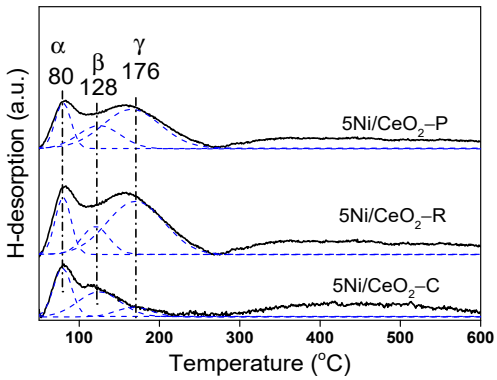

Figure 7. H_2-TPD profiles of 5Ni/CeO_2 catalysts.

In order to meticulously understand the difference in the capability of hydrogen activation between three various catalysts, quantitative assessment of the desorption of H was conducted and the results are given in Table 3. From Table 3, the amount of H_2 desorption for the Ni/CeO_2-R specimen is superior to other samples (such as interface-adsorbed H_β, vacancy-adsorbed H_α, and chemically adsorbed H_β on free Ni). The higher amount of H_2 uptake for the Ni/CeO_2-R explains it possesses higher dispersion and tinier size of Ni particle, which is in compliance with the results of XRD. Regarding the attribution of the peaks of H_2-TPD, the dispersion of Ni could be quantified by the metal-related hydrogen activation (sum of γ- and β-H_2), which is distinct from the total amount of H_2 activation for the catalysts. As given in Table 3, the values of Ni dispersion for the 5Ni/CeO_2

catalysts are shown to be diminishing according to the following order: 5Ni/CeO_2-R > 5Ni/CeO_2-P > 5Ni/CeO_2-C. The results are in a favorable agreement with the TPR and Raman assessments. Furthermore, by means of comparative evaluations of H_2-TPD and H_2-TPR for three catalysts, we can deduce that the catalyst of Ni/CeO_2-R represents more active sites for reversible adsorption/desorption of H-species, leading to fast conversion between H_2 and the dissociated H species on the catalyst in MAH process and thus facilitating the MA conversion rate. Consequently, it can be estimated that the catalyst Ni/CeO_2-R with rod shape has more activity in the reaction of hydrogenation.

Table 3. H_2 uptake and Ni dispersion on the 5Ni/CeO_2 catalysts.

Sample	H_α (μmol/g)	H_β (μmol/g)	H_γ (μmol/g)	Ni Dispersion (%)
5Ni/CeO_2-P	29.8	29.7	84.5	25.7
5Ni/CeO_2-R	48.8	56.3	208.6	66.1
5Ni/CeO_2-C	21.7	30.6	13.5	10.9

H_α, H_β, H_γ represent the amount of H_2 desorbed at different temperatures. The Ni dispersion = (Ni_{surf}/Ni_{total}), Ni_{total} implies the total amount of Ni in the catalysts, and Ni_{surf} demonstrates the amount of surface-exposed Ni on the catalysts, considering H/Ni = 1 and Ni = 2 × (amount of H_2 desorption).

3.2. Catalytic Performance

Figure 8A shows the conversion of MA (X_{MA}) along the courses of hydrogenation on Ni/CeO_2 catalysts in a batch reactor at 180 °C and the pressure of hydrogen was considered of about 5.0 MPa. As shown in Figure 8A, the 5Ni/CeO_2-R catalyst is shown to present the highest activity for the conversion of MA, obtaining ~98% conversion of MA in 1 h. In the meantime, the conversion of MA on 5Ni/CeO_2-C and 5Ni/CeO_2-P in the same duration only obtains 90% and 92%, respectively. It is worth mentioning that the MA is completely converted into succinic anhydride (SA) on all three Ni/CeO_2 catalysts (not shown) and exhibits 100% selectivity to SA within the 1.0 h continuous MAH without other products observed in the reaction, indicating it is inert for SA hydrogenolysis to other products in the current condition. The considerable difference of the MA conversion on three kinds of 5Ni/CeO_2 catalysts can be attributed to the morphology and particle size, which can cause the difference of Ni dispersion and Ovac amount.

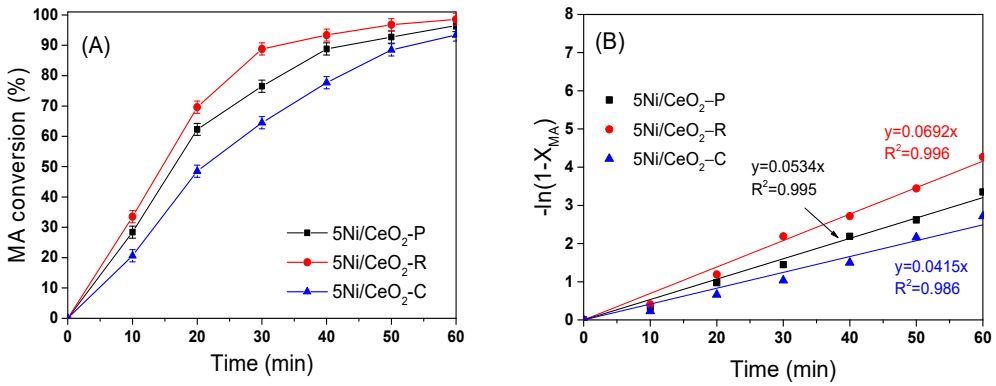

Figure 8. The conversion of maleic anhydride (MA) over 5Ni/CeO_2 catalysts (**A**) and their $-\ln(1 - X_{MA})$ plots versus reaction time (**B**) at 180 °C and under 5 MPa of H_2.

Figure 8B represents the $-\ln(1 - X_{MA})$ curves vs. time during the first 1 h, which are well-fitted conforming to the first-order kinetic law in respect of the conversion of MA on the metal-based catalysts [48]. The linear kinetic diagrams over three catalysts of Ni/CeO_2 define that the hydrogenation of C=C obeys the quasi-first order reaction in respect of the conversion of MA. The MA hydrogenation rate coefficients (k) on these catalysts are determined according to the gradients of their linear plots and summarized in Figure 8B. The k values for 5Ni/CeO_2-R, 5Ni/CeO_2-P, and 5Ni/CeO_2-C are around

0.0692, 0.0534, and 0.0415, respectively. The greater k value for 5Ni/CeO_2-R specimen in comparison with others indicates that the 5Ni/CeO_2-R is more reactive than other two catalysts.

Furthermore, the influence of the reaction temperature (393–453 K) on the activity of three catalysts in the hydrogenation of MA is carefully investigated. An Arrhenius diagram illustrating lnk vs. reaction temperature (1/T) is depicted in Figure 9. According to Figure 9, the constants of pseudo-first reaction rate lay entirely to the straight line, and an increase in activity with increasing temperature from 393 K to 453 K is observed. The apparent activation energies (Ea), evaluated from the slope of the Arrhenius plot straight line (shown in Figure 9), are revealed to be 47.93 ± 4.95 kJ/mol for 5Ni/CeO_2-R, 50.69 ± 3.33 kJ/mol for 5Ni/CeO_2-P and 58.22 ± 7.92 kJ/mol for 5Ni/CeO_2-C, respectively. The values of Ea follow the order of: 5Ni/CeO_2-R < 5Ni/CeO_2-P < 5Ni/CeO_2-C, which implies that the 5Ni/CeO_2-R can represent the higher ability for MA hydrogenation.

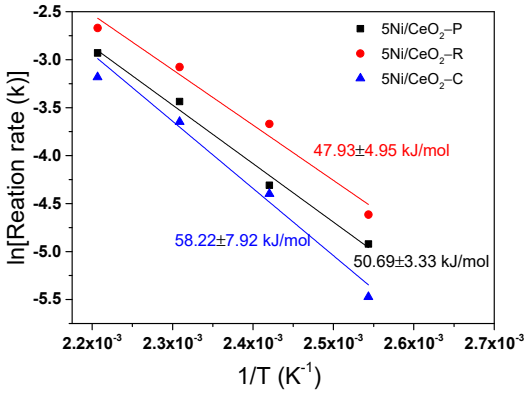

Figure 9. Arrhenius plot for the hydrogenation of maleic anhydride on three 5Ni/CeO_2 catalysts and the relationship between ln(k_{MA}) versus 1/T.

From the above results, it can be seen that the surface structure, namely the morphology (crystal plane) of CeO_2, is the key parameter influencing the interaction between Ni and CeO_2 support. As shown in TEM images (Figures 1 and 2), the CeO_2-C, CeO_2-R, and CeO_2-P samples expose predominantly the (100), (110 or 220), and (111) planes, respectively. Because the typical CeO_2 could be regarded as an array of cations creating a face-centered cubic lattice with oxygen ions situating at the tetrahedral interstitial sites, the Ni^{2+} is capable of penetrating easily into the lattices of (220) and (111) planes by placing in these sites, along with the capping oxygen atom to compensate the charge. This structural impact may lead to the differences in the synergistic interactions between CeO_2 and Ni, thus affecting the catalytic behavior of Ni/CeO_2 catalysts. The above analysis reasonably explained why Ni/CeO_2-R shows a higher catalytic property compared to that of Ni/CeO_2-P and Ni/CeO_2-C.

Besides the interaction between CeO_2 support and Ni, the oxygen vacancy (Ovac) is considered as another factor for enhancing the hydrogenation of C=C since the oxygen vacancy is capable of enriching the electron density of active metals, which promotes the electron donating capability and the dissociation of H2 [4,49]. In this study, the catalyst of Ni/CeO_2-R possesses richer oxygen vacancies and hence can donate more electrons to the metallic nickel compared with the Ni/CeO_2-C and Ni/CeO_2-P, which shows higher activity of Ni/CeO_2-R in the hydrogenation of MA. Thus, it can be concluded that the rod-shape of CeO_2 can enhance the dispersion of metallic nickel, presenting stronger interaction between support and Ni and more oxygen vacancies, as a result the catalyst of 5Ni/CeO_2-R shows higher reactivity in MAH compared with other two samples.

4. Conclusions

In this study, we have prepared three kinds of the catalysts of Ni/CeO_2 with various morphologies of CeO_2 support, namely cube-like, rod-like, and particle-like, and investi-

gated the crystal-plane and morphology influences on catalytic behaviors in the reaction of maleic anhydride hydrogenation (MAH). The results of characterization demonstrate that nickel species can incorporate into the lattice of CeO_2, and cause an increase in oxygen vacancies by occupying the empty sites. The catalytic features relate to the exposed plane and shape of the CeO_2 supports. For all considered catalysts, the MA is able to be completely converted into succinic anhydride (SA), and represent 100% selectivity to SA in the current conditions. Among three catalysts, the Ni/CeO_2-R exhibits excellent catalytic performance in stability and catalytic behavior, which is because of the stronger anchoring influence of CeO_2 to nickel species. The oxygen vacancies concentration as well as the mobility of lattice oxygen within the Ni/CeO_2 indicate the morphology dependencies. With the aid of reactivity assessments, the redox features and crystal structures of the catalysts achieved from various characterization methods, it can be deduced that the desirable behavior of $5Ni/CeO_2$-R is strongly associated with the higher dispersion of metallic nickel species, the higher availability of oxygen vacancies, and the stronger interaction between CeO_2 and Ni. The obtained findings confirm that the catalytic performances and structures of Ni/CeO_2 catalysts could be modulated through modifying the CeO_2 support morphology. This investigation provides a deep understanding of the reaction MA hydrogenation by means of Ni/CeO_2 catalysts.

Author Contributions: Conceptualization, H.W., Y.Z. (Yin Zhang), and Y.Z. (Yongxiang Zhao); methodology, S.L.; formal analysis, Q.Z.; writing—original draft preparation, S.L. and X.L.; writing—review and editing, H.W. and Y.Z. (Yin Zhang); supervision, Y.Z. (Yongxiang Zhao); funding acquisition, Y.Z. (Yongxiang Zhao). All authors have read and agreed to the published version of the manuscript.

Funding: This research was funded by the National Natural Science Foundation (U1710221, 21303097, 22075167); Shanxi Province International Science and Technology Cooperation Program Project (201803D421074).

Data Availability Statement: Not Applicable.

Conflicts of Interest: The authors declare no conflict of interest.

References

1. Papageorgiou, G.Z.; Grigoriadou, I.; Andriotis, E.; Bikiaris, D.N.; Panayiotou, C. Miscibility and Properties of New Poly(propylene succinate)/Poly(4-vinylphenol) Blends. *Ind. Eng. Chem. Res.* **2013**, *52*, 11948–11955. [CrossRef]
2. Bertone, M.E.; Meyer, C.I.; Regenhardt, S.A.; Sebastian, V.; Garetto, T.F.; Marchi, A.J. Highly selective conversion of maleic anhydride to γ-butyrolactone over Ni-supported catalysts prepared by precipitation–deposition method. *Appl. Catal. A Gen.* **2015**, *503*, 135–146. [CrossRef]
3. Meyer, C.I.; Regenhardt, S.A.; Marchi, A.J.; Garetto, T.F. Gas phase hydrogenation of maleic anhydride at low pressure over silica-supported cobalt and nickel catalysts. *Appl. Catal. A* **2012**, *417–418*, 59–65. [CrossRef]
4. Liao, X.; Zhang, Y.; Hill, M.; Xia, X.; Zhao, Y.; Jiang, Z. Highly efficient Ni/CeO_2 catalyst for the liquid phase hydrogenation of maleic anhydride. *Appl. Catal. A* **2014**, *488*, 256–264. [CrossRef]
5. Regenhardt, S.A.; Meyer, C.I.; Garetto, T.F.; Marchi, A.J. Selective gas phase hydrogenation of maleic anhydride over Ni-supported catalysts: Effect of support on the catalytic performance. *Appl. Catal. A Gen.* **2012**, *449*, 81–87. [CrossRef]
6. Jung, S.M.; Godard, E.; Jung, S.Y.; Park, K.C.; Choi, J.U. Liquid-phase hydrogenation of maleic anhydride over $Pd\text{-}Sn/SiO_2$. *Catal. Today* **2003**, *87*, 171–177. [CrossRef]
7. Wang, N.; Shen, K.; Huang, L.; Yu, X.; Qian, W.; Chu, W. Facile Route for Synthesizing Ordered Mesoporous Ni-Ce-Al Oxide Materials and Their Catalytic Performance for Methane Dry Reforming to Hydrogen and Syngas. *ACS Catal.* **2013**, *3*, 1638–1651. [CrossRef]
8. Zhang, S.; Muratsugu, S.; Ishiguro, N.; Tada, M. Ceria-Doped Ni/SBA-16 Catalysts for Dry Reforming of Methane. *ACS Catal.* **2013**, *3*, 1855–1864. [CrossRef]
9. Guo, H.; He, Y.; Wang, Y.; Liu, L.; Yang, X.; Wang, S.; Huang, Z.; Wei, Q. Morphology-controlled synthesis of cage-bell $Pd@CeO_2$ structured nanoparticle aggregates as catalysts for the low-temperature oxidation of CO. *J. Mater. Chem. A* **2013**, *1*, 7494–7499. [CrossRef]
10. Zhu, Y.; Zhang, S.; Shan, J.; Nguyen, L.; Zhan, S.; Gu, X.; Tao, F. In Situ Surface Chemistries and Catalytic Performances of Ceria Doped with Palladium, Platinum, and Rhodium in Methane Partial Oxidation for the Production of Syngas. *ACS Catal.* **2013**, *3*, 2627–2639. [CrossRef]
11. Senanayake, S.D.; Stacchiola, D.; Evans, J.; Estrella, M.; Barrio, L.; Pérez, M.; Hrbek, J.; Rodriguez, J.A. Probing the reaction intermediates for the water-gas shift over inverse CeOx/Au(111) catalysts. *J. Catal.* **2010**, *271*, 392–400. [CrossRef]

12. Nga, N.L.T.; Potvin, C.; Djéga-Mariadassou, G.; Delannoy, L.; Louis, C. Catalytic reduction of nitrogen monoxide by propene in the presence of excess oxygen over gold based ceria catalyst. *Top. Catal.* **2007**, *42–43*, 91–94. [CrossRef]
13. Wang, N.; Qian, W.; Chu, W.; Wei, F. Crystal-plane effect of nanoscale CeO_2 on the catalytic performance of Ni/CeO_2 catalysts for methane dry reforming. *Catal. Sci. Technol.* **2016**, *6*, 3594–3605. [CrossRef]
14. Liao, X.; Zhang, Y.; Guo, J.; Zhao, L.; Hill, M.; Jiang, Z.; Zhao, Y. The Catalytic Hydrogenation of Maleic Anhydride on CeO_2-delta-Supported Transition Metal Catalysts. *Catalysts* **2017**, *7*, 272. [CrossRef]
15. Zhou, K.; Wang, X.; Sun, X.; Peng, Q.; Li, Y. Enhanced catalytic activity of ceria nanorods from well-defined reactive crystal planes. *J. Catal.* **2005**, *229*, 206–212. [CrossRef]
16. Wu, Z.; Li, M.; Howe, J.; Meyer, H.M.; Overbury, S.H. Probing defect sites on CeO_2 nanocrystals with well-defined surface planes by raman spectroscopy and O_2 adsorption. *Langmuir* **2010**, *26*, 16595–16606. [CrossRef]
17. Mai, H.-X.; Sun, L.-D.; Zhang, Y.-W.; Si, R.; Feng, W.; Zhang, H.-P.; Liu, H.-C.; Yan, C.-H. Shape-selective synthesis and oxygen storage behavior of Ceria Nanopolyhedra, Nanorods, and Nanocubes. *J. Phys. Chem. B* **2005**, *109*, 24380–24385. [CrossRef]
18. Liu, X.; Zhou, K.; Wang, L.; Wang, B.; Li, Y. Oxygen vacancy clusters promoting reducibility and activity of ceria nanorods. *J. Am. Chem. Soc.* **2009**, *131*, 3140–3141. [CrossRef]
19. Agarwal, S.; Lefferts, L.; Mojet, B.L. Ceria nanocatalysts: Shape dependent reactivity and formation of OH. *ChemCatChem* **2013**, *5*, 479–489. [CrossRef]
20. Wu, Z.; Li, M.; Overbury, S.H. On the structure dependence of CO oxidation over CeO_2 nanocrystals with well-defined surface planes. *J. Catal.* **2012**, *285*, 61–73. [CrossRef]
21. Agarwal, S.; Lefferts, L.; Mojet, B.L.; Ligthart, D.A.J.M.; Hensen, E.J.M.; Mitchell, D.R.G.; Erasmus, W.J.; Anderson, B.G.; Olivier, E.J.; Neethling, J.H.; et al. Exposed Surfaces on shape-controlled ceria nanoparticles revealed through AC-TEM and water-gas shift reactivity. *ChemSusChem* **2013**, *6*, 1898–1906. [CrossRef] [PubMed]
22. Han, W.-Q.; Wen, W.; Hanson, J.C.; Teng, X.; Marinkovic, N.; Rodriguez, J.A. Onedimensional ceria as catalyst for the low-temperature water-gas shift reaction. *J. Phys. Chem. C* **2009**, *113*, 21949–21955. [CrossRef]
23. Cao, T.; You, R.; Li, Z.; Zhang, X.; Li, D.; Chen, S.; Zhang, Z.; Huang, W. Morphology-dependent CeO_2 catalysis in acetylene semihydrogenation reaction. *Appl. Surf. Sci.* **2020**, *501*, 144120. [CrossRef]
24. Si, R.; Flytzani-Stephanopoulos, M. Shape and crystal-plane effects of nanoscale ceria on the activity of $Au-CeO_2$ catalysts for the water-gas shift reaction. *Angew. Chem. Int. Ed.* **2008**, *47*, 2884–2887. [CrossRef] [PubMed]
25. Liu, L.; Yao, Z.; Deng, Y.; Gao, F.; Liu, B.; Dong, L. Morphology and crystal-plane effects of nanoscale ceria on the activity of CuO/CeO_2 for NO reduction by CO. *ChemCatChem* **2011**, *3*, 978–989. [CrossRef]
26. Chang, S.; Li, M.; Hua, Q.; Zhang, L.; Ma, Y.; Ye, B.; Huang, W. Shape-dependent interplay between oxygen vacancies and $Ag–CeO_2$ interaction in Ag/CeO_2 catalysts and their influence on the catalytic activity. *J. Catal.* **2012**, *293*, 195–204. [CrossRef]
27. Wu, Z.; Schwartz, V.; Li, M.; Rondinone, A.J.; Overbury, S.H. Support shape effect in metal oxide catalysis: Ceria-nanoshape-supported Vanadia catalysts for oxidative dehydrogenation of isobutane. *J. Phys. Chem. Lett.* **2012**, *3*, 1517–1522. [CrossRef]
28. Du, X.; Zhang, D.; Shi, L.; Gao, R.; Zhang, J. Morphology dependence of catalytic properties of Ni/CeO_2 nanostructures for carbon dioxide reforming of methane. *J. Phys. Chem. C* **2012**, *116*, 10009–10016. [CrossRef]
29. Zhang, X.; You, R.; Li, D.; Cao, T.; Huang, W. Reaction sensitivity of ceria morphology effect on Ni/CeO_2 catalysis in propane oxidation reactions. *ACS Appl. Mater. Interfaces* **2017**, *9*, 35897–35907. [CrossRef]
30. Liu, Y.; Luo, L.; Gao, Y.; Huang, W. CeO_2 morphology-dependent $NbOx-CeO_2$ interaction, structure and catalytic performance of $NbOx/CeO_2$ catalysts in oxidative dehydrogenation of propane. *Appl. Catal. B* **2016**, *197*, 214–221. [CrossRef]
31. Wu, Z.; Li, M.; Overbury, S.H. A Raman spectroscopic study of the speciation of Vanadia supported on ceria nanocrystals with defined surface planes. *ChemCatChem* **2012**, *4*, 1653–1661. [CrossRef]
32. Gao, Y.; Wang, W.; Chang, S.; Huang, W. Morphology effect of CeO_2 support in the preparation, metal-support interaction, and catalytic performance of Pt/CeO_2 catalysts. *ChemCatChem* **2013**, *5*, 3610–3620. [CrossRef]
33. You, R.; Zhang, X.; Luo, L.; Pan, Y.; Pan, H.; Yang, J.; Wu, L.; Zheng, X.; Jin, Y.; Huang, W. $NbOx/CeO_2$-rods catalysts for oxidative dehydrogenation of propane: $Nb-CeO_2$ interaction and reaction mechanism. *J. Catal.* **2017**, *348*, 189–199. [CrossRef]
34. Riley, C.; Zhou, S.; Kunwar, D.; De La Riva, A.; Peterson, E.; Payne, R.; Gao, L.; Lin, S.; Guo, H.; Datye, A. Design of effective catalysts for selective alkyne hydrogenation by doping of ceria with a single-atom promotor. *J. Am. Chem. Soc.* **2018**, *140*, 12964–12973. [CrossRef]
35. Vilé, G.; Colussi, S.; Krumeich, F.; Trovarelli, A.; Pérez-Ramírez, J. Opposite face sensitivity of CeO_2 in hydrogenation and oxidation catalysis. *Angew. Chem. Int. Ed.* **2014**, *53*, 12069–12072. [CrossRef] [PubMed]
36. Zhu, H.-Z.; Lu, Y.-M.; Fan, F.-J.; Yu, S.-H. Selective hydrogenation of nitroaromatics by ceria nanorods. *Nanoscale* **2013**, *5*, 7219–7223. [CrossRef]
37. Matte, L.P.; Kilian, A.S.; Luza, L.; Alves, M.C.; Morais, J.; Baptista, D.L.; Dupont, J.; Bernardi, F. Influence of the CeO_2 Support on the Reduction Properties of Cu/CeO_2 and Ni/CeO_2 Nanoparticles. *J. Phys. Chem. C* **2015**, *119*, 26459–26470. [CrossRef]
38. Rodriguez, J.A.; Wang, X.; Liu, G.; Hanson, J.C.; Hrbek, J.; Peden, C.H.F.; Iglesias-Juez, A.; Fernández-Garc, M. Physical and chemical properties of $Ce1-xZrxO_2$ nanoparticles and $Ce1-xZrxO_2(111)$ surfaces: Synchrotron-based studies. *J. Mol. Catal. A Chem.* **2005**, *228*, 11–19. [CrossRef]
39. Francisco, M.S.P.; Mastelaro, V.R.; Nascente, P.A.P.; Florentino, A.O. Activity and Characterization by XPS, HR-TEM, Raman Spectroscopy, and BET Surface Area of CuO/CeO_2-TiO_2 Catalysts. *J. Phys. Chem. B* **2001**, *105*, 10515–10522. [CrossRef]

40. Li, Y.; Zhang, B.C.; Tang, X.L.; Xu, Y.D.; Shen, W.J. Hydrogen production from methane decomposition over Ni/CeO_2 catalysts. *Catal. Commun.* **2006**, *7*, 380–386. [CrossRef]
41. Shan, W.J.; Luo, M.F.; Ying, P.L.; Shen, W.J.; Li, C. Reduction property and catalytic activity of $Ce1\text{-}XNiXO_2$ mixed oxide catalysts for CH_4 oxidation. *Appl. Catal. A Gen.* **2003**, *246*, 1–9. [CrossRef]
42. Sa, J.; Kayser, Y.; Milne, C.J.; Abreu Fernandes, D.L.; Szlachetko, J. Temperature-programmed reduction of NiO nanoparticles followed by time-resolved RIXS. *Phys. Chem. Chem. Phys.* **2014**, *16*, 7692–7696. [CrossRef] [PubMed]
43. Burroughs, P.; Hamnett, A.; Orchard, A.F.; Thornton, G. Satellite structure in the X-ray photoelectron spectra of some binary and mixed oxides of lanthanum and cerium. *J. Chem. Soc. Dalton Trans.* **1976**, *17*, 1686–1698. [CrossRef]
44. Nelson, A.E.; Schulz, K.H. Surface chemistry and microstructural analysis of $Ce_xZr_{1\text{-}x}O_{2\text{-}y}$ model catalyst surfaces. *Appl. Surf. Sci.* **2003**, *210*, 206–221. [CrossRef]
45. Santos, V.P.; Carabineiro, S.A.C.; Bakker, J.J.W.; Soares, O.S.G.P.; Chen, X.; Pereira, M.F.R.; Órfão, J.J.M.; Figueiredo, J.L.; Gascon, J.; Kapteijn, F. Stabilized gold on cerium-modified cryptomelane: Highly active in low-temperature CO oxidation. *J. Catal.* **2014**, *309*, 58–65. [CrossRef]
46. Boaro, M.; Giordano, F.; Recchia, S.; Dal Santo, V.; Giona, M.; Trovarelli, A. On the mechanism of fast oxygen storage and release in ceria–zirconia model catalysts. *Appl. Catal. B* **2004**, *52*, 225–237. [CrossRef]
47. Liu, Q.; Gao, J.; Zhang, M.; Li, H.; Gu, F.; Xu, G.; Zhong, Z.; Su, F. Highly active and stable $Ni/\gamma\text{-}Al_2O_3$ catalysts selectively deposited with CeO_2 for CO methanation. *RSC Adv.* **2014**, *4*, 16094–16103. [CrossRef]
48. Torres, C.C.; Alderete, J.B.; Mella, C.; Pawelec, B. Maleic anhydride hydrogenation to succinic anhydride over mesoporous Ni/TiO_2 catalysts: Effects of Ni loading and temperature. *J. Mol. Catal. A Chem.* **2016**, *423*, 441–448. [CrossRef]
49. Zhang, S.; Li, J.; Xia, Z.; Wu, C.; Zhang, Z.; Ma, Y.; Qu, Y. Towards highly active Pd/CeO_2 for alkene hydrogenation by tuning Pd dispersion and surface properties of the catalysts. *Nanoscale* **2017**, *9*, 3140–3149. [CrossRef]

nanomaterials

MDPI

Article

Transesterification of Glycerol to Glycerol Carbonate over Mg-Zr Composite Oxide Prepared by Hydrothermal Process

Yihao Li, Hepan Zhao, Wei Xue, Fang Li * and Zhimiao Wang *

Key Laboratory of Green Chemical Technology and High Efficient Energy Saving of Hebei Province, Tianjin Key Laboratory of Chemical Process Safety, School of Chemical Engineering, Hebei University of Technology, Tianjin 300401, China; 201921503002@stu.hebut.edu.cn (Y.L.); hgdzhao16029@hebut.edu.cn (H.Z.); weixue@hebut.edu.cn (W.X.)

* Correspondence: lifang@hebut.edu.cn (F.L.); wangzhimiao@hebut.edu.cn (Z.W.)

Abstract: A series of Mg-Zr composite oxide catalysts prepared by the hydrothermal process were used for the transesterification of glycerol (GL) with dimethyl carbonate (DMC) to produce glycerol carbonate (GC). The effects of the preparation method (co-precipitation, hydrothermal process) and Mg/Zr ratio on the catalytic performance were systematically investigated, and the deactivation of the catalyst was also explored. The Mg-Zr composite oxide catalysts were characterized by XRD, TEM, TPD, N_2 adsorption-desorption, and XPS. The characterization results showed that compared with the co-precipitation process, the catalyst prepared by the hydrothermal process has a larger specific surface area, smaller grain size, and higher dispersion. Mg1Zr2-HT catalyst calcined at 600 °C in a nitrogen atmosphere exhibited the best catalytic performance. Under the conditions of reaction time of 90 min, reaction temperature of 90 °C, catalyst dosage of 3 wt% of GL, and GL/DMC molar ratio of 1/5, the GL conversion was 99% with 96.1% GC selectivity, and the yield of GC was 74.5% when it was reused for the fourth time.

Keywords: glycerol carbonate; transesterification; hydrothermal process; Mg-Zr oxides

Citation: Li, Y.; Zhao, H.; Xue, W.; Li, F.; Wang, Z. Transesterification of Glycerol to Glycerol Carbonate over Mg-Zr Composite Oxide Prepared by Hydrothermal Process. *Nanomaterials* **2022**, *12*, 1972. https://doi.org/10.3390/nano12121972

Academic Editor: Sónia Carabineiro

Received: 26 April 2022
Accepted: 7 June 2022
Published: 8 June 2022

1. Introduction

With the increasing consumption of fossil fuels and the consequent environmental problems, especially the threat of global warming, China has put forward the strategic goal of "carbon peaking and carbon neutralization". The realization of this goal needs to accelerate clean energy substitution and energy transformation. Biodiesel is a promising clean and renewable energy, and has become a hot spot for the sustainable development of global energy and the environment [1]. Biodiesel is obtained by transesterification of vegetable oil and waste oil with methanol or ethanol and will produce by-product glycerol (GL). By 2024, the global biofuel market is expected to reach US $153.8 billion, but for every 1000 kg biodiesel produced, there will be 100 kg GL [2].

In order to solve the problem of crude glycerol utilization, scientists have explored and developed different synthetic procedures to convert GL into high value-added derivatives, such as the steam reforming of glycerol [3–7], catalytic esterification of glycerol, catalytic hydrogenolysis of glycerol and among others. Among various GL derivatives, glycerol carbonate (4-hydroxymethyl-1,3-dioxolane-2-one, GC) has the advantages of low flammability, low toxicity, high boiling point, and biodegradability [8]. It is widely used as a solvent in the cosmetics industry, and can also be used in the manufacture of paint, fiber, plastic, coating, cement curing agent, biological lubricant, and so on [9].

At present, the routes for the synthesis of GC using GL as raw material mainly include phosgenaion [10], oxidative carbonylation [11], urea alcoholysis [12], and transesterification [13]. Among them, transesterification (Scheme 1) has the advantages of mild reaction conditions and simple operation, which is considered to be one of the most direct and feasible ways in the industry [14].

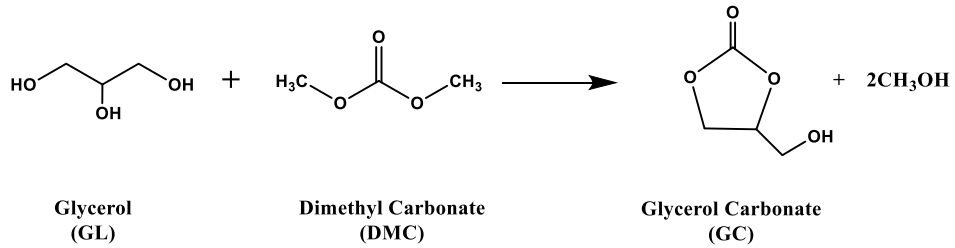

Scheme 1. Synthesis of GC by transesterification from GL and DMC.

In recent years, alkali catalysts such as MgO [15,16] and CaO [17] have been widely used in GC synthesis by transesterification. However, CaO can be dissolved into the reactant GL and form a calcium-glycerin bond [18]. Moreover, CaO may produce $CaCO_3$ with DMC in the presence of water [19], which reduces the catalytic activity, limiting the reuse of catalysts. In addition, single metal oxides such as MgO and CaO will react with water and CO_2 in the air during preparation and storage, and then deactivate [20]. In general, composite oxides have stronger acidity and basicity and larger specific surface areas than single metal oxides; the lattice structure can also be changed by doping metal cations with different electronegativity, thereby changing the acidity and basicity of the catalyst surface [21]. So it shows good application prospects in heterogeneous alkali catalytic reactions [22]. Zhang [23] prepared a large specific surface area CaO-ZrO_2 catalyst with the mesoporous structure for continuous transesterification synthesis of GC in a fixed bed reactor. Under the optimized conditions, the yield of GC can reach 90%. However, the catalysts prepared by the co-precipitation process have some disadvantages, such as easy loss of active components and deactivation due to carbon species deposited on the surface [24]. The hydrothermal process has been widely used in the synthesis of oxide nanoparticles in recent years. Compared with other preparation processes, hydrothermally synthesized nanoparticles have high purity, good dispersibility, and controllable grain size [25]. Cui prepared MgO nanosheets with a two-dimensional flaky porous structure by simple hydrothermal process, which has a larger specific surface area than commercial MgO nanoparticles [26]. The ZrO_2 nanocrystals prepared by hydrothermal synthesis of Akune [27] show high catalytic activity due to their high specific surface area and high crystallinity. Wang compared the Mg/Sn/W composite oxide catalysts prepared by co-precipitation process and hydrothermal process, and pointed out that the catalysts prepared by the hydrothermal process had smaller particles, higher thermal stability, and catalytic activity [28].

In this article, Mg-Zr composite oxide catalysts with different Mg/Zr molar ratios were prepared by hydrothermal process for the transesterification of GL and DMC to synthesize GC. The effects of the preparation method and Mg/Zr molar ratio were systematically investigated. The catalysts were characterized by XRD, N_2 adsorption-desorption, TEM, TPD, and XPS, and the structure-activity relationship of the Mg-Zr oxide catalysts was discussed. In addition, the transesterification reaction conditions were optimized, the reusability of the catalyst was investigated, and the deactivation reasons of the catalysts were explored.

2. Materials and Methods

2.1. Materials

Glycerol (99%, AR); methanol (99.5%, AR); magnesium nitrate hexahydrate (99%, AR) and sodium hydroxide were purchased from Kemio Reagent Co, Ltd. (Tianjin, China). Zirconium oxychloride octahydrate (99%, AR); dimethyl carbonate (99%, AR), and n-butanol (99%, AR) were purchased from Damao Chemical Reagent Factory (Tianjin, China). Glycidyl (98%) and glycerol carbonate (90%) were purchased from Aladdin Biochemical Technology Co, Ltd. (Shanghai, China).

2.2. Catalyst Preparation

A series of Mg-Zr composite oxide catalysts with different Mg/Zr ratio were prepared by hydrothermal process. Briefly, the typical preparation route could be described as follows: Mg $(NO_3)_2 \cdot 6H_2O$ (0.64 g, 2.5 mmol) and $ZrOCl_2 \cdot 8H_2O$ (1.61 g, 5 mmol) were dissolved in the deionized water at room temperature, and the solution was added drop by drop to the 500 mL flask with the suitable amount of 2 mol/L NaOH solution at the same time by the co-current-precipitation process under vigorous stirring. Until the pH of the solution reached 11, and then stirred continuously for 30 min. Subsequently, the suspension was hydrothermally treated in a Teflon-lined stainless-steel autoclave at 150 °C for 6 h, and then calcined at 600 °C in flowing nitrogen atmosphere for 3 h. Depending on the molar ratio of Mg/Zr used in the preparation step, the catalysts were marked as Mg1Zr3, Mg1Zr2, Mg1Zr1, Mg2Zr1 and Mg3Zr1. Single metal oxide catalysts ZrO_2 and MgO were synthesized in the same way as above composite oxide catalysts. The difference between co-precipitation process and hydrothermal process is that the mixture after stirring is allowed to stand at room temperature for 6 h without high-temperature treatment, and other steps remain unchanged. The catalyst samples prepared by hydrothermal method and coprecipitation method were named Mg_xZr_y-HT and Mg_xZr_y-CP respectively, where x/y was n(Mg)/n(Zr) molar ratio.

2.3. Characterization

The crystal phases of all samples were identified by powder X-ray diffractometer using D8 FOCUS (German Brook AXS Company, Karlsruhe, Germany) with Cu Kα radiation (40 kV) and a secondary beam graphite monochromator (SS/DS = 1°, RS 0.15 mm, counter SC). Talos F200s field emission transmission electron microscope (FEI company, Hillsboro, OR, USA) was used to observe the morphology and grain size of the catalysts. The strength and distribution of the basic/acid sites of the catalyst were determined by temperature programmed desorption of preadsorbed CO_2 or NH_3, which was performed using Auto Chem 2920 instrument. (Micromeritics, Norcross, GA, USA). The texture properties including the specific surface area, pore volume, and pore size of the catalysts were derived from N_2 adsorption-desorption technique using 3H-2000PS2 (Beishied, Beijing, China) at −196 °C. The catalysts were pretreated by outgassing in vacuum at 200 °C for 3 h before measurement. X-ray photoelectron spectroscopy (XPS) data were collected on a Thermo Scientific K-Alpha electron spectrometer (Thermo Fisher, Waltham, MA, USA) equipped with Al Kα radiation (hv = 1486.6 eV).

2.4. Catalytic Activity Test

Transesterification of GL to GC was carried out in a round bottom flask with reflux condenser at atmospheric pressure. A total of 3.3 g of GL and 16.3 g of DMC were added into a 100 mL round-bottomed flask, the reaction mixture was heated to 90 °C while stirring in oil bath, then the catalyst of 3 wt% of GL was added to the reaction mixture. After the desired time, the products were separated by centrifugation and analyzed by gas chromatography using an Agilent 7890B gas chromatograph equipped with a DB-wax capillary column (30 m × 0.32 mm × 0.25 μm) and a hydrogen flame detector. The injector and detector temperatures were 250 °C and 300 °C, respectively. The yield of GC was calculated using internal standard method, in which N-butanol was the internal standard. The GL conversion, GC selectivity and yield were calculated by the following equations:

$$\text{GL conversion}(\%) = \frac{\text{mole of GL, feed} - \text{mole of GL, final}}{\text{mole of GL, feed}} \times 100 \quad (1)$$

$$\text{GC selectivity}(\%) = \frac{\text{mole of GC, produced}}{\text{mole of GL, feed} - \text{mole of GL, final}} \times 100 \quad (2)$$

$$\text{GC yield}(\%) = \frac{\text{GL conversion} \times \text{GC selectivity}}{100} \quad (3)$$

3. Results and Discussion

3.1. Effect of Preparation Method

The XRD patterns of Mg1Zr2-HT catalyst prepared by hydrothermal process and Mg1Zr2-CP catalyst prepared by co-precipitation are shown in Figure 1. It can be seen from the figure that the diffraction peaks at 30.2°, 34.9°, 50.7° and 60.2° belong to tetragonal ZrO_2 (t-ZrO_2, JCPDS No. 50-1089), and there is no monoclinic ZrO_2. t-ZrO_2 has a unique bridging hydroxyl group and strong surface basicity, which is conducive to transesterification reaction [29]. Compared with ZrO_2, the diffraction peak intensity of MgO is relatively weak, which is not due to the low content of Mg, but due to the low atomic scattering factor (atomic number) of Mg [30]. In addition, the grain sizes of Mg1Zr2-CP and Mg1Zr2-HT calculated by Scherrer formula are 13.4 nm and 13.1 nm respectively, and there is little difference between them.

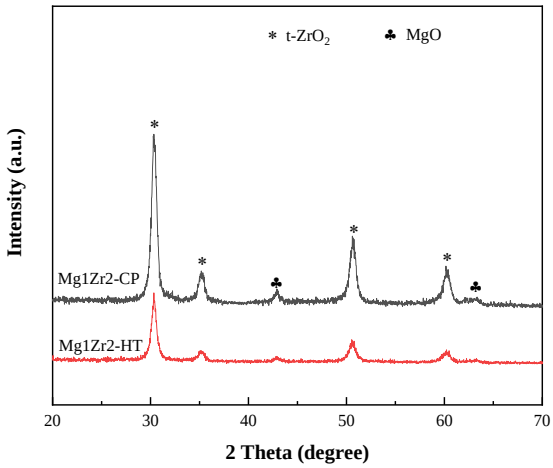

Figure 1. XRD patterns of Mg1Zr2-HT and Mg1Zr2-CP.

The textural properties and surface basicity of Mg1Zr2-HT and Mg1Zr2-CP are summarized in Table 1. It can be seen that the Mg1Zr2-HT has a larger specific surface area and pore volume than Mg1Zr2-CP. This is because the intense collision between colloidal particles promotes the secondary pore formation of composite oxides under hydrothermal conditions, whereas the condensation between colloidal particles is a very slow process at room temperature. Therefore, the hydrothermal process is conducive to the formation of a more developed pore network structure, thereby improving the specific surface area and pore volume of Mg1Zr2-HT [31]. In addition, the dissolution deposition/crystallization process also occurs in the hydrothermal process [32]. Due to the dissolution of some precursors under hydrothermal conditions, the local solubility at the junction (neck) of the two colloidal particles will be lower than that at the nearby surface. Therefore, the deposition process will occur preferentially in the neck, resulting in the reinforcement of the colloidal network structure. During the subsequent calcination, the specific surface area and pore volume of the xerogel prepared by co-precipitation decrease rapidly due to the collapse of the gel skeleton and the sintering and growth of the catalyst particles [33].

Table 1. Texture properties and surface basicity of Mg1Zr2-HT and Mg1Zr2-CP.

Catalyst	ZrO_2 Crystallite Size [a] (nm)	MgO Crystallite Size [b] (nm)	S_{BET} [c] (m^2/g)	D_P [d] (nm)	V_P [e] (cm^3/g)	Basicity [f] (μmol/g)		
						W	M + S	Total
Mg1Zr2-HT	13.1	13.2	68.8	24.0	0.41	57.1	88.2	145.3
Mg1Zr2-CP	13.4	14.9	42.8	26.9	0.28	53.2	82.6	135.8

[a] Calculated by Scherrer formula using the full width at half maximum of ZrO_2 (011) plane. [b] Calculated by Scherrer formula using the full width at half maximum of MgO (200) plane. [c] S_{BET} was measured by the multi-point BET method. [d] Average pore size was calculated from the desorption branch of the isotherm using the BJH method. [e] Total pore volume was measured at P/P_0 = 0.99. [f] Calculated by the results of CO_2-TPD.

The catalytic performance of the above two catalysts for GL transesterification was investigated, and the results are shown in Table 2. As can be seen from the data in Table 2, Mg1Zr2-HT and Mg1Zr2-CP both have good catalytic performance for GL transesterification, with GL conversion greater than 90% and GC selectivity of about 95%. Because Mg1Zr2-HT catalyst has a larger specific surface area, reactant molecules are more easily in contact with active sites, therefore have higher catalytic activity.

Table 2. Catalytic performance of Mg1Zr2-HT and Mg1Zr2-CP for transesterification of GL with DMC.

Catalyst	GL Conversion (%)	GC Selectivity (%)	GC Yield (%)
Mg1Zr2-HT	96.0	95.1	91.3
Mg1Zr2-CP	91.0	94.0	85.5

Reaction condition: GL/DMC molar ratio = 1/5, catalyst loading = 3 wt% of GL, 90 °C, 60 min.

3.2. Effect of Mg-Zr Molar Ratio

The XRD patterns of catalysts with different Mg/Zr molar ratios are shown in Figure 2. It can be seen that with the increase of the Mg/Zr ratio, the diffraction peak of t-ZrO_2 at 2θ of 30° gradually shifts to a high angle, which may be due to the doping of Mg^{2+} into the lattice of ZrO_2, and some Zr^{4+} ions are replaced by Mg^{2+}, resulting in the distortion of the crystal structure. Because the ion radius of Mg^{2+} is smaller than that of Zr^{4+} (the ion radius of Mg^{2+} and Zr^{4+} is 0.780 Å and 0.840 Å, respectively), the lattice shrinks, and the cell parameters decrease, so the corresponding 2θ shifts to high angle [34]. At a low Mg/Zr molar ratio, no diffraction peak of MgO is observed, indicating the formation of a solid solution. With the increase of Mg content, the characteristic diffraction peaks of periclase MgO (JCPDS No. 45-0946) were detected at 2θ of 43.2° (200) and 62.5° (220), and the intensity and sharpness gradually increased with the increase of Mg content, indicating that the particle size of MgO increased significantly. The lattice parameters and crystal plane spacing of Mg-Zr catalysts were analyzed by Jade, and the results are listed in Table 3. It was found that the lattice constant "a" and crystal plane spacing of (011) crystal plane of Mg-Zr catalyst decreased with the increase of Mg content, indicating that a stable and uniform Mg-Zr composite oxide structure was generated after the introduction of Mg^{2+} into t-ZrO_2.

Figure S1a displays the Mg 1s spectra of Mg-Zr composite oxides catalysts, and the XPS spectrum of a single MgO is also presented for comparison. All the catalysts exhibited a broad and intense band centered at 1360 eV related to the emission from Mg 1s of Mg^{2+} in the oxide state. More importantly, the binding energies of Mg 1s in all the mixed oxides were lower than that of pure MgO, because the Mg-Zr oxides possessed a solid solution structure. The typical Zr 3d spectra are presented in Figure S1b. For pristine ZrO_2, there appeared two peaks at 184.8 and 182.4 eV with a high intensity, which were associated with Zr $3d_{3/2}$ and Zr $3d_{5/2}$ energy states of Zr (IV) oxide species, respectively. The intensity of these two reflections gradually decreased with an increase in Mg content. Meanwhile, it is worth noting that adding Mg into ZrO_2 support could give rise to a continuous increase of Zr 3d binding energy. These observations also support that Mg^{2+} had entered into the t-ZrO_2 lattice, creating a solid solution. Dis-cussing the peak fitted O 1s spectra from Figure S1c. The peak at 531 eV, 533 eV, and 534 eV can be attributed to the presence of lattice oxygen species (O_L), oxygen vacancies (O_V), and chemisorbed oxygen species (O_C). In general, the chemical valence of Zr ion is 4, but the Mg ion has only 2 valence, thus some vacancies are generated when substitution in order to keep charge neutrality in the ionic crystal, and these vacancies are favorable for heterogeneous catalysis [35]. It is worth noting that the Mg1Zr2 catalyst has the highest concentration of oxygen vacancies.

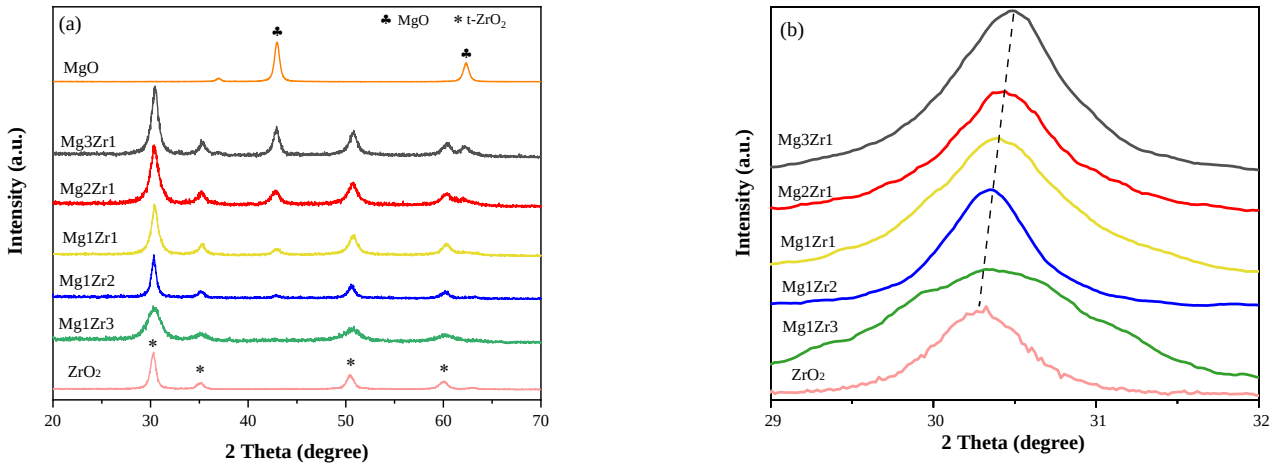

Figure 2. (**a**) XRD patterns of Mg-Zr composite oxides with different Mg/Zr ratios; (**b**) same as (**a**) but in region 2θ = 29–32.

Table 3. Texture properties and surface basicity of various Mg-Zr composite oxides.

Catalyst	ZrO_2 (011)		Lattice Parameter (nm)		Particle Size [a] (nm)	S_{BET} [b] (m^2/g)	Dp [c] (nm)	Vp [d] (cm^3/g)	Basicity [e] (μmol/g)		
	2θ (°)	d (nm)	a	c					W	M + S	Total
ZrO_2	30.25	0.2952	0.3622	0.5112	12.3	46.4	22.9	0.27	72.9	20.4	93.3
Mg1Zr3	30.30	0.2947	0.3601	0.5097	9.6	86.8	19.5	0.42	65.3	64.1	129.4
Mg1Zr2	30.33	0.2945	0.3596	0.5116	13.1	68.8	24.0	0.41	57.1	88.2	145.3
Mg1Zr1	30.36	0.2942	0.3594	0.5119	8.0	78.5	27.0	0.46	38.6	86.1	124.7
Mg2Zr1	30.38	0.2940	0.3593	0.5102	7.6	87.0	22.5	0.49	31.2	89.3	118.5
Mg3Zr1	30.45	0.2933	0.3586	0.5106	9.7	112.0	18.3	0.52	19.8	92.6	112.4
MgO	-	-	-	-	-	114.0	27.5	0.78	10.5	96.1	106.6

[a] Calculated by Scherrer formula using the full width at half maximum of ZrO_2 (011) plane. [b] S_{BET} was measured by the multi-point BET method. [c] Average pore size was calculated from the desorption branch of the isotherm using the BJH method. [d] Total pore volume was measured at $P/P_0 = 0.99$. [e] Calculated by the results of CO_2-TPD.

In order to observe the microstructure and morphology of the catalyst, the Mg-Zr composite oxides with different Mg/Zr ratios were characterized by TEM, and the results are shown in Figure 3. It can be seen from the TEM image of ZrO_2 that its particle size is relatively uniform, with an average particle size of 23 nm (based on the statistics of 91 particles in the TEM image), but its dispersion is poor, and a large number of particles agglomerate together. After adding a small amount of Mg, the uniformity of particle size of Mg1Zr3 becomes worse, indicating that the addition of Mg affects the crystallization and growth process of ZrO_2. In addition, compared with ZrO_2, there are some substances between the Mg1Zr3 particles, which may be extremely small MgO particles according to the preparation process and XRD results. With the increase of Mg content, the uniformity of ZrO_2 particle size becomes worse, and the particles with a size of about 50 nm appear in Mg1Zr2. When Mg content exceeds Zr, ZrO_2 particles gradually become smaller. Especially in Mg3Zr1, flake particle aggregates appear, and the large particle ZrO_2 disappears completely. Sádaba et al. [30] prepared the Mg-Zr catalyst by co-precipitation method. They pointed out that in the preparation process, Zr^{4+} preferentially precipitated to form $Zr(OH)_4$ or $ZrO_2(H_2O)_X$. When most of Zr^{4+} was precipitated, Mg^{2+} formed $Mg(OH)_2$ precipitation at pH 8~10. Therefore, Mg-Zr catalyst has an embedded structure with ZrO_2 as core and MgO as a shell. According to the conclusion of Sádaba et al. [30] and TEM results, it can be inferred that MgO was formed in the outer layer of ZrO_2 in the Mg-Zr catalysts prepared in this paper, which can be regarded as MgO wrapping ZrO_2. Guan et al. [36] also believed that Mg^{2+} could enter the ZrO_2 lattice to form Mg-Zr solid solution. When Mg content is large, MgO which cannot enter the lattice of ZrO_2 can appear as an independent crystal

phase and attach to the surface of magnesium-zirconium solid solution. The EDX spectrum and Elemental composition (Figure S2) show the presence of Mg and Zr. Even though several random areas were selected for the EDX test, the detected Mg/Zr molar ratio was almost the same as the theoretical value. The existence of all the elements in the oxide forms can be confirmed due to the presence of the high amount of oxygen and also the presence of Mg in Mg-Zr composite oxides enhances the basicity and stability of the catalyst.

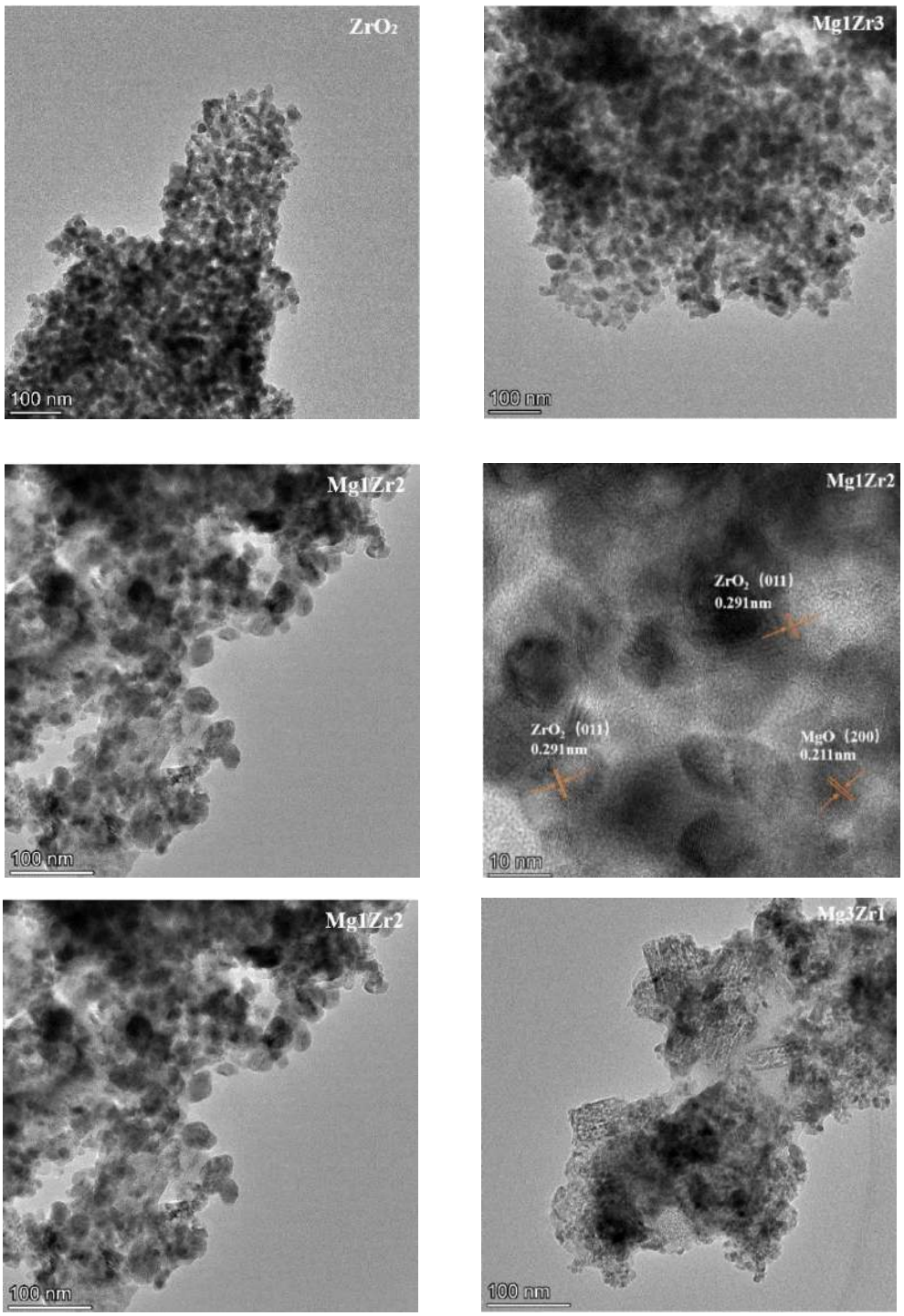

Figure 3. TEM images of Mg-Zr composite oxides with different Mg/Zr ratios.

The N_2 adsorption-desorption isotherms of Mg-Zr composite oxide catalysts are shown in Figure 4. There are obvious type IV adsorption equilibrium isotherms in the range of P/P_0 = 0.5~1.0, indicating that the catalysts had mesoporous structures. ZrO_2, Mg1Zr3, Mg1Zr2, and Mg1Zr1 catalysts all have H2 type hysteresis loops, indicating that the catalyst internal pore structure is ink bottle; The N_2 adsorption-desorption isotherms of Mg2Zr1, Mg3Zr1, and MgO catalysts have no obvious saturated adsorption platform, accompanied by H3 hysteresis loop, indicating that the pore structure of the catalyst is very irregular, combined with the TEM results, it can be seen that there is the slit hole formed by the accumulation of flake particles.

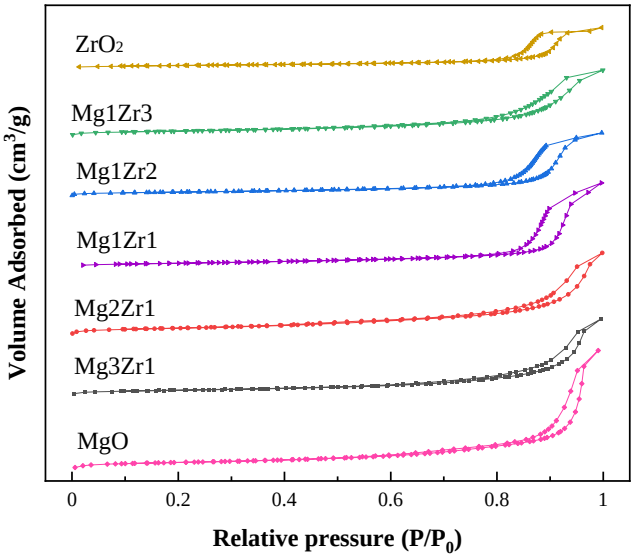

Figure 4. N_2 adsorption-desorption isotherms of Mg-Zr oxides with different Mg/Zr ratios.

The specific surface area, pore diameter, and pore volume of the catalysts are listed in Table 3. It can be seen that the specific surface area of Mg1Zr2 is 68.8 m^2/g, and then the specific surface area increases with the addition of Mg, which is consistent with the experimental results of Guan [36]. As the Mg content increased, the specific surface area of Mg-Zr oxide catalysts has an upward trend, which may be due to the multi-layer dispersion of MgO attached to the surface of magnesium-zirconium solid solution, resulting in the increase of specific surface area. MgO has the largest specific surface area, but the catalytic performance is not the best, indicating that although the structure of the catalyst has a certain impact on the catalytic performance, it is not a completely decisive factor.

To better understand the intrinsic acid-base functionalities and correlate the catalysts with their catalytic behavior, CO_2-TPD and NH_3-TPD measurements were performed to quantitatively determine the distribution of surface acidity and basicity and the number of acidic and basic sites of MgO-ZrO_2 catalysts. The CO_2-TPD characterization of Mg-Zr oxide catalysts was carried out, and the influence of the Mg/Zr molar ratio on the basicity of the catalyst was investigated. The results are shown in Figure 5 and Table 3. It can be seen from Figure 5 that the Mg/Zr molar ratio has a significant effect on the basicity of Mg-Zr oxide catalysts. When the Mg content is 0 (ZrO_2), there are mainly weak basic sites on the surface of the catalyst with a CO_2 desorption temperature lower than 200 °C. With the addition of Mg, the number of medium strong basic sites (CO_2 desorption temperature is in the range of 200–600 °C) on the catalyst surface gradually increases, while the number of weak basic sites decreases. Among them, Mg1Zr2 has the largest number of total basic sites, because it has more weak sites and medium and strong sites at the same time. With the further increase of Mg content, the number of weak basic sites decreased rapidly. The surface of the Mg3Zr1 catalyst is mainly composed of medium and strong basic sites, while the weak sites almost disappear. Its CO_2-TPD curve is similar to that of MgO. The results showed that the weak basic sites on the surface of Mg-Zr oxide catalysts were mainly provided by ZrO_2,

while the medium and strong sites were mainly related to MgO. Zhang et al. [34] believed that the weak basic sites of the MgO-ZrO_2 catalyst were related to its surface hydroxyl group, while the medium and strong basic sites were related to metal-oxygen pairs (Mg-O and Zr-O) and low coordination oxygen atoms (O^{2-}). In addition, according to the data in Table 3, the total number of surface basic sites of ZrO_2 and MgO is similar, but the number of Mg-Zr oxide catalysts increases significantly. In particular, the number of total basic sites of Mg1Zr2 catalyst reaches 145.3 μmol/g, which is 55.7% and 36.3% higher than that of the two single metal oxides, respectively. It is considered that Mg^{2+} and Zr^{4+} are fully mixed during the hydrothermal preparation of the catalyst, and part of Zr^{4+} in the lattice of ZrO_2 is replaced by Mg^{2+} after calcination. Due to that Zr^{4+} is more positive than Mg^{2+}, the electron density of O^{2-} in Mg-Zr oxide catalysts increases, thus increasing the number of medium and strong basic sites of the catalyst [28].

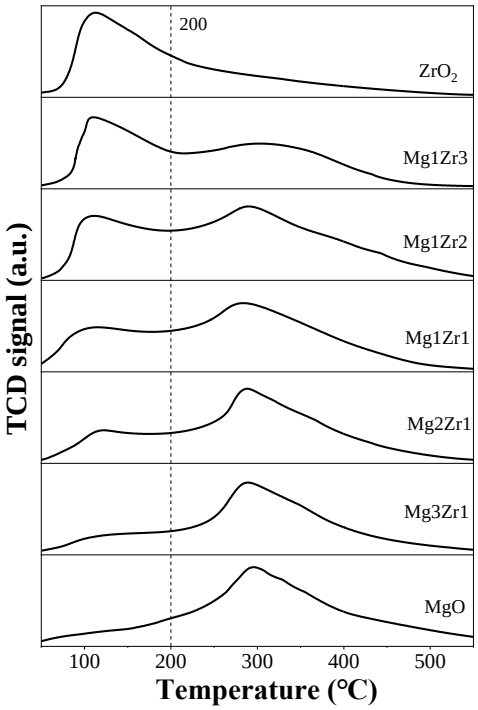

Figure 5. CO_2-TPD of Mg-Zr composite oxides with different Mg/Zr ratios.

As shown in Figure S3, in the NH_3-TPD curve of bare ZrO_2, there are two NH_3 desorption peaks at 130 °C and 530 °C, corresponding to weak acidic sites and strong acidic sites respectively. With the increase of MgO content, the medium-strength acid sites of the catalyst increased, while the weak and strong acid sites decreased. The results showed that there was no strong correlation between catalyst acidity and glycerol conversion. Although the role of acid sites in the activation of DMC cannot be completely ruled out, the effect of acid sites is less clear and predictable compared to the evident effect of basic sites [37].

The effect of the Mg/Zr ratio on the transesterification of GL and DMC to GC over Mg-Zr composite oxide was studied, and the results are shown in Figure 6. As can be seen from the figure, ZrO_2 and MgO alone are active for the transesterification of GL, and GL conversion is 67.2% and 73.8%, respectively. The activity of the Mg-Zr oxide catalysts was higher than that of the two single metal oxides, indicating the interaction between ZrO_2 and MgO and improving the performance of the catalyst. When Mg1Zr3 was used, the GL conversion was 84.0%. With the increase of Mg content, the catalyst activity increased first and then decreased. Among them, Mg1Zr2 has the highest activity for transesterification of GL, with GL conversion of 96.0% and GC selectivity of 95.3%. The Mg/Zr ratio had little effect on the selectivity of GC. The byproduct was glycidyl, and no other products were detected. According to the characterization results, Mg1Zr2 has the highest number

of total basic sites. Moreover, the order of GL conversion is basically the same as that of the number of basic sites on the catalyst surface. This indicates that the influence of the Mg/Zr ratio on catalyst performance lies in the change in the number of catalyst basic sites. In this transesterification reaction, the main function of the solid catalyst is to support the abstraction of H^+ from glycerol by the basic sites so as to form glycerol anion. The higher the basicity of the catalyst, the more negative the charge of the glyceroxide anion ($C_3H_7O_3^-$), and consequently, the lower the free energy of the reaction [38]. In other words, the deprotonation of glycerol (on basic sites) is likely more important than the activation of dimethyl carbonate (on acidic sites) for the transesterification of glycerol and dimethyl carbonate [39].

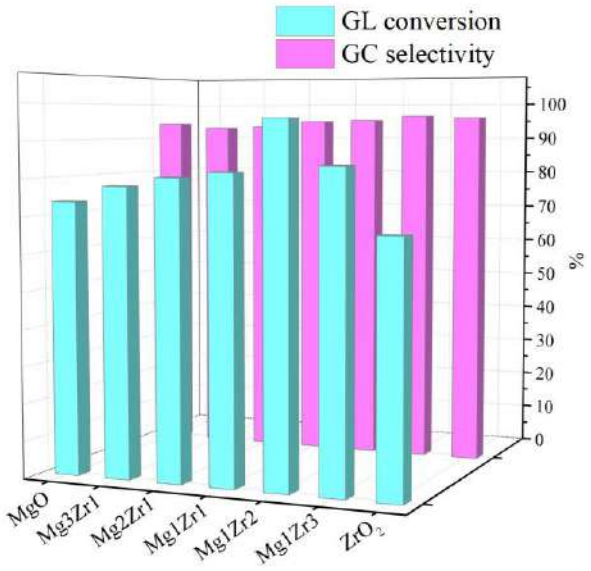

Figure 6. Catalytic performance of Mg-Zr oxides for transesterification of GL with DMC to GC (Reaction conditions: GL/DMC molar ratio = 1/5, catalyst loading = 3 wt% of GL, 90 °C, 60 min).

3.3. Effect of Reaction Conditions on Transesterification of GL over Mg1Zr2-HT

Using Mg1Zr2-HT as a catalyst, the effects of reaction time, reaction temperature, catalyst amount, and GL/DMC molar ratio on the transesterification of GL with DMC to GC were investigated.

3.3.1. Effect of Reaction Time

As shown in Figure 7a, the effect of reaction time on the transesterification of GL with DMC was investigated. It can be seen that GL conversion increased gradually with the increase in reaction time. When the reaction time was 90 min, the GL conversion was 99.0% and GC selectivity was 96.1%; With the continuous extension of reaction time, GL conversion remained unchanged and GC selectivity decreased. This was caused by the decomposition of GC into glycidyl.

3.3.2. Effect of Reaction Temperature

It can be seen from Figure 7b that increasing temperature before 90 °C is conducive to promoting the reaction. This is because the reaction equilibrium constant of this reaction increases with the increase of temperature, so heating is conducive to the reaction. At 90 °C, GL conversion was 99.0% with GC selectivity of 96.1%. When the temperature continues to rise, the decomposition of GC into glycidyl occurs more readily [40], so GC selectivity decreases.

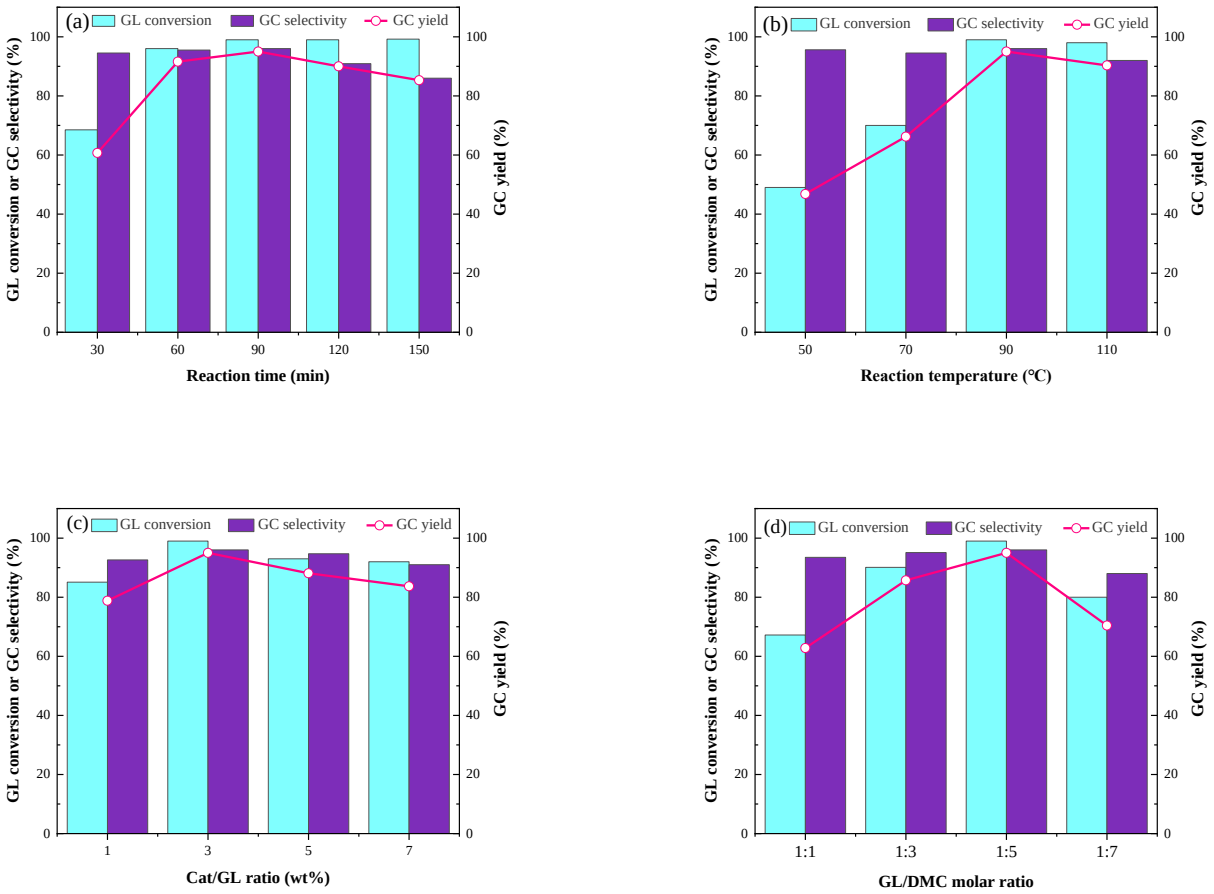

Figure 7. Effect of reaction conditions on the GL transesterification over Mg1Zr2-HT catalyst: (**a**) effect of reaction time (GL/DMC molar ratio = 1/5, catalyst amount = 3 wt% of GL, 90 °C), (**b**) effect of reaction temperature(GL/DMC molar ratio = 1/5, catalyst amount = 3 wt% of GL, 90 min), (**c**) effect of catalyst amount(GL/DMC molar ratio = 1/5, 90 °C, 90 min), (**d**) effect of GL/DMC molar ratio(catalyst amount = 3 wt% of GL, 90 °C, 90 min).

3.3.3. Effect of Catalyst Amount

The transesterification reaction of glycerol was highly influenced by the catalyst amount (wt% based on GL) and presented in Figure 7c, the increase of the amount of catalyst from 1 wt% to 3 wt%, the GL conversion and GC yield gradually increased, which was attributed to the increase in the basic sites of the transesterification catalyst. However, the amount of catalyst increased from 3 wt% to 7 wt%, and the GC yield decreased slowly, which may be due to the agglomeration of catalyst at a higher amount, which makes the reactants unable to enter the active center of the catalyst. The higher the amount of catalyst is, the greater the mass transfer resistance is, which may hinder the transesterification of GL with DMC [41].

3.3.4. Effect of the Molar Ratio of GL/DMC

The molar ratio of GL/DMC has a great influence on the GL conversion and GC yield during the transesterification. Since the transesterification reaction is essentially reversible, excessive DMC is needed to shift the reaction equilibrium to GC. From Figure 7d, it is clear that with the increase of the molar ratio of DMC/GL, the conversion of GL showed an upward trend, and when the molar ratio was 1/5 (GL/DMC), the maximum conversion was 99.0% and the GC selectivity was 96.1%. If the molar ratio of DMC/GL continues to increase, the conversion of GL and GC yield decreases. This may be due to the excessive DMC diluting the catalyst and limiting the contact between GL and the catalyst, thus reducing the reaction rate [40].

3.4. Catalyst Stability

The reusability of a catalyst is an important index to evaluate the performance of the catalyst. In this study, the reusability of Mg1Zr2-HT and Mg1Zr2-CP catalysts for transesterification of GL with DMC is compared, as shown in Figure 8. After the reaction, the catalyst was centrifuged, washed three times with methanol, dried at 100 °C, and then calcined at 600 °C in air for 3 h. As can be seen from the figure, GC selectivity was little affected by repeated use and was almost constant. However, GL conversion gradually decreased, and there were significant differences between the Mg1Zr2-HT and Mg1Zr2-CP catalysts. When a fresh catalyst was used, the GL conversion over Mg1Zr2-HT and Mg1Zr2-CP catalysts was 99.0% and 95.2%, respectively. Moreover, when repeated for the fourth time, GL conversions were 80.1% and 58.2%, respectively. The stability of Mg1Zr2-HT is much better than that of Mg1Zr2-CP.

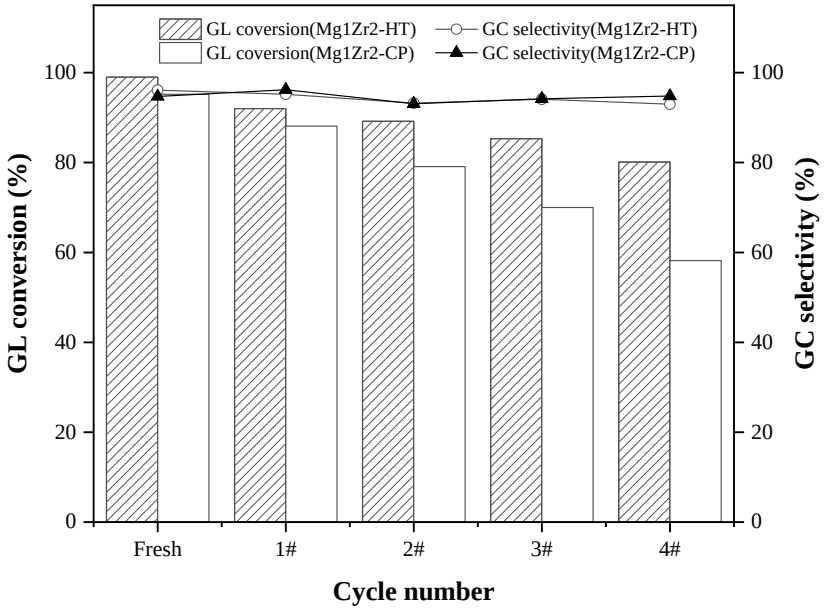

Figure 8. Reusability of Mg1Zr2-HT and Mg1Zr2-CP (Reaction condition: GL/DMC molar ratio = 1/5, catalyst loading = 3 wt%, 90 °C, 90 min).

In order to explore the reasons for the differences between the two catalysts, Mg1Zr2-HT and Mg1Zr2-CP catalysts after four times of reused were characterized by XRD, N_2 adsorption-desorption, CO_2-TPD, TEM, and XPS.

The XRD patterns of Mg1Zr2-HT-used and Mg1Zr2-CP-used catalysts after the fourth cycle are presented in Figure 9. It can be seen that there are obvious characteristic diffraction peaks at 2θ of 30.2°, 34.8°, 50.7°, 60.2°, and 62.9°, corresponding to (011), (110), (020), (121) and (202) crystal planes of tetragonal ZrO_2, respectively. The characteristic diffraction peaks appear at 2θ of 43.2° and 62.5°, corresponding to the (200) and (220) crystal planes of MgO, respectively. Based on the diffraction peaks of ZrO_2 (011) and MgO (200) crystal planes, the grain sizes of ZrO_2 and MgO in Mg1Zr2-HT-used are 15.8 nm and 15.0 nm by the Scherrer formula, respectively; The grain sizes of ZrO_2 and MgO in Mg1Zr2-CP-used are 16.6 nm and 31.4 nm, respectively. Compared with the fresh catalyst, the particle sizes of the two catalysts after repeated use both increased, but the grain size of MgO in Mg1Zr2-CP-used increased by about double, while the grain size of MgO in Mg1Zr2-HT-used increased by only 14%. Under hydrothermal conditions, ions in the solution automatically aggregate to form the most stable chemical structure that cannot be decomposed in the system during the temperature change, so they have good grain stability.

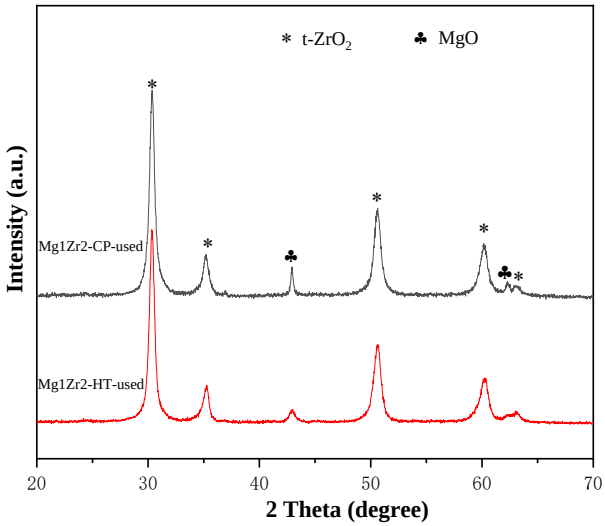

Figure 9. XRD patterns of Mg1Zr2-HT-used and Mg1Zr2-CP-used.

It can be seen from Figure 10 that after transesterification, the particle sizes of both two catalysts increased significantly and the particle sizes became uneven, indicating that the catalyst particles appeared aggregate and sintering, resulting in the gradual increase of grain size and the decrease of dispersion. The Mg1Zr2-CP-used catalyst had serious agglomeration, while the Mg1Zr2-HT-used catalyst had slight sintering but no obvious agglomeration, indicating that the catalyst prepared by the hydrothermal process had strong sintering resistance. This is because under hydrothermal conditions, the compounds in the solution may renucleate and restructure, so that the particles after hydrothermal treatment have better dispersion and grain stability than those particles only by neutralization precipitation [42].

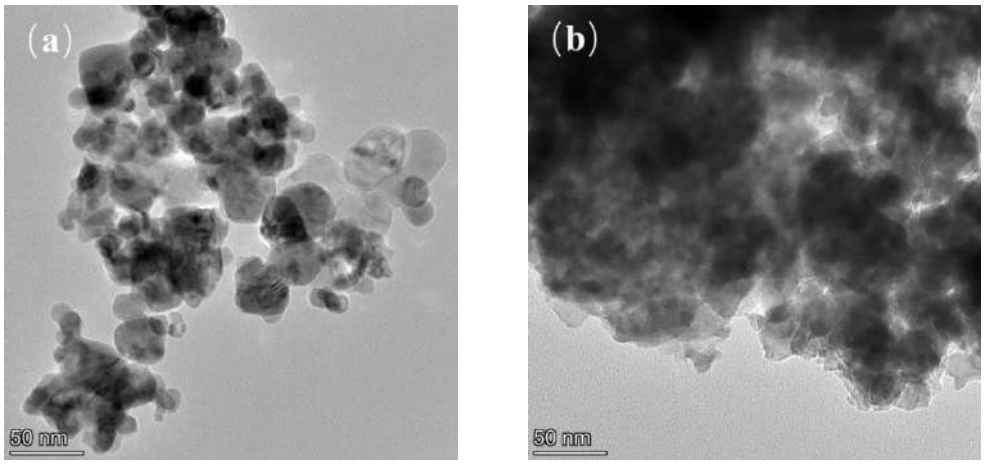

Figure 10. TEM images of Mg1Zr2-HT-used (**a**) and Mg1Zr2-CP-used (**b**).

Compares the deconvoluted Mg 1s, Zr 3d, and O 1s XPS spectra of fresh and used Mg1Zr2-HT. The relative abundances of the Mg 1s, Zr 3d, and O 1s of the samples from Figure S4 showed that the content of the oxygen vacancy decreased from 26.5% to 23.1% and the content of the chemisorbed oxygen species increased from 1.1% to 3.9%, respectively, indicating that irreversible deactivation was caused.

As can be seen from Table 4 that the Mg1Zr2-HT-used catalyst has a larger specific surface area than the Mg1Zr2-CP-used catalyst, and more active sites can be retained. This may be because the colloidal network structure formed in the hydrothermal process is more stable through dissolution-deposition, which alleviates the collapse of the structure and the sintering of particles, so that it still maintains a large specific surface area in the reaction

process [43]. Since the catalytic reaction occurs on the surface of active components, the agglomeration and growth of grains lead to the decrease of active surface area, the decrease of active sites, and the reduction in catalytic activity [44]. Compared with fresh catalysts, the number of weak basic sites of Mg1Zr2-HT and Mg1Zr2-CP catalysts decreased by 12% and 13%, respectively, but the number of medium and strong basic sites decreased by 25% and 50%, respectively. Moreover, it was observed that Mg1Zr2-CP-used suffered a greater loss of basic sites than Mg1Zr2-HT-used. This is probably the reason why Mg1Zr2-HT showed better catalytic performance than Mg1Zr2-CP after four cycles. Mg1Zr2-HT possesses a more stable crystal structure to avoid the irreversible reduction of basic sites amount.

Table 4. Texture properties and surface basicity of Mg1Zr2-HT-used and Mg1Zr2-CP-used.

Catalyst	ZrO_2 Crystallite Size [a] (nm)	MgO Crystallite Size [b] (nm)	S_{BET} [c] (m^2/g)	D_P [d] (nm)	V_P [e] (cm^3/g)	Basicity [f] (μmol/g)		
						W	M + S	Total
Mg1Zr2-HT-used	15.8	15.0	40.1	30.3	0.30	50.3	66.2	116.5
Mg1Zr2-CP-used	16.6	31.4	25.5	29.7	0.19	46.2	42.0	88.2

[a] Calculated by Scherrer formula using the full width at half maximum of ZrO_2 (011) plane. [b] Calculated by Scherrer formula using the full width at half maximum of MgO (200) plane. [c] S_{BET} was measured by the multi-point BET method. [d] Average pore size was calculated from the desorption branch of the isotherm using the BJH method. [e] Total pore volume was measured at $P/P_0 = 0.99$. [f] Calculated by the results of CO_2-TPD.

4. Conclusions

In this work, Mg-Zr composite oxide catalysts with different Mg/Zr molar ratios were prepared by hydrothermal process and their activity and stability towards GC synthesis were studied. The results showed that the catalysts prepared by the hydrothermal process had larger specific surface area, smaller grain size, and higher dispersion than those prepared by the co-precipitation process. The Mg1Zr2-HT catalyst calcined at 600 °C in a nitrogen atmosphere showed the best catalytic performance, with GL conversion of 99% and GC selectivity of 96.1% under mild reaction conditions. This is attributed to the balanced strong and weak basic sites and highly dispersed MgO. Moreover, the GL conversion was demonstrated to increase in parallel with the total amount of basic sites. Compared with the Mg1Zr2-CP catalyst, the Mg1Zr2-HT catalyst has good thermal stability and reproducibility. The conversion of GL is still up to 80.1% and the selectivity of GC is 93.0% in the fourth reuse, while the regenerated Mg1Zr2-CP catalyst is 58.2% and 94.8% in the fourth reuse. The reason for the difference may be that in the cyclic reaction process, Mg1Zr2-HT has good grain stability and small growth amplitude, but the grain growth of active species in Mg1Zr2-CP is large, which will greatly reduce the effective active surface area of the catalyst, resulting in a significant decrease in the catalytic performance.

Supplementary Materials: The following supporting information can be downloaded at: https://www.mdpi.com/article/10.3390/nano12121972/s1, Figure S1: X-ray photoelectron spectra of Mg-Zr composite oxides. Regions: Mg 1s (a), Zr 3d (b) and O 1s (c); Figure S2: EDX spectrum and Elemental composition of Mg-Zr composite oxides with different Mg/Zr ratio; Figure S3: NH_3-TPD of Mg-Zr composite oxides with different Mg/Zr ratio; Figure S4: X-ray photoelectron spectra of fresh and used Mg1Zr2 composite oxides. Regions: Mg 1s (a), Zr 3d (b) and O 1s (c).

Author Contributions: Y.L.: Investigation, Data curation, Writing—Original Draft. H.Z.: Methodology, Visualization. W.X.: Formal analysis, Investigation. F.L.: Conceptualization, Writing—Review & Editing, Funding acquisition. Z.W.: Methodology, Supervision. All authors have read and agreed to the published version of the manuscript.

Funding: This work was funded by the National Natural Science Foundation of China (Nos. 21776057, U20A20152, U21A20306).

Institutional Review Board Statement: Not applicable.

Informed Consent Statement: Not applicable.

Data Availability Statement: The data presented in this study are available on request from the corresponding author.

Acknowledgments: All individuals consent to the acknowledgement.

Conflicts of Interest: The authors declare no conflict of interest.

References

1. Rozulan, N.; Halim, S.A.; Razali, N.; Lam, S.S. A Review on Direct Carboxylation of Glycerol Waste to Glycerol Carbonate and Its Applications. In *Biomass Conversion and Biorefinery*; Springer International Publishing: Cham, Switzerland, 2022; pp. 1–18.
2. Procopio, D.; Di Gioia, M.L. An Overview of the Latest Advances in the Catalytic Synthesis of Glycerol Carbonate. *Catalysts* **2022**, *12*, 50. [CrossRef]
3. Polychronopoulou, K.; Dabbawala, A.A.; Sajjad, M.; Singh, N.; Anjum, D.H.; Baker, M.A.; Charisiou, N.D.; Goula, M.A. Hydrogen Production Via Steam Reforming of Glycerol over Ce-La-Cu-O Ternary Oxide Catalyst: An Experimental and Dft Study. *Appl. Surf. Sci.* **2022**, *586*, 152798. [CrossRef]
4. Qingli, X.; Zhengdong, Z.; Kai, H.; Shanzhi, X.; Chuang, M.; Chenge, C.; Huan, Y.; Yang, Y.; Yongjie, Y. Ni Supported on MgO Modified Attapulgite as Catalysts for Hydrogen Production from Glycerol Steam Reforming. *Int. J. Hydrogen Energy* **2021**, *46*, 27380–27393. [CrossRef]
5. Dang, T.N.M.; Sahraei, O.A.; Olivier, A.; Iliuta, M.C. Effect of Impurities on Glycerol Steam Reforming over Ni-Promoted Metallurgical Waste Driven Catalyst. *Int. J. Hydrogen Energy* **2022**, *47*, 4614–4630. [CrossRef]
6. Sahraei, O.A.; Desgagnés, A.; Larachi, F.; Iliuta, M.C. A Comparative Study on the Performance of M (Rh, Ru, Ni)-Promoted Metallurgical Waste Driven Catalysts for H_2 Production by Glycerol Steam Reforming. *Int. J. Hydrogen Energy* **2021**, *46*, 32017–32035. [CrossRef]
7. Charisiou, N.D.; Siakavelas, G.; Tzounis, L.; Dou, B.; Sebastian, V.; Hinder, S.J.; Baker, M.A.; Polychronopoulou, K.; Goula, M.A. $Ni/Y_2O_3–ZrO_2$ Catalyst for Hydrogen Production through the Glycerol Steam Reforming Reaction. *Int. J. Hydrogen Energy* **2020**, *45*, 10442–10460. [CrossRef]
8. Keogh, J.; Deshmukh, G.; Manyar, H. Green Synthesis of Glycerol Carbonate Via Transesterification of Glycerol Using Mechanochemically Prepared Sodium Aluminate Catalysts. *Fuel* **2022**, *310*, 122484. [CrossRef]
9. Christy, S.; Noschese, A.; Lomelí-Rodriguez, M.; Greeves, N.; Lopez-Sanchez, J.A. Recent Progress in the Synthesis and Applications of Glycerol Carbonate. *Curr. Opin. Green Sustain. Chem.* **2018**, *14*, 99–107. [CrossRef]
10. Caro, S.D.; Bandres, M.; Urrutigoty, M.; Cecutti, C.; Thiebaud-Roux, S. Recent Progress in Synthesis of Glycerol Carbonate and Evaluation of Its Plasticizing Properties. *Front. Chem.* **2019**, *7*, 308. [CrossRef]
11. Lukato, S.; Kasozi, G.N.; Naziriwo, B.; Tebandeke, E. Glycerol Carbonylation with CO_2 to Form Glycerol Carbonate: A Review of Recent Developments and Challenges. *Curr. Res. Green Sustain. Chem.* **2021**, *4*, 100199. [CrossRef]
12. Zhang, J.; He, D. Lanthanum-Based Mixed Oxides for the Synthesis of Glycerol Carbonate from Glycerol and Urea. *React. Kinet. Mech. Catal.* **2014**, *113*, 375–392. [CrossRef]
13. Changmai, B.; Laskar, I.B.; Rokhum, L. Microwave-Assisted Synthesis of Glycerol Carbonate by the Transesterification of Glycerol with Dimethyl Carbonate Using Musa Acuminata Peel Ash Catalyst. *J. Taiwan Inst. Chem. Eng.* **2019**, *102*, 276–282. [CrossRef]
14. Pradhan, G.; Sharma, Y.C. Green Synthesis of Glycerol Carbonate by Transesterification of Bio Glycerol with Dimethyl Carbonate over Mg/ZnO: A Highly Efficient Heterogeneous Catalyst. *Fuel* **2021**, *284*, 118966. [CrossRef]
15. Manikandan, M.; Sangeetha, P. Optimizing the Surface Properties of MgO Nanoparticles Towards the Transesterification of Glycerol to Glycerol Carbonate. *ChemistrySelect* **2019**, *4*, 6672–6678. [CrossRef]
16. Bai, Z.; Zheng, Y.; Han, W.; Ji, Y.; Yan, T.; Tang, Y.; Chen, G.; Zhang, Z. Development of a Trapezoidal MgO Catalyst for Highly-Efficient Transesterification of Glycerol and Dimethyl Carbonate. *CrystEngComm* **2018**, *20*, 4090–4098. [CrossRef]
17. Roschat, W.; Phewphong, S.; Kaewpuang, T.; Promarak, V. Synthesis of Glycerol Carbonate from Transesterification of Glycerol with Dimethyl Carbonate Catalyzed by CaO from Natural Sources as Green and Economical Catalyst. *Mater. Today Proc.* **2018**, *5*, 13909–13915. [CrossRef]
18. Simanjuntak, F.; Kim, T.K.; Sang, D.L.; Ahn, B.S.; Kim, H.S.; Lee, H. CaO-Catalyzed Synthesis of Glycerol Carbonate from Glycerol and Dimethyl Carbonate: Isolation and Characterization of an Active Ca Species. *Appl. Catal. A Gen.* **2011**, *401*, 220–225. [CrossRef]
19. Praikaew, W.; Kiatkittipong, W.; Aiouache, F.; Najdanovic-Visak, V.; Termtanun, M.; Lim, J.W.; Lam, S.S.; Kiatkittipong, K.; Laosiripojana, N.; Boonyasuwat, S. Mechanism of CaO Catalyst Deactivation with Unconventional Monitoring Method for Glycerol Carbonate Production Via Transesterification of Glycerol with Dimethyl Carbonate. *Int. J. Energy Res.* **2022**, *46*, 1646–1658. [CrossRef]
20. Ying, T.; Yan, T.; Bo, S.; Li, H.; Jeje, A. Synthesis of No-Glycerol Biodiesel through Transesterification Catalyzed by CaO from Different Precursors. *Can. J. Chem. Eng.* **2016**, *94*, 1466–1471.
21. Liu, Y.; Xia, C.; Wang, Q.; Zhang, L.; Huang, A.; Ke, M.; Song, Z. Direct Dehydrogenation of Isobutane to Isobutene over Zn-Doped ZrO_2 Metal Oxide Heterogeneous Catalysts. *Catal. Sci. Technol.* **2018**, *8*, 4916–4924. [CrossRef]
22. Bing, W.; Wei, M. Recent Advances for Solid Basic Catalysts: Structure Design and Catalytic Performance. *J. Solid State Chem.* **2019**, *269*, 184–194. [CrossRef]

23. Zhang, X.L.; Wei, S.W.; Zhao, X.Y.; Chen, Z.; Wu, H.W.; Rong, P.; Sun, Y.; Li, Y.; Yu, H.; Wang, D.F. Preparation of Mesoporous Cao-Zro2 Catalysts without Template for the Continuous Synthesis of Glycerol Carbonate in a Fixed-Bed Reactor. *Appl. Catal. A Gen.* **2020**, *590*, 12. [CrossRef]
24. Otor, H.O.; Steiner, J.B.; García-Sancho, C.; Alba-Rubio, A.C. Encapsulation Methods for Control of Catalyst Deactivation: A Review. *ACS Catal.* **2020**, *10*, 7630–7656. [CrossRef]
25. Chandrasekar, M.; Subash, M.; Logambal, S.; Udhayakumar, G.; Uthrakumar, R.; Inmozhi, C.; Al-Onazi, W.A.; Al-Mohaimeed, A.M.; Chen, T.-W.; Kanimozhi, K. Synthesis and Characterization Studies of Pure and Ni Doped CuO Nanoparticles by Hydrothermal Method. *J. King Saud Univ.-Sci.* **2022**, *34*, 101831. [CrossRef]
26. Cui, H.; Wu, X.; Chen, Y.; Boughton, R. Synthesis and Characterization of Mesoporous MgO by Template-Free Hydrothermal Method. *Mater. Res. Bull.* **2014**, *50*, 307–311. [CrossRef]
27. Akune, T.; Morita, Y.; Shirakawa, S.; Katagiri, K.; Inumaru, K. ZrO_2 Nanocrystals as Catalyst for Synthesis of Dimethylcarbonate from Methanol and Carbon Dioxide: Catalytic Activity and Elucidation of Active Sites. *Langmuir* **2018**, *34*, 23–29. [CrossRef]
28. Yichao, W.; Yachun, C.; Guangxu, Z.; Yuntao, Y. Preparation of Mg/Sn/W Composite Oxide Catalyst by Hydrothermal Method and Its Performance Evaluation. *Petrochem. Technol.* **2019**, *48*, 1212.
29. Varkolu, M.; Burri, D.R.; Kamaraju, S.R.R.; Jonnalagadda, S.B.; Van Zyl, W.E. Transesterification of Glycerol with Dimethyl Carbonate over Nanocrystalline Ordered Mesoporous MgO–ZrO_2 Solid Base Catalyst. *J. Porous Mater.* **2015**, *23*, 185–193. [CrossRef]
30. Sádaba, I.; Ojeda, M.; Mariscal, R.; Fierro, J.L.G.; Granados, M.L. Catalytic and Structural Properties of Co-Precipitated Mg–Zr Mixed Oxides for Furfural Valorization Via Aqueous Aldol Condensation with Acetone. *Appl. Catal. B Environ.* **2011**, *101*, 638–648. [CrossRef]
31. Zhu, W.; Jiang, X.; Liu, F.; You, F.; Yao, C. Preparation of Chitosan—Graphene Oxide Composite Aerogel by Hydrothermal Method and Its Adsorption Property of Methyl Orange. *Polymers* **2020**, *12*, 2169. [CrossRef]
32. Pan, Q.; Xie, J.; Zhu, T.; Cao, G.; Zhao, X.; Zhang, S. Reduced Graphene Oxide-Induced Recrystallization of Nis Nanorods to Nanosheets and the Improved Na-Storage Properties. *Inorg. Chem.* **2014**, *53*, 3511–3518. [CrossRef] [PubMed]
33. Walker, R.C.; Potochniak, A.E.; Hyer, A.P.; Ferri, J.K. Zirconia Aerogels for Thermal Management: Review of Synthesis, Processing, and Properties Information Architecture. *Adv. Colloid Interface Sci.* **2021**, *295*, 102464. [CrossRef] [PubMed]
34. Zhang, X.; Wang, D.; Wu, G.; Wang, X.; Jiang, X.; Liu, S.; Zhou, D.; Xu, D.; Gao, J. One-Pot Template-Free Preparation of Mesoporous MgO-ZrO_2 Catalyst for the Synthesis of Dipropyl Carbonate. *Appl. Catal. A Gen.* **2018**, *555*, 130–137. [CrossRef]
35. Liu, B.; Li, C.; Zhang, G.; Yan, L.; Li, Z. Direct Synthesis of Dimethyl Carbonate from CO_2 and Methanol over CaO–CeO_2 Catalysts: The Role of Acid–Base Properties and Surface Oxygen Vacancies. *New J. Chem.* **2017**, *41*, 12231–12240. [CrossRef]
36. Guan, H.; Liang, J.; Zhu, Y.; Zhao, B.; Xie, Y. Structure Characterization and Monolayer Dispersion Phenomenon of MgO-ZrO_2 Prepared by Co-Precipitation. *Acta Phys.-Chim. Sin.* **2005**, *21*, 1011–1016.
37. Poolwong, J.; Del Gobbo, S.; D'Elia, V. Transesterification of Dimethyl Carbonate with Glycerol by Perovskite-Based Mixed Metal Oxide Nanoparticles for the Atom-Efficient Production of Glycerol Carbonate. *J. Ind. Eng. Chem.* **2021**, *104*, 43–60. [CrossRef]
38. Kumar, P.; With, P.; Srivastava, V.C.; Gläser, R.; Mishra, I.M. Glycerol Carbonate Synthesis by Hierarchically Structured Catalysts: Catalytic Activity and Characterization. *Ind. Eng. Chem. Res.* **2015**, *54*, 12543–12552. [CrossRef]
39. Chang, C.-W.; Gong, Z.-J.; Huang, N.-C.; Wang, C.-Y.; Yu, W.-Y. MgO Nanoparticles Confined in ZIF-8 as Acid-Base Bifunctional Catalysts for Enhanced Glycerol Carbonate Production from Transesterification of Glycerol and Dimethyl Carbonate. *Catal. Today* **2020**, *351*, 21–29. [CrossRef]
40. Liu, Z.; Li, B.; Qiao, F.; Zhang, Y.; Wang, X.; Niu, Z.; Wang, J.; Lu, H.; Su, S.; Pan, R. Catalytic Performance of Li/Mg Composites for the Synthesis of Glycerol Carbonate from Glycerol and Dimethyl Carbonate. *ACS Omega* **2022**, *7*, 5032–5038. [CrossRef]
41. Pradhan, G.; Sharma, Y.C. A Greener and Cheaper Approach Towards Synthesis of Glycerol Carbonate from Bio Waste Glycerol Using CaO–TiO_2 Nanocatalysts. *J. Clean. Prod.* **2021**, *315*, 127860. [CrossRef]
42. Zhang, Q.; Tang, T.; Wang, J.; Sun, M.; Wang, H.; Sun, H.; Ning, P. Facile Template-Free Synthesis of Ni-SiO_2 Catalyst with Excellent Sintering-and Coking-Resistance for Dry Reforming of Methane. *Catal. Commun.* **2019**, *131*, 105782. [CrossRef]
43. Ma, Z.; Meng, X.; Liu, N.; Yang, C.; Shi, L. Preparation, Characterization, and Isomerization Catalytic Performance of Palladium Loaded Zirconium Hydroxide/Sulfated Zirconia. *Ind. Eng. Chem. Res.* **2018**, *57*, 14377–14385. [CrossRef]
44. Grams, J.; Ruppert, A.M. Catalyst Stability—Bottleneck of Efficient Catalytic Pyrolysis. *Catalysts* **2021**, *11*, 265. [CrossRef]

nanomaterials

MDPI

Article

Alternative Controlling Agent of *Theobroma grandiflorum* Pests: Nanoscale Surface and Fractal Analysis of Gelatin/PCL Loaded Particles Containing *Lippia origanoides* Essential Oil

Ana Luisa Farias Rocha [1,2], Ronald Zico de Aguiar Nunes [1], Robert Saraiva Matos [3], Henrique Duarte da Fonseca Filho [2,4], Jaqueline de Araújo Bezerra [5], Alessandra Ramos Lima [6], Francisco Eduardo Gontijo Guimarães [6], Ana Maria Santa Rosa Pamplona [7], Cláudia Majolo [7], Maria Geralda de Souza [7], Pedro Henrique Campelo [8], Ştefan Ţălu [9,*], Vanderlei Salvador Bagnato [6,10], Natalia Mayumi Inada [6] and Edgar Aparecido Sanches [1,2]

1 Laboratory of Nanostructured Polymers (NANOPOL), Federal University of Amazonas (UFAM), Manaus 69067-005, AM, Brazil
2 Graduate Program in Materials Science and Engineering (PPGCEM), Federal University of Amazonas (UFAM), Manaus 69067-005, AM, Brazil
3 Amazonian Materials Group, Federal University of Amapá (UNIFAP), Macapá 68903-419, AP, Brazil
4 Laboratory of Nanomaterials Synthesis and Nanoscopy (LSNN), Federal University of Amazonas (UFAM), Manaus 69067-005, AM, Brazil
5 Analytical Center, Federal Institute of Education, Science and Technology of Amazonas (IFAM), Manaus 69020-120, AM, Brazil
6 São Carlos Institute of Physics (IFSC), University of São Paulo (USP), São Carlos 13563-120, SP, Brazil
7 EMBRAPA Western Amazon, Manaus AM-010 Km 29, Manaus 69010-970, AM, Brazil
8 Department of Food Technology, Federal University of Viçosa (UFV), Viçosa 36570-900, MG, Brazil
9 The Directorate of Research, Development and Innovation Management (DMCDI), Technical University of Cluj-Napoca, 15 Constantin Daicoviciu St., 400020 Cluj-Napoca, Cluj County, Romania
10 Hagler Institute for Advanced Studies, Texas A&M University, College Station, TX 77843, USA
* Correspondence: stefan.talu@auto.utcluj.ro

Citation: Rocha, A.L.F.; de Aguiar Nunes, R.Z.; Matos, R.S.; da Fonseca Filho, H.D.; de Araújo Bezerra, J.; Lima, A.R.; Guimarães, F.E.G.; Pamplona, A.M.S.R.; Majolo, C.; de Souza, M.G.; et al. Alternative Controlling Agent of *Theobroma grandiflorum* Pests: Nanoscale Surface and Fractal Analysis of Gelatin/PCL Loaded Particles Containing *Lippia origanoides* Essential Oil. *Nanomaterials* **2022**, *12*, 2712. https://doi.org/10.3390/nano12152712

Academic Editor: Meiwen Cao

Received: 16 July 2022
Accepted: 5 August 2022
Published: 7 August 2022

Abstract: A new systematic structural study was performed using the Atomic Force Microscopy (AFM) reporting statistical parameters of polymeric particles based on gelatin and poly-ε-caprolactone (PCL) containing essential oil from *Lippia origanoides*. The developed biocides are efficient alternative controlling agents of *Conotrachelus humeropictus* and *Moniliophtora perniciosa*, the main pests of *Theobroma grandiflorum*. Our results showed that the particles morphology can be successfully controlled by advanced stereometric parameters, pointing to an appropriate concentration of encapsulated essential oil according to the particle surface characteristics. For this reason, the absolute concentration of 1000 $\mu g \cdot mL^{-1}$ (P_{1000} system) was encapsulated, resulting in the most suitable surface microtexture, allowing a faster and more efficient essential oil release. Loaded particles presented zeta potential around (–54.3 ± 2.3) mV at pH = 8, and particle size distribution ranging from 113 to 442 nm. The hydrodynamic diameter of 90% of the particle population was found to be up to (405 ± 31) nm in the P_{1000} system. The essential oil release was evaluated up to 80 h, with maximum release concentrations of 63% and 95% for P_{500} and P_{1000}, respectively. The best fit for the release profiles was obtained using the Korsmeyer–Peppas mathematical model. Loaded particles resulted in 100% mortality of *C. humeropictus* up to 48 h. The antifungal tests against *M. perniciosa* resulted in a minimum inhibitory concentration of 250 $\mu g \cdot mL^{-1}$, and the P_{1000} system produced growth inhibition up to 7 days. The developed system has potential as alternative controlling agent, due to its physical stability, particle surface microtexture, as well as pronounced bioactivity of the encapsulated essential oil.

Keywords: *Lippia origanoides*; *Theobroma grandiflorum*; controlling agent; nanoscale surface; fractal analysis; controlled release; *Conotrachelus humeropictus*; *Moniliophtora perniciosa*

1. Introduction

The increasing interest in biodegradable particles has accelerated their development process for new technological applications [1–5], particularly in environmentally friendly polymeric particles containing encapsulated essential oils [6–13].

The combination of biomaterials with different physicochemical properties has allowed the development of layered particles, to protect and release secondary metabolites [14–17]. The evaluation of surface nanotexture and fractal analyses through Atomic Force Microscopy (AFM) technique has been useful to investigate the influence of texture parameters on the controlled release mechanism and concentration of encapsulated bioactive compounds [18,19].

Essential oils have long been considered as alternative natural agents for pest control [20–22]. *Lippia origanoides* Kunth [23] is popularly known as "Erva-de-Marajó" in northern Brazil. Carvacrol and thymol (the major constituents of its essential oil) present significant chemopreventive properties [24–26], antimicrobial activity against several pathogen groups [27], as well as repellency and a low toxicity [28]. The encapsulation of essential oils for controlled release formulations can improve their efficiency and reduce environmental damage [29,30].

The cupuaçu tree (*Theobroma grandiflorum* (Willd. *ex* Spreng.) K. Schum.) (Malvaceae) is one of the main fruit trees cultivated in the Brazilian Amazon. The high commercial value of the cupuaçu pulp derives from the food industry, mainly as juice, liqueur, and jelly, as well as in the manufacture of chocolate ("cupulate") from its almonds [31–33]. *Conotrachelus humeropictus* Fiedler, 1940 (Coleoptera: Curculionidae), known as "Broca-do-Cupuaçu", is the main pest of this culture in the Amazon region, especially in Rondônia and Amazonas [34]. This pest is difficult to control, as both the egg and larva are lodged in galleries inside the fruits. Infested fruits fall off before ripening or have the pulp completely destroyed [35]. Moreover, from the phytosanitary point of view, the disease caused by the fungus *Moniliophtora perniciosa* (known as "Vassoura-de-Bruxa") [36] represents the main limiting factor to the expansion of this fruit tree. This pest significantly reduces the economic production, and phytosanitary pruning is the main economic tool to control this pest [37].

The use of nanotechnology to control pests in agriculture has resulted in nanoscale materials able to enhance the stability and activity of natural controlling agents [38,39]. Reports on the encapsulation of *L. origanoides* essential oil in biodegradable particles to control *C. humeropictus* and *M. perniciosa* have not been found in the scientific literature. For this reason, particles based on gelatin and poly-ε-caprolactone (PCL) were loaded with this essential oil, aiming at the development of a controlled release formulation.

The AFM technique allowed understanding the influence of the essential oil concentration on statistical parameters (based on nanoscale surface and fractal analyses), such as roughness, peak/height distributions, and nanotexture homogeneity. Size distribution measurements and nanoparticle surface charge were evaluated, respectively, by nanoparticle tracking analysis (NTA) and zeta potential. Laser Scanning Confocal Microscopy (LSCM) and fluorescence measurements were applied to confirm the essential oil encapsulation. Encapsulation Efficiency (EE%) was measured by UV-VIS spectroscopy, and the release kinetics of the essential oil was analyzed as a log cumulative percentage of released essential oil *versus* log time by fitting the data according to the Higuchi [40] and Korsmeyer–Peppa's [41] mathematical models. Finally, the insecticidal and fungicidal efficiency of the developed formulation was assessed in vitro, respectively, against *C. humeropictus* and *M. perniciosa*.

2. Materials and Methods

2.1. Nanoparticle Development and Essential Oil Encapsulation

Colloidal system development was based on previous reports with marginal modification [14]. *L. origanoides* (SISGEN authorization code AD0C7DB) essential oil was

encapsulated at absolute concentrations of 500 $\mu g \cdot mL^{-1}$ (P_{500}) and 1000 $\mu g \cdot mL^{-1}$ (P_{1000}). Unloaded particles (P_0) were also prepared.

Encapsulation Efficiency (EE%) was evaluated on a Epoch2 Microplate Reader Biotek (Agilent, CA, USA) [42]. From the calibration curve, the unknown concentration of essential oil was obtained by measuring the absorbance values at 278 nm. Particles were separated by centrifugation (Daiki Sciences, Seoul City, Republic of Korea) (20,000 rpm) and the supernatant absorbance allowed obtaining the percentage of free essential oil. Then, EE% was calculated using the formula: (EE%) = (amount of encapsulated essential oil/total amount of essential oil used in the formulation) $\times$ 100. Experiments were carried out in triplicate.

2.2. Zeta Potential and Nanoparticle Tracking Analysis (NTA)

Zeta potential values (in mV) were obtained from pH = 1 to 10 at 25 °C. Measurements were performed in triplicate. Size characterization was performed on a NanoSight NS300 device (Malvern Instruments, Malvern, UK), equipped with a green laser type and a SCMOS camera. Data collection and analysis were performed using the software NTA 3.0 (Malvern Instruments, Malvern, UK). Samples were diluted in MilliQ water (1:100 v/v). A standard operating procedure was created using 749 frames for 30 s. Measurements were performed in triplicate. The evaluation of the particle size distribution (PSD) was performed using the parameters Mean, Mode, SD, D_{10}, D_{50} (Median), and D_{90}, which indicate, respectively, the average, most frequent particle class size, standard deviation, and the 10%, 50%, and 90% percentiles of the analyzed particles.

2.3. Laser Scanning Confocal Microscopy (LSCM) and Fluorescence Measurements

Images were taken on a Carl Zeiss microscope (inverted model LSM 780) (ZEISS Research Microscopy Solutions, Jena, Germany), with a Ti: Sapphire LASER, a 40$\times$ objective lens, 1.2 NA, and a 0.28 mm work distance. Systems containing unloaded (P_0) and loaded particles (P_{500} and P_{1000}) were centrifuged. A volume of the supernatant was discarded for visualization of the largest particles. Then, a few drops were placed on a microscopy glass slide. Measurements of fluorescence were carried out with a 63$\times$ objective and SPAD (single photon avalanche diode) detector, with a temporal resolution of 70 ps. A Coherent Chameleon tunable 690–1100 nm laser was used as the excitation source. Measurements were taken at 800 nm.

2.4. Atomic Force Microscopy (AFM)

Colloidal systems containing unloaded (P_0) or loaded particles ((P_{500} and P_{1000}); 1 μL) were dripped on a glass slide and dried using liquid nitrogen. Then, the glass slides containing the formed films were fixed on a sample holder using a double-sided adhesive tape. Measurements were performed at room temperature (296 $\pm$ 1 K) and (40 $\pm$ 1)% R.H. on a Innova equipment (Bruker, MA, USA) operated in tapping mode and equipped with a silicon tip and Al coated cantilever with a spring constant of 42 N/m (Tap190AL-G) (Budget Sensors, Sofia, Bulgaria). Scans were performed using (10 $\times$ 10) μm^2 with (256 $\times$ 256) pixels at a scan rate of 1 Hz.

2.4.1. Nanoscale Surface Analysis

Topographic images obtained were processed using the commercial MountainsMap® software version 8.0 (Besançon, France) [43]. Stereometric parameters of height, Sk, and volume were obtained. In addition, quantitative parameters obtained from qualitative renderings (such as furrows and contour lines) were also obtained.

2.4.2. Fractal Analysis

Fractal analysis was carried out based on the following superficial statistical parameters: fractal dimension (FD), surface entropy (H), fractal succolarity (FS), and fractal lacunarity (FL). Fractal dimension (FD) is commonly used for quantification of surface

texture homogeneity, as well as for surface complexity evaluation. However, an analysis based only on the FD parameter is not sufficient to evaluate aspects of general texture [44], because the surface irregularity usually increases as a function of FD [45]. The free software Gwyddion 2.55 [46] (Brno, Czech Republic) was used to perform calculations.

Surface entropy (H) values quantify the uniformity of the height distribution by relating pixels and heights as a function of intensity. Measurements are based on the Shannon's entropy (Equation (1)) [47]:

$$H^{(2)} = -\sum_{i=1}^{N} \sum_{j=1}^{N} p_{ij} \cdot \log p_{ij} \quad (1)$$

where p_{ij} represents the probability of finding accessible pixels on the evaluated pixel set. The AFM image (pixel matrix) was converted into a binary height matrix using the free software WSXM (Madri, Spain) [48]. Results were normalized using Equation (2) [49]:

$$H_{matralt} = \frac{H^{(2)} - H^{(2)}_{\min}}{H^{(2)}_{\max} - H^{(2)}_{\min}} \quad (2)$$

where $H^{(2)}_{\max}$ and $H^{(2)}_{\min}$ represent, respectively, the uniform and non-uniform pattern surface (adopting the symbol H as the normalized value of surface entropy). A *R* language algorithm was programmed for H calculation using the free software RStudio 1.2.503 (Boston, MA, USA).

Additional algorithms in *R* language and Fortran 77 were developed to obtain fractal succolarity (FS) and fractal lacunarity (FL). Percolation can be quantified through the FS evaluation (Equation (3)) [50], while FL measures the texture homogeneity by dimensioning gaps on the fractal object surface [51].

$$FS(T(k), dir) = \frac{\sum_{k=1}^{n} P_0(T(k)) \cdot PR(T(k), p_c)}{\sum_{k=1}^{n} PR(T(k), p_c)} \quad (3)$$

where d_{ir} represents the liquid entrance direction; *T(k)* are boxes of equal size *T(n)*; P_0*(T(k))* is the occupancy percentage; *PR* represents the occupancy pressure, and p_c is the centroid position (x,y). FL was obtained from a previous report [52]. Calculations were focused on the lacunarity coefficient according to Equation (4) [53]:

$$L(r) = \alpha \cdot r^{\beta} \quad (4)$$

where *L(r)* is the lacunarity, α represents an arbitrary constant, and *r* is the box size. The lacunarity coefficient *(β)* was estimated by *log(r)* vs. *log [1 + L(r)]*. The free software Force 3.0 (Maribor, Slovenia) [54] was applied for compiling the FL algorithm. Displacement of one unit was applied, due to the small FL values.

2.5. Essential Oil Release

A colloidal system containing loaded particles (15 mL) was inserted in dialysis tubing cellulose membrane and suspended in water (85 mL) at 25 °C. The system was maintained under continuous magnetic stirring (100 rpm). A 3 mL aliquot was withdrawn from flask at regular time intervals (up to 80 h). Absorbance was measured at 278 nm on a Epoch2 Microplate Reader Biotek. The amount of released essential oil was calculated from a standard curve [55]. The cumulative release (%) of essential oil was obtained with the following equation: [Cumulative release (%) = (amount of essential oil released after time *t*/total amount of encapsulated essential oil) × 100]. Experiments were carried out in triplicate.

2.6. Insecticidal and Fungicidal Bioassays

2.6.1. *Conotrachelus humeropictus*

C. humeropictus individuals were obtained from stock colonies at the EMBRAPA Amazônia Ocidental, Manaus/AM, Brazil, without any pesticide exposure. Borers were reared on a diet of sugarcane and kept at 25 °C, with 70–85% R. H., and a 10:14 h light:dark photoperiod. Glass Petri plates (150 mm in diameter × 20 mm in height) were used as chambers.

Filter paper (150 mm in diameter) was placed in the glass Petri dishes. Each concentration (1 mL) of essential oil in natura/acetone solution (125, 250, 500, 625, 750, and 1000 $\mu g \cdot mL^{-1}$) was uniformly applied on filter paper disk. The treated filter paper disks were air-dried for 1 min to remove solvent. Five adults were transferred from stock to the paper disk, allowing direct contact with the essential oil. Then, chambers were sealed to prevent essential oil evaporation. Acetone (1 mL) was used as negative control. Mortality was evaluated after 24 h of exposure. Individuals were considered dead if they did not move when prodded with a fine paintbrush. The experimental design was completely randomized, with three replicates. Mortality data were subjected to PROBIT analysis [56]. Then, the LD_{50} (lethal dosage that kills 50% of the exposed borers), LD_{90} (lethal dosage that kills 90% of the exposed borers), LCL (lower confidence limit) and UCL (upper confidence limit) were estimated [57], with a fiducial limit of 95%.

The toxicity of the encapsulated essential oil was also tested against *C. humeropictus*. Filter paper (150 mm in diameter) was placed in the glass Petri dishes. A volume of 1 mL of loaded particles (P_{1000}) was uniformly applied on the filter paper disk. Five adults were transferred from stock to the paper disk, allowing direct contact with the loaded particles. Then, chambers were sealed to prevent loss of essential oil. Unloaded particles (P_0) were used as negative control. The number of live borers was counted after 24 h of application. The experimental design was completely randomized based on three replicates.

2.6.2. *Moniliophtora perniciosa*

M. perniciosa isolates were provided by the EMBRAPA Amazônia Ocidental, Manaus/AM-Brazil. Bioassays were performed by the disk diffusion method (DDM) adapted from previous report [58]. The culture medium was prepared with potato-dextrose-agar (PDA; 15.6 g) and sucrose (8.0 g), using 400 mL of distilled water, and kept under heating until complete solubilization. Essential oil was diluted in DMSO (1:9 v/v). Different volumes (1, 0.75, 0.5, 0.25, and 0.125 mL) were added to 100 mL of culture media and then transferred to Petri dishes (90 mm in diameter × 10 cm in height). All Petri dishes were inoculated with a mycelial disc (5 mm diameter) of *M. perniciosa*. Then, the Petri-dishes were incubated for 7 days at 25 °C and the colony diameter was measured. DMSO was used in the bioassays instead of essential oil as a negative control. Four replicate plates were used for each treatment.

The Minimum Inhibitory Concentration (MIC) was interpreted as the lowest concentration that inhibited visual growth. Only plates with positive growth and quality control for purity and colony counts were considered. The mycelial growth index was obtained as the ratio of the final average growth diameter to the number of days after inoculation. The relative mycelial growth percentage (RMG%) at each tested concentration was calculated by comparing the growth on amended media (GOA) compared with the growth on the nonamended control (GOC), as follows: RMG% = (GOA/GOC) × 100. The percentage inhibition of mycelium growth at each tested concentration (I) was also calculated as the difference between the radial growth of nonamended control (C) and the radial growth of each tested concentration (T), as follows: I (%) = (1 − T/C) × 100 [59].

The efficiency of the loaded particles (P_{1000}) was tested against *M. perniciosa,* according to the same procedure as describe above. Unloaded particles (P_0) were used as negative control. Four replicate plates were considered for each treatment.

3. Results and Discussion

3.1. AFM Analysis

The morphology of gelatin/PCL particles has been extensively studied in controlled release systems for pest control [14,15,17], scaffolds [60,61], and curatives [62]. Here we focused on the particles surface morphology (unloaded and loaded with *L. origanoides* essential oil), which previously showed significant larvicidal, acaricidal, and insecticidal potential [8,14,15].

Figure 1 shows the 3D topographic images of the unloaded particles (P_0), as well as the particles loaded with 500 $\mu g \cdot mL^{-1}$ (P_{500}) and 1000 $\mu g \cdot mL^{-1}$ (P_{1000}) of essential oil. The P_0 surface presented spherical-conical grains (Figure 1a). A thinning of the rough peaks in the loaded particles (Figure 1b,c) was observed due to the encapsulation of essential oil. Furthermore, the formation of a large spherical protuberance on the P_{500} and P_{1000} surfaces was observed, probably due to the formation of air bubbles during the drying procedure. This phenomenon was also previously observed [63]. In addition, the topography qualitative analysis revealed a different surface morphology: the increasing of the essential oil concentration promoted a smoothing on the particles surface. This behavior was confirmed by the related height surface parameters analysis (Sa and Sq), as shown in Table 1.

The results were expressed as the mean value and standard deviation, where significant difference was observed (p-value < 0.05). The highest roughness value was observed in P_0 (Sq = (20.301 $\pm$ 3.030) nm). However, the Tukey test showed that both P_{500} and P_{1000} presented similar roughness values. Lower-roughness particles can present higher adhesion energy and be faster adsorbed on another surface [64]. This result indicates that the developed loaded systems represent a viable alternative to decrease particles surface roughness through the encapsulation of essential oil.

The P_0, P_{500}, and P_{1000} systems presented positive asymmetric height distributions, with Rsk values slightly greater than zero. However, the asymmetric height distribution increased in P_{1000}, showing that the height distribution was affected by the increase of the essential oil concentration (although the Tukey test also revealed no significant difference between P_{500} and P_{1000}). Greater asymmetry, whether positive or negative, suggests that a particle is more likely to be anchored or adsorbed onto another surface (probability because skewness is an index). This fact was observed because the particle created a preferential slope direction of its rough peaks (as observed in P_{1000}). In addition, all systems also showed a non-platykurtic pattern (Leptokurtic), as the Rku values were greater than 3. Consequently, the data distribution tended to deviate from the normal Gaussian behavior [65]. As shown in Table 1, the P_{1000} system presented the highest Rsk value, differing from P_{500} (p-value < 0.05). These data showed that P_{1000} presented a sharper distribution, confirming its greater tendency to be easily adsorbed on another surface.

Table 1. Surface parameters (Sa, Sq, Rsk, and Rku).

Parameters	Samples		
	P_0	**P_{500}**	**P_{1000}**
Sa (nm)	27.208 $\pm$ 3.030	8.032 $\pm$ 0.664	6.163 $\pm$ 1.352
Sq (nm)	20.301$\pm$ 5.248	10.546 $\pm$ 1.244	8.941 $\pm$ 2.120
Rsk	0.164 $\pm$ 0.572	0.542 $\pm$ 0.064	1.406 $\pm$ 0.456
Rku	4.183 $\pm$ 0.363	4.168 $\pm$ 0.353	6.944 $\pm$ 1.009

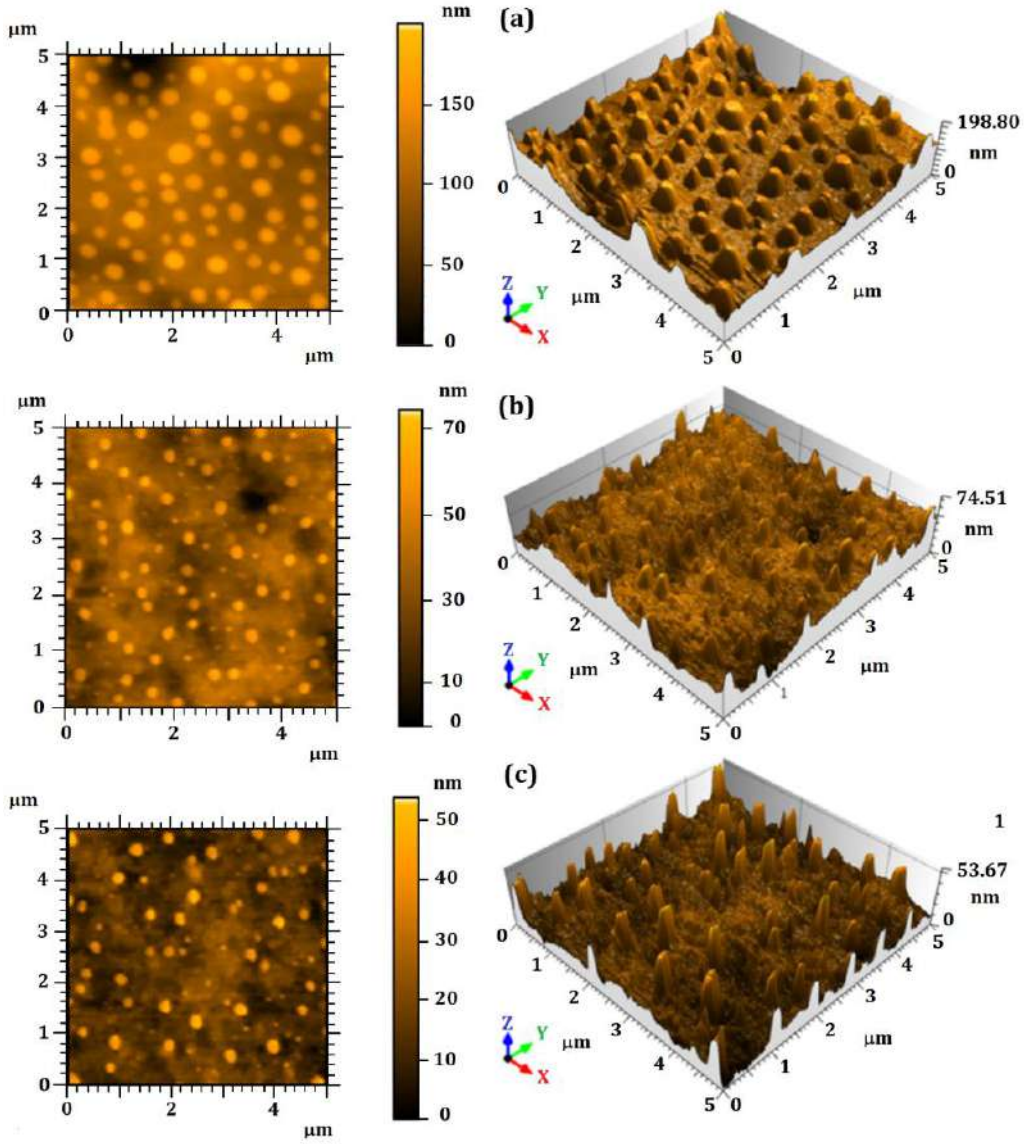

Figure 1. Two-dimensional and three-dimensional AFM micrographs: (**a**) unloaded particles (P_0), (**b**) loaded particles using 500 µg·mL^{-1} of essential oil (P_{500}), and (**c**) loaded particles using 1000 µg·mL^{-1} of essential oil (P_{1000}).

Figure 2 shows the Sk values and volume parameters concerning the height distribution of the particle surface [66,67].

Figure 2a–c indicates that the particle surface of all systems (P_0, P_{500} and P_{1000}) presented a heavy-tailed distribution (Leptokurtic), with great tapering of the height distribution (mainly in P_{1000}). On the other hand, the cumulative curve of Figure 2b (in red) showed better height distribution in P_{500}, since approximately 90% of the relative heights were found between 0 and 0.2568 nm.

Figure 2g–i shows the graphic behaviors considering the volume parameters of the particles surface. As a result of the decrease of surface roughness, especially in P_0 and P_{500}, the volume of material forming the surface topography decreased, as observed by the peak material volume (Vmp), core material volume (Vmc), dale void volume (Vvv), and core void volume (Vvc) parameters. Statistical similarity between P_{500} and P_{1000} was also identified in all parameters. This result confirms that the topography was affected by the encapsulation of essential oil. Furthermore, the particle morphology could be controlled from the observation of advanced stereometric parameters, which could be useful for quality control of the developed material, since they accurately determined the amount of material on the particle surface in different aspects [67].

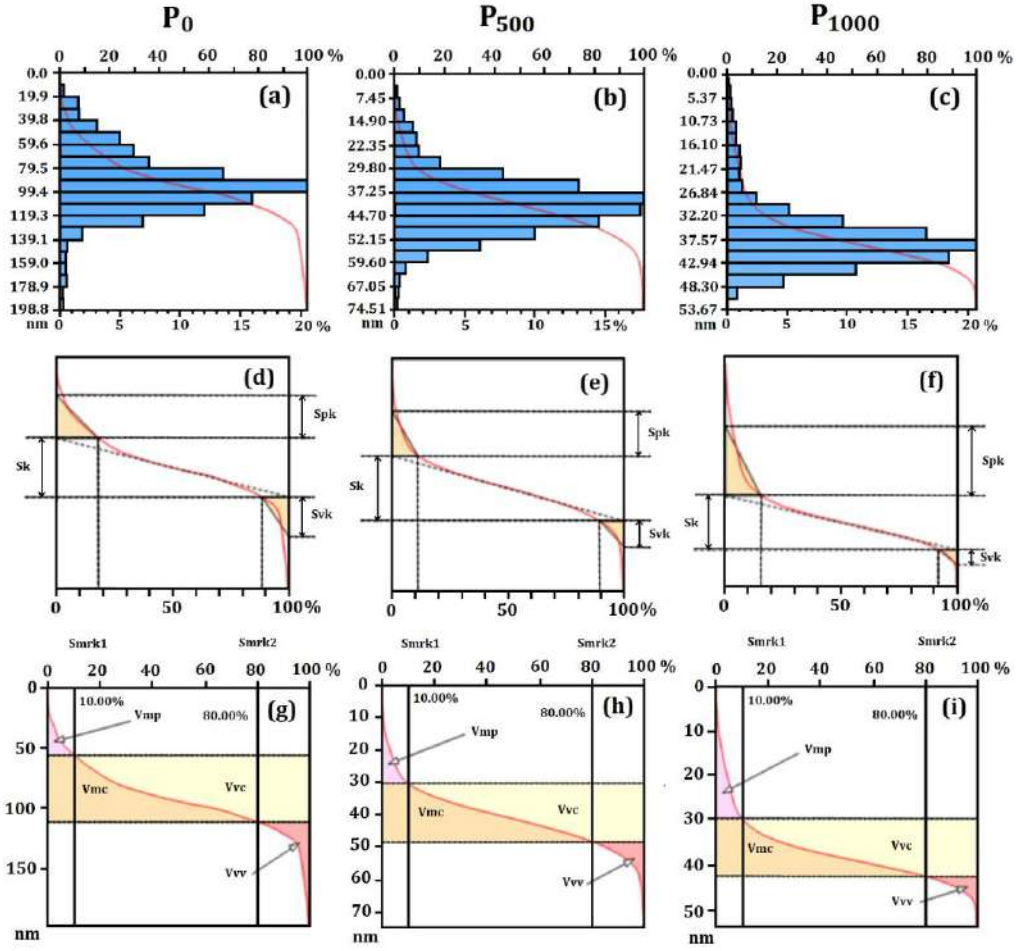

Figure 2. Sk values and volume parameters concerning the height distribution of the particle surface. (**a**–**c**) Particle surface of all systems (P_0, P_{500}, and P_{1000}) presenting a heavy-tailed distribution (Leptokurtic) with great tapering of the height distribution; (**d**–**f**) thickness of material on the particles surface, evaluated by the height distribution according to the Sk parameter family; (**e**,**f**) displacements of the Sk curve; and (**g**–**i**) graphic behaviors considering the volume parameters of the particles surface.

The thickness of material on the particles surface was evaluated by the height distribution according to the Sk parameter family (Figure 2d–f and Table 2). Most of the thickness and volume stereometric parameters exhibited a statistically significant difference (p-value < 0.05), except the valley material portion (Smr2). However, the Tukey test showed that the core thickness (Sk) values were similar to those of P_{500} and P_{1000}, while the highest S_k value was observed in P_0, whose behavior followed that of the surface roughness.

Similarly, the reduced peak height (Spk) and reduced valley depth (Svk) also exhibited similar behavior for P_{500} and P_{1000}, showing that the thickness of the material forming the particle topography did not change from P_{500} to P_{1000}. Figure 2e,f shows the displacements of the Sk curve. In addition, they also suggested that the peak material portion (Smr1) was similar in P_{500} and P_{1000}. These results indicated that the surface microtexture of the particles loaded with essential oil was similar, but still without considering the complexity of the spatial patterns.

Table 2. Sk and volume parameters of the particles surface.

Parameters	Systems		
	P0	**P500**	**P1000**
Sk (μm)	50.398 ± 10.360	23.140 ± 1.829	15.067 ± 2.938
Spk (μm)	39.308 ± 5.400	14.609 ± 0.269	19.946 ± 5.278
Svk (μm)	35.393 ± 13.872	8.009 ± 0.776	6.935 ± 3.758
Smr1(%)	17.842 ± 1.779	12.566 ± 1.217	14.687 ± 1.106
Smr2 (%) *	89.646 ± 1.928	90.028 ± 0.799	90.623 ± 0.703
Vmp (μm/μm2)	0.001 ± 0.000	0.001 ± 0.000	0.001 ± 0.000
Vmc (μm/μm2)	0.020 ± 0.003	0.009 ± 0.001	0.006 ± 0.001
Vvc (μm/μm2)	0.036 ± 0.001	0.012 ± 0.002	0.010 ± 0.003
Vvv (μm/μm2)	0.003 ± 0.001	0.001 ± 0.000	0.001 ± 0.000

* Samples without significant difference ANOVA one-way and Tukey test (p-value > 0.05).

3.2. Surface Microtexture

Renderings of the particles surface microtexture are shown in Figure 3. Images based on furrows and contour lines were obtained for each system. This type of image has been widely used to explain the surface behavior in fluid flooding [68,69], as qualitative renderings that simulate the entrance of fluids and particle arrangement on a nanoparticle surface [52]. A significant reduction in particle size, due to the encapsulation of essential oil, was observed, which was also associated with the decreasing roughness.

Particles presented similar shapes in P_0 (Figure 3a), while P_{500} and P_{1000} (Figure 3c) acquired smaller and more randomized sizes. These results showed that the essential oil encapsulation reduced the particle size, which could result in a better and faster adsorption of the particles on their external environment.

The regions of the images presenting more intense colors are associated with rough peaks, and the darker regions are related to valleys. All parameters associated to furrows presented statistically significant differences (p-value < 0.05). However, the Tukey test showed that P_{500} and P_{1000} presented a similar behavior, exhibiting shallower furrows. These data showed the decrease of the surface roughness.

A similar configuration was also observed for the mean depth of furrows (Table 3). However, P_0 exhibited a lower mean density than those of P_{500} and P_{1000}, showing that the thinning of the rough peaks promoted a greater density of furrows, and suggesting that fluids may have a greater mobility across the particle. In addition, the contour lines of the renderings revealed that the thickness of the central part of the image affected the lines distribution, probably due to the irregular relief of those surfaces.

Table 3. Furrow parameters (maximum depth, mean depth, and mean density).

Furrow Parameters	Systems		
	P_0	**P_{500}**	**P_{1000}**
Maximum depth (μm)	78.973 ± 5.331	33.127 ± 1.762	29.623 ± 3.243
Mean depth (μm)	51.470 ± 3.118	17.722 ± 0.201	17.788 ± 1.506
Mean density (cm/cm^2)	31,933.762 ± 1044.323	42,288.498 ± 433.281	42,358.011 ± 643.838

According to these results, P_{500} e P_{1000} can be more easily penetrated by fluids, explaining the greater empty material volume in the central part of that surface.

All systems presented similar microtexture (Figure 4), because the direct texture parameters (Table 4) did not show a statistically significant difference (p-value > 0.05). Although the particles presented different morphologies, the texture distribution of the topographic patterns was similar. However, such analysis is still too qualitative to propose a specific system presenting the most uniform texture, because it does not take into account the evaluation of the spatial complexity of the surface roughness distribution, which was explored by the fractal parameters.

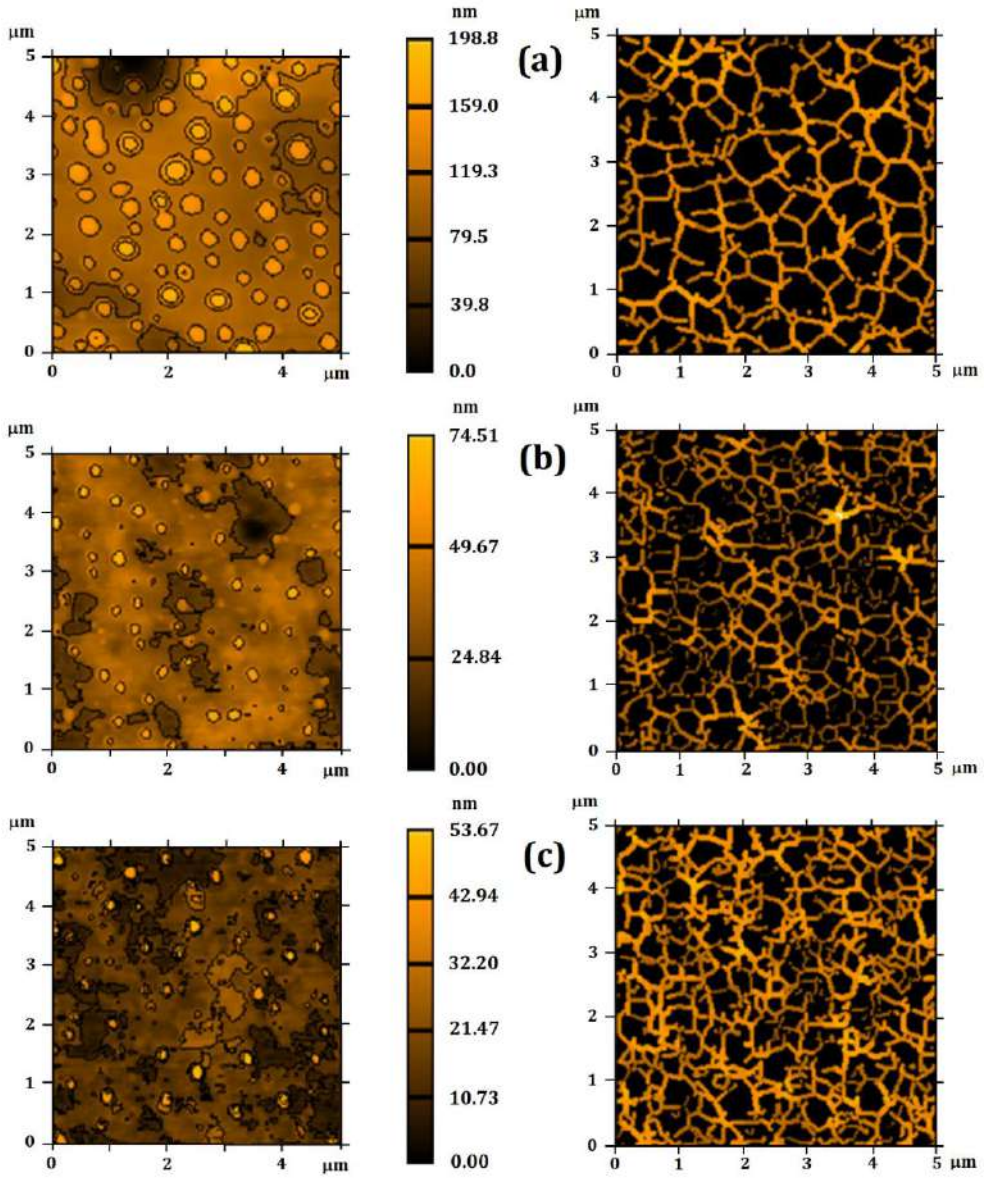

Figure 3. Renderings of the particle surface microtexture. Particles presented similar shapes in (**a**) P_0, while (**b**) P_{500} and (**c**) P_{1000} acquired smaller and more randomized sizes.

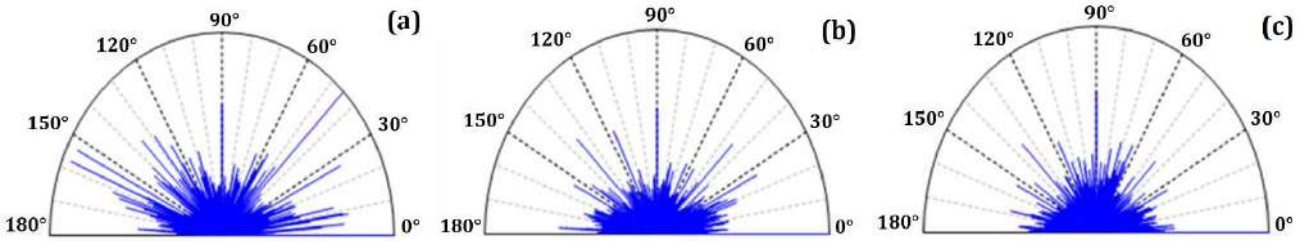

Figure 4. Surface texture directions for (**a**) P_0, (**b**) P_{500}, and (**c**) P_{1000}. All systems presented a similar microtexture, as the direct texture parameters did not show any statistically significant differences (p-value > 0.05).

Table 4. Surface texture isotropy (STI) and the respective directions.

Time (s)	First Direction (°) *	Second Direction (°) *	Third Direction (°) *	STI (%) *
P_0	134.995 ± 77.938	112.501 ± 38.974	88.624 ± 49.674	61.817 ± 19.551
P_{500}	165.995 ± 9.578	135.321 ± 0.453	37.626 ± 7.138	64.913 ± 7.4248
P_{1000}	67.503 ± 74.616	123.749 ± 37.310	112.511 ± 38.965	49.691 ± 17.423

* Samples without significant difference ANOVA One-Way and Tukey Test (p-value < 0.05).

3.3. Advanced Fractal Parameters

The fractal behavior of the particle surface was also evaluated, to obtain more quantitative information on the homogeneity of the microtexture. Microtexture evaluation using fractals and other related parameters has been extensively reported [70,71]. Since a fractal behavior has been attributed to objects in nature [44], several reports have focused on fractal theory to evaluate texture behavior in micro and nanoscales [72–74].

Table 5 presents the parameters fractal dimension (FD), surface entropy (H), fractal succolarity (FS), and lacunarity coefficient (β). FD is the first quantitative parameter associated with texture homogeneity. The fractal dimension presented similar values (p-value > 0.05), suggesting similar spatial complexity in all systems. For this reason, the surface microtexture was similar in P_{500} and P_{1000}, although showing different morphology. However, β was smaller in P_{1000}, suggesting more homogeneous surface microtexture. It is likely that the decrease of the surface roughness promoted the organization of surface gaps, resulting in a more homogeneous surface pattern for the system containing higher concentrations of essential oil. This homogeneity of the surface texture can allow a uniform mobility of fluids, improving its adsorption and release of essential oil.

Table 5. Fractal dimension (FD), surface entropy (H), fractal succolarity (FS), and lacunarity coefficient (β). Average results are expressed as mean values and standard deviations.

Time (s)	P_0	P_{500}	P_{1000}
FD *	2.30 ± 0.03	2.266 ± 0.006	2.29 ± 0.04
H *	0.93 ± 0.04	0.95 ± 0.03	0.90 ± 0.02
FS	0.61 ± 0.04	0.52 ± 0.01	0.59 ± 0.03
$\lvert\beta\rvert$	$5.74 \times 10^{-4} \pm 2.79 \times 10^{-5}$	$2.93 \times 10^{-4} \pm 6.43 \times 10^{-5}$	$1.18 \times 10^{-4} \pm 1.53 \times 10^{-5}$

* Samples without significant difference ANOVA One-Way and Tukey Test (p-value < 0.05).

On the other hand, the surface entropy analysis revealed that, although P_{500} presented more uniform height distribution (H~0.95), all particles exhibited $H \geq 0.9$ (p-value > 0.05). According to a previous report [49], surfaces with a H higher than 0.9 are significantly uniform, indicating that both P_{500} and P_{1000} can present similar adhesion and adsorption properties, although only P_{1000} presented a more homogeneous microtexture.

Although the FS values presented a significant difference (p-value < 0.05), the Tukey test revealed that P_{500} and P_{1000} were similar and could be equally penetrated by fluids. These values were close to 0.5, which is considered the ideal surface percolation value [50]. Adsorption and adhesion processes on other surfaces can also be influenced, as the entrances (allowing the interaction of ligand receptor sites between surfaces) are highly dependent on the surface texture [64]. Thus, it is important to obtain an FS value lower or close to 5, so that the encapsulated systems can release the essential oil in a controlled manner (as found in P_{500} and P_{1000}). These results revealed that the fractal parameters corroborated the results found in the stereometric parameters. However, the fractal lacunarity showed that P_{1000} presented the most suitable surface microtexture for adhesion to another surface, suggesting that this system could release the essential oil faster and more efficiently. For this reason, only the system P_{1000} was considered in further analyses.

3.4. Zeta Potential and Nanoparticle Tracking Analysis (NTA)

Zeta potential as a function of pH and NTA analysis was evaluated for the systems P_0 and P_{1000}. Zeta potential represents an important parameter for the evaluation of surface

charge; besides, it is directly related to the colloidal system, influencing the particle size distribution and stability [15]. Furthermore, higher values (in module) of zeta potential are related to significant repulsion and reduction of aggregation/agglomeration [75].

A higher surface charge was found from pH $\geq$ 7 in the P_0 system (data not shown), allowing formulation stability. The surface charge ranged from (–5.0 $\pm$ 0.3) mV in pH = 7 to (–12.0 $\pm$ 0.8) mV in pH = 10. The isoelectric point was verified as close to pH = 4 and was related mainly to the type B gelatin carrier. It is known that two types of gelatin (A or B) can be produced, depending on the collagen pre-treatment [76].

The particles loaded with essential oil (P_{1000}) presented zeta potential values around (–54.3 $\pm$ 2.3) mV in pH = 8. The higher surface charge (in module) of the loaded particles can be attributed to the presence of the essential oil. The increased charges may be related to the compounds used to produce the particles and also to rearrangements among the essential oil constituents. The presence of these constituents probably resulted in an improved stabilization, due to new intermolecular interactions [15]: the surface electrostatic charge of particles can be influenced by several factors, including surface functional groups and solution ions [77]. On the other hand, electrostatic stability occurs due to the repulsion between particles, resulting from their high surface charge, never reaching the isoelectric point [78]. Thus, values equal to or greater than 30 mV (in modulus) are important for formulation stability [79]. For this reason, the surface charge of the P_{1000} system was found in a range that guarantees its stability as a colloidal system.

Unloaded (P_0) and loaded particles (P_{1000}) were characterized for number and size distribution by NTA (Figure 5). Table 6 shows the average particle size of P_0 and P_{1000}. The developed colloidal systems were compared, in terms of both size and concentration (particles/mL) as a function of encapsulated essential oil. No significant change in number of particles or in their size was observed, as registered by all the size descriptors.

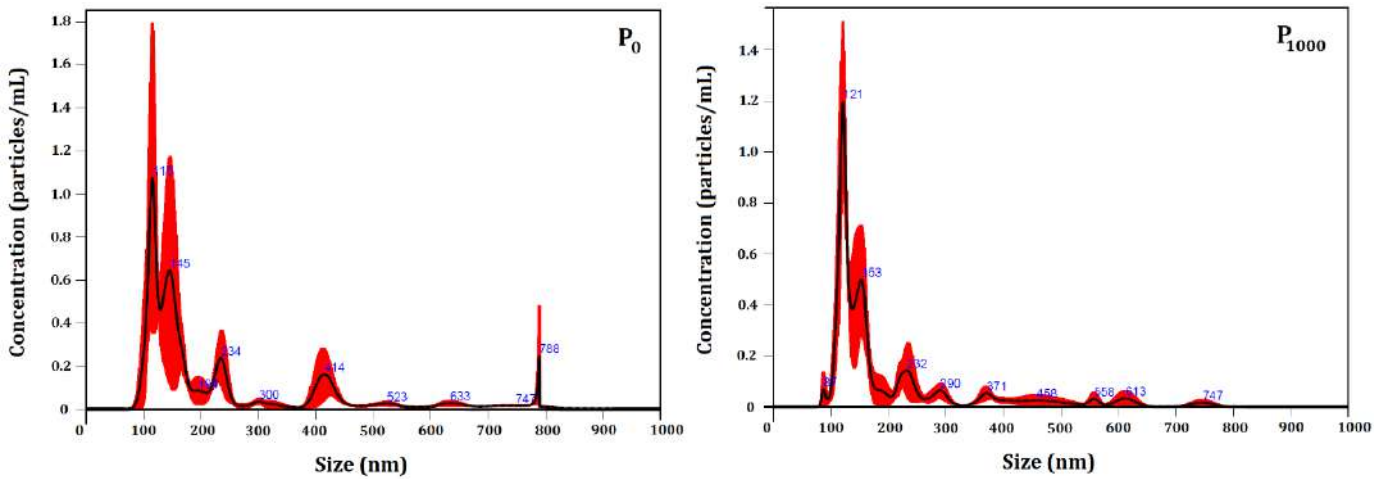

Figure 5. NTA particle size distribution analysis of P_0 and P_{1000} systems. Representative histograms of the average size distribution (black line) from three measurements of a single sample. Red areas specify the standard deviation (SD) between measurements, and blue numbers indicate the maxima of individual peaks.

The developed systems presented a polydisperse particle size distribution, ranging from 113 nm to 442 nm. Moreover, 90% of the particle population in the P_0 and P_{1000} systems presented a size up to (442 $\pm$ 12) nm and (405 $\pm$ 31) nm, respectively.

The mode parameter shows the particle size (or size range) most commonly found in the population distribution, and it is helpful to describe the midpoint for nonsymmetric distributions [80]. The value that best represents the encapsulated particle size was (128 $\pm$ 8) nm.

Table 6. Average particle size measured by NTA considering the P_0 and P_{1000} systems.

Parameters	P_0	P_{1000}
Mean (nm)	215 ± 14	202 ± 7
Mode (nm)	122 ± 12	128 ± 8
SD (nm)	161 ± 1	134 ± 15
D_{10} (nm)	113 ± 10	113 ± 3
D_{50} (nm)	135 ± 11	141 ± 8
D_{90} (nm)	442 ± 12	405 ± 31
Concentration (particles/mL)	$(6.0 \pm 0.9) \times 10^{10}$	$(5.0 \pm 0.6) \times 10^{10}$

Parameters D_{10}, D_{50}, and D_{90} indicated that 10%, 50%, or 90% of the particle's population, respectively, presented a diameter of less than or equal to the specified value.

Our results showed that the particle size distribution profile was not significantly influenced after the encapsulation of the essential oil. However, the presence of the essential oil in the P_{1000} system positively influenced its stability through the increase of the particle surface charge.

3.5. Laser Scanning Confocal Microscopy (LSCM) and Fluorescence Measurements

Figure 6 shows the particles images of the loaded particles, P_{1000}. Larger particles (μm) were selected. According to the NTA measurements, 10% of the loaded particles were larger than (405 ± 31). The essential oil was homogeneously located within the loaded particles/capsules. Moreover, an absence of essential oil was observed in the unloaded system (data not shown), as expected.

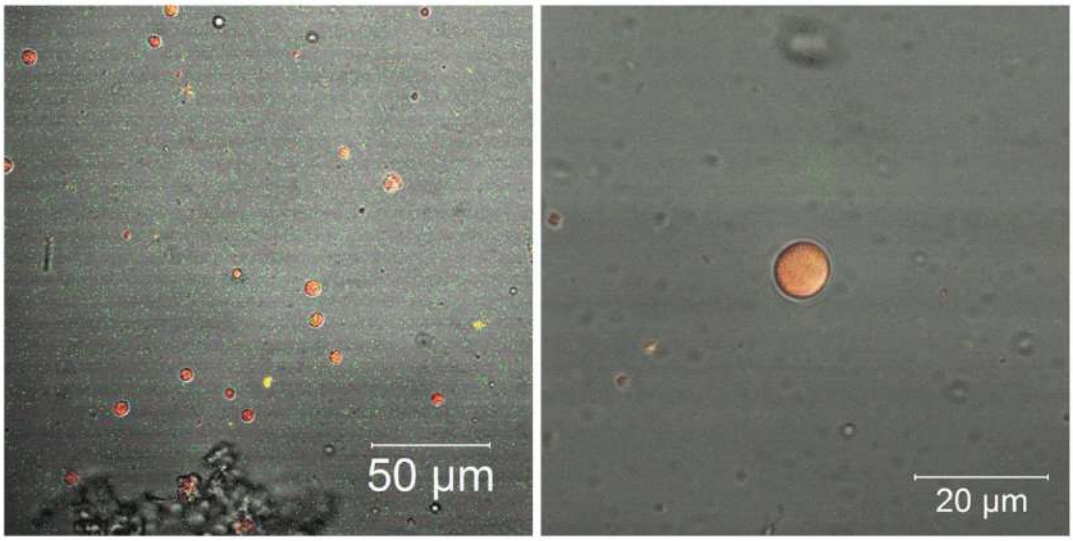

Figure 6. Confocal microscopy images of the particles from loaded system (P_{1000}).

Since the fluorescent properties of various molecules are highly dependent on the environment, this is a potentially useful method for determining material complexation [81].

Fluorescence measurements were performed on the unloaded and loaded particles. Emission spectra are presented in Figure 7 and show that the fluorescence intensity was mainly dependent on the essential oil. The luminance phenomenon of essential oil is caused by the π-electron conjugated system present in its constituents.

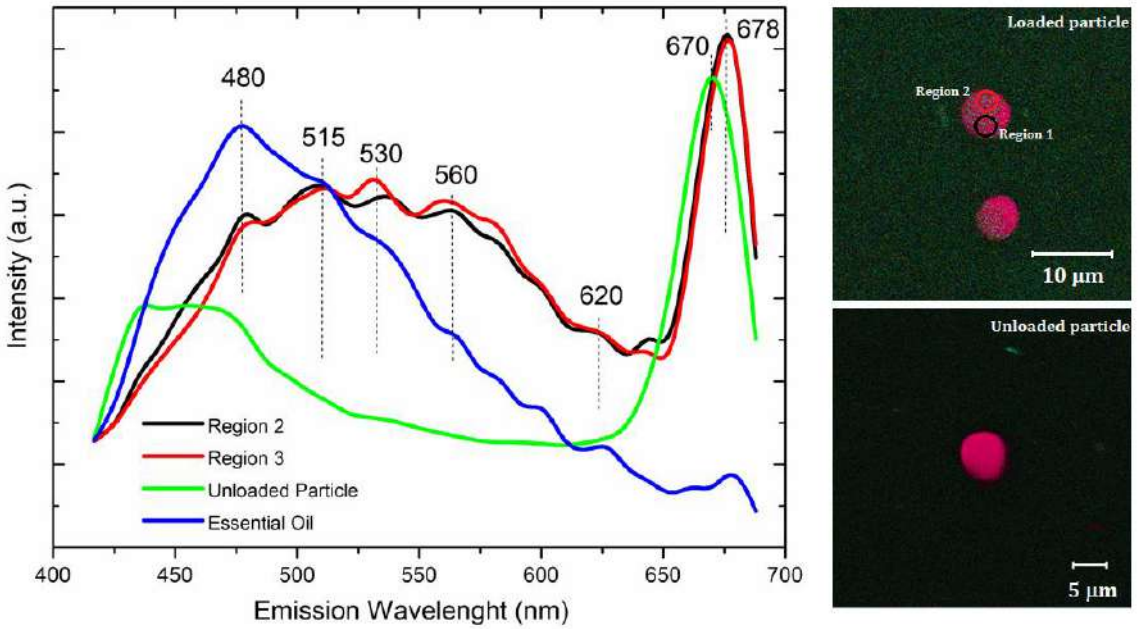

Figure 7. Fluorescence measurements of the loaded (regions 1 and 2) and unloaded particles.

The loaded particles presented a sensitive fluorescence response, under the same wavelength as the free essential oil. The emission spectrum of the P_{1000} system (regions 1 and 2) presented similar peaks, mainly at 480 nm, 515 nm, 530 nm, 560 nm, 620 nm, 670 nm, and 678 nm, confirming the essential oil encapsulation. In these cases, the fluorescence of the loaded particles was observed at a definite excitation length, owing to the fluorescent of secondary metabolites encapsulated within the polymeric particles. However, the fluorescence intensity of the loaded particles increased from 515 nm to 650 nm. In this system, well-defined and more intense emission peaks were assigned to the carriers (such as gelatin and PCL) and observed mainly at 678 nm. A blue shift of this peak was observed from 678 nm to 670 nm, due to the presence of essential oil. In conclusion, the results suggested weak interactions of an electrostatic nature that connected essential oil molecules with polymeric carriers. These interactions did not cause chemical changes in the essential oil. The emission peaks of the essential oil were not observed in the P_0 system, as expected.

Fluorescence measurements have been widely applied to evaluate chemical interactions in material complexation [82]. Similar results were observed elsewhere [83]. The composite of *bis*-eugenol/mesoporous silica presented a sensitive fluorescence response similar to that of free *bis*-eugenol obtained from clove oil. The authors suggested a weak hydrogen bond connecting the *bis*-eugenol molecules with the Si–OH groups of the silica porous wall. On the other hand, a significant enhancement of the fluorescence intensity of *Salvia sclarea* L. essential oil (SEO), due to its complexation with β-cyclodextrin (β-CD), was also investigated [82].

3.6. Controlled Release

The release kinetics were investigated, to understand the mechanisms of release of essential oil from the gelation/PCL particles as a function of the encapsulated concentration. Encapsulation efficiency (EE%) was found to be higher than 99% in both the P_{500} and P_{1000} systems.

Figure 8a shows the profile of release of essential oil. A significant difference was observed in the released concentration of essential oil in the P_{500} and P_{1000} systems. The essential oil release was evaluated up to 80 h, with maximum release concentrations of 63% and 95% for P_{500} and P_{1000}, respectively. These results agree with the fractal lacunarity values from AFM, which suggested that the P_{1000} system presented the most suitable surface microtexture for a more efficient release of essential oil. As also observed, the

decrease of the surface roughness of P_{1000} resulted in a more homogeneous surface pattern. Thus, this observed homogeneity favors uniform mobility of fluids on the surface particle, as well as the solubilization of the gelatin carrier, improving its adsorption and the release of the bioactive compound. This is a possible reason for the lower concentration of essential oil released from the P_{500} system. A similar behavior of the encapsulated systems was also observed previously for gelatin/PCL particles containing essential oil from *Piper aduncum* and *Piper hispidinervum* [14].

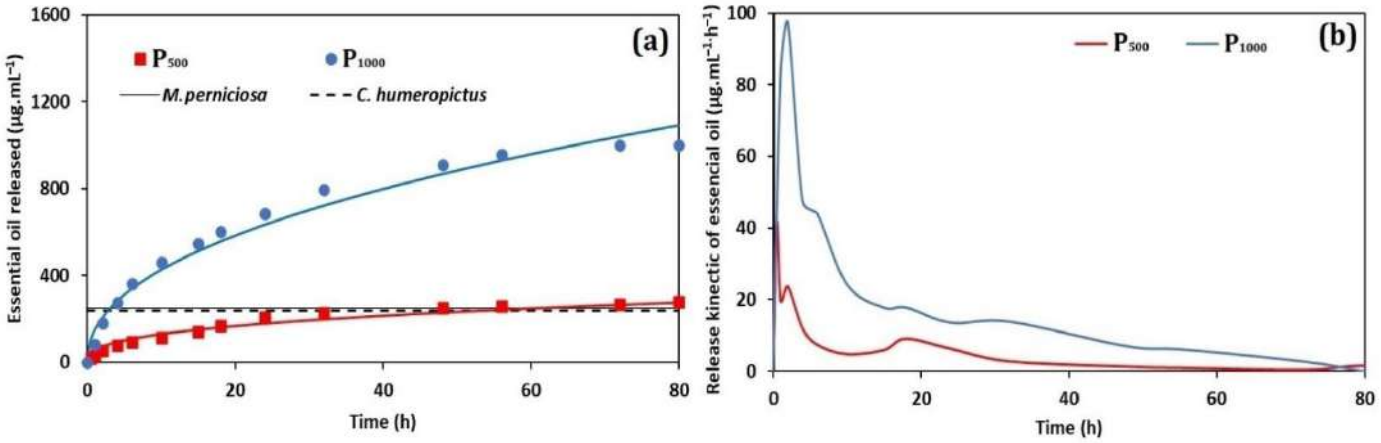

Figure 8. Controlled release curves of the P_{500} and P_{1000} systems: (**a**) concentration of released essential oil ($\mu g \cdot mL^{-1}$), and (**b**) kinetic essential oil release ($\mu g \cdot mL^{-1}\ h^{-1}$).

After 24 h, the P_{1000} system released (51.5 ± 0.3)% of the total amount of encapsulated essential oil and, after 48 h, the released concentration reached (90.2 ± 0.4)%.

Figure 8b shows the derived curves from controlled release. All curves show a large release peak, representing a rapid release of essential oil in the first minutes of evaluation, resulting in the flow of essential oil into the solution. A rapid initial release followed by more sustained release was previously reported considering the essential oil of oregano in chitosan nanoparticles [84]: approximately 82% of the encapsulated essential oil was released up to 3 h. A rapid release of essential oil favors its high concentration in the medium, maintaining its effectiveness for a longer period [85].

The concentration of released essential oil observed in Figure 8a suggests that only the P_{1000} system may show effectiveness in controlling *C. humeropictus* and *M. perniciosa*, because their lethal dosages were reached (as shown in the next section). The profile of release of essential oil from the loaded particles was analyzed by applying the Higuchi [40] and Korsmeyer-Peppas [41] mathematical models. Linear regression was used to calculate the values of the release constants (k) and the correlation coefficients (R^2). The results are summarized in Table 7.

Table 7. Coefficients obtained from the controlled release according to the Higuchi and Korsmeyer–Peppas mathematical models.

Model	Coefficient	P_{500}	P_{1000}
Higuchi	K	31.1	12.46
	R^2	0.95	0.95
Korsmeyer–Peppas	K	57.0	14.4
	n	0.36	0.47
	R^2	0.99	0.99

The mathematical models presented good adjusted to the experimental curves, resulting in a R^2 from 0.95 to 0.99. The best fit to the release profiles of both P_{500} and P_{1000} was obtained using the Korsmeyer–Peppas mathematical model. Release profile curves

were analyzed using a simple empirical model, [$f = kt^n$] [86–88]. The kinetic constant k is a characteristic of a particular system considering structural and geometrical aspects; n is the release exponent representing four different mechanisms (Fickian diffusion, anomalous transport, Case-II transport, and Super Case-II transport) [89], considering spherical particles, and t is the release time.

The release mechanism by Fickian diffusion is the mechanism in which the active diffusion through the particle is exclusively determined by Fickian diffusion. In the case of anomalous transport, the active release is due both to Fickian diffusion and swelling/relaxation of the carrier. Case-II transport is controlled by the swelling and relaxation of carriers and it is independent of time. In Super Case-II transport, the release is ruled by the macromolecular relaxation of the polymeric chains [86].

In general, the n value determines the dominant release mechanism. Considering spherical particles, $n \leq 0.43$ represents a Fickian diffusion (Case I); $0.43 \leq n \leq 0.85$ represents an anomalous transport. When $n = 0.85$, the release is governed by Case-II transport, and $n > 0.85$ is related to Super Case-II transport [40].

The release assays showed that for the same period (80 h), there was a greater release of essential oil from the P_{1000} system. However, the release constant (k) values obtained for both P_{500} and P_{1000} systems (based on the Korsmeyer–Peppas mathematical model) showed that the release rate of the P_{1000} system (14.4 h^{-1}) was slower. Furthermore, the concentration of the encapsulated essential oil influenced the release mechanism. Particles containing a higher concentration of encapsulated essential oil (P_{1000}) were released according to the non-Fickian transport ($n = 47$). On the other hand, the P_{500} system presented a Fickian diffusion (Case-I) ($n = 0.36$) [90,91].

3.7. Insecticidal and Fungicidal Bioassays

The bioactivity of the *L. origanoides* essential oil against various pests can occur in different ways, causing mortality, deformation at different stages of development, as well as repellency [92]. Secondary metabolites have shown insect toxicity in the vapor phase, being reported as more toxic to microorganisms than in the contact form [14].

Our results indicated that the essential oil in natura presented an insecticidal activity against *C. humeropictus*. The LD_{50} was found to be around (240 ± 25) $\mu g \cdot mL^{-1}$ after 24 h of exposure, with a lower confidence limit (LCL) and upper confidence limit (UCL), respectively, of 131 $\mu g \cdot mL^{-1}$ and 350 $\mu g \cdot mL^{-1}$. The fiducial limit was considered as 95%.

The P_{1000} system was submitted to bioassays against *C. humeropictus*. Particles containing *L. origanoides* showed 100% mortality up to 48 h. About 80% of the borers were killed within 24 h. These results agree with the released concentration of essential oil from the controlled release curves and show that P_{1000} system was efficient against this tested pest, resulting in their control for up to 24 h. Similar works were found in the scientific literature considering other borer species [93,94].

The repellent activity of *Lippia origanoides*, *L. alba*, *Tagetes lucida*, *Rosmarinus officinalis*, *Cananga odorata*, *Eucalyptus citriodora*, and *Cymbopogon citratus* essential oils from Columbia were previously tested against the borer *Sitophilus zeamais* [95]. The authors observed that *L. origanoides* was found to be the most effective, causing (92 ± 3)% repellency at a 0.503 $\mu L.cm^{-2}$ dose. The insecticidal activity of essential oils from *Thymus vulgaris* (thyme) and *Cymbopogon citratus* (lemongrass) against the devastating pest *Tuta absoluta* was also reported [96]. The resultant biological parameters for lemongrass and thyme oils were LD_{50} of 1479 $\mu L \cdot mL^{-1}$ and 3046 $\mu L \cdot mL^{-1}$ for lemongrass and thyme oils, respectively, considering their fumigant toxicity.

The antifungal activity of *L. origanoides* has been extensively reported [97]. Considering the concentrations of essential oil added to the culture medium (0.125, 0.25, 0.5, 0.75, and 1 $mg \cdot mL^{-1}$), the mycelial growth of *M. perniciosa* was observed only at 0.125 $\mu g \cdot mL^{-1}$. For this reason, the tested concentration of 250 $\mu g \cdot mL^{-1}$ was considered as the MIC value.

The bioassays presented statistically significant differences (p-value < 0.05) between the essential oil and control. The treatments resulted in a percentage inhibition of mycelium growth of (57 ± 8)%, as shown in Table 8.

Table 8. Growth and inhibition parameters of *M. perniciosa,* considering the *L. origanoides* essential oil and the tested control.

	Diameter (mm)	RGM (%)	I (%)	MGI (mm/day)
L. origanoides	32 ± 6	43 ± 8	57 ± 8	4.6 ± 0.8
Control	74.8 ± 0.5	100.00	0.00	10.7 ± 0.1

RGM: relative mycelial growth percentage; I: percentage inhibition of mycelium growth; MGI: mycelial growth index. Negative control: DMSO.

The efficiency of the P_{1000} system was evaluated against *M. perniciosa*. After 7 days of incubation, no mycelial growth percentage was observed. Carvacrol has been reported as the major constituent of the essential oil from *L. origanoides* [23] and has shown efficiency in controlling bacteria [98,99], fungi [98,100], and insects [23,101]. The inhibition of *Phytophthora infestans*, a phytopathogen of potato, was reported with MIC = 150 μg mL^{-1}, confirming the efficiency of this essential oil in controlling pathogenic fungi [102].

4. Conclusions

The present study successfully developed gelatin/PCL-based particles as useful carriers of the essential oil from *L. origanoides*. The proposed colloidal system can release lethal dosage concentrations to control *C. humeropictus* and *M. perniciosa* for up to 24 h, which are the main pests of *Theobroma grandiflorum*. The AFM data also showed that the encapsulation of essential oil affected the particle's surface morphology. The surface roughness decreased as a function of the concentration of encapsulated essential oil. The homogeneity of the surface texture observed in the P_{1000} system allowed a uniform mobility of fluids on the surface, improving its adsorption and release of essential oil. These results were observed in the controlled release assays. The nanoscale surface and fractal analysis based on AFM technique represent an useful tool for quality standards in manufacturing particles containing encapsulated essential oil. For this reason, our results suggested that the developed particles containing encapsulated essential oil could be applied as a sustainable alternative controlling agent for the tested pests, combined with their biodegradability and adequate controlled release, with promising future applications.

Author Contributions: E.A.S.: project coordination and administration. A.L.F.R., R.Z.d.A.N. and E.A.S.: conceptualization, methodology and data collecting/analysis. A.L.F.R.: particles development and essential oil encapsulation. E.A.S., V.S.B., N.M.I. and Ş.Ţ.: original draft preparation, data analysis and funding acquisition. J.d.A.B. and P.H.C.: controlled release assays and interpretation. A.L.F.R., E.A.S., V.S.B. and N.M.I.: Zeta potential and nanoparticle tracking analysis (NTA) measurement and data interpretation. R.S.M. and H.D.d.F.F.: AFM measurements and interpretation. A.R.L., E.A.S. and F.E.G.G.: laser scanning confocal microscopy and fluorescence measurements and interpretation. A.L.F.R., R.Z.d.A.N., A.M.S.R.P., C.M. and M.G.d.S.: insecticidal and fungicidal bioassays and interpretation. All authors have read and agreed to the published version of the manuscript.

Funding: CAPES (Coordenação de Aperfeiçoamento de Pessoal de Nível Superior—Código Financeiro 001), CNPq (Conselho Nacional de Desenvolvimento Científico e Tecnológico, grant number 403496/2013-6, Programa Sisfóton and INCT), FAPEAM (Fundação de Amparo à Pesquisa do Estado do Amazonas, Edital 004/2018—Amazonas Estratégico—062.01305/2018—Pedro H. Campelo Felix, Jaqueline de A. Bezerra, Ana Luisa F. Rocha and Ronald Z. Aguiar), FAPESP (Fundação de Amparo à Pesquisa do Estado de São Paulo/CEPOF (Centro de Pesquisas em Óptica e Fotônica) grant number 2013/07276-1 and FAPESP (EMU) grant number 09/54035-4.

Institutional Review Board Statement: Not applicable.

Informed Consent Statement: Not applicable.

Data Availability Statement: Not applicable.

Acknowledgments: The authors thank CAPES (Coordenação de Aperfeiçoamento de Pessoal de Nível Superior, CNPq (Conselho Nacional de Desenvolvimento Científico e Tecnológico), FAPEAM (Fundação de Amparo à Pesquisa do Estado do Amazonas), FAPESP (Fundação de Amparo à Pesquisa do Estado de São Paulo), CEPOF (Centro de Pesquisas em Óptica e Fotônica) for the financial support, and to the Grupo de Nanomedicina e Nanotoxicologia (GNano – IFSC/USP) for the measurements of Nanoparticle Tracking Analysis (NTA) and EMBRAPA Amazônia Ocidental (Manaus/AM) for providing the *C. humeropictus* individuals and *M. perniciosa* fungi, as well as the fungicidal bioassays infrastructure.

Conflicts of Interest: The authors declare no conflict of interest.

References

1. Abdelaziz, D.; Hefnawy, A.; Al-Wakeel, E.; El-Fallal, A.; El-Sherbiny, I.M. New biodegradable nanoparticles-in-nanofibers based membranes for guided periodontal tissue and bone regeneration with enhanced antibacterial activity. *J. Adv. Res.* **2021**, *28*, 51–62. [CrossRef] [PubMed]
2. Babaee, M.; Garavand, F.; Rehman, A.; Jafarazadeh, S.; Amini, E.; Cacciotti, I. Biodegradability, physical, mechanical and antimicrobial attributes of starch nanocomposites containing chitosan nanoparticles. *Int. J. Biol. Macromol.* **2022**, *195*, 49–58. [CrossRef]
3. Wang, C.; Gong, C.; Qin, Y.; Hu, Y.; Jiao, A.; Jin, Z.; Qiu, C.; Wang, J. Bioactive and functional biodegradable packaging films reinforced with nanoparticles. *J. Food Eng.* **2022**, *312*, 110752. [CrossRef]
4. Wang, L.; Gao, Y.; Xiong, J.; Shao, W.; Cui, C.; Sun, N.; Zhang, Y.; Chang, S.; Han, P.; Liu, F.; et al. Biodegradable and high-performance multiscale structured nanofiber membrane as mask filter media via poly(lactic acid) electrospinning. *J. Colloid Interface Sci.* **2022**, *606*, 961–970. [CrossRef]
5. Sharma, R.; Tripathi, A. Green synthesis of nanoparticles and its key applications in various sectors. *Mater. Today Proc.* **2022**, *48*, 1626–1632. [CrossRef]
6. Reddy, L.H.; Arias, J.L.; Nicolas, J.; Couvreur, P. Magnetic nanoparticles: Design and characterization, toxicity and biocompatibility, pharmaceutical and biomedical applications. *Chem. Rev.* **2012**, *112*, 5818–5878. [CrossRef] [PubMed]
7. Wang, B.; Tang, Y.; Oh, Y.; Lamb, N.W.; Xia, S.; Ding, Z.; Chen, B.; Suarez, M.J.; Meng, T.; Kulkarni, V.; et al. Controlled release of dexamethasone sodium phosphate with biodegradable nanoparticles for preventing experimental corneal neovascularization. *Nanomed. Nanotechnol. Biol. Med.* **2019**, *17*, 119–123. [CrossRef]
8. Silva, J.S.M.; Rabelo, M.S.; Lima, S.X.; Rocha, A.N.A.L.F.; Tadei, W.P.; Chaves, F.C.M.; Bezerra, J.D.E.A.; Biondo, M.M.; Campelo, P.H.; Sanches, E.A. Biodegradable nanoparticles loaded with Lippia alba essential oil: A sustainable alternative for *Aedes aegypti* larvae control. *Eur. Acad. Res.* **2020**, *VII*, 6237–6258.
9. Pandey, V.K.; Islam, R.U.; Shams, R.; Dar, A.H. A comprehensive review on the application of essential oils as bioactive compounds in nano-emulsion based edible coatings of fruits and vegetables. *Appl. Food Res.* **2022**, *2*, 100042. [CrossRef]
10. Khizar, S.; Zine, N.; Errachid, A.; Jaffrezic-Renault, N.; Elaissari, A. Microfluidic-based nanoparticle synthesis and their potential applications. *Electrophoresis* **2021**, *43*, 819–838. [CrossRef] [PubMed]
11. Corrado, I.; Di Girolamo, R.; Regalado-González, C.; Pezzella, C. Polyhydroxyalkanoates-based nanoparticles as essential oil carriers. *Polymers* **2022**, *14*, 166. [CrossRef] [PubMed]
12. Nair, A.; Mallya, R.; Suvarna, V.; Khan, T.A.; Momin, M.; Omri, A. Nanoparticles—Attractive carriers of antimicrobial essential oils. *Antibiotics* **2022**, *11*, 108. [CrossRef] [PubMed]
13. Zhang, W.; Jiang, H.; Rhim, J.-W.; Cao, J.; Jiang, W. Effective strategies of sustained release and retention enhancement of essential oils in active food packaging films/coatings. *Food Chem.* **2022**, *367*, 130671. [CrossRef] [PubMed]
14. Silva, L.S.; Mar, J.M.; Azevedo, S.G.; Rabelo, M.S.; Bezerra, J.A.; Campelo, P.H.; Machado, M.B.; Trovati, G.; Santos, L.; Fonseca, D.; et al. Encapsulation of Piper aduncum and Piper hispidinervum essential oils in gelatin nanoparticles: A possible sustainable control tool of Aedes aegypti, Tetranychus urticae and Cerataphis lataniae. *J. Sci. Food Agric.* **2018**, *99*, 685–695. [CrossRef]
15. De Oliveira, L.M.; Silva, L.S.; Mar, J.M.; Azevedo, S.G.; Rabelo, M.S.; Da Fonseca Filho, H.D.; Lima, S.X.; Bezerra, J.D.A.; Machado, M.B.; Campelo, P.H.; et al. Alternative biodefensive based on the essential oil from *Allium sativum* encapsulated in PCL/Gelatin nanoparticles. *J. Food Eng. Technol.* **2019**, *8*, 65–74. [CrossRef]
16. Kusumastuti, Y.; Istiani, A.; Rochmadi; Purnomo, C.W. Chitosan-based polyion multilayer coating on NPK fertilizer as controlled released fertilizer. *Adv. Mater. Sci. Eng.* **2019**, *2019*, 2958021. [CrossRef]
17. De Oliveira, L.M.; Lima, S.X.; Silva, L.S.; Mar, J.M.; Azevedo, S.G.; Rabelo, M.S.; Henrique, D.; Filho, F.; Campelo, P.H.; Sanches, E.A. Controlled release of *Licaria puchury-major* essential oil encapsulated in PCL/gelatin-based colloidal systems and membranes. *Am. J. Essent. Oils Nat. Prod.* **2019**, *7*, 23–29.
18. da Costa, Í.C.; Saraiva Matos, R.S.; de Azevedo, S.G.; Costa, C.A.R.; Sanches, E.A.; da Fonseca FIlho, H. Microscopy-based infrared spectroscopy as a tool to evaluate the influence of essential oil on the surface of loaded bilayered-nanoparticles. *Nanotechnology* **2021**, *32*, 345703. [CrossRef]

19. de Oliveira, L.M.; Matos, R.S.; Campelo, P.H.; Sanches, E.A.; da Fonseca Filho, H.D. Evaluation of the nanoscale surface applied to biodegradable nanoparticles containing *Allium sativum* essential oil. *Mater. Lett.* **2020**, *275*, 128111. [CrossRef]
20. Nguyen, M.-H.; Nguyen, T.-H.-N.; Tran, T.-N.-M.; Vu, N.-B.-D.; Tran, T.-T. Comparison of the nematode-controlling effectiveness of 10 different essential oil-encapsulated lipid nanoemulsions. *Arch. Phytopathol. Plant Prot.* **2022**, *55*, 420–432. [CrossRef]
21. Elumalai, K.; Krishnappa, K.; Pandiyan, J.; Alharbi, N.S.; Kadaikunnan, S.; Khaled, J.M.; Barnard, D.R.; Vijayakumar, N.; Govindarajan, M. Characterization of secondary metabolites from Lamiaceae plant leaf essential oil: A novel perspective to combat medical and agricultural pests. *Physiol. Mol. Plant Pathol.* **2022**, *117*, 101752. [CrossRef]
22. Pedrotti, C.; Caro, I.M.D.D.; Franzoi, C.; Grohs, D.S.; Schwambach, J. Control of anthracnose (*Elsinoë ampelina*) in grapevines with *Eucalyptus staigeriana* essential oil. *Org. Agric.* **2022**, *12*, 81–89. [CrossRef]
23. Mar, J.M.; Silva, L.S.; Azevedo, S.G.; França, L.P.; Goes, A.F.F.; dos Santos, A.L.; Bezerra, J.d.A.; de Cássia, S.; Nunomura, R.; Machado, M.B.; et al. *Lippia origanoides* essential oil: An efficient alternative to control *Aedes aegypti*, *Tetranychus urticae* and *Cerataphis lataniae*. *Ind. Crops Prod.* **2018**, *111*, 292–297. [CrossRef]
24. Vicuña, G.C.; Stashenko, E.E.; Fuentes, J.L. Chemical composition of the *Lippia origanoides* essential oils and their antigenotoxicity against bleomycin-induced DNA damage. *Fitoterapia* **2010**, *81*, 343–349. [CrossRef]
25. Stashenko, E.E.; Martínez, J.R.; Cala, M.P.; Durán, D.C.; Caballero, D. Chromatographic and mass spectrometric characterization of essential oils and extracts from Lippia (Verbenaceae) aromatic plants. *J. Sep. Sci.* **2013**, *36*, 192–202. [CrossRef]
26. Hassan, H.F.H.; Mansour, A.M.; Salama, S.A.; El-Sayed, E.-S.M. The chemopreventive effect of thymol against dimethylhydrazine and/or high fat diet-induced colon cancer in rats: Relevance to NF-κB. *Life Sci.* **2021**, *274*, 119335. [CrossRef]
27. Borges, A.R.; de Albuquerque Aires, J.R.; Higino, T.M.M.; de Medeiros, M.d.G.F.; Citó, A.M.d.G.L.; Lopes, J.A.D.; de Figueiredo, R.C.B.Q. Trypanocidal and cytotoxic activities of essential oils from medicinal plants of Northeast of Brazil. *Exp. Parasitol.* **2012**, *132*, 123–128. [CrossRef]
28. Caballero-Gallardo, K.; Olivero-Verbel, J.; Stashenko, E.E. Repellency and toxicity of essential oils from *Cymbopogon martinii*, *Cymbopogon flexuosus* and *Lippia origanoides* cultivated in Colombia against *Tribolium castaneum*. *J. Stored Prod. Res.* **2012**, *50*, 62–65. [CrossRef]
29. Perlatti, B.; Souza Bergo, P.L.; Silva, M.F.d.G.F.d.; Batista, J.; Rossi, M. Polymeric nanoparticle-based insecticides: A controlled release purpose for agrochemicals. *Insectic. Dev. Safer More Eff. Technol.* **2013**, 521–548. [CrossRef]
30. Papanikolaou, N.E.; Kalaitzaki, A.; Karamaouna, F.; Michaelakis, A.; Papadimitriou, V.; Dourtoglou, V.; Papachristos, D.P. Nano-formulation enhances insecticidal activity of natural pyrethrins against *Aphis gossypii* (Hemiptera: Aphididae) and retains their harmless effect to non-target predators. *Environ. Sci. Pollut. Res.* **2017**, *25*, 10243–10249. [CrossRef]
31. Santos, R.A.R.S.; Silva, N.M. Primeiro registro de *Conotrachelus humeropictus* Fiedler, 1940 (Coleoptera: Curculionidae) no estado do Amapá, Brasil. *Biota Amaz.* **2020**, *10*, 69–70.
32. Pereira, A.L.F.; Abreu, V.K.G.; Rodrigues, S. Cupuassu— *Theobroma grandiflorum*. In *Exotic Fruits*; Elsevier: Amsterdam, The Netherlands, 2018; pp. 159–162.
33. Moura Rebouças, A.; Martins da Costa, D.; Priulli, E.; Teles, J.; Roberta Freitas Pires, C. Aproveitamento tecnológico das sementes de cupuaçu e de okara na obtenção do cupulate. *DESAFIOS Rev. Interdiscip. Univ. Fed. Tocantins* **2020**, *7*, 59–64. [CrossRef]
34. Lopes, C.M.D.; Silva, N.M. Impacto econômico da broca do cupuaçu, *Conotrachelus humeropictus* Field (Coleoptera: Curculionidae) nos estados do Amazonas e Rondônia. *An. Soc. Entomológica Bras.* **1998**, *27*, 481–483. [CrossRef]
35. Thomazini, M.J. Flutuação populacional e intensidade de infestação da Broca-dos-frutos em cupuaçu. *Sci. Agric.* **2002**, *59*, 463–468. [CrossRef]
36. Lopes, J.R.M.; Luz, E.D.M.N.; Bezerra, J.L. Suscetibilidade do cupuaçuzeiro e outras espécies vegetais a isolados de *Crinipellis perniciosa* obtidos de quatro hospedeiros diferentes no sul da Bahia. *Fitopatol. Bras.* **2001**, *26*, 601–605. [CrossRef]
37. Falcão, M.D.A.; De Morais, R.R.; Clement, C.R. Influência da vassoura de bruxa na fenologia do Cupuaçuzeiro. *Acta Amaz.* **1999**, *29*, 13. [CrossRef]
38. Kah, M.; Hofmann, T. Nanopesticide research: Current trends and future priorities. *Environ. Int.* **2014**, *63*, 224–235. [CrossRef]
39. Khot, L.R.; Sankaran, S.; Maja, J.M.; Ehsani, R.; Schuster, E.W. Applications of nanomaterials in agricultural production and crop protection: A review. *Crop Prot.* **2012**, *35*, 64–70. [CrossRef]
40. Boyapally, H.; Nukala, R.K.; Bhujbal, P.; Douroumis, D. Controlled release from directly compressible theophylline buccal tablets. *Colloids Surf. B Biointerfaces* **2010**, *77*, 227–233. [CrossRef]
41. Korsmeyer, R.; Peppas, N. Macromolecular and modeling aspects of swelling controlled systems. In *Controlled Release Delivery Systems*; Springer: Berlin/Heidelberg, Germany, 1983; pp. 77–90.
42. Ghasemishahrestani, Z.; Mehta, M.; Darne, P.; Yadav, A.; Ranade, S. Tunable synthesis of gelatin nanoparticles employing sophorolipid and plant extract, a promising drug carrier. *World J. Pharm. Pharm. Sci.* **2015**, *4*, 1365–1381.
43. Matos, R.S.; Pinto, E.P.; Ramos, G.Q.; da Fonseca de Albuquerque, M.D.; da Fonseca Filho, H.D. Stereometric characterization of kefir microbial films associated with *Maytenus rigida* extract. *Microsc. Res. Tech.* **2020**, *83*, 1401–1410. [CrossRef] [PubMed]
44. Mandelbrot, B.B.; Wheeler, J.A. The fractal geometry of nature. *Am. J. Phys.* **1983**, *51*, 286–287. [CrossRef]
45. de Assis, T.A.; Vivas Miranda, J.G.; de Brito Mota, F.; Andrade, R.F.S.; de Castilho, C.M.C. Geometria fractal: Propriedades e características de fractais ideais. *Rev. Bras. Ensino Fis.* **2008**, *30*, 2304.1–2304.10. [CrossRef]
46. Nečas, D.; Klapetek, P. Gwyddion: An open-source software for SPM data analysis. *Cent. Eur. J. Phys.* **2012**, *10*, 181–188. [CrossRef]

47. Nosonovsky, M. Entropy in tribology: In the search for applications. *Entropy* **2010**, *12*, 1345–1390. [CrossRef]
48. Horcas, I.; Fernández, R.; Gómez-Rodríguez, J.M.; Colchero, J.; Gómez-Herrero, J.; Baro, A.M. WSXM: A software for scanning probe microscopy and a tool for nanotechnology. *Rev. Sci. Instrum.* **2007**, *78*, 013705. [CrossRef]
49. Matos, R.S.; Lopes, G.A.C.; Ferreira, N.S.; Pinto, E.P.; Carvalho, J.C.T.; Figueiredo, S.S.; Oliveira, A.F.; Zamora, R.R.M. Superficial characterization of Kefir biofilms associated with açaí and cupuaçu extracts. *Arab. J. Sci. Eng.* **2018**, *43*, 3371–3379. [CrossRef]
50. Heitor, R.; De Melo, C.; De Melo, R.H.C.; Conci, A. Succolarity: Defining a method to calculate this fractal measure. In Proceedings of the 2008 15th International Conference on Systems, Signals and Image Processing, Bratislava, Slovakia, 25–28 June 2008; pp. 291–294. [CrossRef]
51. Henebry, G.M.; Kux, H.J. Lacunarity as a texture measure for SAR imagery. *Int. J. Remote Sens.* **1995**, *16*, 565–571. [CrossRef]
52. Ţălu, Ş.; Abdolghaderi, S.; Pinto, E.P.; Matos, R.S.; Salerno, M. Advanced fractal analysis of nanoscale topography of Ag/DLC composite synthesized by RF-PECVD. *Surf. Eng.* **2020**, *36*, 713–719. [CrossRef]
53. Ricardo, L.; De Lucena, R.; Stosic, T. Utilização de lacunaridade para detecção de padrões de imagens de retinas humanas. *Rev. Estatística Univ. Fed. Ouro Preto* **2014**, *3*, 789–793.
54. Severina, O. *Programsko Okolje Force 3.0*; Fakulteta za Kemijo in Kemijsko Tehnologijo: Ljubljana, Slovenia, 2012.
55. Naidu, B.V.K.; Paulson, A.T. A new method for the preparation of gelatin nanoparticles: Encapsulation and drug release characteristics. *J. Appl. Polym. Sci.* **2011**, *121*, 3495–3500. [CrossRef]
56. Gaddum, J.H. *Probit Analysis*; Cambridge University Press: Cambridge, UK, 1948; Volume 60, ISBN 0-521-08041-X.
57. Barci, L.A.G.; de Almeida, J.E.M.; de Campos Nogueira, A.H.; do Prado, A.P. Determinação da CL90 e TL90 do isolado IBCB66 de *Beauveria bassiana* (Ascomycetes: Clavicipitaceae) para o controle de *Rhipicephalus (Boophilus) microplus* (Acari: Ixodidae). *Rev. Bras. Parasitol. Vet.* **2009**, *18*, 34–39. [CrossRef] [PubMed]
58. Pietrobelli, S.R.; Portolan, I.B.; Moura, G.S.; Franzener, G. Preparados de plantas bioativas na indução de fitoalexinas e no controle in vitro de fitopatógenos do tomateiro/Preparations of bioative plants in phytoalexins induction and in vitro control of tomato phytopathogens. *Brazilian J. Dev.* **2020**, *6*, 102316–102331. [CrossRef]
59. Kim, C.H.; Hassan, O.; Chang, T. Diversity, pathogenicity, and fungicide sensitivity of Colletotrichum species associated with apple anthracnose in South Korea. *Plant Dis.* **2020**, *104*, 2866–2874. [CrossRef]
60. Gautam, S.; Dinda, A.K.; Mishra, N.C. Fabrication and characterization of PCL/gelatin composite nanofibrous scaffold for tissue engineering applications by electrospinning method. *Mater. Sci. Eng. C* **2013**, *33*, 1228–1235. [CrossRef] [PubMed]
61. Gautam, S.; Chou, C.F.; Dinda, A.K.; Potdar, P.D.; Mishra, N.C. Surface modification of nanofibrous polycaprolactone/gelatin composite scaffold by collagen type I grafting for skin tissue engineering. *Mater. Sci. Eng. C* **2014**, *34*, 402–409. [CrossRef] [PubMed]
62. Shokrollahi, M.; Bahrami, S.H.; Nazarpak, M.H.; Solouk, A. Multilayer nanofibrous patch comprising chamomile loaded carboxyethyl chitosan/poly(vinyl alcohol) and polycaprolactone as a potential wound dressing. *Int. J. Biol. Macromol.* **2020**, *147*, 547–559. [CrossRef]
63. Tyrrell, J.W.G.; Attard, P. Images of nanobubbles on hydrophobic surfaces and their interactions. *Phys. Rev. Lett.* **2001**, *87*, 176104. [CrossRef]
64. Israelachvili, J.N. *Intermolecular and Surface Forces*, 3rd ed.; Elsevier: Amsterdam, The Netherlands, 2011; pp. 1–676. [CrossRef]
65. Yu, N.; Polycarpou, A.A. Contact of rough surfaces with asymmetric distribution of asperity heights. *J. Tribol.* **2002**, *124*, 367–376. [CrossRef]
66. Leach, R. *Characterisation of Areal Surface Texture*; Springer: Berlin/Heidelberg, Germany, 2013; ISBN 9783642364587.
67. Franco, L.A.; Sinatora, A. 3D surface parameters (ISO 25178-2): Actual meaning of Spk and its relationship to Vmp. *Precis. Eng.* **2015**, *40*, 106–111. [CrossRef]
68. Solaymani, S.; Ţălu, Ş.; Nezafat, N.B.; Rezaee, S.; Kenari, M.F. Diamond nanocrystal thin films: Case study on surface texture and power spectral density properties. *AIP Adv.* **2020**, *10*, 045206. [CrossRef]
69. Ţălu, Ş.; Ghaderi, A.; Stępień, K.; Mwema, F.M. Advanced Micromorphology Analysis of Cu/Fe NPs Thin Films. *IOP Conf. Ser. Mater. Sci. Eng.* **2019**, *611*, 012016. [CrossRef]
70. Mahboob Kanafi, M.; Kuosmanen, A.; Pellinen, T.K.; Tuononen, A.J. Macro-and micro-texture evolution of road pavements and correlation with friction. *Int. J. Pavement Eng.* **2015**, *16*, 168–179. [CrossRef]
71. Ţălu, Ş.; Matos, R.S.; Pinto, E.P.; Rezaee, S.; Mardani, M. Stereometric and fractal analysis of sputtered Ag-Cu thin films. *Surf. Interfaces* **2020**, *21*, 100650. [CrossRef]
72. Gonçalves, E.C.M.; Pinto, E.P.; Ferreira, N.; De Sergipe, U.F.; Matos, R.S. Fractal study of kefir biofilms. In Proceedings of the XVIII Brazil MRS Meeting, Balneário Camboriú, Brazil, 25–26 September 2019.
73. Omar, M.; Salcedo, C.; Ronald, R.; Zamora, M.; Tavares, C. Study fractal leaf surface of the plant species Copaifera sp. using the Microscope Atomic-Force-AFM. *Rev. ECIPerú* **2016**, *13*, 10–16. [CrossRef]
74. Szerakowska, S.; Woronko, B.; Sulewska, M.J.; Oczeretko, E. Spectral method as a tool to examine microtextures of quartz sand-sized grains. *Micron* **2018**, *110*, 36–45. [CrossRef]
75. Honary, S.; Zahir, F. Effect of zeta potential on the properties of nano-drug delivery systems—A review (Part 2). *Trop. J. Pharm. Res.* **2013**, *12*, 265–273. [CrossRef]
76. Young, S.; Wong, M.; Tabata, Y.; Mikos, A.G. Gelatin as a delivery vehicle for the controlled release of bioactive molecules. *J. Control. Release* **2005**, *109*, 256–274. [CrossRef]

77. Mahmoudi, M.; Lynch, I.; Ejtehadi, M.R.; Monopoli, M.P.; Bombelli, F.B.; Laurent, S. Protein-nanoparticle interactions: Opportunities and challenges. *Chem. Rev.* **2011**, *111*, 5610–5637. [CrossRef]
78. Campelo, P.H.; Junqueira, L.A.; de Resende, J.V.; Zacarias, R.D.; de Fernandes, R.V.B.; Botrel, D.A.; Borges, S.V. Stability of lime essential oil emulsion prepared using biopolymers and ultrasound treatment. *Int. J. Food Prop.* **2017**, *20*, S564–S579. [CrossRef]
79. Roland, I.; Piel, G.; Delattre, L.; Evrard, B. Systematic characterization of oil-in-water emulsions for formulation design. *Int. J. Pharm.* **2003**, *263*, 85–94. [CrossRef]
80. Seibert, J.B.; Viegas, J.S.R.; Almeida, T.C.; Amparo, T.R.; Rodrigues, I.V.; Lanza, J.S.; Frézard, F.J.G.; Soares, R.D.O.A.; Teixeira, L.F.M.; de Souza, G.H.B.; et al. Nanostructured systems improve the antimicrobial potential of the essential oil from Cymbopogon densiflorus leaves. *J. Nat. Prod.* **2019**, *82*, 3208–3220. [CrossRef] [PubMed]
81. Marques, H.M.C. A review on cyclodextrin encapsulation of essential oils and volatiles. *Flavour Fragr. J.* **2010**, *25*, 313–326. [CrossRef]
82. Tian, X.-N.; Jiang, Z.-T.; Li, R. Inclusion interactions and molecular microcapsule of *Salvia sclarea* L. essential oil with β-cyclodextrin derivatives. *Eur. Food Res. Technol.* **2008**, *227*, 1001–1007. [CrossRef]
83. Guntero, V.; Ferretti, C.; Mancini, P.; Kneeteman, M. Synthesis and encapsulation of bis-eugenol in a mesoporous solid material: Enhancement of the antioxidant activity of a natural compound from clove oil. *Chem. Sci. Int. J.* **2018**, *22*, 1–10. [CrossRef]
84. Hosseini, S.F.; Zandi, M.; Rezaei, M.; Farahmandghavi, F. Two-step method for encapsulation of oregano essential oil in chitosan nanoparticles: Preparation, characterization and in vitro release study. *Carbohydr. Polym.* **2013**, *95*, 50–56. [CrossRef]
85. Peng, H.; Xiong, H.; Li, J.; Xie, M.; Liu, Y.; Bai, C.; Chen, L. Vanillin cross-linked chitosan microspheres for controlled release of resveratrol. *Food Chem.* **2010**, *121*, 23–28. [CrossRef]
86. Korsmeyer, R.W.; Gurny, R.; Doelker, E.; Buri, P.; Peppas, N.A. Mechanisms of solute release from porous hydrophilic polymers. *Int. J. Pharm.* **1983**, *15*, 25–35. [CrossRef]
87. Maderuelo, C.; Zarzuelo, A.; Lanao, J.M. Critical factors in the release of drugs from sustained release hydrophilic matrices. *J. Control. Release* **2011**, *154*, 2–19. [CrossRef]
88. Siepmann, J.; Siepmann, F. Mathematical modeling of drug dissolution. *Int. J. Pharm.* **2013**, *453*, 12–24. [CrossRef] [PubMed]
89. Vinceković, M.; Jurić, S.; Đermić, E.; Topolovec-Pintarić, S. Kinetics and mechanisms of chemical and biological agents release from biopolymeric microcapsules. *J. Agric. Food Chem.* **2017**, *65*, 9608–9617. [CrossRef]
90. de Oliveira, E.F.; Paula, H.C.B.; Paula, R.C.M. de Alginate/cashew gum nanoparticles for essential oil encapsulation. *Colloids Surf. B Biointerfaces* **2014**, *113*, 146–151. [CrossRef]
91. Paula, H.C.B.; Oliveira, E.F.; Carneiro, M.J.M.; De Paula, R.C.M. Matrix Effect on the spray drying nanoencapsulation of *Lippia sidoides* essential oil in chitosan-native gum blends. *Planta Med.* **2017**, *83*, 392–397. [CrossRef]
92. Isman, M.B. Botanical insecticides, deterrents, and repellents in modern agriculture and an increasingly regulated world. *Annu. Rev. Entomol.* **2006**, *51*, 45–66. [CrossRef]
93. Babarinde, S.A.; Olaniran, O.A.; Ottun, A.T.; Oderinde, A.E.; Adeleye, A.D.; Ajiboye, O.; Dawodu, E.O. Chemical composition and repellent potentials of two essential oils against larger grain borer, *Prostephanus truncatus* (Horn.) (Coleoptera: Bostrichidae). *Biocatal. Agric. Biotechnol.* **2021**, *32*, 101937. [CrossRef]
94. Campolo, O.; Cherif, A.; Ricupero, M.; Siscaro, G.; Grissa-Lebdi, K.; Russo, A.; Cucci, L.M.; Di Pietro, P.; Satriano, C.; Desneux, N.; et al. Citrus peel essential oil nanoformulations to control the tomato borer, *Tuta absoluta*: Chemical properties and biological activity. *Sci. Rep.* **2017**, *7*, 13036. [CrossRef]
95. Chaudhari, A.K.; Singh, V.K.; Kedia, A.; Das, S.; Dubey, N.K. Essential oils and their bioactive compounds as eco-friendly novel green pesticides for management of storage insect pests: Prospects and retrospects. *Environ. Sci. Pollut. Res.* **2021**, *28*, 18918–18940. [CrossRef]
96. Ngongang, M.D.T.; Eke, P.; Sameza, M.L.; Mback, M.N.L.N.; Lordon, C.D.-; Boyom, F.F. Chemical constituents of essential oils from *Thymus vulgaris* and *Cymbopogon citratus* and their insecticidal potential against the tomato borer, *Tuta absoluta* (Lepidoptera: Gelechiidae). *Int. J. Trop. Insect Sci.* **2022**, *42*, 31–43. [CrossRef]
97. Brandão, R.M.; Ferreira, V.R.F.; Batista, L.R.; Alves, E.; Santiago, W.D.; Barbosa, R.B.; Caetano, A.R.S.; Nelson, D.L.; das G. Cardoso, M. Antifungal activity and the effect of the essential oil of *Lippia origanoides* Kunth on *Aspergillus mycotoxins* production. *Aust. J. Crop Sci.* **2021**, *15*, 1005–1012. [CrossRef]
98. Jesus, F.P.K.; Ferreiro, L.; Bizzi, K.S.; Loreto, É.S.; Pilotto, M.B.; Ludwig, A.; Alves, S.H.; Zanette, R.A.; Santurio, J.M. In vitro activity of carvacrol and thymol combined with antifungals or antibacterials against Pythium insidiosum. *J. Mycol. Med.* **2015**, *25*, e89–e93. [CrossRef]
99. Takahashi, H.; Nakamura, A.; Fujino, N.; Sawaguchi, Y.; Sato, M.; Kuda, T.; Kimura, B. Evaluation of the antibacterial activity of allyl isothiocyanate, clove oil, eugenol and carvacrol against spoilage lactic acid bacteria. *LWT* **2021**, *145*, 111263. [CrossRef]
100. Yang, R.; Miao, J.; Shen, Y.; Cai, N.; Wan, C.; Zou, L.; Chen, C.; Chen, J. Antifungal effect of cinnamaldehyde, eugenol and carvacrol nanoemulsion against *Penicillium digitatum* and application in postharvest preservation of citrus fruit. *LWT* **2021**, *141*, 110924. [CrossRef]

101. Kordali, S.; Cakir, A.; Ozer, H.; Cakmakci, R.; Kesdek, M.; Mete, E. Antifungal, phytotoxic and insecticidal properties of essential oil isolated from Turkish Origanum acutidens and its three components, carvacrol, thymol and *p*-cymene. *Bioresour. Technol.* **2008**, *99*, 8788–8795. [CrossRef]
102. Arango Bedoya, O.; Hurtado Benavides, A.M.; Pantoja Daza, D.; Santacruz Chazatar, L. Actividad inhibitoria del aceite esencial de *Lippia origanoides* H.B.K sobre el crecimiento de *Phytophthora infestans*. *Acta Agronómica* **2014**, *64*, 116–124. [CrossRef]

nanomaterials

MDPI

Review

Application of Peptides in Construction of Nonviral Vectors for Gene Delivery

Yujie Yang, Zhen Liu, Hongchao Ma * and Meiwen Cao *

State Key Laboratory of Heavy Oil Processing, Department of Biological and Energy Chemical Engineering, College of Chemical Engineering, China University of Petroleum (East China), 66 Changjiang West Road, Qingdao 266580, China

* Correspondence: mahc@upc.edu.cn (H.M.); mwcao@upc.edu.cn (M.C.)

Abstract: Gene therapy, which aims to cure diseases by knocking out, editing, correcting or compensating abnormal genes, provides new strategies for the treatment of tumors, genetic diseases and other diseases that are closely related to human gene abnormalities. In order to deliver genes efficiently to abnormal sites in vivo to achieve therapeutic effects, a variety of gene vectors have been designed. Among them, peptide-based vectors show superior advantages because of their ease of design, perfect biocompatibility and safety. Rationally designed peptides can carry nucleic acids into cells to perform therapeutic effects by overcoming a series of biological barriers including cellular uptake, endosomal escape, nuclear entrance and so on. Moreover, peptides can also be incorporated into other delivery systems as functional segments. In this review, we referred to the biological barriers for gene delivery in vivo and discussed several kinds of peptide-based nonviral gene vectors developed for overcoming these barriers. These vectors can deliver different types of genetic materials into targeted cells/tissues individually or in combination by having specific structure–function relationships. Based on the general review of peptide-based gene delivery systems, the current challenges and future perspectives in development of peptidic nonviral vectors for clinical applications were also put forward, with the aim of providing guidance towards the rational design and development of such systems.

Keywords: peptide; gene delivery; nonviral vector; self-assembly; gene therapy

Citation: Yang, Y.; Liu, Z.; Ma, H.; Cao, M. Application of Peptides in Construction of Nonviral Vectors for Gene Delivery. *Nanomaterials* **2022**, *12*, 4076. https://doi.org/10.3390/nano12224076

Academic Editor: Alicia Rodríguez-Gascón

Received: 21 October 2022
Accepted: 16 November 2022
Published: 19 November 2022

1. Introduction

Gene therapy refers to the introduction of exogenous genes into target cells to correct defective and abnormal genes for the purpose of treating diseases. With the development of modern molecular biology and progress of human genome project, gene therapy has become a promising strategy to treat cancer, gene diseases, infectious diseases, cardiovascular diseases and nervous system diseases [1]. The therapeutic nucleic acids used in gene therapy include plasmid DNA, siRNA and other free nucleic acids [2]. However, it is difficult for these nucleic acids to reach the target tissue due to their large molecular weight and huge number of negative charges [3]. Therefore, developing safe and effective gene delivery vectors is essential for gene therapy.

Generally, gene delivery vectors are categorized into two types, that is, viral vectors and nonviral ones. Typically, viral vectors use modified viruses including retroviruses, lentiviruses, adenoviruses and adeno-associated viruses to carry genes into cells due to their advantages of high infection level of host cells [4]. Their accurate programmed infection characteristics and efficient delivery ability of exogenous gene into host cells make them the most widely used gene vectors in clinical trials. However, viral vectors have inherent disadvantages such as potential carcinogenic effects, limited DNA encapsulation ability, lack of targeting ability and difficulty in production [5]. Moreover, they may also activate the host's immune system and reduce the effectiveness of subsequent gene

delivery [6]. These defects greatly limit the usage of virus vectors in clinical treatment and further promote the development of nonviral gene delivery systems [7]. Compared with viral vectors, nonviral vectors are usually easier to synthesize and operate, having lower immune response, larger loading capacity of genetic material and better targeting ability. Recently, a large number of efficient and safe nonviral vectors have been designed for gene therapy. When using nonviral vectors to deliver nucleic acids such as DNA [8], messenger (m)RNA [9], short interfering (si)RNA [10] and micro (mi)RNA into cells [11], they need to overcome several biological barriers (Figure 1). First, the vectors should protect the nucleic acids from degradation by endonucleases and exonucleases and help them evade immune detection [12–14]. Second, the vectors need to contain specific groups and ligands both to make nucleic acid molecules exude from the bloodstream to the target tissue and to mediate cell entry. Third, siRNA and miRNA mimics must be loaded into the RNA-induced silencing complex, while mRNA must bind to the translational machinery and DNA must be further transported to the nucleus to play its function (Figure 2) [15]. The commonly used nonviral vectors include cationic liposomes, cationic polymers, dendrimers, peptides and so on [16]. Among them, peptides have been considered as unique tools for delivering nucleic acid drugs due to their excellent biocompatibility and biodegradability, ease of production and modification as well as being able to respond to external stimuli [17–19].

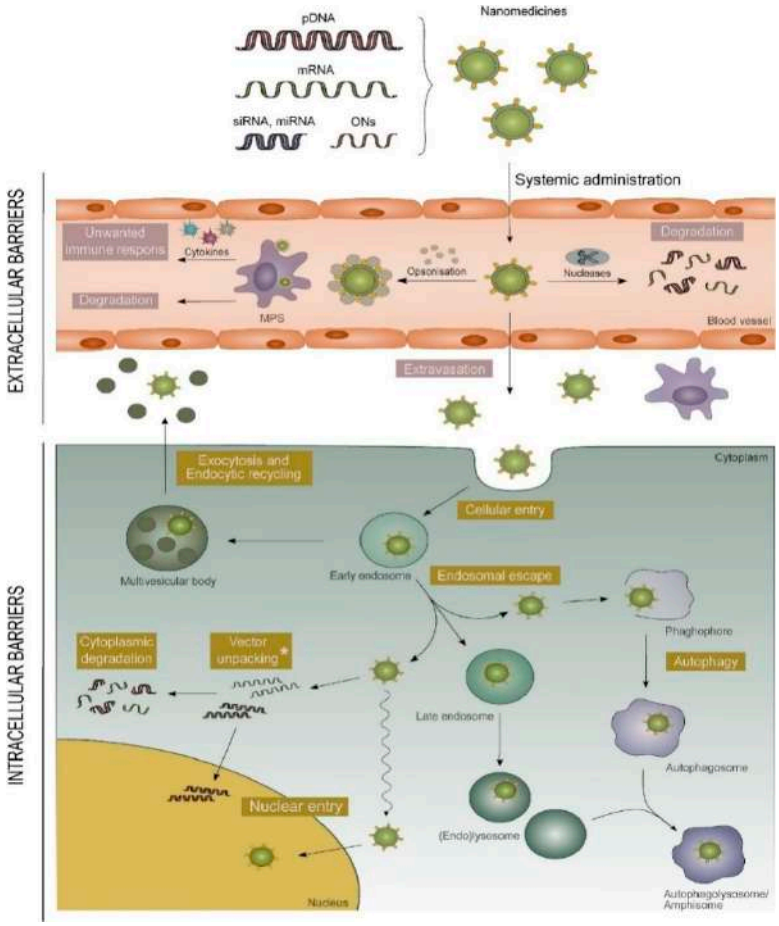

Figure 1. Biological barriers to overcome when using nonviral vectors to deliver nucleic acids in vivo. Nucleic acids bind to peptides through electrostatic interactions, transferring them across the cell membrane via endocytosis, providing endosome escape, and ultimately releasing the associated nucleic acids in the cytoplasm or nucleus. Reprinted with permission from Ref. [20]. Copyright 2018, Elsevier.

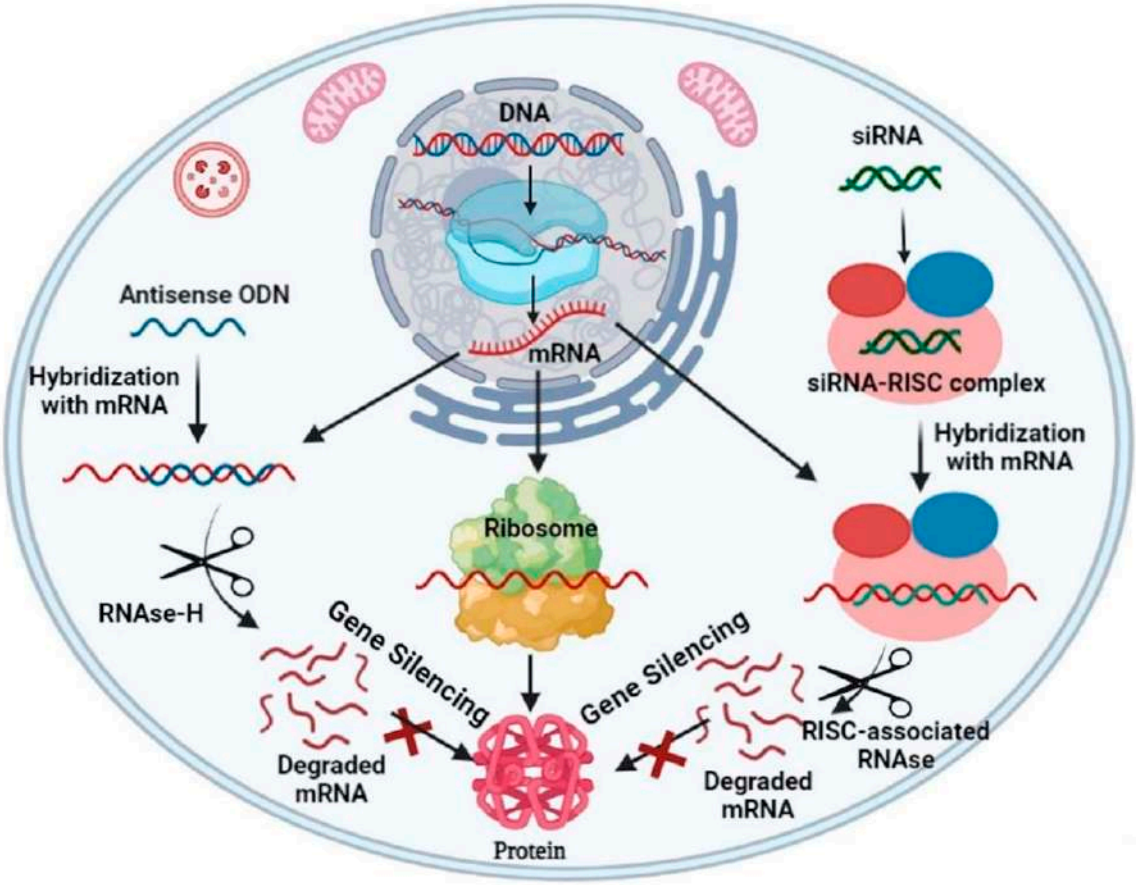

Figure 2. Schematic illustration of different cellular pathways involved in gene silencing. Reprinted with permission from Ref. [21]. Copyright 2022, Elsevier.

Nowadays, many peptides have been incorporated as functional components into nonviral gene delivery systems to overcome various biological obstacles and deliver nucleic acid drugs to target sites with high efficiency. Peptides used as non-viral gene vectors can be divided into the following types according to their functions: cell penetrating peptides (CPPs), membrane active peptides, targeting peptides, and nuclear localization signal (NLS) peptides (Table 1). In this review, we first talk about the strategies for constructing peptide–nucleic acid complexes, and then summarize the applications of these peptides in gene delivery, as well as how to combine these peptides with other nonviral vectors to achieve the purpose of improving transfection efficiency.

Table 1. Types of peptides designed for use in gene delivery.

Peptide Type	Name	Sequence [a]	Reference
CPPs	CHAT	CHHHRRRWRRRHHHC	[22]
	LH2	Ac, T, C-LHHLCHLLHHLCHLAG Ac-GALHCLHHLLHCLHHL Ac -LHHLCHLLHHLCHLGA Ac -LHHLCHLLHHLCHLGA	[23,24]
	SRCRP2-11	GRVEVLYRGSW	[25]
	SRCRP2-11-R	GRVRVLYRGSW	
	R_8	RRRRRRRR	[26–29]
	Penetratin	RQIKIWFQNRRMKWKK	[30]
	WTAS	PLKTPGKKKKGKPGKRKEQEKKKRRTR	[31]
	PF14	Stearyl-AGYLLGKLLOOLAAAALOOLL-NH2	[32]
	CPP	CGRRMKWKK	[33]

Table 1. *Cont.*

Peptide Type	Name	Sequence [a]	Reference
Targeted peptides	circular NGR	CNGRCG	[28]
	NGR	NGR	[33,34]
	RGD	RGD	[29,35–37]
	Trivalent cRGD	HCACAE[cyclo(RGD-D-FK)]E[cyclo(RGD-D-FK)]$_2$	[38]
	cRGD	cyclo(RGD-D-FK)	[39,40]
	cyclic iRGD	cyclo (CRGDKGPDC)	[41]
Membrane active peptides	RALA	WEARLARALARALARHLARALAHALHACEA	[42–44]
	HALA2	WEARLARALARALARHLARALAHALHACEA	[45]
	(LLHH)3	CLLHHLLHHLLHH	[46]
	(LLKK)3-H6	LLKKLLKKLLKKCHHHHHH	[46]
	LAH4	KKALLALALHHLAHLALHLALALKKA	[47]
	KH27K	KHHHHHHHHHHHHHHHHHHHHHHHHHHHK	[48,49]
	G3	GIIKKIIKKIIKKI	[50]
	Melittin	GIGAVLEVLTTGLPALISWIEEEEQQ	[51]
	CMA-1	EEGIGAVLKVLTTGLPALISWIKRKRQQC	[52]
	CMA-2	GIGAVLKVLTTGLPALISWIHHHHEEC	[53,54]
	CMA-3	GIGAVLKVLTTG LPALISWIKRKREEC	[54]
	CMA-4	EEGIGAVLKVLTTG LPALISWIHHHHQQC	[52]
	NMA-3	CGIGAVLKVLTTGLPALISWI KRKREE	[52,53]
	acid-Melittin	GIGAVLKVLTTGLPALISWIKRKRQQ	[51]
	Mel-L6A10	GIGAIEKVLETGLPTLISWIKNKRKQ	[55]
	RV-23	RIGVLLARLPKLFSLFKLMGKKV	[53]
NLS peptides	SV40 T antigen	PKKKRKV	[56–60]
	Mouse FGF3	RLRRDAGGRGGVYEHLGGAPRRRK	[61]
	NLSV404	PKKKRKVGPKKKRKVGPKKKVGPKKKRKVGC	[62]
	Ku7O$_2$	CKVTKRKHGAAGAASKRPKGKVTKRKHGAAGAASKRPK	[63]
Other peptides	Smart peptide	Nap-FFGPLGLAG(CK$_m$)$_n$C	[64]
	24-mer β-annulus peptide	INHVGGTGGAIMAPVAVTRQLVGS	[65,66]
	β-annulus-GGGCG peptide	INHVGGTGGAIMAPVAVTRQLVGSGGGCG	[67]
	H4K5HC$_{BZl}$C$_{BZl}$H	HHHHKKKKKC12LLHC$_{BZl}$C$_{BZl}$HLLGSPD	[68]
	K3C6SPD	KKKC6WLVFFAQQGSPD	[69,70]
	CC	REGVAKALRAVANALHYNASALEEVADALQKVKM	[71]
	Surfactant-like peptide	IIIVVVAAAGGGKKK	[72]

[a] All peptide sequences are given in the one-letter code amino acid name (Table A1, Appendix A).

2. Construction of Peptide–Nucleic Acid Complexes for Gene Delivery

To achieve the purpose of gene delivery, the functional peptides should be first fused with nucleic acids to form complexes so as to play the roles of gene condensing, protection, and delivery. Three main strategies can be adopted to achieve peptide/nucleic acid fusion. The first is to link the peptide segment covalently with nucleic acid to produce a conjugated molecule. For this strategy, the functional peptide segments are conjugated to the to-be-delivered nucleic acid via chemical bonds (e.g., ester bond, disulfide bridge, thiol-maleimide linkage) [73]. The superior advantage of this strategy is that the peptide–nucleic acid conjugated molecule has defined structure and stoichiometry as well as high stability, which can lead to repeatable delivery performance. This approach is particularly suitable for charge-neutral nucleic acid analogs such as phosphonodiamidate morpholino oligomer (PMO) and peptide nucleic acid (PNA) [74,75]. The peptide–nucleic acid conjugate can easily cross the cell membranes and enter the nucleus and fulfill its biological functions. Currently, this strategy has exhibited promise in clinical trials. For example, peptide-PNA conjugates have been utilized in preclinical studies targeting c-myc for severe combined immunodeficiency, while peptide-PMO conjugates have been employed for Duchenne muscular dystrophy [76,77]. However, for this strategy, the covalent bond formation may reduce the biological activity of nucleic acids or inhibit their release and expression in cells, which may hinder their application. The second is the noncovalent complexation strategy, which is to complex peptides with nucleic acids directly via noncovalent forces. For this

strategy, the peptides are usually designed to have various positive charges, which can fist bind with negatively charged nucleic acids to result in charge neutralization and then induce hydrophobic collapse of the nucleic acid molecules into condensed nanoparticles [78]. This strategy has superior advantages including ease of vector construction, high loading amount of gene drug, and controllable genome release by introducing stimuli responsibility. It is suitable for delivery of most nucleic acids involving plasmid DNA, siRNA, mRNA and so on. Peptide–nucleic acid nanocomposites obtained by this method are easy to prepare and have been attempted to treat a series of diseases including cancer and cardiovascular diseases [79,80]. However, it should be noted that the peptide should be well designed to endow the peptide carrier with high functionality and avoid loss of peptide function because of its electrostatic binding with nucleic acids. The third strategy is to modify functional peptide segments on the surface of specific nanoparticles to produce composite nanoplatforms, which can further be used to complex with nucleic acids for delivery purposes. This strategy can take advantage of the nanoparticles to facilitate cellular uptake as well as to give multifunctionalities [81], which is especially suitable for development of systems for combined therapy. In summary, the above three strategies, each having specific features in peptide/nucleic acid fusion, have been extensively used in gene delivery.

3. Application of CPPs in Gene Delivery

Composed of 10–20 amino acids, CPPs are one class of peptides which have the potential to penetrate bio-membrane and transport bioactive substances into cells [82]. In recent years, a variety of substances such as hydrophilic proteins, nucleic acids and even nanoparticles have been carried by CPPs across cell membrane into the cytoplasm to serve specific functions. This rapid intracellular transport is not destructive to cell membranes, and the active substances can be delivered into a variety of cells regardless of the cell type. Use of CPPs to deliver nucleic acids and drugs for gene therapy and disease treatment has therefore attracted extensive attention. For example, Emma et al. designed a new 15-amino acid linear peptide CHAT that contains six arginine residues, the minimum number of residues required for cell uptake [22]. The cysteine residues located at both ends can enhance the stability of the delivery system and achieve cargo release in cells. Experiments demonstrated that CHAT peptide can transfect plasmid (p)DNA into various cell lines, resulting in successful reporter-gene expression in vivo in 4T1 and MDA-MB-231 breast xenograft models (Figure 3a). The transfection efficiency in tumor sites is comparable to that of commercial transfectants, making it a low-cost, easily formulated delivery system for the administration of nucleic acid therapeutics. However, some inherent properties of CPPs limit their clinical application. First, when CPPs are administered in vivo, they are penetrable only at concentrations above micromoles, which will cause many systemic side effects. In this case, designing new CPPs and improving their ability to penetrate cell membranes are of great importance for enhancing the safety of CPP application. Recently, a pH-active CPP called dimer LH2 was designed by Dougherty and co-workers because they found that amphiphilic CPPs in dimeric form showed higher cell-penetrating activity compared with the monomeric ones [23]. As expected, dimer LH2 can effectively deliver nucleic acid drugs to triple-negative breast cancer cell MDA-MB-231 with only tens of nanomolar concentration, showing strong membrane penetrating ability and antitumor effects [24]. In addition to using CPPs as carriers to deliver pDNA into cells, naked siRNA must be protected and delivered by carriers to enter the cell, because it is unstable, and readily degraded by nucleases in the serum environment and absorbed by tissues [83]. To solve this problem, Martina et al. used DMBT1-derived peptides with membrane penetrating ability as carriers to prepare siRNA delivery nanoparticles, which can complex with siRNA and transfect human breast metastatic adenocarcinoma MCF7 cells [25]. The delivered siRNA exhibited effective gene silencing in MCF7-recombinant cells. The study laid the foundation for developing a new vector for therapeutic siRNA delivery.

Second, most CPPs can be internalized by all cell types and lack the ability to target specific tissues as particular objectives. This imprecise feature will lead to their low stability

in blood, poor tissue penetration and limited cell uptake, thus greatly reducing their targeting efficiency towards specific tissues. To solve this problem, several strategies have been developed to improve the specificity of CPPs to pathological tissues. Among them, combing targeting molecules such as RGD (Arginine-Glycine-Aspartic acid), NGR (Asparagine-Glycine-Arginine) peptide, folic acid (FA) and hyaluronic acid with CPPs is a very effective strategy [84–86]. These targeting molecules are usually overexpressed in tumor types, but not in normal cells. Therefore, they can improve the targeting effect for pathological tissues, whilst healthy tissues are not affected by drug delivery. For example, Qi-ying Jiang conjugated the target ligand of FA and the CPP segment of octaarginine (R_8) to an existing vector (PEI600-CD) composed of β-cyclodextrin and low-molecular-weight polyethylenimine (PEI) to produce a new gene vector FA-PC/R_8-PC [26]. This vector can form ternary nanocomplexes with pDNA, and further deliver it to tumor sites in vivo with excellent gene transfection efficiency (Figure 3b). Moreover, hyaluronic acid coupled with CPPs can effectively deliver siRNA to macrophages within the atherosclerotic plaques and enhance gene delivery to macrophages in antiatherosclerotic therapy [30], which is a promising nanocarrier for efficient macrophage-targeted gene delivery and antiatherogen (Figure 3c).

In addition to being used as vectors for gene delivery alone, CPPs can also be combined with other non-viral vectors such as liposomes and cationic polymers to achieve high gene transfection efficiency. Integrating different types of functional vectors into one gene delivery system can exert a synergistic effect between the components, improving the low permeability and poor selectivity of CPPs, and so enhance the gene delivery efficiency. Ikramy et al. developed an efficient gene delivery system by combining a CPP segment (R_8) and pH-sensitive cationic lipid (YSK05) [27]. Positive nanoparticles can be formed by attaching high density R8 to the surface of YSK05 nanoparticles. The particles can further encapsulate pDNA to produce complexes that can lead to high gene transfection efficiency due to the synergistic effect between R_8 and YSK05. Obdulia and co-workers also developed a gene delivery vector by co-assembly of CPP (WTAS) and a poly β-amino ester (PBAE) polymer [31]. The WTAS-PBAE vector showed high transfection rate, and the results of cell transfection experiments with GL26 cells revealed that WTAS-PBAE vector loaded with GFP pDNA led to virtually complete transfection (> 90%). This excellent transfection efficiency makes it a very promising gene delivery vector for delivering a variety of genetic materials. In addition, the combination of CPPs and inorganic nanoparticles also shows great potential in the application of delivering nucleic acid drugs. For example, Dowaidar et al. found that the conjugation of CPPs-oligonucleotides with magnetic iron oxide nanoparticles can promote cellular uptake of the plasmid and improve the transfection efficiency, which opens up a new way for selective and efficient gene therapy [32].

4. Application of Targeted Peptides in Gene Delivery

During gene delivery, an off-target effect may occur when the therapeutic nucleic acids bind to non-specific cells, which is undesirable and will decrease the therapeutic effect of gene therapy. Therefore, selectively delivering vector-nucleic acid complexes to the target cells and exerting the therapeutic effect at specific sites are critical to improve the transfection efficiency of gene therapy [87]. Conjugating targeting ligands such as FA, hyaluronic acid and biomolecules including peptides and proteins can greatly increase the targeting of the gene delivery systems because they can specifically bind to the receptors on cells. Among them, peptides are excellent gene delivery targeting ligands due to their good biocompatibility, ease of synthesis and modification as well as their high response to stimuli. Thus far, more than 700 targeted peptides have been discovered for targeting different cells. The most widely used target peptides among them are NGR and RGD which can specifically recognize tumor angiogenic markers and provide new venues for exploring tumor targeting agents [84].

The NGR motif, whose tumor-targeting ability relies on its specific interaction with CD13 (aminopeptidase N), was identified from a tumor homing peptide. It is often selec-

tively overexpressed in neovascular and some tumor cells, but seldom expressed in quiet vascular endothelial cells. NGR peptides have now been used to promote the targeted delivery of therapeutic agents and enhance antitumor effects [88]. A bi-functional peptide, NGR-10R, which consists of an N-terminal circular NGR motif (CNGRCG) and a C-terminal R_8 sequence was designed for gene therapy. The R_8 sequence at the end of NGR-10R can bind to siRNA through electrostatic interaction to form NGR-10R/siRNA nanoparticles. Thanks to the NGR motif, NGR-10R/siRNA nanoparticles can be specifically delivered to MDA-MB-231 cells and localized around the nucleus, thus robustly repressing gene expression in MDA-MB-231 and HUVEC (a $CD13^+/\alpha_v\beta_3{}^+$ cell) (Figure 4a) [28]. In the study of Yang, as a targeted peptide, NGR plays a navigational effect, enabling the pcCPP/NGR-LP dual-modified liposomes vector to accumulate at the tumor site. Finally, with the aid of CPPs, the siRNA-loaded vector enters target cells efficiently [33]. In addition to targeting siRNA to MDA-MB-231 cells, the NGR motif can effectively deliver siRNA to HT-1080 cells and downregulate target genes with the synergistic effect of other vectors. Chen et al. designed the LPD-poly(ethylene glycol) (PEG)-NGR vector by modifying PEGylated LPD using the NGR motif. It can target CD13 expressed in the tumor cells or tumor vascular endothelium, effectively delivering siRNA to the cytoplasm of HT-1080 cells and silence the target gene [34].

Different from NRG, the RGD peptide can specifically bind to integrin in tumor endothelial cells and act as ligand to target tumor cells that overexpress $\alpha_v\beta_3$ integrin [89,90]. As an attractive tumor cell receptor, integrin plays a major role in promoting the proliferation, migration, invasion and survival of tumor cells. Therefore, gene vectors modified by RGD peptide can block cell–cell and cell-matrix adhesions by competing with adhesion proteins for cell surface integrins, thus achieving targeted selectivity to tumor cells and improving the efficiency of gene transfection. In view of this, a large number of RGD peptide-based gene vectors have been developed. Recently, lung cancer and bronchial cancer have become the most deadly cancers due to the aggravation of air pollution. In order to develop new targeted, effective and less painful therapies, Yang et al. synthesized the RRPH (RGD-R_8-PEG-HA) which is composed of peptide (RGD-R_8) and PEGylation on HA to coat PFC (plasmid complex). The obtained RRPHC nanoparticles (RRPH coated PFC complex) achieve long-term circulation and tumor tissue-penetration while maintaining the high transfection efficiency of PFC [29]. Kim et al. designed a targeted gene vector, RGD/PEI/WSC, which can combine the RGD to chitosan and PEI, for $\alpha_V\beta_3$ integrin-overexpressing tumor cells [35]. In vivo experiments show that the vector can suppress the growth of PC3 prostate tumor cell xenograft model by silencing BCL2 mRNA, which is expected to be a good candidate for a specific targeted gene vector without cytotoxicity (Figure 4b).

Oncolytic adenovirus has been widely used in clinical trials of cancer gene therapy [91,92]. Moreover, tumor targeted gene virus therapy (CTGVT) may be an effective strategy for the treatment of advanced or metastatic cancer [93]. In a previous study, Luo et al. found that replicating adenovirus (AD-ZD55-miR-143) showed specific anti-rectal cancer efficacy in vitro. However, its anti-tumor effect in vivo is not ideal, because the vector does not increase the chance of reaching target cells. To solve this problem, they developed AD-RGD-survivin-ZD55-miR-143, a novel triple regulatory oncolytic adenovirus which significantly enhanced the anti-tumor effect and directly broadened the treatment options for colorectal cancer [36]. RGD peptides with a circular structure, i.e., cyclic (c)RGDs can also be used for tumor targeting studies—being more active due to their conformation-less assembly than linear RGD oligopeptides. Moreover, (c)RCDs are resistant to proteolysis and have higher affinity to integrin receptors [94]. Therefore, many five membered ring RGDs containing pentapeptides have been used to endow gene vectors with tumor targeting [95]. Alam et al. reported that cRGDs can selectively enter cancer cells overexpressing $\alpha_v\beta_3$ integrin carrying siRNA for gene silencing [38]. A further study indicated that cRGDs can specifically guide siRNA to cells expressing $\alpha_v\beta_3$, resulting in effective knocking out of selected genes and significantly reducing tumor growth [39]. In addition,

cRGDs were employed to promote cellular internalization of polyplex micelles encapsulating anti-angiogenic pDNA by tumor vascular endothelial cells, which abundantly express RGD-specific $\alpha_v\beta_3$ and $\alpha_v\beta_5$ integrin receptors and thereby exhibit anti-tumor activity against pancreatic adenocarcinoma upon systemic injection [96,97]. Moreover, liposomes modified with cRGD peptide can be used to deliver drugs to targeted cancer cells [40].

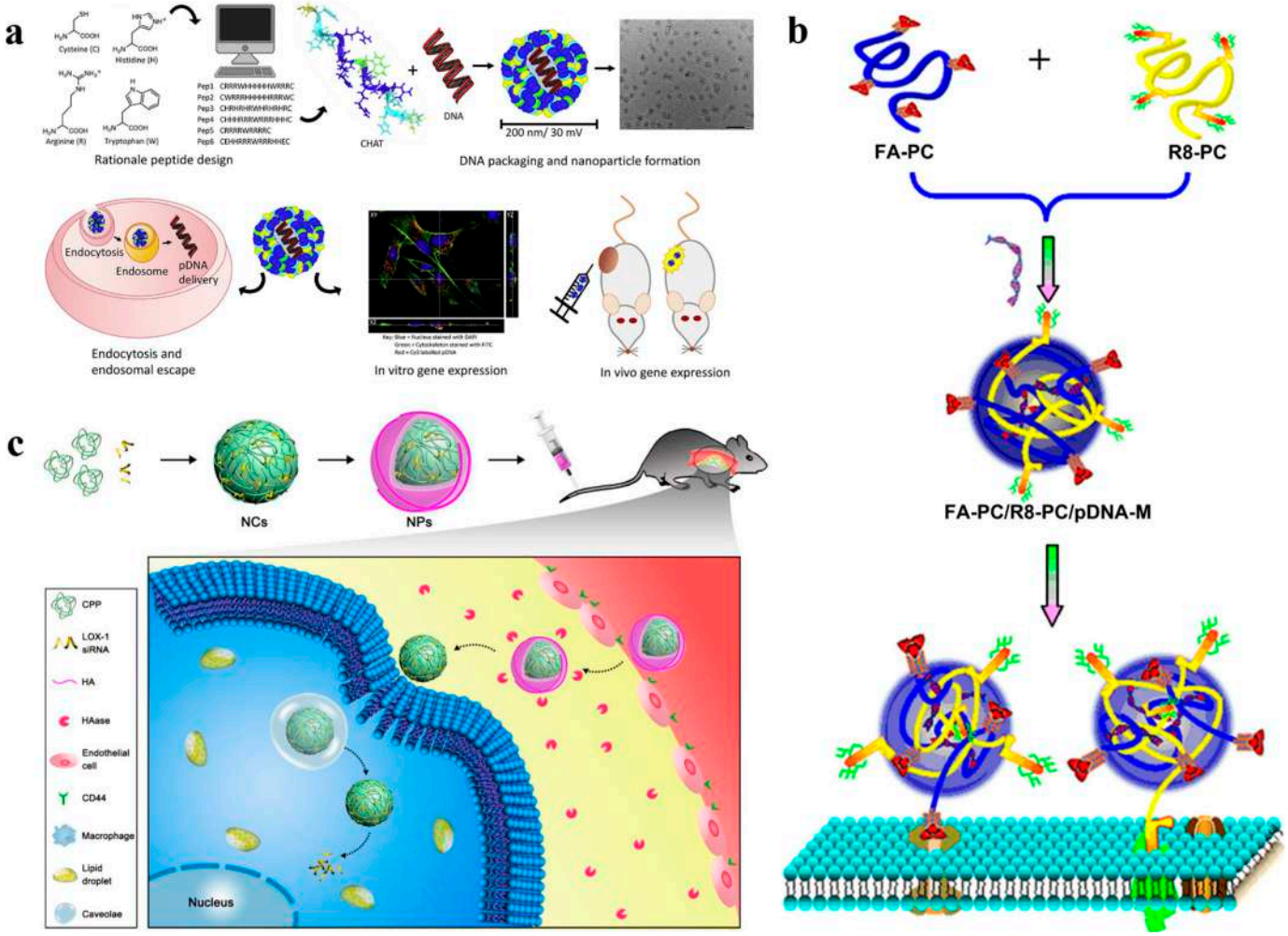

Figure 3. (**a**) CHAT peptide condenses pDNA to produce cationic nanoparticles less than 200 nm in diameter. The complex can cross the cell membrane through endocytosis and successfully escape from the endosomes, obtaining high transfection efficiency. Reprinted with permission from Ref. [22]. Copyright 2020, Elsevier. (**b**) The process of preparation of nanoparticles formed from FA-PC/R8-PC/pDNA complex. Reprinted with permission from Ref. [26]. Copyright 2011, Elsevier. (**c**) CPPs condense siRNA and deliver it to macrophages. Reprinted with permission from Ref. [30]. Copyright 2018, American Chemical Society.

Our group is also devoted to designing peptide carriers with targeting functions. Recently, we have designed an amphiphilic peptide Ac-RGDGPLGLAGI_3GR_8-NH_2 with two charged chain segments distributed at the end and a hydrophobic chain segment in the middle [37]. It can selectively kill cancer cells through the specific recognition and binding of RGD fragments to cancer cell membranes and cleavage of PLGLA fragments by tumor-overexpressed matrix metalloproteinase-7 enzymes. The R_8 sequence can induce efficient condensation of DNA into dense nanoparticles, resist enzymatic degradation of DNA, ensure successful delivery of DNA into cells, and improve the expression level as well as transfection rate of target genes [87]. Moreover, we also combined the cRGD peptide to gold nanoparticles (AuNPs) which has been widely used in the delivery of nucleic acid

molecules due to its good biocompatibility and easy surface functionalization [98,99]. We designed the peptide of sequence (CRGDKGPDC)GPLGLAGIIIGRRRRRRRR-NH_2 (CPIR28) which was grafted onto the surface of AuNPs by the one-pot synthesis method [41]. The CPIR28-AuNPs nanocomposite can effectively condense DNA and improve the intracellular transport of genes (Figure 4c).

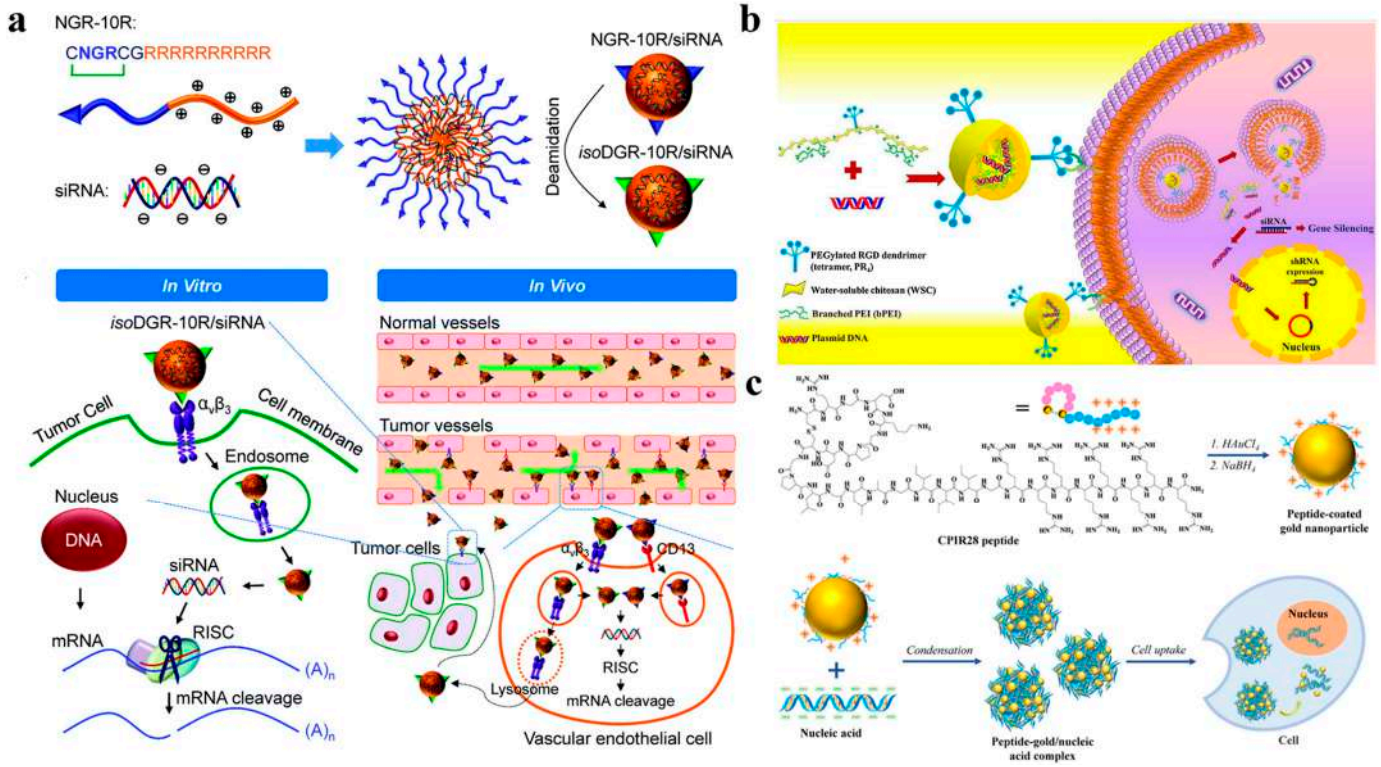

Figure 4. (**a**) Bi-functional NGR-10R peptide condenses siRNA to form spherical nanostructures which can enter cells by receptor $\alpha_v\beta_3$ and CD13 mediated endocytosis. After escaping from the endosomes/lysosomes, siRNA is released into the cytoplasm and loaded by the RISC. Reprinted with permission from Ref. [28]. Copyright 2015, Biomaterials Science. (**b**) RPgWSC-pDNA complexes can suppress solid tumor growth by silencing BCL2 mRNA. Reprinted with permission from Ref. [35]. Copyright 2017, Elsevier. (**c**) CRIP28-AuNPs form nanocomplexes with nucleic acids by electrostatic interaction for cellular delivery. Reprinted with permission from Ref. [41]. Copyright 2022, Elsevier.

5. Application of Membrane Active Peptides in Gene Delivery

After cell uptake, successful release of vector/nucleic acid complexes from endosomes is a major obstacle for effective gene therapy. After the vector/nucleic acid complexes cross the membrane barrier into the cell through endocytosis, vesicles will enclose them and develop into early endosomes, which then mature to form late endosomes and then fuse with lysosomes. In order to exert the therapeutic effect of nucleic acid drugs, the complexes need to escape from the endosomes and enter into the cytoplasm. Otherwise, the nucleic acid drugs will be degraded by hydrolases [46]. Therefore, developing vectors with endosomal escape ability is essential for efficient gene delivery. There are two ways to achieve endosomal escape. First, considering the acidic environment inside the endosomes, materials with a buffer effect in the acidic environment, such as chlorine and calcium, can be added to assist endosomal escape. These buffer agents can prevent endosomes from binding to lysosomes, vacuolate endosomes and then decrease the membrane stability. However, these chemicals are generally only used in vitro and not suitable for clinical applications due to their potential cytotoxicity. Nevertheless, the acidic endosomal environment suggests that we can introduce amino acids with a acidic buffering effect into the carrier to destroy the endosome membrane by proton pump for the purpose of endosomal escape. Since only

histidine has a buffering effect among the 20 common amino acids due to its imidazole group, it is often embedded into the carrier to improve endosomal escape during delivery of nucleic acids. RALA, which is a 30-mer cationic amphipathic helical peptide, contains seven hydrophilic arginine residues on one side of the helix, and hydrophobic leucine residues on the other side. When the pH drops, the α-helicity of RALA increases to achieve endosomal escape and release of the cargo [42]. Therefore, Vimal K et al. used RALA peptides to condense mRNA and effectively deliver them to dendritic cells [43]. Subsequently, the RALA-mRNA nanocomplexes successfully escaped from endosomes and expressed mRNA in the cell cytosol to promote antigen specific T cell proliferation as well as evoking T cell immunity in vivo (Figure 5a). In addition to delivering mRNA, RALA can also deliver siRNA with high efficiency. Eoghan J. Mulholland et al. reported that RALA is an effective siRNA carrier targeting the FK506-binding protein and has great potential in promoting angiogenesis for advanced wound healing applications (Figure 5b) [44]. Recent studies have found that the introduction of histidine into RALA peptide can further improve the endosomal escape ability of the vectors, thereby increasing the transfection efficiency. For example, Liu et al. designed a new peptide-based vector HALA2 with ability of endosomal escape and high cell transfection efficiency by adjusting the ratio of histidine and arginine in the RALA peptide [45]. HALA2 replaced two arginines close to the C-terminal of RALA with histidine, which reduced the number of positively charged amino acids in HALA2 from 7 to 5, resulting in a better transfection rate than RALA. In addition, introducing histidine fragments into other kinds of vectors can also improve their endosomal escape ability. Chitosan has the advantages of non-toxicity, non-immunogenicity, biodegradability and good biocompatibility as a gene vector. However, chitosan cannot mediate the escape of endosome due to its low endosomal escape rate and poor buffer capacity. For this reason, Liu et al. introduced histidine into chitosan and obtained a new vector with good solubility, strong binding ability to siRNA and excellent endosomal escape performance [100].

Secondly, using membrane active peptides with membrane destruction capability to destroy the endosomal membrane can also realize endosomal escape and release the vector/nucleic acid complex into the cytoplasm. Recently, a series of membrane active peptides have been designed. For example, $(LLHH)_3$ and $(LLKK)_3$-H_6 are two typical amphiphilic membrane active peptides that can destroy endosomal membranes and regulate the "proton sponge effect". Introducing them into vectors containing rigid acyl and polyarginine, Yang et al. designed two multifunctional peptide vectors, C_{18}-$C(LLKK)_3$-H_6-R_8 and C_{18}-$C(LLHH)_3C$-R_8. They found that each functional fragment showed a synergistic effect, and the presence of membrane active peptide significantly improved the endosomal escape efficiency and transfection rate, which greatly promotes the application of peptide-based vectors in the treatment of genetic diseases [46]. In the past few years, Bechinger and co-workers have been devoted to developing pH-responsive cationic amphiphilic membrane active peptides rich in histidine residues for gene delivery. They have designed a variety of LAH4-based peptides which have been proven to be able to bind to plasmid DNA and facilitate its cellular uptake and endosomal escape [47,101–103]. Among them, some derivative peptides of LAH4 not only have the ability to bind to plasmid DNA, but also have strong siRNA and mRNA delivery capabilities [47]. To date, the interactions of LAH4-based peptides and bio-membrane have been studied in detail by biophysical methods, and the results indicate that these peptides show strong delivery capacity for a variety of cargoes, including nucleic acids, peptides and proteins [104]. The histidine-rich amphiphilic peptide KH27K has also been developed as a "proton sponge" escape endosomal agent. Unlike LAH4, KH27K is currently mainly used to deliver virus particles into the cell to achieve the intracellular release of the virus, and this "membrane release" activity is consistent with its pH dependent hemolysis activity. However, there is no clear study on the intracellular delivery of nucleic acid molecules [48,49].

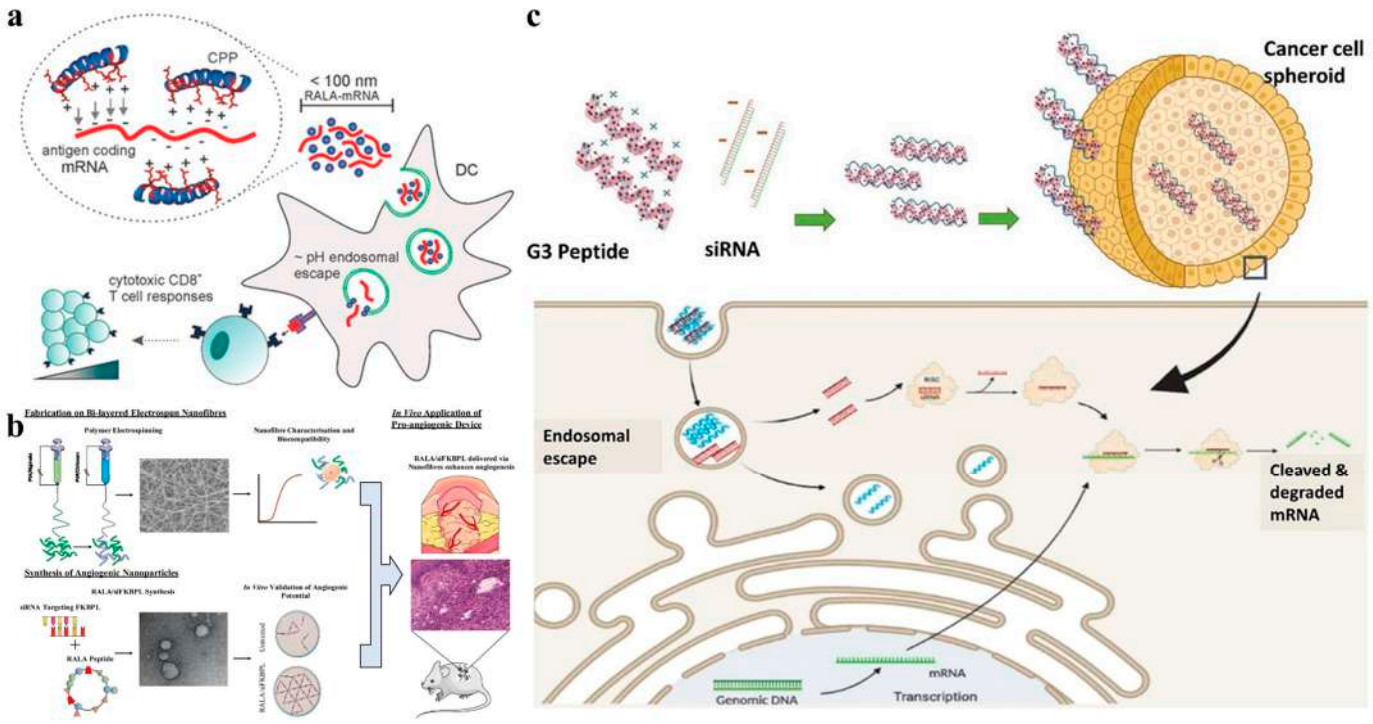

Figure 5. (**a**) RALA peptides condense mRNA into nanoparticles, releasing mRNA in dendritic cell cytosol to promote antigen specific T cell proliferation. Reprinted with permission from Ref. [43]. Copyright 2017, Wiley Online Library. (**b**) RALA peptides form a complex with siRNA to deliver siRNA into the cell and promote the regeneration of blood vessels. Reprinted with permission from Ref. [44]. Copyright 2019, Elsevier. (**c**) G3 peptide was assembled with siRNA and delivered to cancer cells, where siRNA was released to regulate gene expression in cancer cells. Reprinted with permission from Ref. [50]. Copyright 2021, American Chemical Society.

Antibacterial peptides (AMPs) with an α-helical amphiphilic structure can also effectively promote endosomal escape. They are primarily found in bacteria and have activities against a variety of microorganisms. Most of them are composed of nearly 50% hydrophobic residues and are usually positively charged due to the presence of lysine and arginine fragments. The spatially separated hydrophobic and charged regions endow them with membrane interaction activity. In view of the characteristics of AMPs, Cirillo et al. designed a short cationic amphiphilic α-helical peptide $G(IIKK)_3I\text{-}NH_2$ with endosomal escape ability and high affinity towards colon cancer cells [50]. They report that when interacting with negatively charged DPPG small unilamellar vesicles, the peptides fold into α-helical structure helping to carry nucleic acids across the cell membrane and achieving endosomal escape, thus enabling the protection and selective delivery of siRNA to cancer cells (Figure 5c). Melittin is a multifunctional AMP that can inhibit many Gram-negative and Gram-positive bacteria. It is widely used to facilitate the endosomal escape of nanoparticles because of its significant cleavage activity in mammals both in vivo and in vitro. However, this amphiphilic peptide from bee venom has obvious toxicity to mammalian cells. If it is directly used to deliver nucleic acids, the transfection efficiency will be reduced due to the increase of cytotoxicity [105]. Therefore, melittin analogues have been designed in order to reduce the toxicity while promoting the ability to promote endosomal escape [106]. Glutamic acid and histidine residues on peptides are negatively charged due to deprotonation in the extracellular medium; however, in endosomes with a pH of about 5, the two amino acids are protonated, which reduces the hydrophilicity of the peptide and exposes its cleavage activity. Therefore, the method of replacing the basic amino acids in melittin with glutamic acid or histidine can be used to enhance the cleavage ability of the pH sensitive peptide. In views of this principle, a series of novel pH-sensitive peptides have

been developed. Melittin analogues such as CMA-1, CMA-2, CMA-3, CMA-4, NMA-3 [52] and acid-melittin [51] have been obtained and used to conjugate with PEI to improve the intracellular endosomal escape of the PEI/DNA complex. Compared with CMA-1-PEI and CMA-4-PEI that covalently linked PEI to the N-terminal of peptide, C-terminal modified CMA-2-PEI, CMA-3-PEI and acid-melittin-PEI complexes showed strong cleavage activity at pH 5. The transfection experiments also showed that CMA-2-PEI and CMA3-PEI complexes induced significant gene expression [53,54]. Not all N-terminal modified melittin analogues have poor cleavage ability. For example, Kloeckneret al. proved that the transfection efficiency can be significantly improved by introducing N-terminal PEI-coupled melittin analogue NMA-3 into the EGF/OEI-HD-1 complex gene vector [52]. In addition, considering the effect of glutamate replacement location on peptide cleavage activity, Tamemoto et al. designed four melittin analogues and studied the optimal position of glutamate substitution. The results showed that a novel attenuated cationic cleavage peptide MEL-L6A10 with higher delivery activity, relatively lower cytotoxicity and higher endolytic activity can be designed by placing Glu on the boundary of the hydrophobic/hydrophilic region [55]. RV-23 is a pH-sensitive endolytic peptide extracted from Rana Linnaeus. Zhang et al. obtained a pH-sensitive endolytic peptide by replacing the positive charge residues in RV with glutamate. This substituted RV-23 peptide can promote the obvious destruction of cell intima and promote the entry of the carrier/nucleic acid complex into the cytoplasm. Thus, the gene transfection rate was significantly increased and the PEI-mediated cell transfection rate promoted [53].

6. Application of NLS Peptides in Gene Delivery

In gene delivery, some nucleic acid drugs, such as siRNA and mRNA, can directly play a therapeutic role in the cytoplasm after endosomal escape. However, for pDNA, DNA needs to be further transferred into the nucleus to realize its therapeutic effect. In such cases, whether DNA can be assisted to enter the nucleus is a key factor to evaluate the delivery capacity of non-viral gene vectors [56]. Macromolecules such as proteins cannot directly enter the nucleus due to the strong impedance from the nuclear envelope, and their transport into the nucleus must be regulated by the nuclear pore complex (NPC) [107,108]. When the protein enters the nucleus, the NLS (a short cationic peptide sequence) on the proteins can be recognized by the corresponding nuclear transporter, which helps them reach the nucleus through NPC with the assistance of transporter and nucleoporin [109,110]. Based on this, introducing NLS peptide sequences into non-viral vectors may achieve efficient delivery of the therapeutic DNA into the nucleus. Generally, NLS peptides can be divided into two categories, termed monopartite NLS (MP NLS) and bipartite NLS (BP NLS). The MP NLS is a single cluster composed of 4–8 basic amino acids, and the most common MP NLS is the basic heptad-peptide derived from SV40 virus large T antigen. Since this NLS is only related to nuclear transport and has no effect on improving cell uptake, it needs to enter the cytoplasm first to assist gene drugs to enter the nucleus [57]. The MP NLS peptides are often combined with CPPs to fabricate vectors which can promote transmembrane transport, nuclear localization and further realize targeting delivery of pDNA. For example, Yan et al. constructed a new nucleus-targeted NLS (KALA-SA) vector by combining MP NLS, KALA (a cationic CPP) and stearic acid (SA). Besides enhancing cytoplasmic transport, this vector realized targeting localization and provided a promising strategy for the treatment of lung cancer [56]. Moreover, conjugating MP NLS peptide with targeted peptide RGD can also achieve an excellent therapeutic effect. Following this strategy, Ozcelik modified MP NLS peptide and RGD peptide onto AuNPs with radio-sensitizer ability to initiate X-ray radiation-induced cell death and achieve the effect of killing or inhibiting cancer cells while retaining the normal cells. Interestingly, the results indicated that AuNPs with both cancer cell targeting and nuclear targeting capabilities are far more specific and lethal than AuNPs modified by NLS or RGD alone [58]. In order to significantly improve the delivery capacity, Hao et al. integrated NLS with CPPs (TAT) and RGD (REDV) with a selectively targeting function for endothelial cells to obtain the REDV-TAT-NLS triple tandem peptides [59].

By inserting glycine sequences with different repeats into the triple tandem peptides, the functions of each peptide were synergistically performed. The peptide complexes can be used as vector to deliver pZNF580 plasmid in endothelial cells, which can significantly improve the revascularization ability of human umbilical vein endothelial cells in vitro and in vivo, thus providing a promising and effective delivery option for angiogenesis treatment of vascular diseases (Figure 6a). Recent studies revealed that Mice Fibroblast Growth Factor 3 (FGF3) is a peptide containing multiple NLS peptides. RLRR and RRRK are two peptide sequences that can induce nuclear localization in this NLS. Introducing the RRRK peptide fragment into PAMAM non-viral vectors can significantly improve the transfection efficiency and gene expression of the vectors [61]. In addition, using four NLS derived from SV40 virus with glycine residues as spacers, Ritter synthesized the NLS tetramer of SV40 large T antigen. This lysine-rich peptide solves the past problem of NLS interfering with gene expression by covalent binding to nucleic acid molecules: it binds and concentrates nucleic acid molecules by electrostatic interaction to form stable polymers with nuclear transport properties [62]. More importantly, NLS has also been used in clustered regularly interspersed short palindromic repeats (CRISPR)/CRISPR-associated protein 9 (Cas9) gene editing technology which is widely studied nowadays. As a nuclear targeting peptide, NLS can specifically transport the vector into the nucleus, so that the Cas9/sgRNA plasmids can be accurately delivered to the tumor sites. Studies have shown that combination of NLS peptides with other non-viral vectors can significantly improve the gene editing ability of Cas9/sgRNA. For example, using NLS peptide and AS1411 aptamer as delivery vector, Cas9/sgRNA can achieve effective genome editing in targeted tumor cells [60], down-regulate the expression of FAK protein in tumor cells, and thus lead to tumor cell apoptosis (Figure 6b).

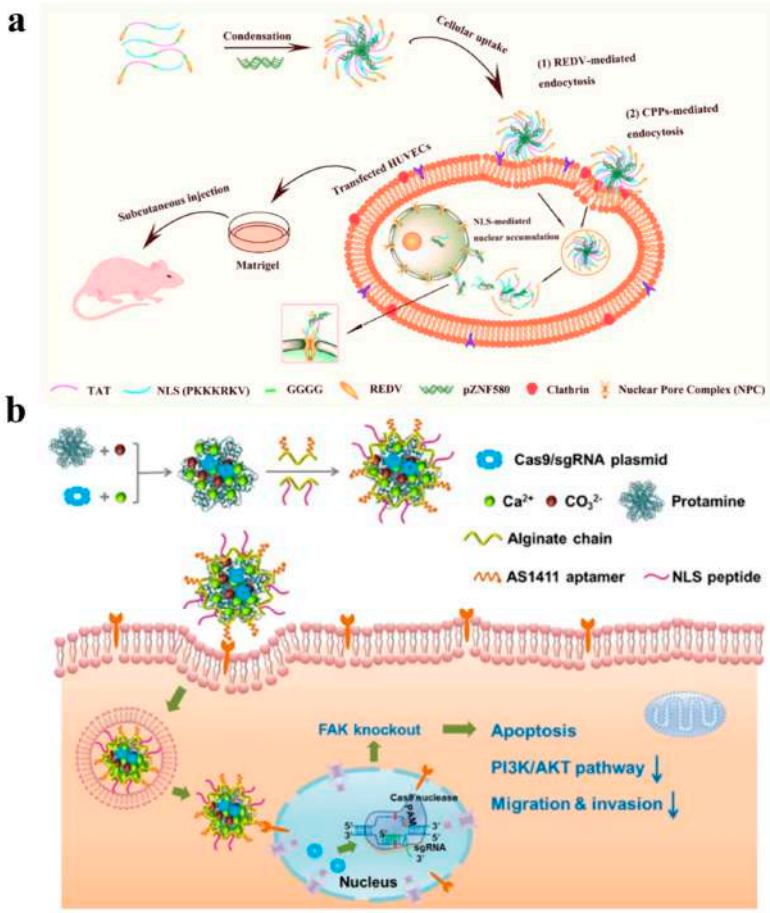

Figure 6. (**a**) The REDV-G4 -TAT-G4-NLS peptide assembles with pZNF580 plasmid to form nanocomplexes, which are transported to endothelial cells by the targeting effect of REDV. After the transmembrane

and endosomal escape, the complexes enter the nucleus by the action of NLS to promote the expression of pZNF580 plasmid and enhance the revascularization ability of cells. Reprinted with permission from Ref. [59]. Copyright 2017, American Chemical Society. (**b**) The Cas9/sgRNA plasmid gene delivery system was prepared by the self-assembly method, which can specifically deliver the plasmid to the nuclei of tumor cells by the targeting of NLS, and knock down the protein tyrosine kinase 2 (PTK2) gene to the down-regulated local adhesion kinase (FAK). Reprinted with permission from Ref. [60]. Copyright 2019, American Chemical Society.

In addition to adding MP NLS to various nonviral vectors to achieve efficient nuclear delivery of therapeutic DNA, BP NLS composed of two or more positively charged amino acid clusters have also been developed and used for gene delivery. Matschke synthesized a modified NLS dimer structure, NLS-Ku7O_2. Highly efficient nuclear transport and transgenic expression were realized by co-assembling this BP NLS-Ku7O_2 with PEI and DNA into a ternary gene carrier complex [63].

7. Application of Other Peptides in Gene Delivery

To date, great success has been achieved in developing nonviral vectors using materials including peptides, proteins, dendrimer and liposomes. Although the gene transduction efficiency has been improved, the gene expression level is still far lower than that of viral vectors and cannot meet the clinical requirements. However, the inherent toxicity, immunogenicity and complex preparation process of viral vectors greatly limit their clinical application [64]. Therefore, great efforts have been devoted to building supramolecular assemblies that can simulate both the viral structure and function. The therapeutic nucleic acids are encapsulated into these supramolecular assemblies and delivered into cells, in the hope of obtaining efficient gene delivery vectors while reducing the inherent risk of viruses [111–113]. Recently, because of the good biocompatibility and low cytotoxicity of peptides, more and more research has been focused on imitating the virus structure through the co-assembly of peptide and nucleic acid [114,115]. Spherical viral capsids have discrete nanospace, good cell transfection ability and biodegradability, and can therefore be used as nanocarriers for nucleic acid drug delivery [116–118]. Inspired by the spherical virus, Matsuura found that the 24-mer β-annulus peptide involved in dodecahedral skeleton formation of tomato bushy stunt virus can spontaneously assemble into a "spherical artificial virus-like capsid" with a size of 30–50 nm. The cationic interior of the artificial viral capsid is hollow, allowing DNA molecules to be effectively encapsulated [65,66]. Based on the above, Matsuura K. used β-cyclic GGGCG peptide as the binding site of AuNPs, which finally self-assembled into nanocapsules with a diameter of 50 nm. This strategy extends the design of artificial viral capsids and can be further used for the delivery of nucleic acid molecules [67]. The short peptide H4K5H$C_{BZl}C_{BZl}$H obtained by rational design is also a spherical viral capsid. Compared with the past research on spherical artificial viruses, this spherical viral capsid has a low aspect ratio because of adding the cysteine in the center of the short peptide H4K5H$C_{BZl}C_{BZl}$H. This nanostructure can not only mimic the sequential decomposition of spherical viruses in response to stimuli, but also simulate the complex morphology and intracellular transformation of spherical viruses, making it an effective DNA delivery vector [68]. In addition to spherical artificial virus particles, filamentous, rod-shaped and cocoon-like virus particles have also been developed as artificial viruses. For example, the short peptide K3C6SPD which contains three fragments including N-terminal cationic fragment, β-sheet forming fragment and C-terminal hydrophilic fragment can be co-assembled to obtain cocoon-like artificial virus particles (Figure 7a) [69,70]. Ruff designed triblock molecules SP-CC-PEG which can self-assemble into mushroom nanostructures [71]. Using self-assembled non-centrosymmetric nanostructures similar to supramolecular mushrooms as caps, virus-like particles with a certain length are created and then wrapped on DNA to generate filamentous particles (Figure 7b). Marchetti designed a triblock peptide C−S10−B containing a segment of

artificial lysine capsid using a de novo design method. Through electrostatic interaction, it interacted with the phosphate of single stranded or double stranded DNA and co-assembled into coronavirus-like particles, mimicking the corresponding function of viral capsid proteins [119]. These theoretical studies provide new ideas for current nucleic acid delivery.

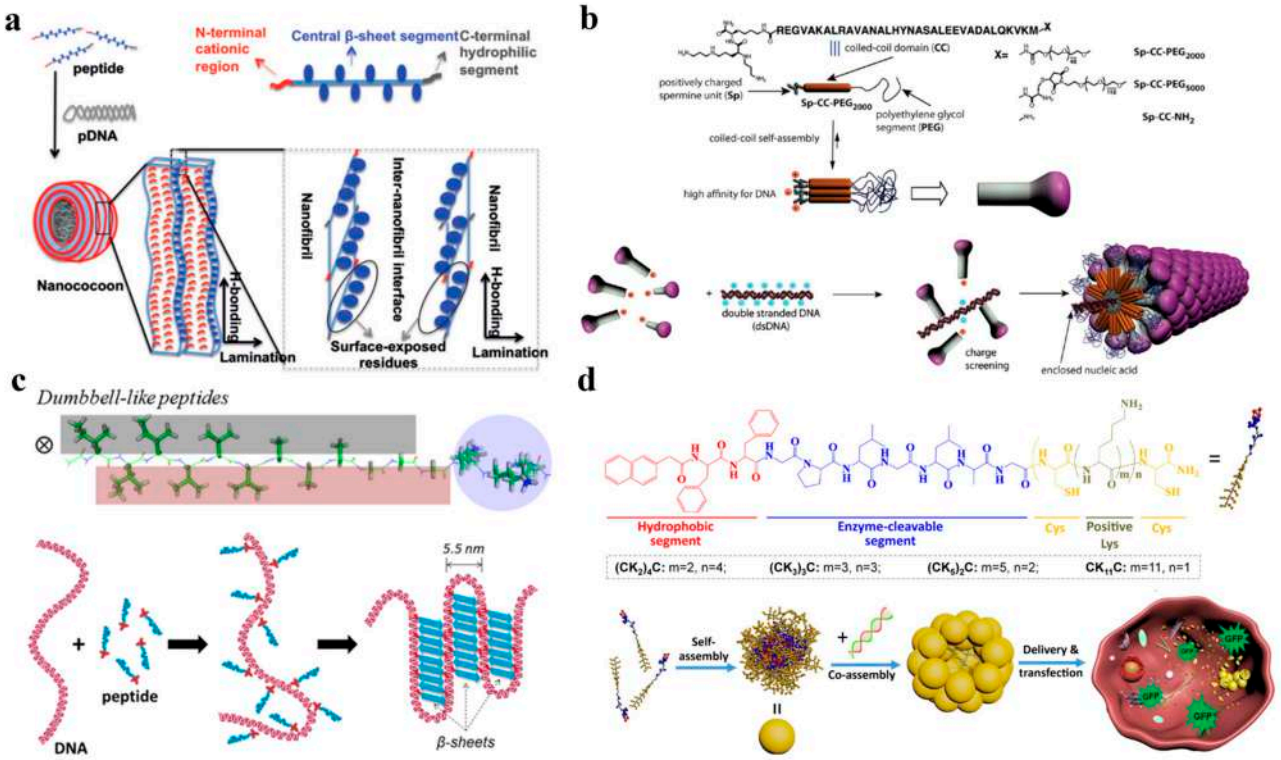

Figure 7. (**a**) Co-assembly of the K3C6SPD short peptide with plasmid DNA develops cocoon-like viral mimics. Reprinted with permission from Ref. [70]. Copyright 2017, German Chemical Society. (**b**) The mushroom shaped nanostructures SP-CC-PEG created by the synergistic self-assembly of three functional fragments, which has high affinity with DNA by electrostatic interaction, is used to prepare synthetic filamentous viruses. Reprinted with permission from Ref. [71]. Copyright 2013, American Chemical Society. (**c**) The dumbbell-like peptide, $I_3V_3A_3G_3K_3$, binds onto the DNA chain through electrostatic interactions, and then self-associates into β-sheets under hydrophobic interactions and hydrogen bonding, the resulting final formed structure being able to imitate the essence of viral capsid to condense and wrap DNA. Reprinted with permission from Ref. [72]. Copyright 2018, American Chemical Society. (**d**) NapFFGPLGLAG$(CK_m)_nC$ peptides, containing the multifunctional segment, self-assemble into stable nanospheres which can encapsulate DNA by interacting with DNA in the interior, and finally realize intracellular delivery and release of genome. Reprinted with permission from Ref. [64]. Copyright 2022, Elsevier.

The efficient delivery of nucleic acids has been achieved by constructing new nonviral delivery systems using single or several lysines as functional fragments. Furthermore, many studies have shown that cationic poly(L-lysine) (PLL) can also be used to achieve efficient nucleic acid transport in vivo. PLL can mediate condensation of anionic nucleic acids to form smaller nanoparticles and protect them from enzymatic and physical degradation [120]. Yugyeong Kim et al. synthesized a new cationic AB2 miktoarm block copolymer consisting of two cationic PLL blocks and one PEG block, which can form effective nanocomplexes with pDNA. The nanocomplexes can release pDNA effectively under reducing conditions and show high level of gene expression [121]. However, for PLL, its in vitro transfection efficiency is poor in the absence of any covalently attached functional moieties to promote gene targeting or uptake [120]. To solve this problem, researchers have

discovered a new cationic poly-amino acid, that is, poly(L-ornithine) (PLO). Compared to PLL that contains a tetramethylene spacer, PLO possesses a trimethylene unit in the side chain. It can complex with pDNA or mRNA and enhance transfection efficiency [122]. One big issue of nonviral gene delivery is unnecessary uptake by the reticuloendothelial system, mainly the liver. In general, 60–70% of nucleic acid molecules are taken up by scavenger receptors on liver Kupffer cells when being injected into the body without the protection of carrier molecules. This nonspecific scavenging behavior results in a significant reduction in the efficiency of drug entry into target tissues [123]. Lysine polymer exhibits excellent potential in solving this problem by avoiding unwanted uptake by the reticuloendothelial system. Recently, Anjaneyulu Dirisala et al. found that oligo(L-lysine) conjugated linear or two-armed PEG can transiently and selectively mask liver scavenger cells, effectively inhibiting sinusoidal clearance of nonviral gene carriers, thereby increasing their gene transduction efficiency in target tissues [124].

The formation of artificial viruses is based on the non-covalent interaction of peptide/peptide or peptide/DNA. By rational design of the peptide structure, the morphology, stability and transfection efficiency of the peptide/DNA hybrid structure can be regulated to construct artificial viruses [125]. In recent years, our group has been focusing on the design and study of different surfactant-like peptides to induce effective DNA condensation and so produce artificial viruses for protecting DNA from enzymatic degradation. For example, we designed six surfactant-like peptides with the same amino acid composition but different primary sequences. Because the peptide residues have different side chain size and hydrophobicity, this can lead to different self-assembled structures [126]. Among them, $I_3V_3A_3G_3K_3$ is a dumbbell-like peptide which can effectively induce DNA condensation into a virus-like structure through non-covalent interactions such as electrostatic interaction, hydrophobic interaction and hydrogen bonding [72]. The final formed structure can imitate the essence of a viral capsid to condense and wrap DNA, which is conducive to effective gene delivery in the later stage (Figure 7c). AKAEAKAE, another peptide segment we designed, has strong β-sheet forming capability and can co-assemble with PNA to obtain peptide nucleic acid-peptide conjugate, $T'_3(AKAE)_2$. It can condense DNA at low micromole concentrations, which suggests it can be a gene delivery vector [112,127]. NapFFGPLGLAG$(CK_m)_nC$ peptides have been developed by introducing several functional segments, that is, an aromatic segment of Nap-FF to promote peptide assembly by providing hydrophobic interaction, an enzyme-cleavable segment of GPLGLA to target cancer cells, and several positively charged K residues for DNA binding. These peptides can self-assemble into homogenous capsid-like nanospheres with high stability under the synergy of functional segments [64]. Moreover, they can further co-assemble with DNA to protect the genome from enzymatic digestion and greatly improve the efficiency of gene delivery (Figure 7d).

8. Concluding Remarks and Future Perspectives

Developing versatile vectors to deliver therapeutic nucleic acids into target cells/tissues is critical for gene therapy. As promising candidates, peptide-based vectors have been widely used for delivering therapeutic nucleic acids. In addition to condensing nucleic acids to form nanoparticles for protecting them from being degraded by enzymes, the rationally designed functional peptides can also help to overcome a series of biological barriers including crossing cell membrane, escaping from endosome, entering the nucleus, etc., and finally release the therapeutic nucleic acids at the target sites. These functional peptides can not only be used alone to overcome such biological barriers in gene delivery, but also can be combined to form multifunctional peptide vectors. Moreover, they can also be introduced into other nonviral gene delivery systems as functional elements to enhance the delivery capacity, which greatly expands the application of peptides in gene therapy. However, it is worth noting that although there have been a large number of reports on peptide-based gene delivery systems, most of them are still in the stage of theoretical research and animal experiments, and there are still many challenges before peptide vectors

being considered for clinical use. First, the peptide-based vectors often suffer from short circulating half-time and poor chemical/physical stability, which greatly hinder the use of peptide–nucleic acid complexes in clinical trials. Effective strategies such as modifying the peptides with unnatural amino acids should be developed to improve the structural stability of the peptide-based gene delivery systems. Secondly, although peptide sequences with different functions can be combined to overcome various barriers for efficient gene delivery, this approach carries the risk of reducing individual functions. Therefore, the combination of peptide with other components without affecting the function of each part is still a problem to be solved. Thirdly, how to precisely control the microstructures of the peptide–nucleic acids complexes so as to achieve effective cellular uptake and gene transfection at targeted sites is another important issue. Modifying the peptidic vectors with stimulus-responsive fragments to design smart delivery systems so that they can perceive changes in the disease microenvironment and trigger gene release may be an effective way to solve this problem. In summary, although there has been much study and great success in the field of peptide-based gene vectors, researchers still need to move forward to find solutions for promoting peptidic gene delivery systems for them to become a gene therapy product that can be approved for clinical applications. Such research would not only promote the rapid development of peptide-based gene delivery systems, but also enable some emerging gene therapy strategies, such as CRISPR/CAS9 technology and mRNA vaccines to be applied in the human body at an early date.

Author Contributions: Conceptualization, M.C.; software, Y.Y., Z.L. and H.M.; resources, M.C.; writing—original draft preparation, Y.Y., Z.L. and H.M.; writing—review and editing, H.M. and M.C.; supervision, M.C.; project administration, M.C.; funding acquisition, M.C. All authors have read and agreed to the published version of the manuscript.

Funding: This work was supported by the National Natural Science Foundation of China (22172194, 21872173, 21972167).

Conflicts of Interest: The authors declare no conflict of interest.

Appendix A

Table A1. Full names and corresponding one-letter codes of the amino acids.

Full Amino Acid Names	One-Letter Codes
Alanine	A
Arginine	R
Asparagine	N
Aspartic acid	D
Cysteine	C
Glutamine	Q
Glutamic acid	E
Glycine	G
Histidine	H
Isoleucine	I
Leucine	L
Lysine	K
Methionine	M
Phenylalanine	F
Proline	P
Serine	S
Threonine	T
Tryptophan	W
Tyrosine	Y
Valine	V

References

1. Luo, M.; Lee, L.K.C.; Peng, B.; Choi, C.H.J.; Tong, W.Y.; Voelcker, N.H. Delivering the Promise of Gene Therapy with Nanomedicines in Treating Central Nervous System Diseases. *Adv. Sci.* **2022**, *9*, 2201740. [CrossRef] [PubMed]
2. Zhu, Y.; Shen, R.; Vuong, I.; Reynolds, R.A.; Shears, M.J.; Yao, Z.-C.; Hu, Y.; Cho, W.J.; Kong, J.; Reddy, S.K.; et al. Multistep screening of DNA/lipid nanoparticles and co-delivery with siRNA to enhance and prolong gene expression. *Nat. Commun.* **2022**, *13*, 4282. [CrossRef] [PubMed]
3. Kuriyama, N.; Yoshioka, Y.; Kikuchi, S.; Okamura, A.; Azuma, N.; Ochiya, T. Challenges for the Development of Extracellular Vesicle-Based Nucleic Acid Medicines. *Cancers* **2021**, *13*, 6137. [CrossRef] [PubMed]
4. Isgrig, K.; McDougald, D.S.; Zhu, J.; Wang, H.J.; Bennett, J.; Chien, W.W. AAV2.7m8 is a powerful viral vector for inner ear gene therapy. *Nat. Commun.* **2019**, *10*, 427. [CrossRef] [PubMed]
5. Shirley, J.L.; de Jong, Y.P.; Terhorst, C.; Herzog, R.W. Immune Responses to Viral Gene Therapy Vectors. *Mol. Ther.* **2020**, *28*, 709–722. [CrossRef] [PubMed]
6. Bouard, D.; Alazard-Dany, D.; Cosset, F.L. Viral vectors: From virology to transgene expression. *Br. J. Pharmacol.* **2009**, *157*, 153–165. [CrossRef] [PubMed]
7. Kang, Z.; Meng, Q.; Liu, K. Peptide-based gene delivery vectors. *J. Mater. Chem. B* **2019**, *7*, 1824–1841. [CrossRef]
8. Munagala, R.; Aqil, F.; Jeyabalan, J.; Kandimalla, R.; Wallen, M.; Tyagi, N.; Wilcher, S.; Yan, J.; Schultz, D.J.; Spencer, W.; et al. Exosome-mediated delivery of RNA and DNA for gene therapy. *Cancer Lett.* **2021**, *505*, 58–72. [CrossRef]
9. Gao, Y.; Men, K.; Pan, C.; Li, J.; Wu, J.; Chen, X.; Lei, S.; Gao, X.; Duan, X. Functionalized DMP-039 Hybrid Nanoparticle as a Novel mRNA Vector for Efficient Cancer Suicide Gene Therapy. *Int. J. Nanomed.* **2021**, *16*, 5211–5232. [CrossRef]
10. Sun, W.; Liu, X.Y.; Ma, L.L.; Lu, Z.L. Tumor Targeting Gene Vector for Visual Tracking of Bcl-2 siRNA Transfection and Anti-Tumor Therapy. *ACS Appl. Mater. Interfaces* **2020**, *12*, 10193–10201. [CrossRef]
11. Peng, X.; Ma, X.; Lu, S.; Li, Z. A Versatile Plant Rhabdovirus-Based Vector for Gene Silencing, miRNA Expression and Depletion, and Antibody Production. *Front. Plant Sci.* **2020**, *11*, 627880. [CrossRef] [PubMed]
12. Dirisala, A.; Uchida, S.; Tockary, T.A.; Yoshinaga, N.; Li, J.; Osawa, S.; Gorantla, L.; Fukushima, S.; Osada, K.; Kataoka, K. Precise tuning of disulphide crosslinking in mRNA polyplex micelles for optimising extracellular and intracellular nuclease tolerability. *J. Drug Target.* **2019**, *27*, 670–680. [CrossRef]
13. Devoldere, J.; Dewitte, H.; De Smedt, S.C.; Remaut, K. Evading innate immunity in nonviral mRNA delivery: Don't shoot the messenger. *Drug Discov. Today* **2016**, *21*, 11–25. [CrossRef] [PubMed]
14. Shaikh, S.; Nazam, N.; Rizvi, S.M.D.; Ahmad, K.; Baig, M.H.; Lee, E.J.; Choi, I. Mechanistic Insights into the Antimicrobial Actions of Metallic Nanoparticles and Their Implications for Multidrug Resistance. *Int. J. Mol. Sci.* **2019**, *20*, 2468. [CrossRef] [PubMed]
15. Vickers, T.A.; Crooke, S.T. siRNAs targeted to certain polyadenylation sites promote specific, RISC-independent degradation of messenger RNAs. *Nucleic Acids Res.* **2012**, *40*, 6223–6234. [CrossRef]
16. Wang, D.; Fan, Z.; Zhang, X.; Li, H.; Sun, Y.; Cao, M.; Wei, G.; Wang, J. pH-Responsive Self-Assemblies from the Designed Folic Acid-Modified Peptide Drug for Dual-Targeting Delivery. *Langmuir* **2021**, *37*, 339–347. [CrossRef]
17. Wang, H.; Feng, Z.; Xu, B. Supramolecular Assemblies of Peptides or Nucleopeptides for Gene Delivery. *Theranostics* **2019**, *9*, 3213–3222. [CrossRef]
18. Balbino, T.A.; Serafin, J.M.; Malfatti-Gasperini, A.A.; de Oliveira, C.L.; Cavalcanti, L.P.; de Jesus, M.B.; de La Torre, L.G. Microfluidic Assembly of pDNA/Cationic Liposome Lipoplexes with High pDNA Loading for Gene Delivery. *Langmuir* **2016**, *32*, 1799–1807. [CrossRef]
19. Wang, D.; Sun, Y.; Cao, M.; Wang, J.; Hao, J. Amphiphilic short peptide modulated wormlike micelle formation with pH and metal ion dual-responsive properties. *RSC Adv.* **2015**, *5*, 95604–95612. [CrossRef]
20. Vermeulen, L.M.P.; Brans, T.; De Smedt, S.C.; Remaut, K.; Braeckmans, K. Methodologies to investigate intracellular barriers for nucleic acid delivery in nonviral gene therapy. *Nano Today* **2018**, *21*, 74–90. [CrossRef]
21. Hadianamrei, R.; Zhao, X. Current state of the art in peptide-based gene delivery. *J. Control. Release* **2022**, *343*, 600–619. [CrossRef] [PubMed]
22. McErlean, E.M.; Ziminska, M.; McCrudden, C.M.; McBride, J.W.; Loughran, S.P.; Cole, G.; Mulholland, E.J.; Kett, V.; Buckley, N.E.; Robson, T.; et al. Rational design and characterisation of a linear cell penetrating peptide for nonviral gene delivery. *J. Control. Release* **2021**, *330*, 1288–1299. [CrossRef] [PubMed]
23. Dougherty, P.G.; Wen, J.; Pan, X.; Koley, A.; Ren, J.G.; Sahni, A.; Basu, R.; Salim, H.; Kubi, G.A.; Qian, Z.; et al. Enhancing the Cell Permeability of Stapled Peptides with a Cyclic Cell-Penetrating Peptide. *J. Med. Chem.* **2019**, *62*, 10098–10107. [CrossRef] [PubMed]
24. Nam, S.H.; Jang, J.; Cheon, D.H.; Chong, S.-E.; Ahn, J.H.; Hyun, S.; Yu, J.; Lee, Y. pH-Activatable cell penetrating peptide dimers for potent delivery of anticancer drug to triple-negative breast cancer. *J. Control. Release* **2021**, *330*, 898–906. [CrossRef]
25. Tuttolomondo, M.; Casella, C.; Hansen, P.L.; Polo, E.; Herda, L.M.; Dawson, K.A.; Ditzel, H.J.; Mollenhauer, J. Human DMBT1-Derived Cell-Penetrating Peptides for Intracellular siRNA Delivery. *Mol. Ther. Nucleic Acids* **2017**, *8*, 264–276. [CrossRef] [PubMed]
26. Jiang, Q.-Y.; Lai, L.-H.; Shen, J.; Wang, Q.-Q.; Xu, F.-J.; Tang, G.-P. Gene delivery to tumor cells by cationic polymeric nanovectors coupled to folic acid and the cell-penetrating peptide octaarginine. *Biomaterials* **2011**, *32*, 7253–7262. [CrossRef] [PubMed]

27. Khalil, I.A.; Kimura, S.; Sato, Y.; Harashima, H. Synergism between a cell penetrating peptide and a pH-sensitive cationic lipid in efficient gene delivery based on double-coated nanoparticles. *J. Control. Release* **2018**, *275*, 107–116. [CrossRef]
28. Huang, Y.; Cheng, Q.; Jin, X.; Ji, J.L.; Guo, S.; Zheng, S.; Wang, X.; Cao, H.; Gao, S.; Liang, X.J.; et al. Systemic and tumor-targeted delivery of siRNA by cyclic NGR and isoDGR motif-containing peptides. *Biomater. Sci.* **2016**, *4*, 494–510. [CrossRef]
29. Yang, S.; Ou, C.; Wang, L.; Liu, X.; Yang, J.; Wang, X.; Wang, M.; Shen, M.; Wu, Q.; Gong, C. Virus-esque nucleus-targeting nanoparticles deliver trojan plasmid for release of anti-tumor shuttle protein. *J. Control. Release* **2020**, *320*, 253–264. [CrossRef]
30. Zhao, Y.; He, Z.; Gao, H.; Tang, H.; He, J.; Guo, Q.; Zhang, W.; Liu, J. Fine Tuning of Core-Shell Structure of Hyaluronic Acid/Cell-Penetrating Peptides/siRNA Nanoparticles for Enhanced Gene Delivery to Macrophages in Antiatherosclerotic Therapy. *Biomacromolecules* **2018**, *19*, 2944–2956. [CrossRef]
31. Covarrubias-Zambrano, O.; Shrestha, T.B.; Pyle, M.; Montes-Gonzalez, M.; Troyer, D.L.; Bossmann, S.H. Development of a Gene Delivery System Composed of a Cell-Penetrating Peptide and a Nontoxic Polymer. *ACS Appl. Bio Mater.* **2020**, *3*, 7418–7427. [CrossRef] [PubMed]
32. Dowaidar, M.; Abdelhamid, H.N.; Hallbrink, M.; Freimann, K.; Kurrikoff, K.; Zou, X.; Langel, U. Magnetic Nanoparticle Assisted Self-assembly of Cell Penetrating Peptides-Oligonucleotides Complexes for Gene Delivery. *Sci. Rep.* **2017**, *7*, 9159. [CrossRef] [PubMed]
33. Yang, Y.; Yang, Y.; Xie, X.; Wang, Z.; Gong, W.; Zhang, H.; Li, Y.; Yu, F.; Li, Z.; Mei, X. Dual-modified liposomes with a two-photon-sensitive cell penetrating peptide and NGR ligand for siRNA targeting delivery. *Biomaterials* **2015**, *48*, 84–96. [CrossRef] [PubMed]
34. Chen, Y.; Wu, J.J.; Huang, L. Nanoparticles targeted with NGR motif deliver c-myc siRNA and doxorubicin for anticancer therapy. *Mol. Ther.* **2010**, *18*, 828–834. [CrossRef] [PubMed]
35. Kim, Y.M.; Park, S.C.; Jang, M.K. Targeted gene delivery of polyethyleneimine-grafted chitosan with RGD dendrimer peptide in αvβ3 integrin-overexpressing tumor cells. *Carbohydr. Polym.* **2017**, *174*, 1059–1068. [CrossRef]
36. Luo, Q.; Song, H.; Deng, X.; Li, J.; Jian, W.; Zhao, J.; Zheng, X.; Basnet, S.; Ge, H.; Daniel, T.; et al. A Triple-Regulated Oncolytic Adenovirus Carrying MicroRNA-143 Exhibits Potent Antitumor Efficacy in Colorectal Cancer. *Mol. Ther. Oncolytics* **2020**, *16*, 219–229. [CrossRef]
37. Wang, Y.; Nie, Y.; Ding, Z.; Yao, M.; Du, R.; Zhang, L.; Wang, S.; Li, D.; Wang, Y.; Cao, M. An amphiphilic peptide with cell penetrating sequence for highly efficient gene transfection. *Colloids Surf. A Physicochem. Eng. Asp.* **2020**, *590*, 124529. [CrossRef]
38. Alam, M.R.; Ming, X.; Fisher, M.; Lackey, J.G.; Rajeev, K.G.; Manoharan, M.; Juliano, R.L. Multivalent Cyclic RGD Conjugates for Targeted Delivery of Small Interfering RNA. *Bioconjugate Chem.* **2011**, *22*, 1673–1681. [CrossRef]
39. Liu, X.; Wang, W.; Samarsky, D.; Liu, L.; Xu, Q.; Zhang, W.; Zhu, G.; Wu, P.; Zuo, X.; Deng, H.; et al. Tumor-targeted in vivo gene silencing via systemic delivery of cRGD-conjugated siRNA. *Nucleic Acids Res.* **2014**, *42*, 11805–11817. [CrossRef]
40. Khatri, N.; Baradia, D.; Vhora, I.; Rathi, M.; Misra, A. cRGD grafted liposomes containing inorganic nano-precipitate complexed siRNA for intracellular delivery in cancer cells. *J. Control. Release* **2014**, *182*, 45–57. [CrossRef]
41. Xu, X.; Liu, Y.; Yang, Y.; Wu, J.; Cao, M.; Sun, L. One-pot synthesis of functional peptide-modified gold nanoparticles for gene delivery. *Colloids Surf. A Physicochem. Eng. Asp.* **2022**, *640*, 128491. [CrossRef]
42. Jena, L.N.; Bennie, L.A.; McErlean, E.M.; Pentlavalli, S.; Glass, K.; Burrows, J.F.; Kett, V.L.; Buckley, N.E.; Coulter, J.A.; Dunne, N.J.; et al. Exploiting the anticancer effects of a nitrogen bisphosphonate nanomedicine for glioblastoma multiforme. *J. Nanobiotechnology* **2021**, *19*, 127. [CrossRef] [PubMed]
43. Udhayakumar, V.K.; De Beuckelaer, A.; McCaffrey, J.; McCrudden, C.M.; Kirschman, J.L.; Vanover, D.; Van Hoecke, L.; Roose, K.; Deswarte, K.; De Geest, B.G.; et al. Arginine-Rich Peptide-Based mRNA Nanocomplexes Efficiently Instigate Cytotoxic T Cell Immunity Dependent on the Amphipathic Organization of the Peptide. *Adv. Healthc Mater.* **2017**, *6*, 1601412. [CrossRef]
44. Mulholland, E.J.; Ali, A.; Robson, T.; Dunne, N.J.; McCarthy, H.O. Delivery of RALA/siFKBPL nanoparticles via electrospun bilayer nanofibres: An innovative angiogenic therapy for wound repair. *J. Control. Release* **2019**, *316*, 53–65. [CrossRef]
45. Liu, Y.; Wan, H.-H.; Tian, D.-M.; Xu, X.-J.; Bi, C.-L.; Zhan, X.-Y.; Huang, B.-H.; Xu, Y.-S.; Yan, L.-P. Development and Characterization of High Efficacy Cell-Penetrating Peptide via Modulation of the Histidine and Arginine Ratio for Gene Therapy. *Materials* **2021**, *14*, 4674. [CrossRef]
46. Yang, S.; Meng, Z.; Kang, Z.; Sun, C.; Wang, T.; Feng, S.; Meng, Q.; Liu, K. The structure and configuration changes of multifunctional peptide vectors enhance gene delivery efficiency. *RSC Adv.* **2018**, *8*, 28356–28366. [CrossRef] [PubMed]
47. Ali, S.; Dussouillez, C.; Padilla, B.; Frisch, B.; Mason, A.J.; Kichler, A. Design of a new cell penetrating peptide for DNA, siRNA and mRNA delivery. *J. Gene Med.* **2022**, *24*, e3401. [CrossRef]
48. Vanova, J.; Hejtmankova, A.; Zackova Suchanova, J.; Sauerova, P.; Forstova, J.; Hubalek Kalbacova, M.; Spanielova, H. Influence of cell-penetrating peptides on the activity and stability of virus-based nanoparticles. *Int. J. Pharm.* **2020**, *576*, 119008. [CrossRef]
49. Ferrer-Miralles, N.; Corchero, J.L.; Kumar, P.; Cedano, J.A.; Gupta, K.C.; Villaverde, A.; Vazquez, E. Biological activities of histidine-rich peptides; merging biotechnology and nanomedicine. *Microb. Cell Factories* **2011**, *10*, 101. [CrossRef]
50. Cirillo, S.; Tomeh, M.A.; Wilkinson, R.N.; Hill, C.; Brown, S.; Zhao, X. Designed Antitumor Peptide f or Targeted siRNA Delivery into Cancer Spheroids. *ACS Appl. Mater. Interfaces* **2021**, *13*, 49713–49728. [CrossRef]
51. Blenke, E.O.; Sleszynska, M.; Evers, M.J.; Storm, G.; Martin, N.I.; Mastrobattista, E. Strategies for the Activation and Release of the Membranolytic Peptide Melittin from Liposomes Using Endosomal pH as a Trigger. *Bioconjugate Chem.* **2017**, *28*, 574–582. [CrossRef] [PubMed]

52. Kloeckner, J.; Boeckle, S.; Persson, D.; Roedl, W.; Ogris, M.; Berg, K.; Wagner, E. DNA polyplexes based on degradable oligoethylenimine-derivatives: Combination with EGF receptor targeting and endosomal release functions. *J. Control. Release* **2006**, *116*, 115–122. [CrossRef]
53. Zhang, S.K.; Song, J.W.; Li, S.B.; Gao, H.W.; Chang, H.Y.; Jia, L.L.; Gong, F.; Tan, Y.X.; Ji, S.P. Design of pH-sensitive peptides from natural antimicrobial peptides for enhancing polyethylenimine-mediated gene transfection. *J. Gene Med.* **2017**, *19*, e2955. [CrossRef] [PubMed]
54. Boeckle, S.; Fahrmeir, J.; Roedl, W.; Ogris, M.; Wagner, E. Melittin analogs with high lytic activity at endosomal pH enhance transfection with purified targeted PEI polyplexes. *J. Control. Release* **2006**, *112*, 240–248. [CrossRef] [PubMed]
55. Tamemoto, N.; Akishiba, M.; Sakamoto, K.; Kawano, K.; Noguchi, H.; Futaki, S. Rational Design Principles of Attenuated Cationic Lytic Peptides for Intracellular Delivery of Biomacromolecules. *Mol. Pharm.* **2020**, *17*, 2175–2185. [CrossRef]
56. Yan, C.; Shi, W.; Gu, J.; Lee, R.J.; Zhang, Y. Design of a Novel Nucleus-Targeted NLS-KALA-SA Nanocarrier to Delivery Poorly Water-Soluble Anti-Tumor Drug for Lung Cancer Treatment. *J. Pharm. Sci.* **2021**, *110*, 2432–2441. [CrossRef]
57. Li, Q.; Hao, X.; Wang, H.; Guo, J.; Ren, X.K.; Xia, S.; Zhang, W.; Feng, Y. Multifunctional REDV-G-TAT-G-NLS-Cys peptide sequence conjugated gene carriers to enhance gene transfection efficiency in endothelial cells. *Colloids Surf. B Biointerfaces* **2019**, *184*, 110510. [CrossRef]
58. Ozcelik, S.; Pratx, G. Nuclear-targeted gold nanoparticles enhance cancer cell radiosensitization. *Nanotechnology* **2020**, *31*, 415102. [CrossRef]
59. Hao, X.; Li, Q.; Guo, J.; Ren, X.; Feng, Y.; Shi, C.; Zhang, W. Multifunctional Gene Carriers with Enhanced Specific Penetration and Nucleus Accumulation to Promote Neovascularization of HUVECs in Vivo. *ACS Appl. Mater. Interfaces* **2017**, *9*, 35613–35627. [CrossRef]
60. Liu, B.Y.; He, X.Y.; Xu, C.; Ren, X.H.; Zhuo, R.X.; Cheng, S.X. Peptide and Aptamer Decorated Delivery System for Targeting Delivery of Cas9/sgRNA Plasmid To Mediate Antitumor Genome Editing. *ACS Appl. Mater. Interfaces* **2019**, *11*, 23870–23879. [CrossRef]
61. Lee, J.; Jung, J.; Kim, Y.J.; Lee, E.; Choi, J.S. Gene delivery of PAMAM dendrimer conjugated with the nuclear localization signal peptide originated from fibroblast growth factor 3. *Int. J. Pharm.* **2014**, *459*, 10–18. [CrossRef] [PubMed]
62. Ritter, W.; Plank, C.; Lausier, J.; Rudolph, C.; Zink, D.; Reinhardt, D.; Rosenecker, J. A novel transfecting peptide comprising a tetrameric nuclear localization sequence. *J. Mol. Med. (Berl.)* **2003**, *81*, 708–717. [CrossRef] [PubMed]
63. Matschke, J.; Bohla, A.; Maucksch, C.; Mittal, R.; Rudolph, C.; Rosenecker, J. Characterization of Ku70(2)-NLS as bipartite nuclear localization sequence for nonviral gene delivery. *PLoS ONE* **2012**, *7*, e24615. [CrossRef] [PubMed]
64. Cao, M.; Zhang, Z.; Zhang, X.; Wang, Y.; Wu, J.; Liu, Z.; Sun, L.; Wang, D.; Yue, T.; Han, Y.; et al. Peptide Self-assembly into stable Capsid-Like nanospheres and Co-assembly with DNA to produce smart artificial viruses. *J. Colloid Interface Sci.* **2022**, *615*, 395–407. [CrossRef] [PubMed]
65. Matsuura, K.; Watanabe, K.; Matsuzaki, T.; Sakurai, K.; Kimizuka, N. Self-assembled synthetic viral capsids from a 24-mer viral peptide fragment. *Angew Chem. Int. Ed. Engl.* **2010**, *49*, 9662–9665. [CrossRef] [PubMed]
66. Fujita, S.; Matsuura, K. Encapsulation of CdTe Quantum Dots into Synthetic Viral Capsids. *Chem. Lett.* **2016**, *45*, 922–924. [CrossRef]
67. Matsuura, K.; Ueno, G.; Fujita, S. Self-assembled artificial viral capsid decorated with gold nanoparticles. *Polym. J.* **2014**, *47*, 146–151. [CrossRef]
68. Ni, R.; Chau, Y. Nanoassembly of Oligopeptides and DNA Mimics the Sequential Disassembly of a Spherical Virus. *Angew. Chem. -Int. Ed.* **2020**, *59*, 3578–3584. [CrossRef]
69. Ni, R.; Liu, J.; Chau, Y. Ultrasound-facilitated assembly and disassembly of a pH-sensitive self-assembly peptide. *RSC Adv.* **2018**, *8*, 29482–29487. [CrossRef]
70. Ni, R.; Chau, Y. Tuning the Inter-nanofibril Interaction To Regulate the Morphology and Function of Peptide/DNA Co-assembled Viral Mimics. *Angew. Chem. Int. Ed. Engl.* **2017**, *56*, 9356–9360. [CrossRef]
71. Ruff, Y.; Moyer, T.; Newcomb, C.J.; Demeler, B.; Stupp, S.I. Precision templating with DNA of a virus-like particle with peptide nanostructures. *J. Am. Chem. Soc.* **2013**, *135*, 6211–6219. [CrossRef] [PubMed]
72. Cao, M.; Wang, Y.; Zhao, W.; Qi, R.; Han, Y.; Wu, R.; Wang, Y.; Xu, H. Peptide-Induced DNA Condensation into Virus-Mimicking Nanostructures. *ACS Appl. Mater. Interfaces* **2018**, *10*, 24349–24360. [CrossRef] [PubMed]
73. Järver, P.; Coursindel, T.; Andaloussi, S.E.; Godfrey, C.; Wood, M.J.; Gait, M.J. Peptide-mediated Cell and In Vivo Delivery of Antisense Oligonucleotides and siRNA. *Mol. Ther. -Nucleic Acids* **2012**, *1*, e27. [CrossRef] [PubMed]
74. Vázquez, O.; Seitz, O. Cytotoxic peptide–PNA conjugates obtained by RNA-programmed peptidyl transfer with turnover. *Chem. Sci.* **2014**, *5*, 2850–2854. [CrossRef]
75. Shabanpoor, F.; Gait, M.J. Development of a general methodology for labelling peptide-morpholino oligonucleotide conjugates using alkyne-azide click chemistry. *Chem. Commun.* **2013**, *49*, 10260–10262. [CrossRef] [PubMed]
76. López-Vidal, E.M.; Schissel, C.K.; Mohapatra, S.; Bellovoda, K.; Wu, C.-L.; Wood, J.A.; Malmberg, A.B.; Loas, A.; Gómez-Bombarelli, R.; Pentelute, B.L. Deep Learning Enables Discovery of a Short Nuclear Targeting Peptide for Efficient Delivery of Antisense Oligomers. *JACS Au* **2021**, *1*, 2009–2020. [CrossRef]
77. Eilers, W.; Gadd, A.; Foster, H.; Foster, K. Dmd Treatment: Animal Models. *Neuromuscul. Disord.* **2018**, *28*, S92–S93. [CrossRef]

78. Urello, M.; Hsu, W.-H.; Christie, R.J. Peptides as a Material Platform for Gene Delivery: Emerging Concepts and Converging Technologies. *Acta Biomater.* **2020**, *117*, 40–59. [CrossRef]
79. Samec, T.; Boulos, J.; Gilmore, S.; Hazelton, A.; Alexander-Bryant, A. Peptide-based delivery of therapeutics in cancer treatment. *Mater. Today Bio* **2022**, *14*, 100248. [CrossRef]
80. Khan, M.M.; Filipczak, N.; Torchilin, V.P. Cell penetrating peptides: A versatile vector for co-delivery of drug and genes in cancer. *J. Control. Release* **2021**, *330*, 1220–1228. [CrossRef]
81. Liu, Y.; An, S.; Li, J.; Kuang, Y.; He, X.; Guo, Y.; Ma, H.; Zhang, Y.; Ji, B.; Jiang, C. Brain-targeted co-delivery of therapeutic gene and peptide by multifunctional nanoparticles in Alzheimer's disease mice. *Biomaterials* **2016**, *80*, 33–45. [CrossRef] [PubMed]
82. Lehto, T.; Simonson, O.E.; Mäger, I.; Ezzat, K.; Sork, H.; Copolovici, D.-M.; Viola, J.R.; Zaghloul, E.M.; Lundin, P.; Moreno, P.M.D.; et al. A peptide-based vector for efficient gene transfer in vitro and in vivo. *Mol. Ther.* **2011**, *19*, 1457–1467. [CrossRef] [PubMed]
83. Shajari, N.; Mansoori, B.; Davudian, S.; Mohammadi, A.; Baradaran, B. Overcoming the Challenges of siRNA Delivery: Nanoparticle Strategies. *Curr. Drug Deliv.* **2017**, *14*, 36–46. [CrossRef] [PubMed]
84. Dissanayake, S.; Denny, W.A.; Gamage, S.; Sarojini, V. Recent developments in anticancer drug delivery using cell penetrating and tumor targeting peptides. *J. Control. Release* **2017**, *250*, 62–76. [CrossRef]
85. Wang, H.; Lin, S.; Wang, S.; Jiang, Z.; Ding, T.; Wei, X.; Lu, Y.; Yang, F.; Zhan, C. Folic Acid Enables Targeting Delivery of Lipodiscs by Circumventing IgM-Mediated Opsonization. *Nano Lett.* **2022**, *22*, 6516–6522. [CrossRef]
86. Shin, J.M.; Oh, S.J.; Kwon, S.; Deepagan, V.G.; Lee, M.; Song, S.H.; Lee, H.-J.; Kim, S.; Song, K.-H.; Kim, T.W.; et al. A PEGylated hyaluronic acid conjugate for targeted cancer immunotherapy. *J. Control. Release* **2017**, *267*, 181–190. [CrossRef]
87. Cao, M.; Lu, S.; Wang, N.; Xu, H.; Cox, H.; Li, R.; Waigh, T.; Han, Y.; Wang, Y.; Lu, J.R. Enzyme-Triggered Morphological Transition of Peptide Nanostructures for Tumor-Targeted Drug Delivery and Enhanced Cancer Therapy. *ACS Appl. Mater. Interfaces* **2019**, *11*, 16357–16366. [CrossRef]
88. Kapoor, P.; Singh, H.; Gautam, A.; Chaudhary, K.; Kumar, R.; Raghava, G.P. TumorHoPe: A database of tumor homing peptides. *PLoS ONE* **2012**, *7*, e35187. [CrossRef]
89. Ahmad, K.; Lee, E.J.; Shaikh, S.; Kumar, A.; Rao, K.M.; Park, S.Y.; Jin, J.O.; Han, S.S.; Choi, I. Targeting integrins for cancer management using nanotherapeutic approaches: Recent advances and challenges. *Semin. Cancer Biol.* **2021**, *69*, 325–336. [CrossRef]
90. Liu, F.; Yan, J.R.; Chen, S.; Yan, G.P.; Pan, B.Q.; Zhang, Q.; Wang, Y.F.; Gu, Y.T. Polypeptide-rhodamine B probes containing laminin/fibronectin receptor-targeting sequence (YIGSR/RGD) for fluorescent imaging in cancers. *Talanta* **2020**, *212*, 120718. [CrossRef]
91. Koch, J.; Schober, S.J.; Hindupur, S.V.; Schoning, C.; Klein, F.G.; Mantwill, K.; Ehrenfeld, M.; Schillinger, U.; Hohnecker, T.; Qi, P.; et al. Targeting the Retinoblastoma/E2F repressive complex by CDK4/6 inhibitors amplifies oncolytic potency of an oncolytic adenovirus. *Nat. Commun.* **2022**, *13*, 4689. [CrossRef] [PubMed]
92. Kasala, D.; Lee, S.H.; Hong, J.W.; Choi, J.W.; Nam, K.; Chung, Y.H.; Kim, S.W.; Yun, C.O. Synergistic antitumor effect mediated by a paclitaxel-conjugated polymeric micelle-coated oncolytic adenovirus. *Biomaterials* **2017**, *145*, 207–222. [CrossRef] [PubMed]
93. Yamamoto, Y.; Hiraoka, N.; Goto, N.; Rin, Y.; Miura, K.; Narumi, K.; Uchida, H.; Tagawa, M.; Aoki, K. A targeting ligand enhances infectivity and cytotoxicity of an oncolytic adenovirus in human pancreatic cancer tissues. *J. Control. Release* **2014**, *192*, 284–293. [CrossRef] [PubMed]
94. Yu, J.; Xie, X.; Xu, X.; Zhang, L.; Zhou, X.; Yu, H.; Wu, P.; Wang, T.; Che, X.; Hu, Z. Development of dual ligand-targeted polymeric micelles as drug carriers for cancer therapy in vitro and in vivo. *J. Mater. Chem. B* **2014**, *2*, 2114–2126. [CrossRef] [PubMed]
95. Zhou, L.Y.; Zhu, Y.H.; Wang, X.Y.; Shen, C.; Wei, X.W.; Xu, T.; He, Z.Y. Novel zwitterionic vectors: Multi-functional delivery systems for therapeutic genes and drugs. *Comput. Struct. Biotechnol. J.* **2020**, *18*, 1980–1999. [CrossRef]
96. Vachutinsky, Y.; Oba, M.; Miyata, K.; Hiki, S.; Kano, M.R.; Nishiyama, N.; Koyama, H.; Miyazono, K.; Kataoka, K. Antiangiogenic gene therapy of experimental pancreatic tumor by sFlt-1 plasmid DNA carried by RGD-modified crosslinked polyplex micelles. *J. Control. Release* **2011**, *149*, 51–57. [CrossRef]
97. Dirisala, A.; Osada, K.; Chen, Q.; Tockary, T.A.; Machitani, K.; Osawa, S.; Liu, X.; Ishii, T.; Miyata, K.; Oba, M.; et al. Optimized rod length of polyplex micelles for maximizing transfection efficiency and their performance in systemic gene therapy against stroma-rich pancreatic tumors. *Biomaterials* **2014**, *35*, 5359–5368. [CrossRef]
98. Ghosh, P.; Han, G.; De, M.; Kim, C.K.; Rotello, V.M. Gold nanoparticles in delivery applications. *Adv. Drug Deliv. Rev.* **2008**, *60*, 1307–1315. [CrossRef]
99. Nativo, P.; Prior, I.A.; Brust, M. Uptake and Intracellular Fate of Surface-Modified Gold Nanoparticles. *ACS Nano* **2008**, *2*, 1639–1644. [CrossRef]
100. Liu, T.; Lin, M.; Wu, F.; Lin, A.; Luo, D.; Zhang, Z. Development of a nontoxic and efficient gene delivery vector based on histidine grafted chitosan. *Int. J. Polym. Mater. Polym. Biomater.* **2022**, *71*, 717–727. [CrossRef]
101. Kichler, A.; Leborgne, C.; Danos, O.; Bechinger, B. Characterization of the gene transfer process mediated by histidine-rich peptides. *J. Mol. Med. (Berl)* **2007**, *85*, 191–201. [CrossRef] [PubMed]
102. Lointier, M.; Aisenbrey, C.; Marquette, A.; Tan, J.H.; Kichler, A.; Bechinger, B. Membrane pore-formation correlates with the hydrophilic angle of histidine-rich amphipathic peptides with multiple biological activities. *Biochim. Biophys. Acta Biomembr.* **2020**, *1862*, 183212. [CrossRef] [PubMed]

103. Kichler, A.; Leborgne, C.; März, J.; Danos, O.; Bechinger, B. Histidine-rich amphipathic peptide antibiotics promote efficient delivery of DNA into mammalian cells. *Proc. Natl. Acad. Sci. USA* **2003**, *100*, 1564–1568. [CrossRef] [PubMed]
104. Vanova, J.; Ciharova, B.; Hejtmankova, A.; Epperla, C.P.; Skvara, P.; Forstova, J.; Hubalek Kalbacova, M.; Spanielova, H. VirPorters: Insights into the action of cationic and histidine-rich cell-penetrating peptides. *Int. J. Pharm.* **2022**, *611*, 121308. [CrossRef]
105. Zhang, S.K.; Gong, L.; Zhang, X.; Yun, Z.M.; Li, S.B.; Gao, H.W.; Dai, C.J.; Yuan, J.J.; Chen, J.M.; Gong, F.; et al. Antimicrobial peptide AR-23 derivatives with high endosomal disrupting ability enhance poly(l-lysine)-mediated gene transfer. *J. Gene Med.* **2020**, *22*, e3259. [CrossRef]
106. Peeler, D.J.; Thai, S.N.; Cheng, Y.; Horner, P.J.; Sellers, D.L.; Pun, S.H. pH-sensitive polymer micelles provide selective and potentiated lytic capacity to venom peptides for effective intracellular delivery. *Biomaterials* **2019**, *192*, 235–244. [CrossRef]
107. Cao, X.; Shang, X.; Guo, Y.; Zheng, X.; Li, W.; Wu, D.; Sun, L.; Mu, S.; Guo, C. Lysosomal escaped protein nanocarriers for nuclear-targeted siRNA delivery. *Anal. Bioanal. Chem.* **2021**, *413*, 3493–3499. [CrossRef]
108. Huang, G.; Zhang, Y.; Zhu, X.; Zeng, C.; Wang, Q.; Zhou, Q.; Tao, Q.; Liu, M.; Lei, J.; Yan, C.; et al. Structure of the cytoplasmic ring of the Xenopus laevis nuclear pore complex by cryo-electron microscopy single particle analysis. *Cell Res.* **2020**, *30*, 520–531. [CrossRef]
109. Mangipudi, S.S.; Canine, B.F.; Wang, Y.; Hatefi, A. Development of a Genetically Engineered Biomimetic Vector for Targeted Gene Transfer to Breast Cancer Cells. *Mol. Pharm.* **2009**, *6*, 1100–1109. [CrossRef]
110. Lu, J.; Wu, T.; Zhang, B.; Liu, S.; Song, W.; Qiao, J.; Ruan, H. Types of nuclear localization signals and mechanisms of protein import into the nucleus. *Cell Commun. Signal.* **2021**, *19*, 60. [CrossRef]
111. Noble, J.E.; De Santis, E.; Ravi, J.; Lamarre, B.; Castelletto, V.; Mantell, J.; Ray, S.; Ryadnov, M.G. A De Novo Virus-Like Topology for Synthetic Virions. *J. Am. Chem. Soc.* **2016**, *138*, 12202–12210. [CrossRef] [PubMed]
112. Cao, M.; Wang, N.; Zhou, P.; Sun, Y.; Wang, J.; Wang, S.; Xu, H. Virus-like supramolecular assemblies formed by cooperation of base pairing interaction and peptidic association. *Sci. China Chem.* **2015**, *59*, 310–315. [CrossRef]
113. van der Aa, M.A.; Mastrobattista, E.; Oosting, R.S.; Hennink, W.E.; Koning, G.A.; Crommelin, D.J. The nuclear pore complex: The gateway to successful nonviral gene delivery. *Pharm. Res.* **2006**, *23*, 447–459. [CrossRef] [PubMed]
114. Matsuura, K.; Ota, J.; Fujita, S.; Shiomi, Y.; Inaba, H. Construction of Ribonuclease-Decorated Artificial Virus-like Capsid by Peptide Self-assembly. *J. Org. Chem.* **2020**, *85*, 1668–1673. [CrossRef] [PubMed]
115. Kong, J.; Wang, Y.; Zhang, J.; Qi, W.; Su, R.; He, Z. Rationally Designed Peptidyl Virus-Like Particles Enable Targeted Delivery of Genetic Cargo. *Angew. Chem. Int. Ed. Engl.* **2018**, *57*, 14032–14036. [CrossRef]
116. Nakamura, Y.; Inaba, H.; Matsuura, K. Construction of Artificial Viral Capsids Encapsulating Short DNAs via Disulfide Bonds and Controlled Release of DNAs by Reduction. *Chem. Lett.* **2019**, *48*, 544–546. [CrossRef]
117. Wen, A.M.; Steinmetz, N.F. Design of virus-based nanomaterials for medicine, biotechnology, and energy. *Chem. Soc. Rev.* **2016**, *45*, 4074–4126. [CrossRef]
118. Cao, M.; Shen, Y.; Wang, Y.; Wang, X.; Li, D. Self-Assembly of Short Elastin-like Amphiphilic Peptides: Effects of Temperature, Molecular Hydrophobicity and Charge Distribution. *Molecules* **2019**, *24*, 202. [CrossRef]
119. Marchetti, M.; Kamsma, D.; Vargas, E.C.; Garcia, A.H.; van der Schoot, P.; de Vries, R.; Wuite, G.J.L.; Roos, W.H. Real-Time Assembly of Viruslike Nucleocapsids Elucidated at the Single-Particle Level. *Nano Lett.* **2019**, *19*, 5746–5753. [CrossRef]
120. Walter, E.; Merkle, H.P. Microparticle-mediated transfection of non-phagocytic cells in vitro. *J. Drug Target.* **2002**, *10*, 11–21. [CrossRef]
121. Kim, Y.; Uthaman, S.; Nurunnabi, M.; Mallick, S.; Oh, K.S.; Kang, S.W.; Cho, S.; Kang, H.C.; Lee, Y.K.; Huh, K.M. Synthesis and characterization of bioreducible cationic biarm polymer for efficient gene delivery. *Int. J. Biol. Macromol.* **2018**, *110*, 366–374. [CrossRef]
122. Dirisala, A.; Uchida, S.; Li, J.; Van Guyse, J.F.R.; Hayashi, K.; Vummaleti, S.V.C.; Kaur, S.; Mochida, Y.; Fukushima, S.; Kataoka, K. Effective mRNA Protection by Poly(l-ornithine) Synergizes with Endosomal Escape Functionality of a Charge-Conversion Polymer toward Maximizing mRNA Introduction Efficiency. *Macromol. Rapid Commun.* **2022**, *43*, e2100754. [CrossRef] [PubMed]
123. Collard, W.T.; Yang, Y.; Kwok, K.Y.; Park, Y.; Rice, K.G. Biodistribution, metabolism, and in vivo gene expression of low molecular weight glycopeptide polyethylene glycol peptide DNA co-condensates. *J. Pharm. Sci.* **2000**, *89*, 499–512. [CrossRef]
124. Dirisala, A.; Uchida, S.; Toh, K.; Li, J.; Osawa, S.; Tockary, T.A.; Liu, X.; Abbasi, S.; Hayashi, K.; Mochida, Y.; et al. Transient stealth coating of liver sinusoidal wall by anchoring two-armed PEG for retargeting nanomedicines. *Sci. Adv.* **2020**, *6*, eabb8133. [CrossRef] [PubMed]
125. Cao, M.; Wang, Y.; Hu, X.; Gong, H.; Li, R.; Cox, H.; Zhang, J.; Waigh, T.A.; Xu, H.; Lu, J.R. Reversible Thermoresponsive Peptide-PNIPAM Hydrogels for Controlled Drug Delivery. *Biomacromolecules* **2019**, *20*, 3601–3610. [CrossRef]
126. Cao, M.; Lu, S.; Zhao, W.; Deng, L.; Wang, M.; Wang, J.; Zhou, P.; Wang, D.; Xu, H.; Lu, J.R. Peptide Self-Assembled Nanostructures with Distinct Morphologies and Properties Fabricated by Molecular Design. *ACS Appl. Mater. Interfaces* **2017**, *9*, 39174–39184. [CrossRef]
127. Cao, M.; Zhao, W.; Zhou, P.; Xie, Z.; Sun, Y.; Xu, H. Peptide nucleic acid-ionic self-complementary peptide conjugates: Highly efficient DNA condensers with specific condensing mechanism. *RSC Adv.* **2017**, *7*, 3796–3803. [CrossRef]

nanomaterials

MDPI

Article

Effect of Inlet Flow Strategies on the Dynamics of Pulsed Fluidized Bed of Nanopowder

Syed Sadiq Ali [1], Agus Arsad [2], Kenneth L. Roberts [3] and Mohammad Asif [4,*]

[1] School of Chemical and Energy Engineering, Faculty of Engineering, Universiti Teknologi Malaysia, Johor Bahru 81310, Johor, Malaysia
[2] UTM-MPRC Institute for Oil and Gas, School of Chemical and Energy Engineering, Faculty of Engineering, Universiti Teknologi Malaysia, Johor Bahru 81310, Johor, Malaysia
[3] SmartState Center for Strategic Approaches to the Generation of Electricity (SAGE), College of Engineering and Computing, University of South Carolina, Columbia, SC 29208, USA
[4] Department of Chemical Engineering, King Saud University, P.O. Box 800, Riyadh 11421, Saudi Arabia
* Correspondence: masif@ksu.edu.sa; Tel.: +966-114-676-849; Fax: +966-114-678-770

Abstract: The use of fluidization assistance can greatly enhance the fluidization hydrodynamics of powders that exhibit poor fluidization behavior. Compared to other assistance techniques, pulsed flow assistance is a promising technique for improving conventional fluidization because of its energy efficiency and ease of process implementation. However, the inlet flow configuration of pulsed flow can significantly affect the bed hydrodynamics. In this study, the conventional single drainage (SD) flow strategy was modified to purge the primary flow during the non-flow period of the pulse to eliminate pressure buildup in the inlet flow line while providing a second drainage path to the residual gas. The bed dynamics for both cases, namely, single drainage (SD) and modified double drainage (MDD), were carefully monitored by recording the overall and local pressure drop transients in different bed regions at two widely different pulsation frequencies of 0.05 and 0.25 Hz. The MDD strategy led to substantially faster bed dynamics and greater frictional pressure drop in lower bed regions with significantly mitigated segregation behavior. The spectral analysis of the local and global pressure transient data in the frequency domain revealed a pronounced difference between the two flow strategies. The application of the MDD inlet flow strategy eliminated the disturbances from the pulsed fluidized bed irrespective of the pulsation frequency.

Keywords: fluidization; pulsation; frequency; flow strategy; flow spike; disturbances

Citation: Ali, S.S.; Arsad, A.; Roberts, K.L.; Asif, M. Effect of Inlet Flow Strategies on the Dynamics of Pulsed Fluidized Bed of Nanopowder. *Nanomaterials* **2023**, *13*, 304. https://doi.org/10.3390/nano13020304

Academic Editor: Meiwen Cao

Received: 25 November 2022
Revised: 7 January 2023
Accepted: 10 January 2023
Published: 11 January 2023

1. Introduction

Fluidized bed technology holds great promise for improving the process efficiency in the petrochemical and chemical industries. Its key strength lies in efficient solid dispersion that ensures effective utilization of the solids' surface area and significantly enhances the surface-based rate processes. In the fluidized bed mode of contact, lower pressure drop, greater interfacial contact, efficient gas–solid mixing, and higher heat and mass transfer rates provide a substantial advantage over fixed bed or packed bed processes [1–5].

Particle properties have a strong bearing on fluidization behavior, as pointed out by Geldart, who classified the powders into different groups based on physical properties [6]. The fluidization of fine and ultrafine particles of group C classification is difficult because of their cohesiveness caused by strong inter-particle forces (IPF) [7,8], which often result in poor interphase phase mixing and severe bed non-homogeneities [9–12]. In particular, ultrafine powders display agglomerate bubbling fluidization (ABF) due to the formation of large multi-level agglomerates, leading to low bed expansion and high minimum fluidization velocity. As a result, the high surface area characteristics of ultrafine particles become severely compromised. Moreover, size-based segregation often occurs along the height of the bed during ABF [13–17]. The size of hydrophobic silica agglomerates in the lower

bed region was 5–10 times larger than the ones in the upper layer [18]. Zhao et al. [19] reported more severe size segregation, where an order of magnitude agglomerate size difference between the upper and lower layers occurred, such that agglomerates as large as 2000 μm were found in the lower region. Although higher gas flow tends to mitigate the effect of IPFs, other problems, such as elutriation and entrainment, occur at high velocities. Therefore, various assistance strategies have been suggested in the literature to provide additional energy to overcome cohesive IPFs and improve the hydrodynamics of the fluidized bed. One such strategy is vibration assistance, which can be employed either internally or externally. External vibrations involve oscillating, shaking, or vibrating the complete test section by using a vibrator or an electric motor [19,20]. Despite their proven capability, the implementation of external vibration-based fluidization assistance techniques, whether at a laboratory scale or large-scale units, is challenging and expensive. On the other hand, internal vibrations directly transfer energy to the solid phase in the bed through techniques such as acoustic perturbation and high-shear mixer [21–27]. Similar to external vibrations, these techniques require additional equipment, leading to higher costs. In some cases, the premixing of the resident solid phase with inert or magnetic particles has been suggested to alter the interparticle force equilibrium of ultrafine particles in the bed [15,28–31]. The compatibility and post-processing issues, however, limit the application of particle premixing.

An important prerequisite for large-scale applications of any assisted technique is its amenability to scale up and easy implementation without being energy intensive and any major process modification requirement. One such technique is the pulsation of inlet fluid flow to the fluidized bed [32–34]. The flow pulsation shortened the drying time and improved the bed homogeneity in drying porous pharmaceutical granules [35]. The constant and falling drying rates of the fluidized biomass particles were enhanced by using optimal pulsation frequency [36]. The flow pulsation also promoted the density-based segregation of coal particles [37,38]. During the fluidization of ultrafine nanoparticles using the square wave pulsation strategy, the channeling and plug formation were suppressed, leading to improved bed homogeneity [16,33,39–41]. Moreover, the minimum fluidization velocity significantly decreased, indicating the deagglomeration of large-sized nanoagglomerates [16,39,40]. Besides promoting uniform bed expansion, pulsed flow also helped decrease the bubble velocity and size [40].

The efficacy of pulsed flow strongly depends on inlet flow and deaeration configurations. The effect of the deaeration strategy has been extensively studied in the context of bed collapse [42–44]. Once the inlet flow is stopped, the deaeration of the residual air critically affects the bed collapse process, which is clearly reflected in the evolution of pressure transient profiles in different regions of the bed [43,44]. The ratio of the distributor to bed pressure drop showed a pronounced effect on the collapse process. As this ratio was increased from 0.005 to 0.03, the difference between the two deaeration strategies was substantially mitigated [43]. When the residual air escapes only from the top of the bed, known as single drainage (SD) deaeration, the collapse process is slow. Providing the residual air dual pathways (i.e., from the top as well as from the bottom of the bed through the plenum), also called dual drainage (DD) deaeration, leads to faster bed transients [42]. Of equal importance is the design of the inlet flow configuration because the line pressure inevitably builds up during the no-flow phase of the pulse when the bed collapses. Therefore, once the valve opens to allow the inlet flow, the line pressure leads to a flow spike. This phenomenon leads to intense size segregation of nanoagglomerates along the height of the fluidized bed, thereby affecting the collapse dynamics monitored in different regions of the bed. To suppress the initial flow spike by eliminating the line pressure buildup, Ali et al. suggested to vent the inlet flow to the atmosphere during the no-flow phase of the pulse while allowing dual deaeration routes to residual gas. This modified dual drainage (MDD) strategy significantly suppressed the size segregation of agglomerates and improved the bed homogeneity [18].

The foregoing discussion, although mainly in the context of bed collapse, is of great importance for pulsed fluidized beds. The flow spike resulting from the pressure buildup during the no-flow phase of the square pulse could severely compromise the efficacy of pulsation assistance. This phenomenon could be complicated by pulsation frequency. At a shorter pulsation frequency, the line pressure builds up because of the longer duration of the no-flow phase of the pulse. Therefore, a careful investigation has been undertaken using the MDD strategy for the fluidized bed pulsed with two widely different square wave frequencies, namely, 0.05 and 0.25 Hz. The local and global bed dynamics for both frequencies were monitored using highly sensitive pressure transducers with a response time of 1 ms. The results were compared with SD pulsed bed to obtain a greater understanding of the pulsed fluidized bed. The present study substantially extends the scope of the conventional bed collapse to examine how the regular intermittency of bed collapse affects the evolution of local and global bed transients in the presence of two different deaeration strategies. Modifying the inlet configuration to suppress the initial peak adds another dimension to the problem, that is, how the occurrence of a short-term event affects the subsequent development of fluidization hydrodynamics.

2. Experimental

The experimental setup consisted of a test section that was a 1.6 m long transparent perplex column with a 0.07 m internal diameter (Figure 1). A calming section with a length of 0.3 m was attached beneath the test section to eliminate the effects of the entry of the fluidizing air. A distributor with 0.025 fractional open area and 2 mm perforations on a circular pitch was used to ensure a uniform distribution of the fluidizing gas across the cross-sectional area of the test section. The perforations of the distributor were covered by a fine nylon mesh filter of 20 μm to prevent the falling of particles through the distributor. A disengagement section with a length of 0.5 m and a diameter of 0.14 m was attached above the test section to suppress particle entrainment with the exiting gas. The test section was washed with an anti-static fluid prior to the experiments.

The overall and local pressure drop transients in four different regions of the bed were measured by positioning the pressure taps along the bed height (Table 1). Five highly sensitive bidirectional differential-pressure transducers (Omega PX163-005BD5V; 1 ms response time; range: $\pm 2.5''$ H_2O) recorded the pressure transients at a rate of 100 Hz by using data acquisition system (DAQ) and Labview software. The lower and upper ports of pressure transducers were located diametrically opposite sides of the column to ensure reliable monitoring of cross-sectionally averaged local bed dynamics in different bed regions (Figure 1).

Table 1. Pressure tap positions used to record region-wise pressure transients.

Pressure Drop	Bed Region	Pressure Tap Positions (from the Distributor)
ΔP_1	Lower	0.5–0.1 m
ΔP_2	Lower middle	0.1–0.2 m
ΔP_3	Upper middle	0.2–0.3 m
ΔP_4	Upper	0.3 m–open
ΔP_g	Overall	0.05 m–open

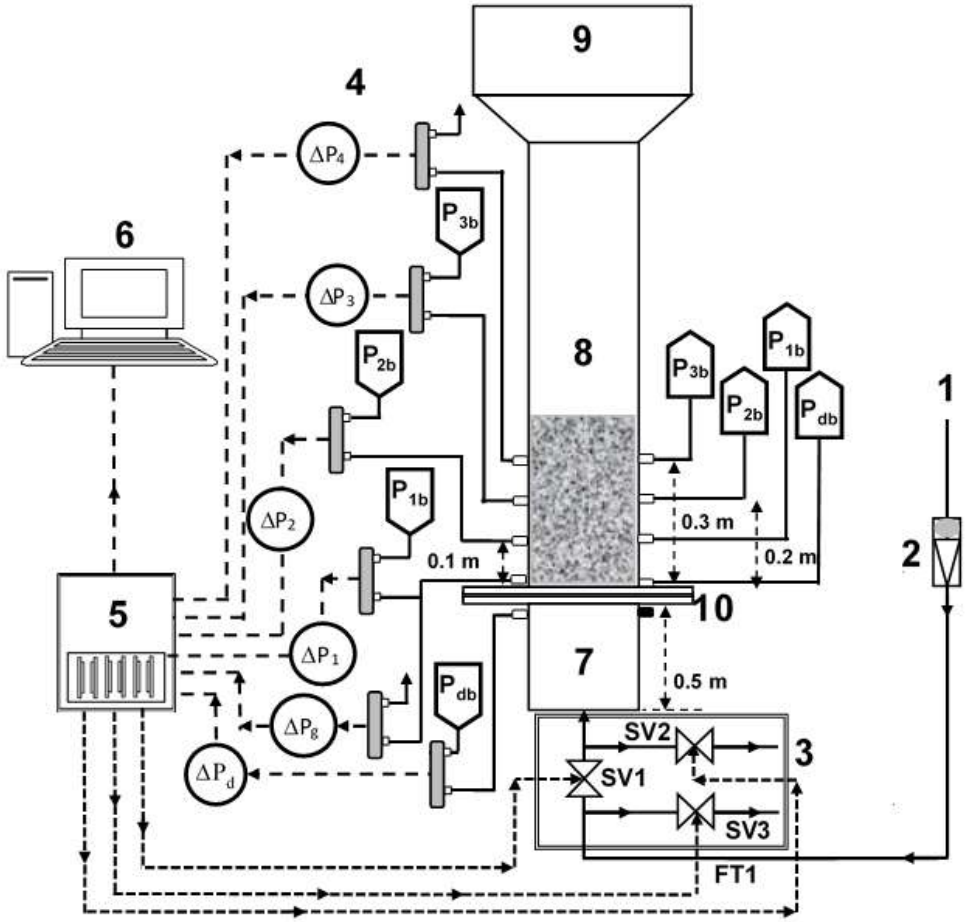

Figure 1. Experimental set-up; (1) Compressed air; (2) Flowmeter; (3) 2-way solenoid valves (for SD and MDD flow strategy); (4) Pressure transducers; (5) Data acquisition system; (6) Computer; (7) Calming section; (8) Test section; (9) Disengagement section; (10) Distributor.

The primary dimension of hydrophilic nanosilica (Aerosil 200) reported by the manufacturer (Evonik, GmBH) was 12 nm with a density of 2200 kg/m^3 [45]. However, the dry particle size analysis (Malvern Panalytical Mastersizer 2000) yielded an average size of 12.5 µm due to the multi-level agglomeration of particles under the effect of IPFs [1,24]. This behavior was clearly evident in the morphological characterization of the nanopowder sample by SEM [13,16]. The specific surface area of the powder was 0.62 m^2/g, which was several orders of magnitude smaller than the reported value of 200 $\pm$ 25 m^2/g [45].

Three different two-way solenoid valves (Model: Omega SV 3310) were used (Figure 1). These valves were controlled using digital IO signals from the DAQ to provide two different inlet flow strategies during pulsation [18].

2.1. Single Drainage (SD) Configuration

In this configuration, only the primary inlet valve, marked as SV1 in Figure 1, was employed. When energized, SV1 allowed the inlet airflow and stopped it when de-energized. The other two valves, namely, SV2 and SV3, remained closed throughout the experiment. This strategy provided only one passage, that is, the top of the bed, for the escape of the trapped residual air during the collapse process. Since the square wave flow pulsations were implemented in our experiments, the closing of the valve during the no-flow phase of the square wave led to the buildup of the line pressure across SV1. This pressure buildup led to an initial airflow spike when the valve opened to allow the inlet flow to the test section.

2.2. Modified Dual Drainage (MDD) Configuration

In this configuration, SV1 was kept open during inlet flow to the test section, while the two other valves (SV2 and SV3) remained closed. However, when SV1 closed, cutting off the airflow, SV2 and SV3 were energized to remain fully open. SV2 provided an alternate passage for the residual air to escape through the plenum, while SV3 vented the primary airflow to the atmosphere, thereby preventing the buildup of the pressure drop. This strategy completely eliminated the initial airflow spike when SV1 opened to allow the inlet flow to the test section.

The opening and closing frequency of the solenoid valves was controlled using a digital IO signal from DAQ and Labview. High-pressure air under ambient conditions was used as the fluidizing gas. Gilmont flowmeters were used to set the initial airflow in the column. The particle bed was allowed to achieve a steady state before the start of the pulsation experiments using two different frequencies, namely 0.05 and 0.25 Hz. Whereas 0.05 Hz pulsations with a time period of 20 s allowed the complete collapse of the bed between two successive pulsations [13], 0.25 Hz pulsations with a much shorter time period of 4 s allowed only partial bed collapse before the occurrence of another pulsation event [1]. Local and global bed dynamics were monitored for four identical pulses of 0.05 Hz and six pulses of 0.25 Hz pulsation.

3. Results and Discussion

Evolution of Local Pressure Drop Transients

Figure 2 shows the local bed dynamics of the 0.05 Hz pulsed fluidized bed under different inlet and deaeration strategies (i.e., SD and MDD). The broken red vertical line indicates the start of the flow pulse, while the collapse process theoretically initiates as soon as the inlet flow is stopped during the no-flow phase of the pulse. At 0.05 Hz, the complete pulse cycle lasted for 20 s that comprised 10 s of inlet flow at a fixed velocity, followed by 10 s of complete flow interruption. A wide spectrum of velocities within 13–87 mm/s were considered in our experiments. The peaks at the onset of the flow pulse, often pronounced for SD configuration, were due to the pressure buildup across the solenoid valve, resulting in the initial flow spike. This phenomenon can promote size-based segregation along the height of the bed [18]. By contrast, the venting of the primary flow in the MDD strategy did not allow the line pressure buildup, thereby suppressing the initial flow spike.

The effect of velocity variation on the SD fluidized bed was not always notable, except in the lower middle region that is represented by ΔP_2 in Figure 2e. Since the bed was not fluidized at 13 mm/s, its dynamics inevitably differed from others. Unlike SD, the effect of velocity on the local dynamics of the MDD fluidized bed was significantly pronounced with substantially faster dynamics. Once the pulsed flow began, the pressure drop almost attained a steady state value within a span of 1 s. The collapse process also finished in one second, with the pressure drop attaining a zero value. However, some exceptions were seen for the upper region (ΔP_4) and the upper middle region (ΔP_3) of the bed. The faster dynamics of the MDD strategy could be due to the availability of second escape routes for the residual air through the plenum in addition to the top of the bed. Being closer to the lower drainage pathway, the difference between the two strategies in behavior was inevitably more pronounced in the lower region (Figure 2g,h). The evolution of pressure transients and their dependence on velocity in Figure 2h clearly highlight the improved bed hydrodynamics obtained using the MDD strategy. However insignificant, the initial pressure drop spike in the MDD pulsed bed could have resulted from the time lag in the closing of the vent valve and the opening of the flow valve.

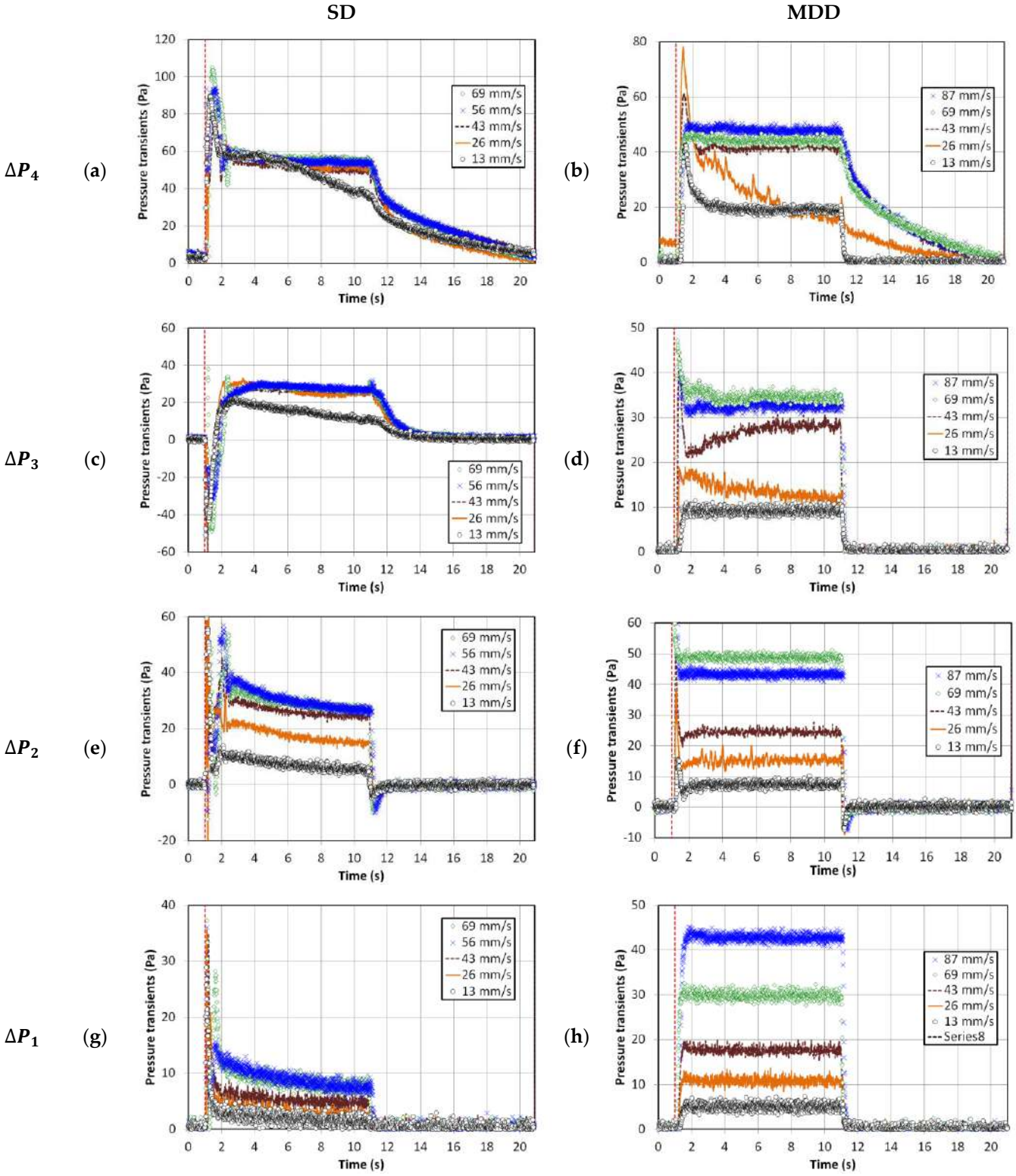

Figure 2. Local pressure drop transients with pulsation frequency 0.05 Hz; (**a**) Upper region (SD); (**b**) Upper region (MDD); (**c**) Upper middle region (SD); (**d**) Upper middle region (MDD); (**e**) Lower middle region (SD); (**f**) Lower middle region (MDD); (**g**) Lower region (SD); (**h**) Lower region (MDD).

In the lower bed region (Figure 2g), the accumulation of rigid and large agglomerates due to segregation resulted in a lower pressure drop than that in the regions above, that is, ΔP_2 to ΔP_4. However, in Figure 2h, the pressure drop was comparable with that in the

middle region with a strong dependence on the velocity, which indicated the presence of smaller agglomerates in the lower region due to feeble segregation tendencies.

The behavior of the higher frequency pulsed fluidized bed is shown in Figure 3. The inlet flow occurred for 2 s only, followed by 2 s of complete interruption. Therefore, neither the expansion nor the collapse process could reach a steady condition in most cases, irrespective of whether SD or MDD strategy was implemented. The evolution of MDD pressure transients were rather predictable, whereas a great deal of disturbances was evident for the SD transients. These disturbances were strongly affected by the change in velocity. In the case of MDD, ΔP_1 and ΔP_2 showed faster transients than ΔP_3 and ΔP_4 owing to the availability of the lower deaeration route through the plenum. Away from the distributor, the transients were slower, especially at higher velocities, because of the presence of a greater amount of residual gas. On the other hand, the complex, unpredictable pressure drop transients in the SD pulsed fluidized bed developed due to the interaction between the solid particles, whether rising or falling and the upward rising gas flow through the bed. The difference between the local bed dynamics in the two cases of different frequencies was also observed in the initial pressure drop spike, which appeared to be significantly mitigated for the higher frequency pulsed flow owing to a lower line pressure buildup due to the shorter duration of the no-flow phase of the pulsed flow.

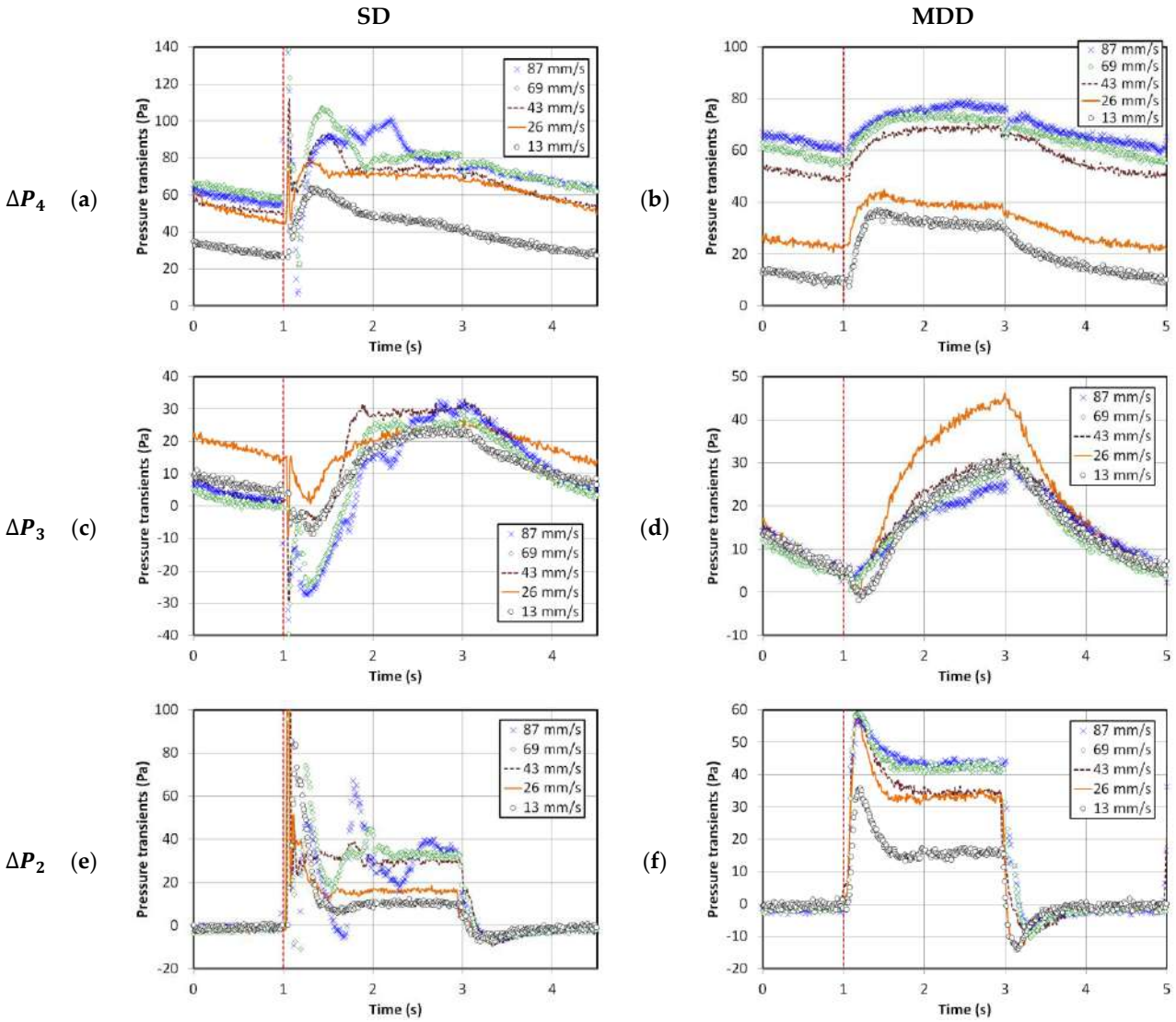

Figure 3. *Cont.*

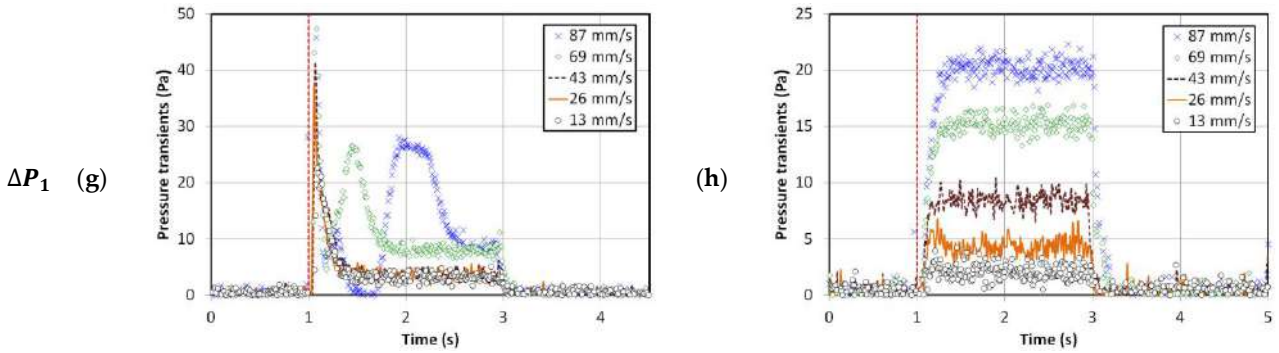

Figure 3. Local pressure drop transients with pulsation frequency 0.25 Hz; (**a**) Upper region (SD); (**b**) Upper region (MDD); (**c**) Upper middle region (SD); (**d**) Upper middle region (MDD); (**e**) Lower middle region (SD); (**f**) Lower middle region (MDD); (**g**) Lower region (SD); (**h**) Lower region (MDD).

The pressure drop ranges were of comparable magnitude in the lower region (ΔP_1) for both strategies at higher frequency pulsation in Figure 3g,h. Moreover, $\Delta P_1 < \Delta P_2$, suggesting similar segregation behavior for both flow strategies. At higher frequencies, although the pulsed bed with SD configuration showed a smaller initial flow spike, their hydrodynamics were more susceptible to intense disturbances.

The global transients are shown in Figure 4 for both cases of 0.05 and 0.25 Hz pulsed fluidized bed. The trends in Figures 2 and 3 were witnessed again. The smooth pressure transients for MDD, irrespective of the pulsation frequency, are a clear reflection of the improved hydrodynamics. At lower frequencies, another aspect of the bed hydrodynamics that was apparently not evident before occurred. Higher pressure drop values were noticed at higher velocities, such as 69 and 87 mm/s, indicating better contact between the solid and fluid phases causing greater frictional losses.

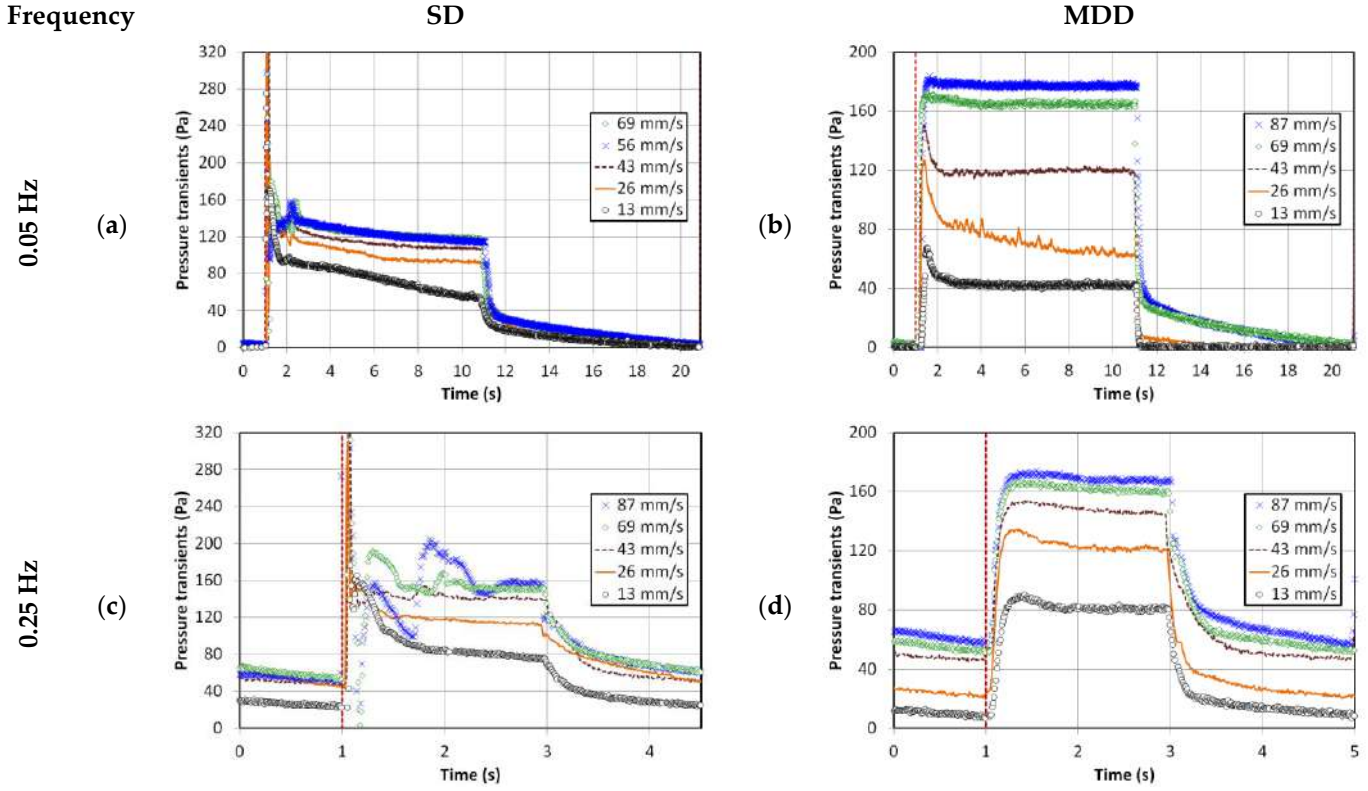

Figure 4. Global pressure drop transients for different pulsation frequencies; (**a**) 0.05 Hz frequency SD; (**b**) 0.05 Hz frequency MDD; (**c**) 0.25 Hz frequency SD; (**d**) 0.25 Hz frequency MDD.

The bed hydrodynamics were further investigated by computing the mean value of the pressure drop from the pressure transients. The latter portion of the flow pulse, immediately before the flow cutoff, was used to evaluate the mean. The case of 0.05 Hz pulsed fluidized bed is considered in Figure 5. Only the defluidization part of the experimental run was compared for SD and MDD, owing to its repeatability. The difference was significantly pronounced in the lower region of the bed (ΔP_1), which was monitored in the bed region from 5–100 mm above the distributor (Figure 5d). At higher flowrates, the difference between the two pressure drop values reached several folds with a steeper rise for the MDD, indicating the presence of smaller agglomerates. A similar difference, albeit less pronounced, was again observed for ΔP_2 (Figure 5c). A smoother pressure drop profile was seen with the MDD in the upper middle region (Figure 5b). The upper region, represented by ΔP_4, fully fluidized at approximately 20 mm/s, with a higher pressure drop for SD. Given that the total weight of solid particles in both cases were the same, the total pressure drops across the bed for the fully fluidized bed in both cases should be comparable. The lower pressure drop values in the lower region obtained with SD were therefore compensated in the upper region of the bed. Owing to the size segregation of nanoagglomerates, the bed showed partial fluidization. The upper region with smaller agglomerates fluidized at 20 mm/s, whereas the lower region with large agglomerates remained un-fluidized even at higher gas velocities.

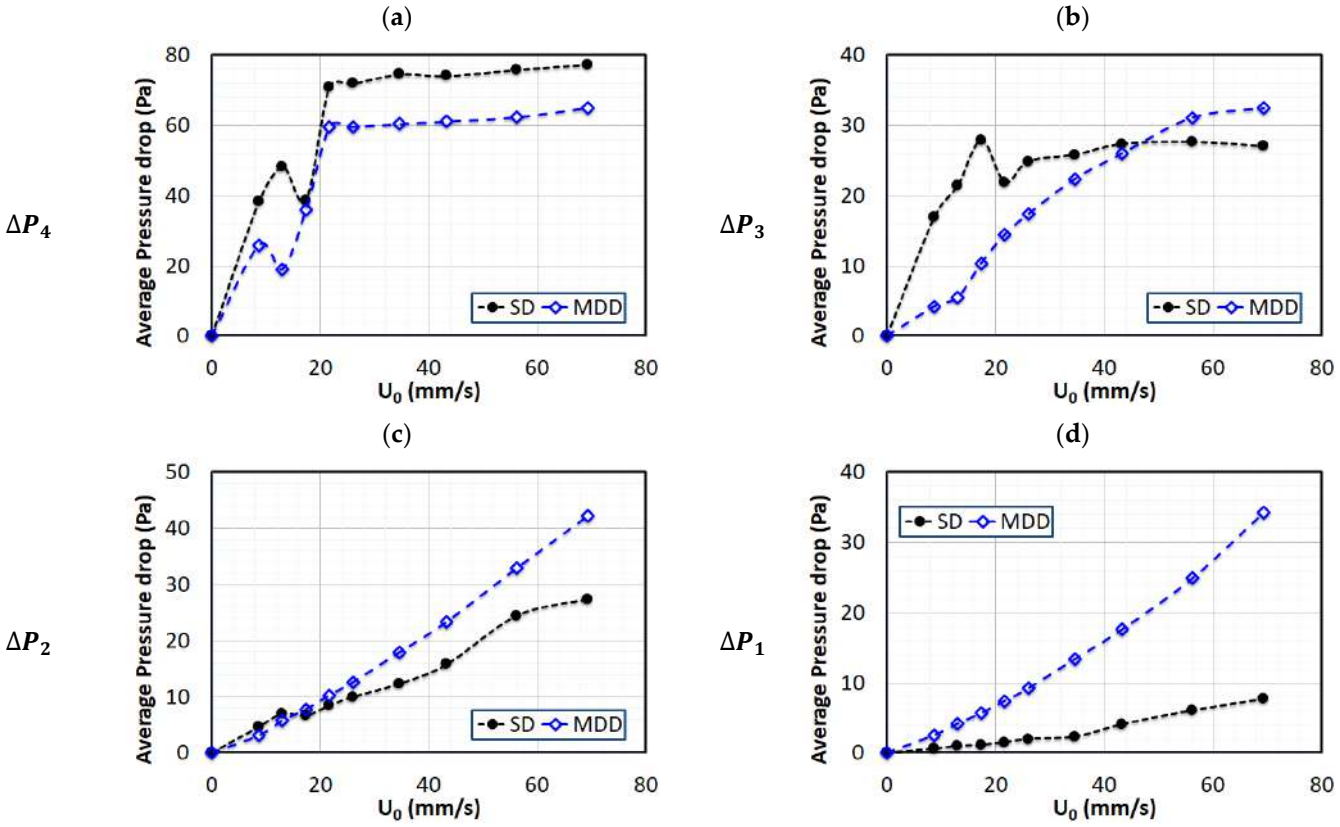

Figure 5. Variations in local pressure drop with air superficial velocity for defluidization runs of 0.05 Hz pulsed fluidized bed; (**a**) Upper region (ΔP_4); (**b**) Upper middle region (ΔP_3); (**c**) Lower region (ΔP_2); (**d**) Lower region (ΔP_1).

Similar behavior was observed for the case of 0.25 Hz pulsed bed in Figure 6. A clear difference between SD and MDD was detected in the lower region, where a higher pressure drop was obtained with MDD, and the difference between the two strategies was more pronounced at higher velocities. However, the difference was not as prominent as it was in the lower frequency case. The trend was reversed for the upper middle region (ΔP_3)

and the upper region (ΔP_4) due to the material balance consideration, as explained in the preceding paragraph. The MDD bed hydrodynamics appeared to be more sensitive to the frequency change. The upper middle region showed a decrease in the pressure drop at higher velocities due to the bed expansion that caused the migration of solids to the upper region, where this phenomenon was reflected in the increase in the pressure drop.

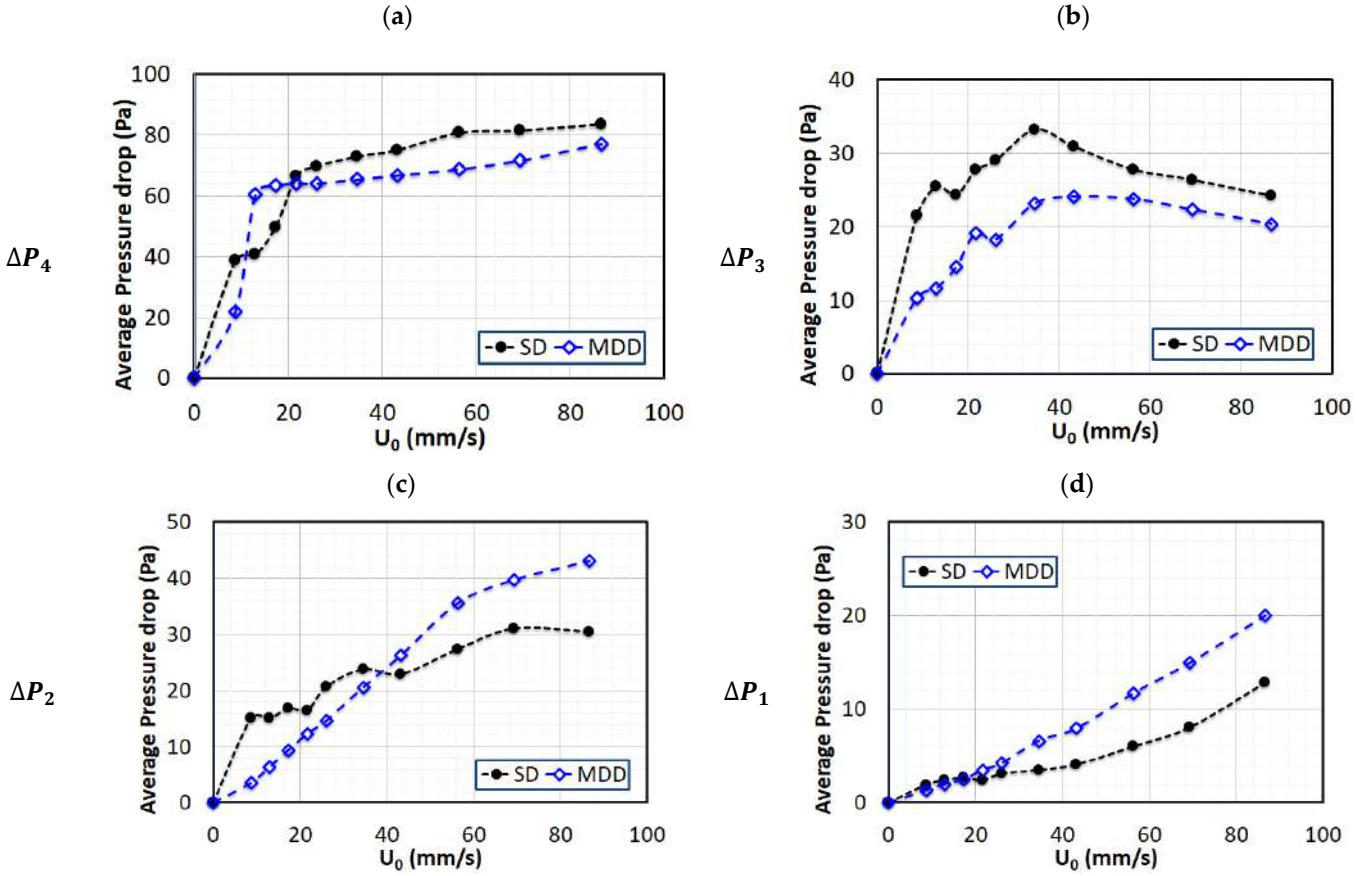

Figure 6. Variations in local pressure drop with air superficial velocity for defluidization runs of 0.25 Hz pulsed fluidized bed; (**a**) Upper region (ΔP_4); (**b**) Upper middle region (ΔP_3); (**c**) Lower region (ΔP_2); (**d**) Lower region (ΔP_1).

A more revealing insight into the bed dynamics is shown in Figure 7, which presents the amplitude spectra of the signals in the frequency domain. The "fft" function of MATLAB was used for computing the spectra. The figure considers the global pressure drop signals that include the disturbances in the whole bed. The comparison for both cases of SD and MDD is also shown. The case of the 0.05 Hz pulsed bed is considered in Figure 7a for different velocities. The difference between the SD and MDD was significant. The amplitude spectra of the pressure drop transients of the SD within the 10–50 Hz range were dominated by the small amplitude events, which decreased in intensity as the frequency increased. This finding clearly indicated the disturbances occurring in the pulsed fluidized bed with SD configuration. The amplitude profile showed the existence of a wide spectrum of pressure fluctuations beginning from below 10 Hz and extending up to 30 Hz. It was caused by the solid particles falling under gravity and were obstructed by the upward flow of the residual air exiting from the top of the bed, thereby generating pressure drop fluctuations. This phenomenon was completely absent in the case of MDD. The case of 0.25 Hz pulsed bed is considered in Figure 7b. The behavior was similar to the one observed earlier for 0.05 Hz. The amplitude of fluctuations for SD at this frequency was higher than that obtained for the case of the lower frequency. This fact was already pointed out while discussing the real-time bed dynamics of SD configuration in Figure 3.

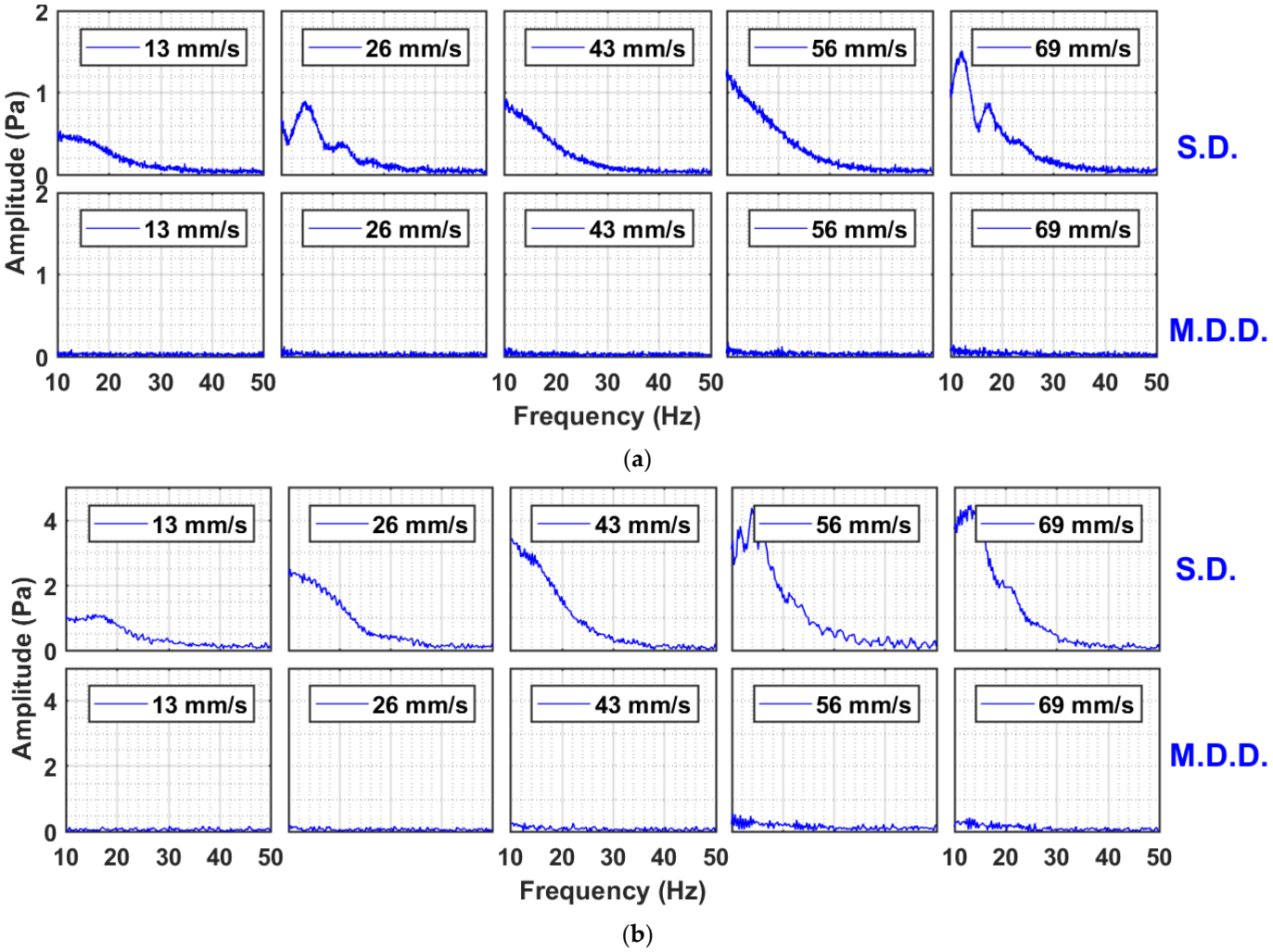

Figure 7. Amplitude spectral analysis of global pressure drop transients of SD and MDD pulsed fluidized bed at (**a**) 0.05 Hz; (**b**) 0.25 Hz.

To obtain further insight into the local bed dynamics, the local amplitude spectra of pressure transients in different regions of the bed at 0.05 Hz flow pulsation are shown in Figure 8 for two different velocities (i.e., 26 and 69 mm/s). Interestingly, the difference between the local dynamics was notable. The case of lower velocity, that is, 26 mm/s, is considered in Figure 8a. The lower region represented by ΔP_1 showed no fluctuations because large and hard agglomerates in the lower region were still stationary at 26 mm/s; therefore, no visible change occurred whether the flow was started or cutoff. The lower middle region pressure transients (ΔP_2) were greatly affected as the falling particles achieved higher kinetic energy by traversing a greater distance in the bed in reaching this region when obstructed by the upwards moving residual air, indicating a great deal of fluctuations. For the same reason, this effect was substantially mitigated in the upper middle region (ΔP_3) because of the lower kinetic energy of falling solids. In the upper region, we observed fluctuations with a lot of distinct frequencies as the smaller particles interacted with the residual air exiting the bed as small bubbles. As the velocity was increased to 69 mm/s, the phenomenon described became more intense (Figure 8b).

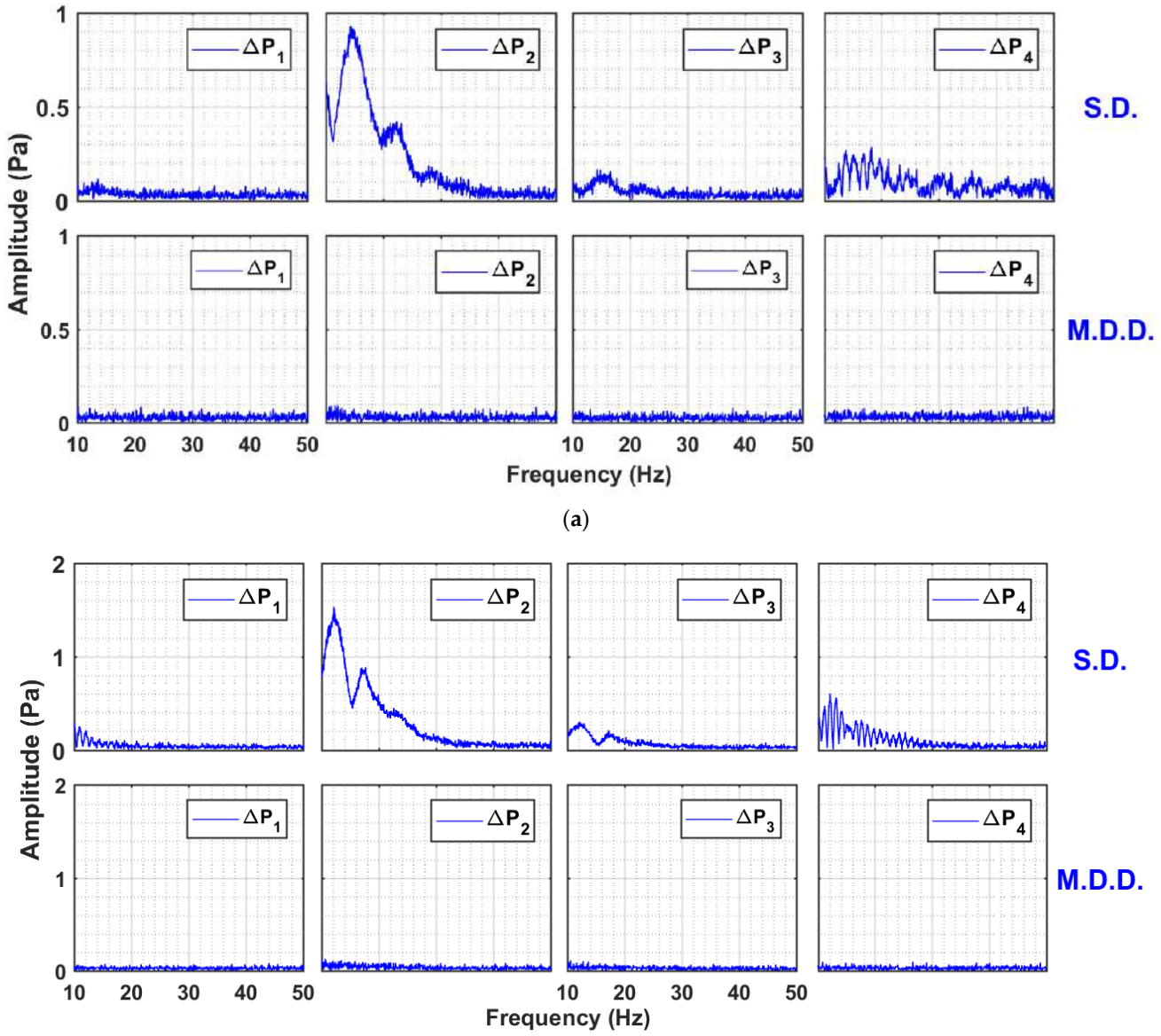

Figure 8. Amplitude spectral analysis of local pressure drop transients of 0.05 Hz pulsed fluidized bed for one complete pulse at (**a**) $U_0 = 26$ mm/s; (**b**) $U_0 = 69$ mm/s.

Similar observations were persistent at high-frequency pulsations (Figure 9a,b). The MDD configuration completely eliminated the disturbances throughout the bed, irrespective of gas velocity. For the SD configuration, the local bed hydrodynamics presented a completely different picture. The amplitude was the highest in the ΔP_2 region, where the swarm of falling particles possessed the highest kinetic energy. In the region above, that is, upper middle, ΔP_3 showed clear periodic events of small amplitude in the range of 10–20 Hz. Increasing the fluid velocity increased the amplitude by more than threefold due to the increased disturbances in the bed. The continuous spectra of ΔP_2 at 26 mm/s changed into discrete high amplitude events occurring at 12 Hz followed by those at 20 Hz, probably due to the development of flow structures.

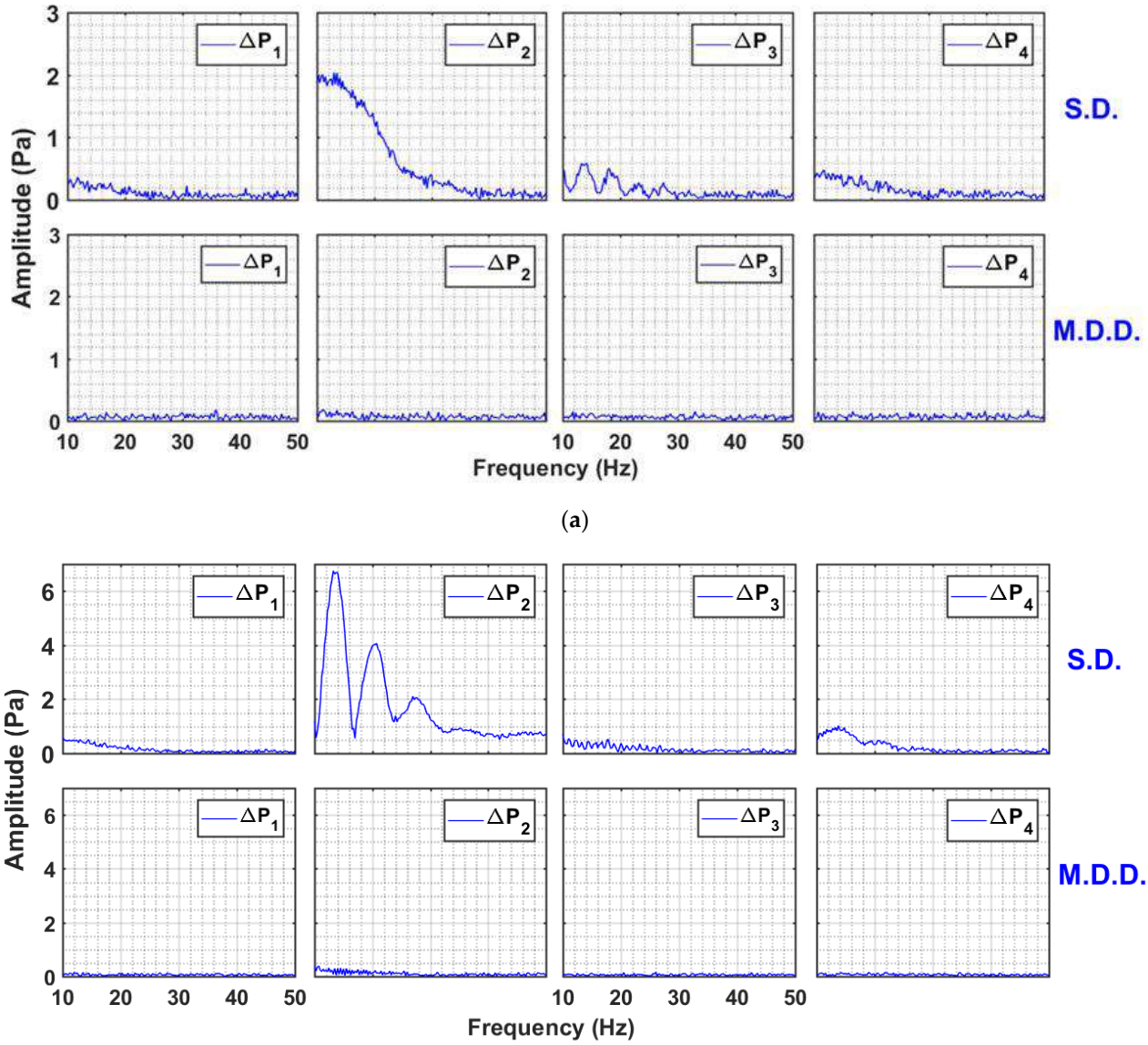

Figure 9. Amplitude spectral analysis of local pressure drop transients of 0.05 Hz pulsed fluidized bed for one complete pulse at (**a**) $U_0 = 26$ mm/s; (**b**) $U_0 = 69$ mm/s.

The average diameters from local dynamics were calculated during the collapse of the bed. The mathematical model based on mass balance proposed by Nie and Liu was used [46]. The diameters of the agglomerates are reported in Figure 10. For 0.05 Hz in Figure 10a–c, the segregation was clearly visible for SD configuration. The range of diameters for upper, middle, and lower regions were 15–22, 30–90, and 140–260 µm, respectively. The agglomerate size in the upper region was almost constant with airflow rate, while agglomerates in the middle and lower regions showed a consistent increase with airflow rate because finer particles moved to the upper region due to segregation. For the case of MDD configuration, the size ranges were 20–30, 90–140, and 100–200 µm in the upper, middle, and lower regions, respectively. The size difference between the agglomerates in the lower and middle regions was not as pronounced as those in the case of the SD configuration. The MDD configuration suppressed the segregation tendencies in the pulsed fluidized beds. At higher frequencies (Figure 10d–f), the size ranges were similar for both flow strategies with strong segregation behavior that was seen for the case of 0.05 Hz SD configuration. This means that the disturbances generated due to high-

frequency pulsation developed a similar impact on the hydrodynamics as the initial airflow spike in the lower frequency. Moreover, the slope of the curve in Figure 10d decreased with increasing airflow, signifying the addition of finer particles in the region. Moreover, the slope of curves in Figure 10e,f was lower than that in Figure 10b,c. This finding could be due to the deagglomeration phenomenon, wherein the size of larger particles decreased, and finer particles moved to the upper region.

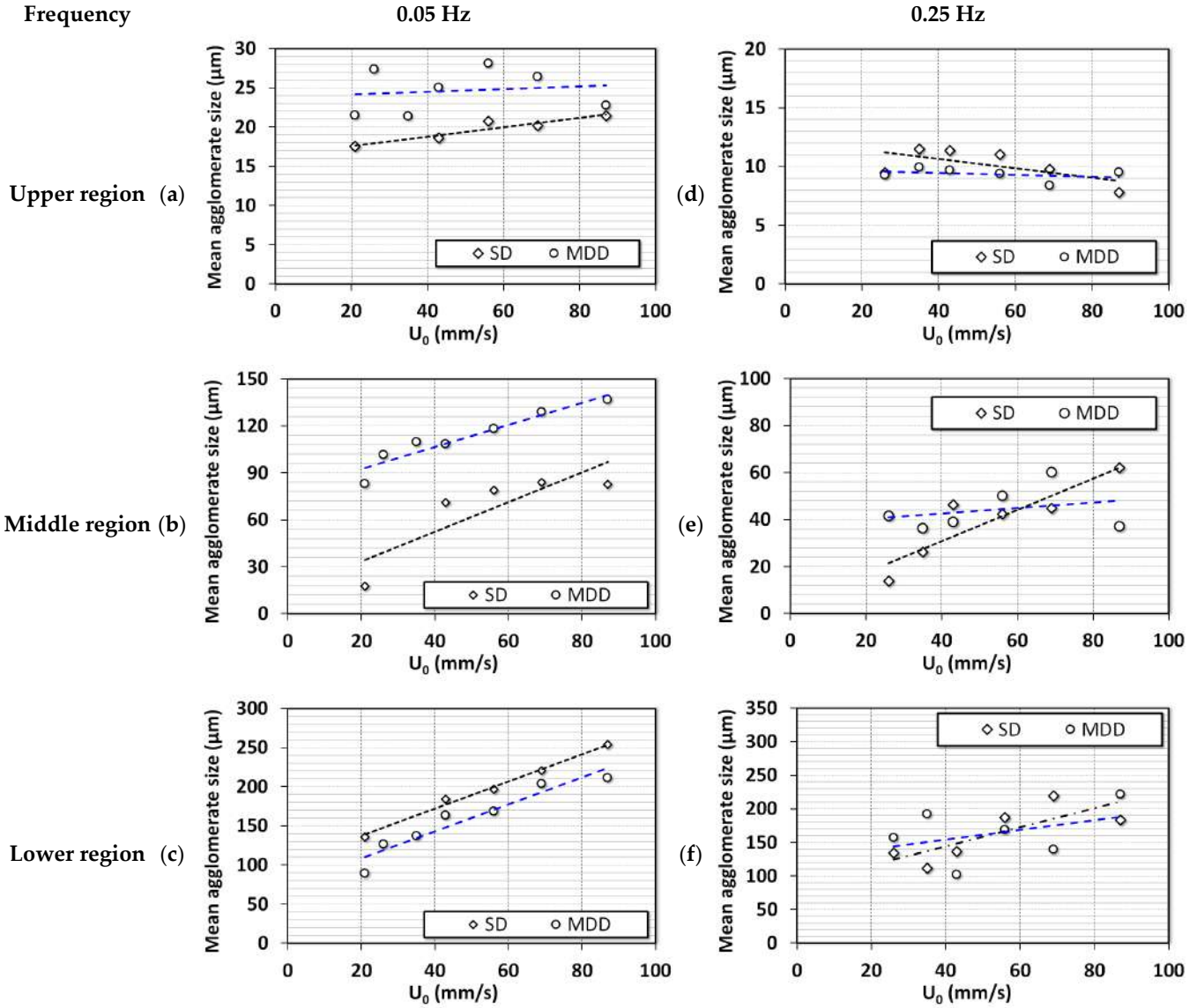

Figure 10. Changes in the average agglomerate diameter of ultrafine particles with the change in fluid velocity in different regions of the bed of nanosilica; (**a**) Upper region (0.05 Hz); (**b**) Middle region (0.05 Hz); (**c**) Lower region (0.05 Hz); (**d**) Upper region (0.25 Hz); (**e**) Middle region (0.25 Hz); (**f**) Lower region (0.25 Hz).

4. Conclusions

The inlet flow strategies greatly affected the hydrodynamics of pulsed fluidized beds. At a low pulsation frequency of 0.05 Hz, large size-based segregation was observed when the SD flow strategy was used. This was caused by the initial airflow spike resulting from pressure built up across the solenoid valve in the collapse process. This phenomenon was eliminated using the MDD airflow strategy, leading to a subdued segregation behavior. The region-wise pressure drop during defluidization displayed the difference in the degree

of segregation, especially in the lower region due to the different flow strategies. However, at a higher pulsation frequency of 0.25 Hz, the flow spike was feeble due to the lower time period of pressure built up across the solenoid valve. The difference in stratification was less between both flow strategies when high-frequency pulsation was used. The particle diameter calculated from the local bed dynamics signified that the segregation was prominent for both flow strategies at high-frequency flow pulsation. The disturbances developed due to the frequent expansion and collapse of the bed promoted segregation and deagglomeration.

Author Contributions: Conceptualization, S.S.A. and M.A.; Methodology, S.S.A. and M.A.; Software, S.S.A.; Validation, S.S.A.; Formal Analysis, S.S.A.; Resources, M.A.; Data Curation, S.S.A.; Writing—Original Draft Preparation, S.S.A.; Writing—Review & Editing, A.A., K.L.R. and M.A.; Supervision, M.A.; Funding Acquisition, M.A. All authors have read and agreed to the published version of the manuscript.

Funding: This research was funded by Researchers Supporting Project, King Saud University, Riyadh, Saudi Arabia, RSP2023R42.

Acknowledgments: The authors acknowledge the Researchers Supporting Project, RSP2023R42, King Saud University, Riyadh, Saudi Arabia, for the financial support.

Conflicts of Interest: The authors declare no conflict of interest.

References

1. Ali, S.S.; Hossain, S.K.S.; Asif, M. Dynamics of partially collapsing pulsed fluidized bed. *Can. J. Chem. Eng.* **2021**, *99*, 2333–2344. [CrossRef]
2. Lehmann, S.; Hartge, E.-U.; Jongsma, A.; Deleeuw, I.-M.; Innings, F.; Heinrich, S. Fluidization characteristics of cohesive powders in vibrated fluidized bed drying at low vibration frequencies. *Powder Technol.* **2019**, *357*, 54–63. [CrossRef]
3. Bakhurji, A.; Bi, X.; Grace, J.R. Hydrodynamics and solids mixing in fluidized beds with inclined-hole distributors. *Particuology* **2019**, *43*, 19–28. [CrossRef]
4. Raganati, F.; Chirone, R.; Ammendola, P. Gas–solid fluidization of cohesive powders. *Chem. Eng. Res. Des.* **2018**, *133*, 347–387. [CrossRef]
5. Fedorov, A.V.; Yazykov, N.A.; Bulavchenko, O.A.; Saraev, A.A.; Kaichev, V.V.; Yakovlev, V. CuFeAl Nanocomposite Catalysts for Coal Combustion in Fluidized Bed. *Nanomaterials* **2020**, *10*, 1002. [CrossRef] [PubMed]
6. Geldart, D. Types of gas fluidization. *Powder Technol.* **1973**, *7*, 285–292. [CrossRef]
7. Lettieri, P.; Macrì, D. Effect of Process Conditions on Fluidization. *KONA Powder Part. J.* **2016**, *33*, 86–108. [CrossRef]
8. Asif, M.; Ali, S.S. Bed collapse dynamics of fluidized beds of nano-powder. *Adv. Powder Technol.* **2013**, *24*, 939–946. [CrossRef]
9. Ali, S.S.; Arsad, A.; Roberts, K.; Asif, M. Effect of Voidage on the Collapsing Bed Dynamics of Fine Particles: A Detailed Region-Wise Study. *Nanomaterials* **2022**, *12*, 2019. [CrossRef]
10. van Ommen, J.R.; Valverde, J.; Pfeffer, R. Fluidization of nanopowders: A review. *J. Nanoparticle Res.* **2012**, *14*, 737. [CrossRef]
11. Shabanian, J.; Jafari, R.; Chaouki, J. Fluidization of Ultrafine Powders. *Int. Rev. Chem. Eng.* **2012**, *4*, 16–50.
12. Shabanian, J.; Chaouki, J. Influence of interparticle forces on solids motion in a bubbling gas-solid fluidized bed. *Powder Technol.* **2016**, *299* (Suppl. C), 98–106. [CrossRef]
13. Asif, M.; Al-Ghurabi, E.H.; Ajbar, A.; Kumar, N.S. Hydrodynamics of Pulsed Fluidized Bed of Ultrafine Powder: Fully Collapsing Fluidized Bed. *Processes* **2020**, *8*, 807. [CrossRef]
14. Ali, S.S.; Asif, M.; Ajbar, A. Bed collapse behavior of pulsed fluidized beds of nano-powder. *Adv. Powder Technol.* **2014**, *25*, 331–337. [CrossRef]
15. Ali, S.S.; Asif, M. Effect of particle mixing on the hydrodynamics of fluidized bed of nanoparticles. *Powder Technol.* **2017**, *310*, 234–240. [CrossRef]
16. Al-Ghurabi, E.H.; Shahabuddin, M.; Kumar, N.S.; Asif, M. Deagglomeration of Ultrafine Hydrophilic Nanopowder Using Low-Frequency Pulsed Fluidization. *Nanomaterials* **2020**, *10*, 388. [CrossRef]
17. Tamadondar, M.R.; Zarghami, R.; Tahmasebpoor, M.; Mostoufi, N. Characterization of the bubbling fluidization of nanoparticles. *Particuology* **2014**, *16*, 75–83. [CrossRef]
18. Ali, S.S.; Arsad, A.; Asif, M. Effect of modified inlet flow strategy on the segregation phenomenon in pulsed fluidized bed of ultrafine particles: A collapse bed study. *Chem. Eng. Process. Process Intensif.* **2021**, *159*, 108243. [CrossRef]
19. Zhao, Z.; Liu, D.; Ma, J.; Chen, X. Fluidization of nanoparticle agglomerates assisted by combining vibration and stirring methods. *Chem. Eng. J.* **2020**, *388*, 124213. [CrossRef]
20. Lee, J.-R.; Lee, K.S.; Park, Y.O.; Lee, K.Y. Fluidization characteristics of fine cohesive particles assisted by vertical vibration in a fluidized bed reactor. *Chem. Eng. J.* **2020**, *380*, 122454. [CrossRef]

21. Ding, P.; Pacek, A. De-agglomeration of goethite nano-particles using ultrasonic comminution device. *Powder Technol.* **2008**, *187*, 1–10. [CrossRef]
22. Ding, P.; Orwa, M.; Pacek, A. De-agglomeration of hydrophobic and hydrophilic silica nano-powders in a high shear mixer. *Powder Technol.* **2009**, *195*, 221–226. [CrossRef]
23. Al-Ghurabi, E.H.; Ali, S.S.; Alfadul, S.M.; Shahabuddin, M.; Asif, M. Experimental investigation of fluidized bed dynamics under resonant frequency of sound waves. *Adv. Powder Technol.* **2019**, *30*, 2812–2822. [CrossRef]
24. Ajbar, A.; Bakhbakhi, Y.; Ali, S.; Asif, M. Fluidization of nano-powders: Effect of sound vibration and pre-mixing with group A particles. *Powder Technol.* **2011**, *206*, 327–337. [CrossRef]
25. Raganati, F.; Ammendolab, P.; Chirone, R. CO_2 capture by adsorption on fine activated carbon in a sound assisted fluidized bed. *Chem. Eng. Trans.* **2015**, *43*, 1033–1038.
26. Ali, S.S.; Arsad, A.; Hossain, S.S.; Asif, M. A Detailed Insight into Acoustic Attenuation in a Static Bed of Hydrophilic Nanosilica. *Nanomaterials* **2022**, *12*, 1509. [CrossRef]
27. Lee, J.-R.; Lee, K.S.; Hasolli, N.; Park, Y.O.; Lee, K.Y.; Kim, Y.H. Fluidization and mixing behaviors of Geldart groups A, B and C particles assisted by vertical vibration in fluidized bed. *Chem. Eng. Process. Process Intensif.* **2020**, *149*, 107856. [CrossRef]
28. Zhou, L.; Diao, R.; Zhou, T.; Wang, H.; Kage, H.; Mawatari, Y. Behavior of magnetic Fe3O4 nano-particles in magnetically assisted gas-fluidized beds. *Adv. Powder Technol.* **2011**, *22*, 427–432. [CrossRef]
29. Emiola-Sadiq, T.; Wang, J.; Zhang, L.; Dalai, A. Mixing and segregation of binary mixtures of biomass and silica sand in a fluidized bed. *Particuology* **2021**, *58*, 58–73. [CrossRef]
30. Ali, S.S.; Basu, A.; Alfadul, S.M.; Asif, M. Nanopowder Fluidization Using the Combined Assisted Fluidization Techniques of Particle Mixing and Flow Pulsation. *Appl. Sci.* **2019**, *9*, 572. [CrossRef]
31. Ali, S.S.; Al-Ghurabi, E.H.; Ibrahim, A.A.; Asif, M. Effect of adding Geldart group A particles on the collapse of fluidized bed of hydrophilic nanoparticles. *Powder Technol.* **2018**, *330*, 50–57. [CrossRef]
32. Ireland, E.; Pitt, K.; Smith, R. A review of pulsed flow fluidisation; the effects of intermittent gas flow on fluidised gas–solid bed behaviour. *Powder Technol.* **2016**, *292*, 108–121. [CrossRef]
33. Ali, S.S.; Asif, M. Fluidization of nano-powders: Effect of flow pulsation. *Powder Technol.* **2012**, *225*, 86–92. [CrossRef]
34. Sung, W.C.; Jung, H.S.; Bae, J.W.; Kim, J.Y.; Lee, D.H. Segregation phenomena of binary solids in a pulsed fluidized bed. *Powder Technol.* **2022**, *410*, 117881. [CrossRef]
35. Akhavan, A.; van Ommen, J.R.; Nijenhuis, J.; Wang, X.S.; Coppens, M.-O.; Rhodes, M.J. Improved Drying in a Pulsation-Assisted Fluidized Bed. *Ind. Eng. Chem. Res.* **2009**, *48*, 302–309. [CrossRef]
36. Jia, D.; Cathary, O.; Peng, J.; Bi, X.; Lim, C.J.; Sokhansanj, S.; Liu, Y.; Wang, R.; Tsutsumi, A. Fluidization and drying of biomass particles in a vibrating fluidized bed with pulsed gas flow. *Fuel Process. Technol.* **2015**, *138*, 471–482. [CrossRef]
37. Dong, L.; Zhang, Y.; Zhao, Y.; Peng, L.; Zhou, E.; Cai, L.; Zhang, B.; Duan, C. Effect of active pulsing air flow on gas-vibro fluidized bed for fine coal separation. *Adv. Powder Technol.* **2016**, *27*, 2257–2264. [CrossRef]
38. Saidi, M.; Tabrizi, H.B.; Chaichi, S.; Dehghani, M. Pulsating flow effect on the segregation of binary particles in a gas–solid fluidized bed. *Powder Technol.* **2014**, *264*, 570–576. [CrossRef]
39. Liu, Y.; Ohara, H.; Tsutsumi, A. Pulsation-assisted fluidized bed for the fluidization of easily agglomerated particles with wide size distributions. *Powder Technol.* **2017**, *316*, 388–399. [CrossRef]
40. Akhavan, A.; Rahman, F.; Wang, S.; Rhodes, M. Enhanced fluidization of nanoparticles with gas phase pulsation assistance. *Powder Technol.* **2015**, *284*, 521–529. [CrossRef]
41. Ali, S.S.; Al-Ghurabi, E.H.; Ajbar, A.; Mohammed, Y.A.; Boumaza, M.; Asif, M. Effect of Frequency on Pulsed Fluidized Beds of Ultrafine Powders. *J. Nanomater.* **2016**, *2016*, 23. [CrossRef]
42. Lorences, M.J.; Patience, G.S.; Dıíez, F.V.; Coca, J. Fines effects on collapsing fluidized beds. *Powder Technol.* **2003**, *131*, 234–240. [CrossRef]
43. Cherntongchai, P.; Innan, T.; Brandani, S. Mathematical description of pressure drop profile for the 1-valve and 2-valve bed collapse experiment. *Chem. Eng. Sci.* **2011**, *66*, 973–981. [CrossRef]
44. Cherntongchai, P.; Brandani, S. A model for the interpretation of the bed collapse experiment. *Powder Technol.* **2005**, *151*, 37–43. [CrossRef]
45. Available online: https://www.l-i.co.uk/contentfiles/270.pdf (accessed on 10 December 2022).
46. Nie, Y.; Liu, D. Dynamics of collapsing fluidized beds and its application in the simulation of pulsed fluidized beds. *Powder Technol.* **1998**, *99*, 132–139. [CrossRef]

nanomaterials

MDPI

Article

Functional Silane-Based Nanohybrid Materials for the Development of Hydrophobic and Water-Based Stain Resistant Cotton Fabrics Coatings

Silvia Sfameni [1,2], Tim Lawnick [3], Giulia Rando [2,4], Annamaria Visco [1,5], Torsten Textor [3,*] and Maria Rosaria Plutino [2,*]

1 Department of Engineering, University of Messina, Contrada di Dio, S. Agata, 98166 Messina, Italy
2 Institute for the Study of Nanostructured Materials, ISMN–CNR, Palermo, c/o Department ChiBioFarAm, University of Messina, Viale F. Stagno d'Alcontres 31, 98166 Messina, Italy
3 TEXOVERSUM School of Textiles, Reutlingen University, 72762 Reutlingen, Germany
4 Department of ChiBioFarAm, University of Messina, Viale F. Stagno d'Alcontres 31, Vill. S. Agata, 98166 Messina, Italy
5 Institute for Polymers, Composites and Biomaterials CNR IPCB, Via Paolo Gaifami 18, 95126 Catania, Italy
* Correspondence: torsten.textor@reutlingen-university.de (T.T.); mariarosaria.plutino@cnr.it (M.R.P.)

Abstract: The textile-finishing industry, is one of the main sources of persistent organic pollutants in water; in this regard, it is necessary to develop and employ new sustainable approaches for fabric finishing and treatment. This research study shows the development of an efficient and eco-friendly procedure to form highly hydrophobic surfaces on cotton fabrics using different modified silica sols. In particular, the formation of highly hydrophobic surfaces on cotton fabrics was studied by using a two-step treatment procedure, i.e., first applying a hybrid silica sol obtained by hydrolysis and subsequent condensation of (3-Glycidyloxypropyl)trimethoxy silane with different alkyl(trialkoxy)silane under acid conditions, and then applying hydrolyzed hexadecyltrimethoxysilane on the treated fabrics to further improve the fabrics' hydrophobicity. The treated cotton fabrics showed excellent water repellency with a water contact angle above 150° under optimum treatment conditions. The cooperative action of rough surface structure due to the silica sol nanoparticles and the low surface energy caused by long-chain alkyl(trialkoxy)silane in the nanocomposite coating, combined with the expected roughness on microscale due to the fabrics and fiber structure, provided the treated cotton fabrics with excellent, almost super, hydrophobicity and water-based stain resistance in an eco-sustainable way.

Keywords: sol–gel; (3-Glycidyloxypropyl)trimethoxy silane; functional cotton fabrics; hydrophobicity; nanohybrid coatings

Citation: Sfameni, S.; Lawnick, T.; Rando, G.; Visco, A.; Textor, T.; Plutino, M.R. Functional Silane-Based Nanohybrid Materials for the Development of Hydrophobic and Water-Based Stain Resistant Cotton Fabrics Coatings. *Nanomaterials* **2022**, *12*, 3404. https://doi.org/10.3390/nano12193404

Academic Editor: Meiwen Cao

Received: 2 September 2022
Accepted: 23 September 2022
Published: 28 September 2022

1. Introduction

Textiles are critical to a country's growth and industrialization. In recent decades, many efforts have been made to develop innovative and nanostructured surface treatments in order to modify the mechanical and surface properties of natural and synthetic fabrics [1], thus replacing commonly used hazardous chemicals with products that are respectful of the environment and of health, while maintaining functional characteristics [2,3]. New multifunctional protective and smart textiles have been developed in response to growing technical breakthroughs, new standards, and a customer demand for textiles that are not only attractive but also practical [4–6]. In this regard, silica-based organic-inorganic nanostructured finishes could be considered an interesting alternative [7,8].

In recent years, the sol–gel approach has shown to be a creative and efficient method of improving the characteristics of fibers [9–13]. This approach comprises a diverse synthetic pathway that may be used to create novel materials with high molecular homogeneity

and excellent physical and chemical characteristics. Due to its biocompatibility and non-toxicity, the sol–gel technique has been used to confer several functional properties to different textiles materials [14–17], such as antimicrobial [18–22], self-cleaning [23], water repellency [24–26], flame retardancy [27–29], and sensing [30–33], as well as improving the dye ability of fabric samples (see Figure 1) [34].

Figure 1. Functional and technical textiles for improved performance, protection, and health: types, application, and market.

Sol–gel synthesis and applications follow a two-step procedure based on the hydrolysis and condensation of metal or semi-metal alkoxides: after forming a hydrolyzed metal alkoxide solution at room temperature, textile materials are impregnated with the latter, and the samples are cured at a specific temperature to obtain a porous 3D fully inorganic or hybrid organic–inorganic nanostructured coating. Consequently, there are many alternatives for the formulation and application of sol–gel coatings in the field of textile functionalization, as choosing the correct and opportune functional silane precursor, which allows for the desired chemical and physical properties improvement of the fabric. Because of the moderate processing conditions required and the use of ordinary commercial textile finishing machines, in recent years, there has been a surge in interest in the application of the sol–gel approach to produce functional coated textiles [35–39], for example water-repellent fabrics. In general, surfaces that exhibit water contact angles > 150° (on which water drops remain almost spherical and easily roll off, also able to remove dirt particles in their path), are usually called superhydrophobic surfaces [40,41]. Superhydrophobic surfaces have recently attracted significant attention within the scientific community because of their unique water-repellent, anti-icing, anti-contamination, anti-sticking, and self-cleaning properties and their potential for practical applications [42,43].

Much of this research has been inspired by lotus leaves and has demonstrated that superhydrophobic surfaces may be produced by combining the right surface roughness and low surface free-energy [44–46]. The surface of lotus leaf was first examined by Barthlott in 1970 using scanning electron microscopy and it was found that the surface has small micro-protrusions covered with nano-hairs which are covered with low surface free-energy wax substances [46].

Surface roughness and surface free-energy were used to create superhydrophobic surfaces on cotton textiles. Different nanoparticles, including zinc oxide, titanium dioxide, silica nanoparticles (SNP), or alkoxysilane-based nano-sols [47] were added to cotton fabric to provide surface roughness. Fluorocarbons and silicones are examples of substances with low surface free-energy that might change the surface energy of cotton substrate [48].

In particular, fluoroalkylsilanes were used to further increase the surface water-repellency. Most recently, the ECHA's committee (Committee for Risk Assessment—ECHA—European Union) recommended restriction for some perfluoroalkyl substances (PFAS) regarding some application fields. In particular, fluoro-chemical finishing products are banned for textile applications in all EU states, while only some exemptions (i.e., in medical, technical, and workwear textiles) are accepted, but a complete restriction is expected in EU shortly, with a movement towards more widespread use of hydrophobic alkyl silanes. Currently, there are reports of the creation of rough surface micro/nanostructures using silane nanoparticles or nano-sols [49–52] and the subsequent modification with hydrophobic materials (e.g., fluoroalkylsilane, long-chain alkyl(trialkoxy)silane) to create superhydrophobic surfaces through a multi-step procedure [53,54].

Lakshmi et al. [55] produced superhydrophobic sol–gel nanocomposite coatings by adding silica nanoparticles to an acid-catalyzed ethanol–water solution of methyltriethoxysilane (MTEOS), while Huang et al. [56] created superhydrophobic surfaces by covering a silane-based coating in ethanol with a low surface-energy material 1H, 1H, 2H, 2H-perfluorooctyltrichlorosilane. By spraying an ethanol suspension of silica sol and silica microspheres, Shang et al.'s method [57] produced superhydrophobic silica coatings that were then hydrophobically treated with a solution of 1H, 1H, 2H, 2H-perfluorodecyltriethoxysilane (PFDTS). In order to create superhydrophobic silica films, Ramezani et al. [58] examined the two-step dip coating method using a sol–gel procedure. They coated a silica-based solution, and then modified it with isooctyltrimethoxysilane as a hydrophobic agent. According to studies [59,60], fluorine-based hybrid materials are the most successful in reducing the free-energy surface. However, some of the molecules are carcinogenic, highly costly, and not environmentally friendly.

In this work, co-condensation of (3-Glycidyloxypropyl)trimethoxysilane (hereafter, GPTMS or G) and different non-fluoro compounds, i.e., Hexadecyltrimethoxysilane C16, Triethoxy(octyl)silane C8 and Triethoxy(ethyl)silaneC2, as showed in Figure 2, was conducted in the presence of an acid catalyst to obtain functional nanohybrids via a one-step process.

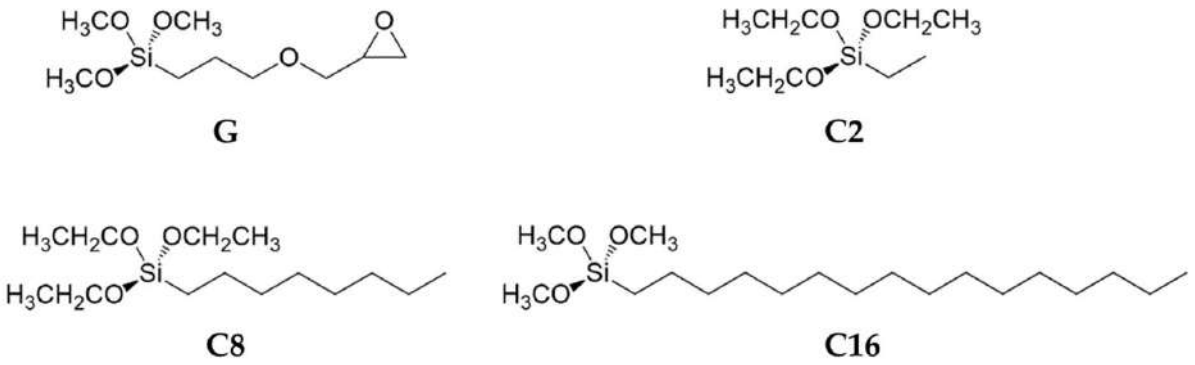

Figure 2. Alkyl(trialkoxy)silanes employed in this work.

By varying the length of the chain of the alky(trialkoxy)silane, R-Si(OR')$_3$, modified silane-based nanocomposite hydrosols, R-Si(O-)$_3$, were obtained with high dispersion stability. By applying R-Si(O-)$_3$ nanocomposite hydrosols to cotton fabrics, almost superhydrophobic cotton surfaces were obtained, as well as surface roughness and low surface energy. This study aimed to employ a multicoating eco-friendly technique in sol–gel textile finishing by examining the impact of various alkyl(trialkoxy) silane precursors on the silica-based mesh and, finally, to study the implemented mechanical characteristics of the treated cotton fabric. GPTMS is a useful molecule capable of forming extensive cross-links between the silanol groups of the polyoxysilane matrix and promoting adhesion through the opening of the epoxy ring on the treated polymers. It is a silica precursor that is frequently used for silica-based hybrid textile finishing [61,62].

The characteristics and the bi-functionality of the GPTMS, as well as its potential as a new textile finishing agent, should be investigated because there has not yet been much research on the impact of GPTMS synthetic parameters on the mechanical properties of fabrics made with both natural and synthetic polymers [63,64]. Indeed, because the chemical structure of fabric substrates is significant for the stability of the applied coatings, which is dependent on the thermodynamic affinity between the silica precursor and the selected textile samples, natural cotton textiles were employed in the current investigation.

Cotton fabrics were chosen as model substrates owing to their unique properties such as high hydroxyl group content, hydrophilic nature, and broad use, which allows them to be used not only in fabrics and garments but also in technical or smart textiles. Moreover, the use of alkyl(trialkoxy)silane has numerous advantages; it is low-cost and once polymerized is a non-toxic material [65–68], and a promising alternative for achieving durable hydrophobic fabrics. The final goal of this work was to illustrate an easy, environmentally friendly, and adaptable technique for generating hybrid coatings that are compatible with cellulose fabrics and their physical intrinsic features so that they can find applications in different sectors such as textiles [69], biomedical [70], furnishings [71], environmental remediation [72] and sensing [73]. The hydrophobicity was evaluated by WCA and WSA measurements.

By the characterization methods, the morphological qualities, surface chemistry, and durability of the sol–gel coatings were mainly evaluated using optical microscopy and SEM, comparing treated and untreated cotton textiles as a reference. Moreover, the water based anti-stain performances of the treated fabrics and, qualitatively, their oil–water separation ability towards paraffin oil were evaluated. In fact, functionalizing textiles with coatings based on the use of GPTMS in conjunction with functional alkyl(trialkoxy)silane could result in useful multifunctional nanocomposites for potential applications in the field of advanced, environmentally friendly nanohybrid materials, which would then find use in numerous nanotechnology fields.

2. Materials and Methods

2.1. Fabric

Knitted pure cotton fabric 100% (scoured and bleached, 1.4 g/cm^2 or 0.014 g/cm^2 and 0.2 mm thick) was used as natural fabric and it was provided by the School of Textile and Design (University of Reutlingen, Germany).

2.2. Chemicals

The (3-Glycidyloxypropyl)trimethoxysilane (G),Triethoxy(ethyl)silane (C2), Triethoxy (octyl)silane (C8) and Hexadecyltrimethoxysilane (C16), were all purchased at the highest purity level and used as received from Sigma Aldrich (Merk GaA, Darmstadt, Germany), without any further purification. Hydrochloric acid HCl 37% was used as sol–gel catalyst. Ethanol 96% vol. was purchased from Sigma Aldrich and used as solvent.

2.3. Preparation of the Nanosol Solution

The sol–gel solution was prepared by mixing the G precursor in combination with an equimolar amount of each of the three different alkoxysilanes featuring increasing length of the hydrocarbon chain (namely, C2, C8, C16). The obtained mixture was stirred while ethanol was added slowly at room temperature. Ethanol was used as dilution medium while HCl was added dropwise to induce the hydrolysis–condensation reaction. The resulting mixture was vigorously stirred at room temperature for 24 h.

2.4. Sol–Gel Treatment of Cotton Fabrics

Cotton fabrics were cut into square pieces (10 × 15 cm), weighted and then impregnated with the solution using the dip-pad-dry-cure method (Figure 3).

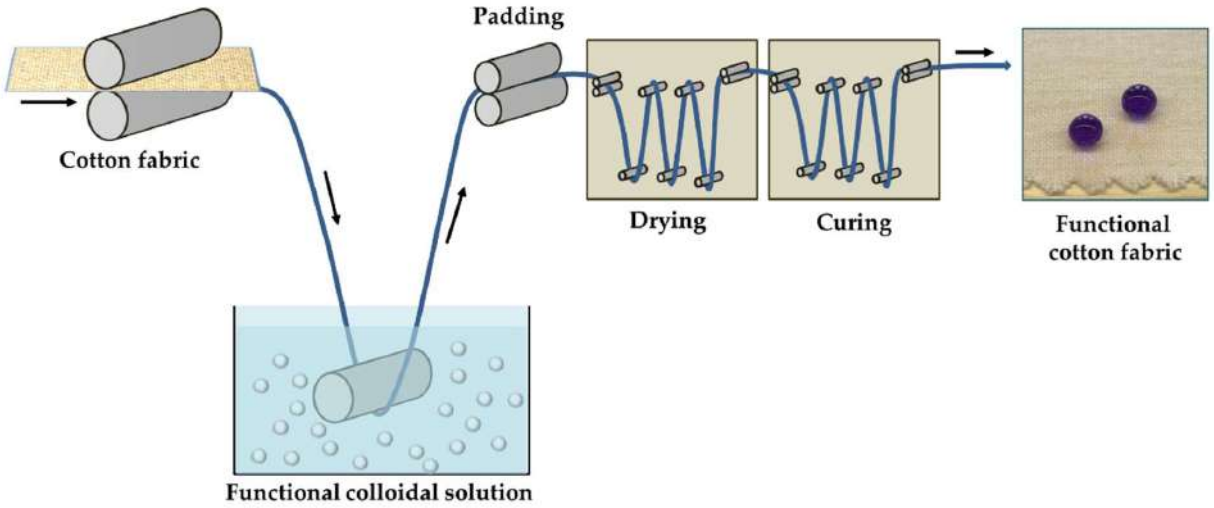

Figure 3. Pad-dry-cure process employed for finishing cotton fabrics.

First, the cotton fabric samples were immersed in the solutions for 5 min at room temperature before being washed with water. Second, an automated padder (simple two roller lab-padder of Mathis, Oberhasli, Switzerland) with a nip pressure of 2 kg/cm^2, was used to pad the cotton fabric samples. They were then dried at 80 °C for 6 min.

The process was repeated three times. In addition, samples of cotton were dipped in the alkyl(trialkoxy)silane-based ethanol solution (1.0 g, 30 mL) for 5 min, giving rise to a double-coating deposition (Figure 4).

Figure 4. Double sol–gel-based coating application for the development of the treated functional cotton fabrics.

The impregnated fabrics were finally put in the oven support and dried to a constant weight in the oven at 130 °C for 6 min: during this time the evaporation of water and ethanol and the sol–gel reactions took place.

This was confirmed by the color change of the fabrics as shown in Figure 5 and then modified cotton fabric was weighted, after being climatized for 24 h in a standard climate chamber. The composition of the functional nanohybrid sols employed for the double deposition process is shown in Table 1.

Table 1. Composition of the functional nanohybrid sols of each deposition.

Sample Code	First Deposition	Second Deposition
G	G	G
G/C2_C′2	G and C2	C2
G/C8 _C′8	G and C8	C8
G/C16 _C′16	G and C16	C16
G/C2_C′16	G and C2	C16
G/C8_C′16	G and C8	C16

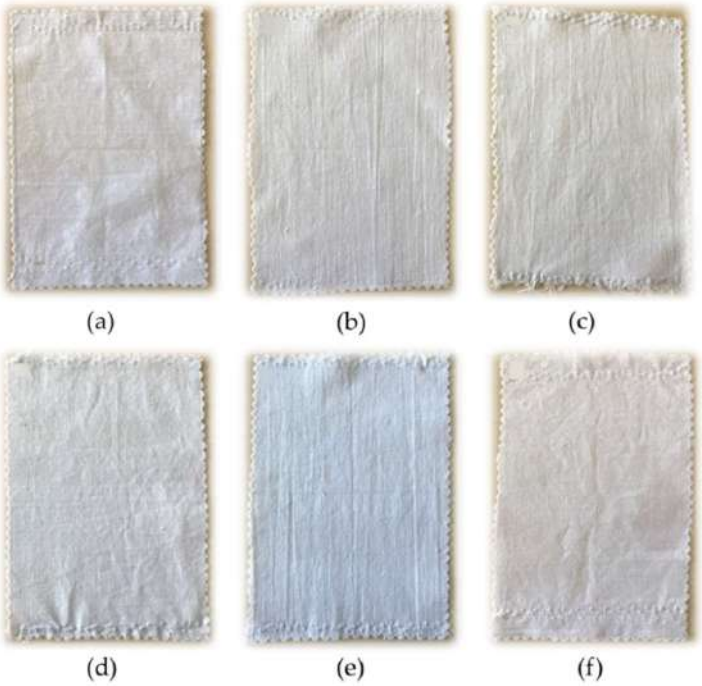

Figure 5. Cotton modified with sol–gel solution. (**a**) COT + G, (**b**) COT + G/C2_C′2, (**c**) COT + G/C8_C′8, (**d**) COT + G/C16_C′16, (**e**) COT + G/C2_C′16, and (**f**) COT + G/C8_C′16.

Subsequently, total dry-solid add-ons on the cotton samples (the weight gain, A wt.%) was determined by weighing each sample before (W_i) and after the impregnation with the solution and the subsequent thermal treatment (W_f) (Table 2).

Table 2. Composition (wt. %) of the investigated treated cotton fabrics (COT).

Sample Code	W_i	W_f	Total Add-on wt.% (A)
COT + G	2.140 g	2.163 g	1.06%
COT + G/C2_C′2	2.237 g	2.292 g	2.39%
COT + G/C8 _C′8	2.121 g	2.201 g	3.63%
COT + G/C16 _C′16	2.157 g	2.217 g	2.70%
COT + G/C2_C′16	2.210 g	2.308 g	4.24%
COT + G/C8_C′16	2.188 g	2.196 g	0.36%

The weight gain of the treated fabric was calculated using the following formula:

$$A = \frac{W_f - W_i}{W_f} \times 100 \quad (1)$$

2.5. Characterization and Functional Properties of Treated Fabrics

Wettability. Aqueous liquid repellency: water/alcohol solution tests were performed using a test reagent formulated using the AATCC test method 193-2007 Aqueous Liquid Repellency: Water/Alcohol Solution Resistance Test. Using a 5 μL water droplet at room temperature, the sessile drop technique (according to the international standard ASTM D7334) was used to measure the static water contact angles (WCA). One representative WCA was generated by averaging ten readings. The AATCC Test Method 22-2005, which is applicable to any textile fabric, was used to conduct the spray testing in order to examine the dynamic wettability of the treated samples. Three fabric samples, measuring 150 mm × 150 mm, are required to obtain one representative value for the spray testing. The tester's funnel is filled with 250 mL of distilled water, which is then sprayed onto a sample of cotton at a 45° angle. Three knocks are applied before the sample is removed.

The water repellency rating (WRR) is used to examine the extent of the wetting. Valuation is carried out by comparing the wetted sample's appearance with the wetted pristine cotton sample used as standard. Better hydrophobicity is indicated by a higher rating. The maximum and minimum ratings are 100 and 0, respectively.

Optical microscopy. Optical images were recorded by means of a Hirox digital microscope, model KH8700 (Hirox, Tokyo, Japan) by mounting a MX(G)-5040Z lens at room temperature.

Scanning Electron Microscopy (SEM) Analysis. The two-dimensional morphology and structure of the surface fibers of the of the original and treated cotton fabrics were observed at 2.0 kV using scanning electron microscope (SEM, SU-70, Hitachi, Chiyoda, Tokyo, Japan) and a magnification of 1000 × and 4000 × for the insets. All the samples were sputter-coated with Aurum prior to testing.

Self-cleaning ability. To evaluate the wetting behavior, several liquids including coffee, milk, tea, methylene-blue-dyed water, pH = 1 acid (HCl), pH = 14 alkali (NaOH), and salt solution (NaCl) were individually placed onto the GC16_C'16-modified cotton fibers. In order to test the self-cleaning abilities, soil was applied to the surface of the modified cotton fibers and washed with blue-dyed water.

Oil/water separation ability. The oil/water separation capabilities of the modified cotton textiles were tested using paraffin oil. The paraffin oil was colored using the coloring agent oil red before to the oil/water separation experiments.

Moisture analysis. The moisture-transfer properties of all the cotton fabrics samples were evaluated by using the KERN DBS moisture meter (KERN & SOHN GmbH-TYPE DBS60-3) that often replaces others drying processes, such as the laboratory dryer, because it allows for shorter measurement times. The moisture-transfer properties of all the cotton fabrics samples were evaluated through the principle of thermogravimetry. In this method, to determine the difference in moisture in a material, the sample is weighed before and after drying. In the case of the KERN DBS moisture meter, the radiation penetrates the sample and is transformed into thermal energy, heating up from the inside out. A small amount of radiation is reflected by the sample and this reflection is larger in dark samples than in light ones. Therefore, light samples, such as cotton in this case, reflect more thermal radiation than dark ones and therefore require a higher drying temperature, which is why a drying temperature of 130 °C is used for the analysis. Moisture measurement protocol (unit indicating the result: M/W, drying mode: TIME, drying temperature: 130 °C). The hygroscopicity ratio was calculated by Equation (2), which was used to as an indicator for evaluating the hygroscopicity of these cotton fabrics.

$$\text{Hygroscopicity ratio}(\%) = \frac{m_2 - m_1}{m_1} \times 100\% \quad (2)$$

where, m_2 is the weight of the conditioned sample and m_1 is the initial weight of original samples.

Air-permeability test. The air permeability of treated fabrics, which serves as an indication of their breathability, was investigated. The permeability of the samples was measured by the use of an apparatus (FX3300, Tex Test AG, Schwerzenbach, Switzland) under the air pressure of 125 Pa, according to the ASTM D737-96 standard test method.

3. Results

3.1. Nanosol Synthesis and Application on Cotton Fabrics

The sol–gel technique is a very versatile method leading to the formation of different kind of interesting functional nano- and micro-structured materials, with a fine control and tuning of their surface chemistry and of the bulk nanocomposite/nanohybrid properties of the end-products. In this study, the sol–gel synthesis and application followed a two-step pathway (Figure 6a,b) to finally yield the desired hydrophobic cotton fabrics.

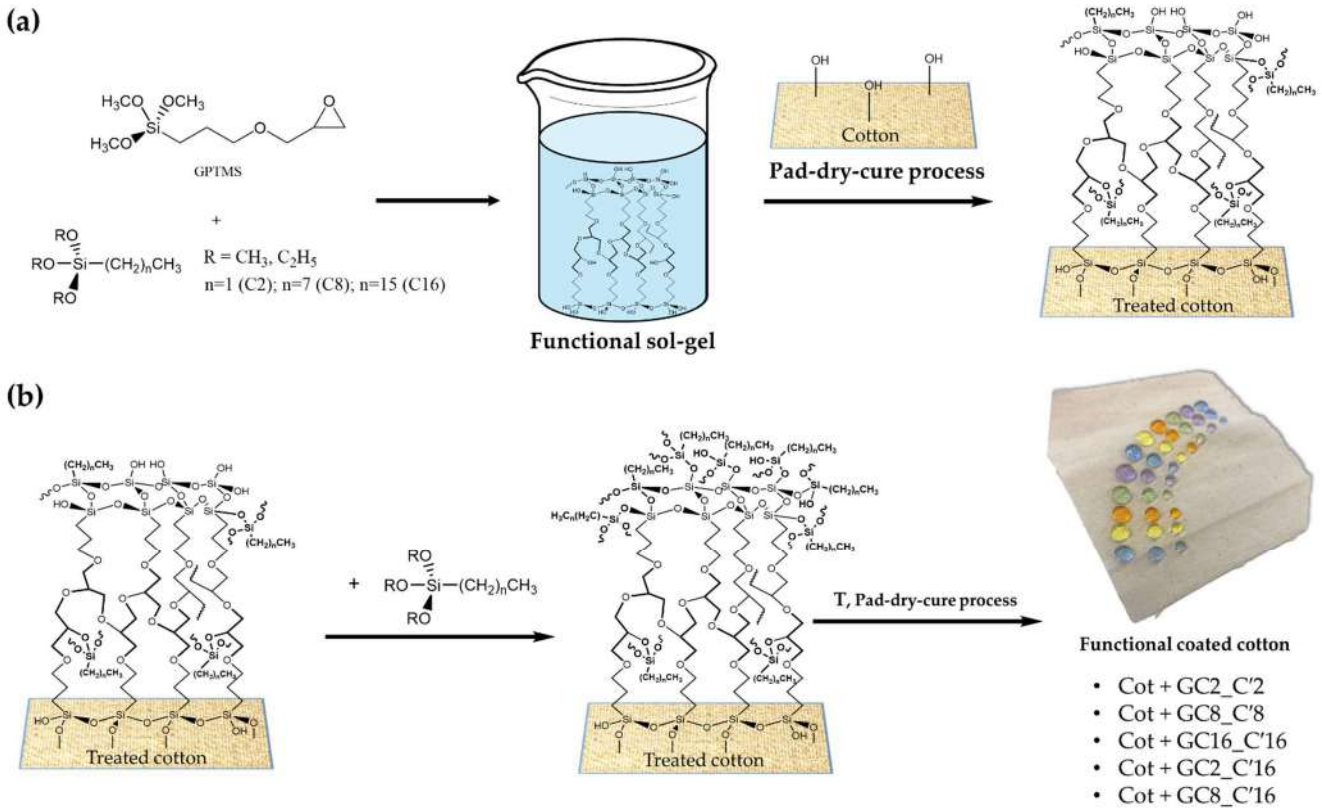

Figure 6. Two-step synthetic pathways for the development of the final functional coated cotton fabrics involving the condensation reaction between the cotton cellulose and alkoxysilane ends (**a**), and subsequent anchorage of alkyl(trialkoxy)silanes (**b**).

In the first step, the functional sol was prepared by reaction of the bifunctional GPTMS alkoxysilane and either the C2, or C8, or C16 alkyl(trialkoxy)silane, respectively, featuring different length alkyl chains. As previously reported [63,64], the functional nanosol solution is obtained by subsequent hydrolysis and condensation reaction, thus producing colloidal particles or dissolved pre-condensed polymeric hybrid polymers. Once applied on cotton fabrics and with additional heat treatment at higher temperatures by a pad-dry-cure process, the gel will give rise to a functional xerogel.

In order to form a more efficient hydrophobic coated cotton, it seemed to be worthwhile to use a second pad-dry-cure step by employing C2, or C8, or C16 alkyl(trialkoxy)silanes, respectively, thus giving rise to five functional treated cotton samples, namely Cot + GC2_ C′2, Cot + GC8_ C′8, Cot + GC16_ C′16, Cot + GC2_ C′16, Cot + GC8_ C′16; Cot + G that was used as cotton fabric reference in all experimental measurements.

3.2. Wettability Measurement

Water contact angle (WCA) measurement was used to explore the static hydrophobicity of the treated cotton samples, and the spraying test was used to evaluate the dynamic water repellence.

3.2.1. Aqueous Liquid Repellency: Water/Alcohol Solution Test

To evaluate the level of anti-wettability or repellency, the contact angles of liquids with different surface tensions was measured, using a test reagent formulated using the AATCC test method 193-2007 Aqueous Liquid Repellency [74]. The aqueous-liquid repellency test (also known as the water-rating method WRA) describes a procedure whereby 20 μL drops of solution with increasing concentration of isopropyl alcohol is placed onto the fabric. If the drops of a solution do not wet the textile within 10 s, the next solution with a higher

share of isopropanol is applied. The rating number is assigned based on the solution with the highest isopropanol share that does not wet the textile within the 10 s.

Table 3 outlines which concentration of isopropyl alcohol solution equates to which rating number.

Table 3. Aqueous-liquid repellency test.

Sample Code	Aqueous-Solution Repellency-Grade Number	Composition (by Volume)
Cot + G	0	100% Water
Cot + GC2_C′2	1	98:2/water:isopropyl alcohol
Cot + GC8_C′8	3	90:10/water:isopropyl alcohol
Cot + GC16_C′16	3	90:10/water:isopropyl alcohol
Cot + GC2_C′16	3	90:10/water:isopropyl alcohol
Cot + GC8_C′16	4	80:20/water:isopropyl alcohol

The fabric must be able to repel the solution for 10 s to be deemed successful. As a static test, this method could be considered to be more stringent than other water-drop methods as it makes use of solutions with surface tensions lower than that of water.

3.2.2. Sessile Drop Method

As a way to examine the effect of the length of the hydrocarbon chains and their distribution/orientation into the nano composite sol on the hydrophobicity of the treated cotton fabric, the cotton fabrics samples were coated by using three different sols, as prepared by changing the length of the functional alkyl(trialkoxy)silane, from 2 to 8 to 16 methylene groups. In a typical process, a deionized water droplet (ca. 5 μL) was dropped carefully onto the surface at ambient temperature and the images were captured using the accessory digital camera. All the water contact-angle values reported herein were obtained as averages of five measurements performed on different points of the sample surface so as to improve the accuracy [75–77]. The results were shown in Figures 7 and 8.

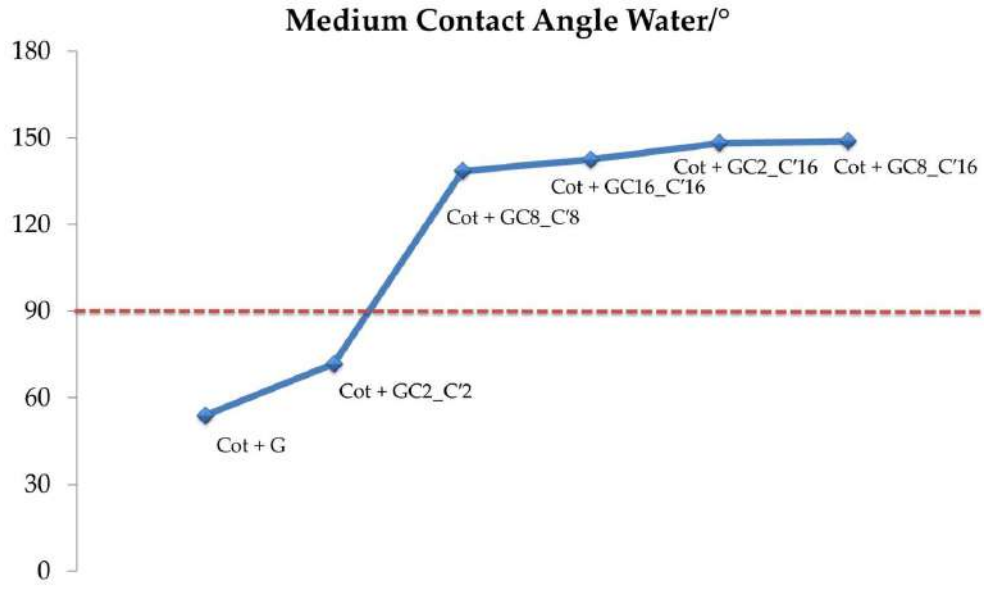

Figure 7. Schematic graph representative of the static water-contact angles of Wenzel θw values. The line between the data points is only a guide for the eye.

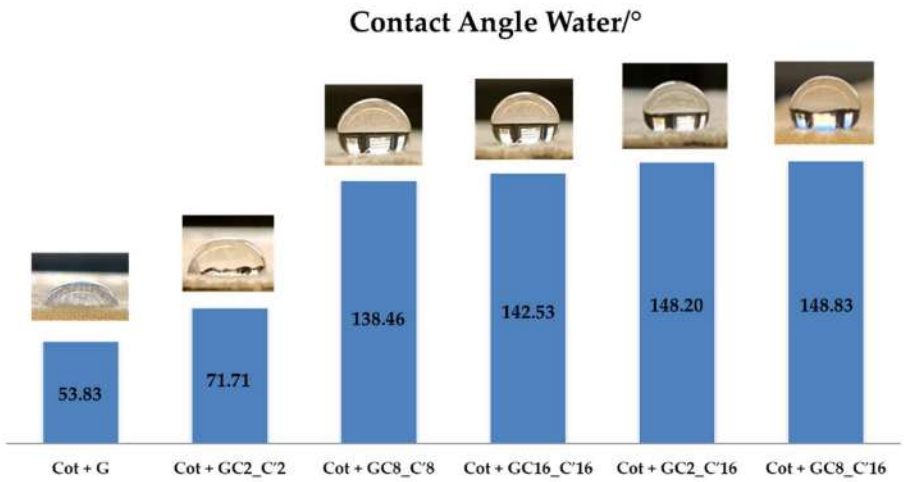

Figure 8. Histograms of the contact angle θw of the cotton fabrics treated by the nanocomposite sol samples G, GC2_C′2, GC8_C′8, GC16_C′16, GC2_C′16, and GC8_C′16 with photos of the representative drops.

WCAs for the treated cotton fabrics ranged from 71.71° to 142.53°. In particular, the cotton fabric coated by the nanocomposite hydrosol with the shortest hydrocarbon chain (GC2_C′2) displayed the poor hydrophobicity, showing the lowest WCA of 71.71°. However, the cotton fabric that had been treated with the nanocomposite sol bearing the longest hydrocarbon chain (GC16_C′16) demonstrated exceptional hydrophobicity with the maximum WCA of 142.53°. In this regard, it was shown that nanocomposite sols, treated with mixed alkyl(trialkoxy)silane (GC2_C′16 and GC8_C′16), are beneficial for the formation of a brush effect surface topography [67] on the coated fabrics, thus resulting in an improvement of the hydrophobicity of treated fabrics of 148.20° and 148.83°, respectively.

Table 4 and Figure 8 indicate the hydrophobicity of the treated cotton samples.

Table 4. Static water contact angles of Wenzel θ_w values.

Sample Code	Static Water Contact Angle θ_w [°]
Cot + G	53.83 ± 0.82
Cot + GC2_C′2	71.71 ± 0.33
Cot + GC8_C′8	138.46 ± 0.40
Cot + GC16_C′16	142.53 ± 0.34
Cot + GC2_C′16	148.20 ± 0.80
Cot + GC8_C′16	148.83 ± 0.29

According to Figure 7, the WCA of the treated cotton increased as well as the length of the alkyl chain. The final treatment with HDTMS-based sol led to a lowering of the surface energy of the cotton fabric, with a consequent improvement in hydrophobicity. As indicated in Figure 8, the WCA of all cotton fabric samples was less than 150°. Although a water droplet can sit on the surface of the coated cotton cloth, it does not achieve super-hydrophobicity.

Furthermore, as shown in Figure 9, when we exposed the coated cotton textile to water droplets, the fabric successfully showed hydrophobicity similar to that present in the rose petals. The double-coating synthetic method used to improve the cotton surface hydrophobicity by pad-dry-cure deposition of the prepared nanohybrid coatings, as demonstrated using water contact angle, was shown to be successful. As a matter of fact, while the control sample had a water contact angle of 53.8°, with the incorporation of hydrophobic long-alkyl-chain silane coupling agent onto surface of cotton fabrics, the water contact angle for the Cot + GC8_C′16 nanohybrid increased to 148.83°. These values are generally higher (ca. 30–40°) than those obtained with a "grafting to" chemisorption

method of the corresponding GC* functional sol–gel, as recorded on a glass slide coated after an opportune commercial primer and tie-coat layer [67].

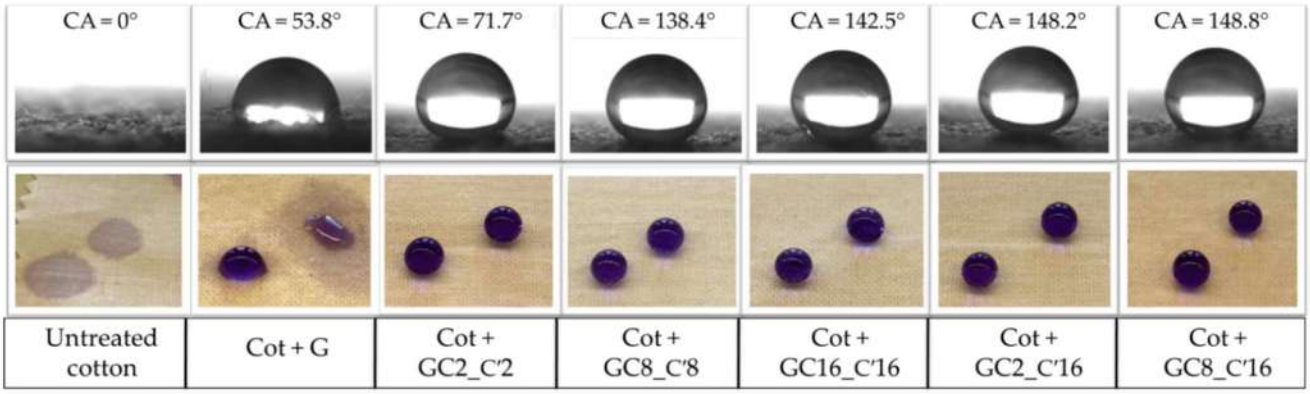

Figure 9. The images show the change in water contact angle and colored water droplets sitting on coated cotton fabrics and untreated cotton.

In this study the key step was shown to be the second coating application of the bulk functional C2, C8, and C16 silanes, especially those featuring increase of the length of the alkyl(trialkoxy) chain (i.e., C8 and C16), by the "grafting from" chemisorption covalent technique [78–80] (Figure 10a). The treated cotton fabrics exploited the observed surface hydrophobicity, as shown in Figure 10b.

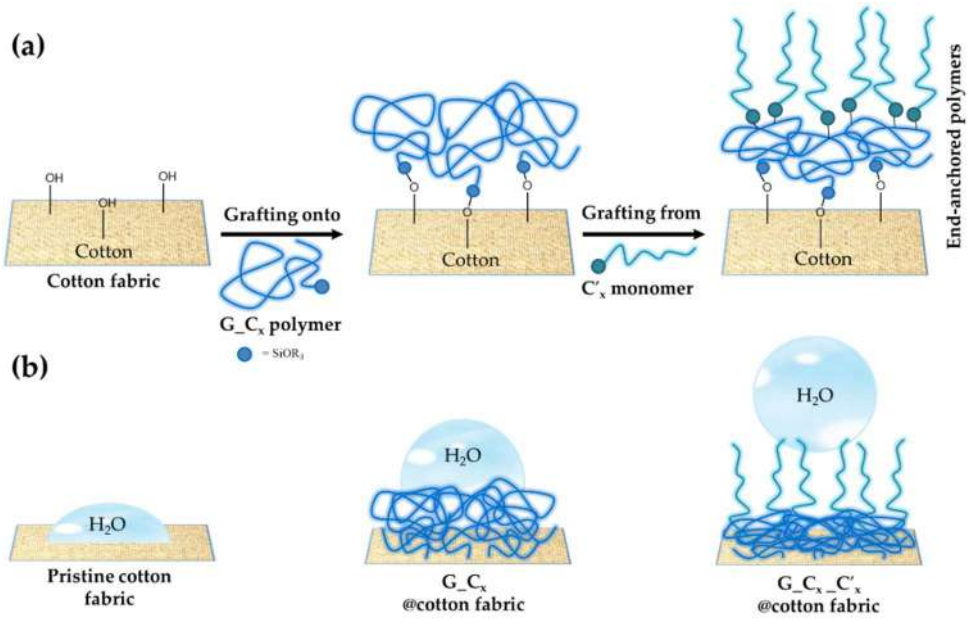

Figure 10. Double surface functionalization of cotton fabrics with alkyl(trialkoxy)silane polymer shell by "grafting to" or "grafting from" covalent grafting techniques (**a**) and corresponding observed surface hydrophobicity of the coated cotton fabrics (**b**).

In this process, on the first coated cotton surface, characterized by a silane-based 3D polymeric matrix obtained through a "grafting onto" procedure, a second functional coating was deposited, and at the end a polymerization process under conventional dry-cure conditions occurred. This latter "grafting from" process could bring a better control of the in-situ grafting density, composition, and molar ratio of the polymer brush shells. It is also not limited by the steric hindrance of the incoming functional alkyl chains, thus resulting significantly in lower surface energy and higher hydrophobicity [81] (Figure 10b).

Moreover, it has been reported that improvement of the properties, morphological characteristics, and fiber roughness of different functional coatings on textile fabrics, leading to enhanced mechanical and hydrophobic behaviors, can be achieved by employing a double-layer deposition approach [82–84].

3.2.3. Spray Test

Spray testing (AATCC 22-2005) was also used to study the dynamic wettability of the treated cotton fabric [85]. Spray testing quantifies the degree of wetness when the fabric is sprayed with water. The water-stain characteristics at different wetting degrees (in ISO standard ratings) are listed in Table 5. The wettability level of the uncoated fabric was 0, referring to no water repellency. After one coating of the sample COT + G, the wettability level was found to be 0, which was similar to uncoated fabric. However, the wettability level of the coated fabrics increased up to 50 after two coatings and remained at the same value after three coatings. This result indicates that the water repellent property of the fabrics could be enhanced by increasing the number of depositions.

Table 5. Wettability levels specified in the ATTCC 22 standard for spray tests.

Sample Code	Wettability Level	Water-Stain Characteristics
Cot + G	50 (ISO 1)	Complete wetting of the entire specimen face
Cot + GC2_ C′2	50 (ISO 1)	Complete wetting of the entire specimen face
Cot + GC8_ C′8	100 (ISO 5)	No wetting of the specimen face
Cot + GC16_ C′16	100 (ISO 5)	No wetting of the specimen face
Cot + GC2_ C′16	100 (ISO 5)	No wetting of the specimen face
Cot + GC8_ C′16	100 (ISO 5)	No wetting of the specimen face

According to the spray test, the treated cotton fabric samples COT + GC8_C′8 and COT + GC16_C′16 had a rating number corresponding to 100. The 250 mL of water in contact with the treated cotton immediately slipped away from the fabric, leaving only a few drops of water attached. In the light of the obtained results, cotton fabrics possess excellent hydrophobicity with a low surface energy. In contrast, when the cotton fabric was coated by the GPTMS-based sol without alkysilane modification, its surface shows higher surface energy. In addition, when a water droplet was applied on the pristine cotton fabric, it quickly spread.

3.2.4. Self-Cleaning Ability Measurement

The self-cleaning capabilities of the GC16_C′16-modified cotton textiles are displayed in Figure 11. The GC16_C′16-modified cotton fabrics, as shown in Figure 11a, exhibited excellent almost super hydrophobicity against blue-dyed water, strong acid (HCl, pH = 1), strong alkali (NaOH, pH = 14), and salt solution (NaCl 0.9 wt.%, pH = 7). They also exhibited excellent, almost super, hydrophobicity against milk, coffee, and tea.

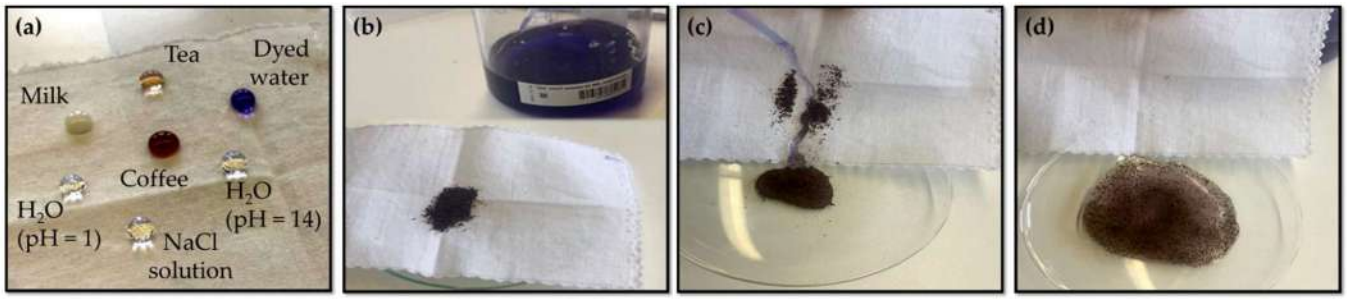

Figure 11. Photograph demonstrating the almost super-hydrophobicity of GC16_C′16-modified cotton textiles against various liquids (**a**) and real-time photographs demonstrating their water-based stain resistance performance (**b**–**d**).

It can be also seen that different liquids all exist in a similar spherical shape and this indicates that the coating has a wide range of adaptability in practical applications and implying that they may be flexible to self-cleaning under a variety of settings. Moreover, it can be clearly observed that the dust on the surface of the coating was completely removed after washing with water. As a matter of fact, water could readily flow over the surface of the sample and remove dust, as illustrated in Figure 11b–d, indicating that GC16_C′16 coating, in particular, has a very good water-based stain resistance.

It is assumed that the hydrophobic properties of the coating may be principally due to the air trapped in the nanoscale gaps of the almost super hydrophobic surface, which decreases the area of interaction between the soil and the coating and assists soil to roll-off from its surface [86,87].

3.3. Oil/Water Separation Ability

It is well known that cotton fabric is capable of absorbing large amounts of water due to its high hydrophilicity [88]. The above-mentioned, GC8_C′8, GC16_C′16, GC2_C′16, and GC8_C′16 coatings endowed the cotton fabrics with almost super hydrophobicity. In contrast, the modified cotton fabrics also have reduced surface energy that allows a repelling of water, but wetting with oils is still possible—that means the surfaces can be able to separate water from oil [89].

Figure 12 shows a sequence of images in which a cotton fabric treated with the GC16_C′16 sol was used to qualitatively study its oil/water separation ability by using paraffin oil as a model oil [90,91]. Paraffin oil was further dyed red for better observation [92]. Therefore, a droplet of red-tinted paraffin oil (with a density lower than that of water) was located in the watch glass, as illustrated in Figure 12a–d. A piece of treated fabric was soaked in the oil/water mixture to make it completely contact with the oil. It can be clearly observed that oil droplets quickly spread and even permeated into fabric, indicating the lipophilic nature of the coating. This selective adsorption is indicative of remarkable hydrophobicity or oleophilicity of the sample [93].

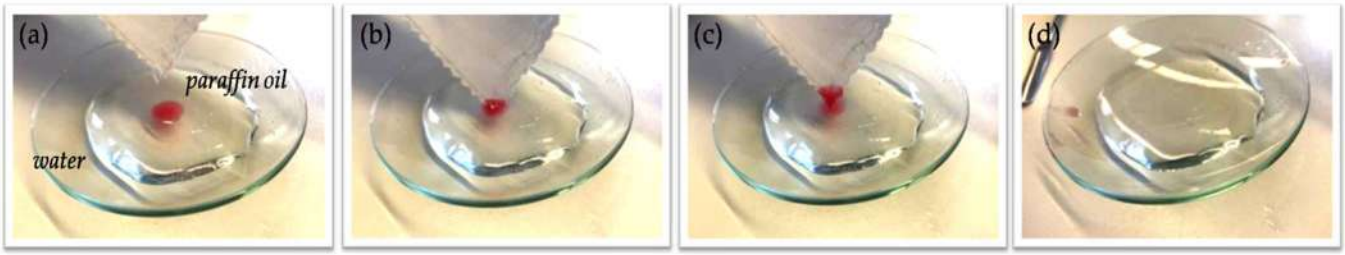

Figure 12. Real-time photos demonstrating the removal of paraffin oil (**a**–**d**) droplets from water using GC16_ C′16 modified cotton fibers.

In particular, the GC16_C′16 coating used in the current experiment can selectively absorb paraffin oil from water, further indicating that the fabric was hydrophobically modified by the coating. This demonstrates, qualitatively, that the as-prepared modified cotton textiles had good separation capacity against the tested oil/water system liquids, indicating that they might have interesting uses in industry for very efficient and long-term oil/water separation processes [94].

3.4. Morphological Characterization

3.4.1. Optical Microscopy (MO)

In order to evaluate at the microstructural level some modification in the roughness of the surface, low-magnification micrographs of the raw cotton fabric were performed and are shown in Figure 13a [95].

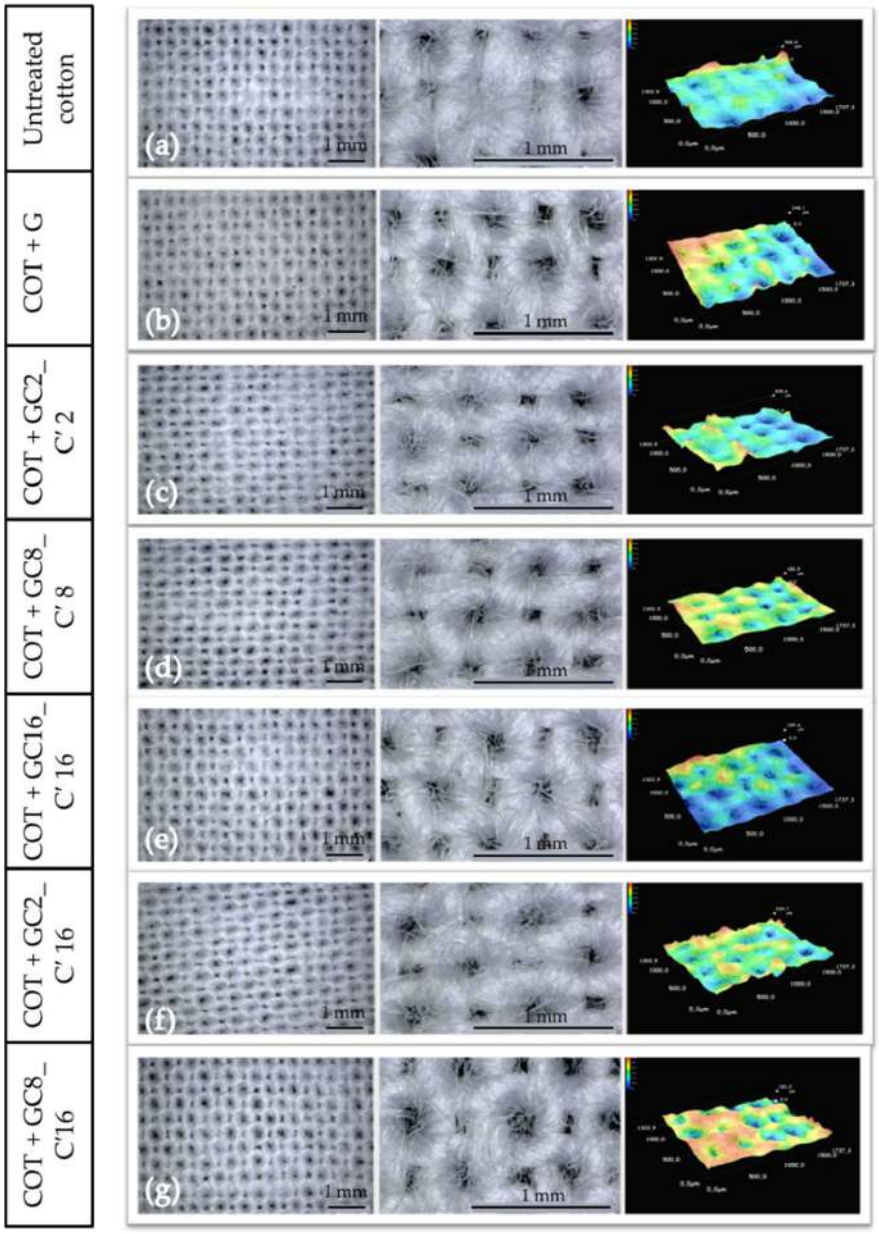

Figure 13. Optical images of untreated (**a**) and treated (**b**–**g**) cotton fabrics at different magnification and 3D image of the roughness of the analyzed samples.

It is difficult to differentiate, at this scale, between the treatment processes applied to the cotton fabric, regardless of their weaving density, mesh size, or physical appearance. Therefore, it is possible that the flux and permeability of the cotton fabric itself are not greatly affected by a microscale porosity occlusion that can lead to a lowering of the breathability of the textile [96]. Figure 13b–g shows the activated cotton fabric with the different sols at high magnifications as obtained by MO. Unfortunately, no distinct structural/morphological changes are shown, therefore a SEM analysis at the nanoscale level was performed in order to investigate how the nanohybrid functional agents can affect the fiber roughness.

3.4.2. Morphological Characterization by SEM Analysis

To evaluate the surface roughness changes of the cotton fabric at the nanoscale level after coating with the functional nanohybrids, a SEM analysis was performed. In Figure 14a the fiber surface of the raw cotton fabric had relatively smooth morphology. In Figure 14b,

after deposition of three layers of GPTMS coatings, the fiber surface of the activated cotton fabrics showed a different surface morphology. Moreover, the fabric surface shows some coarse particles but the natural structure of the single cotton fiber looks flattened when compared the inserts (a) and (b).

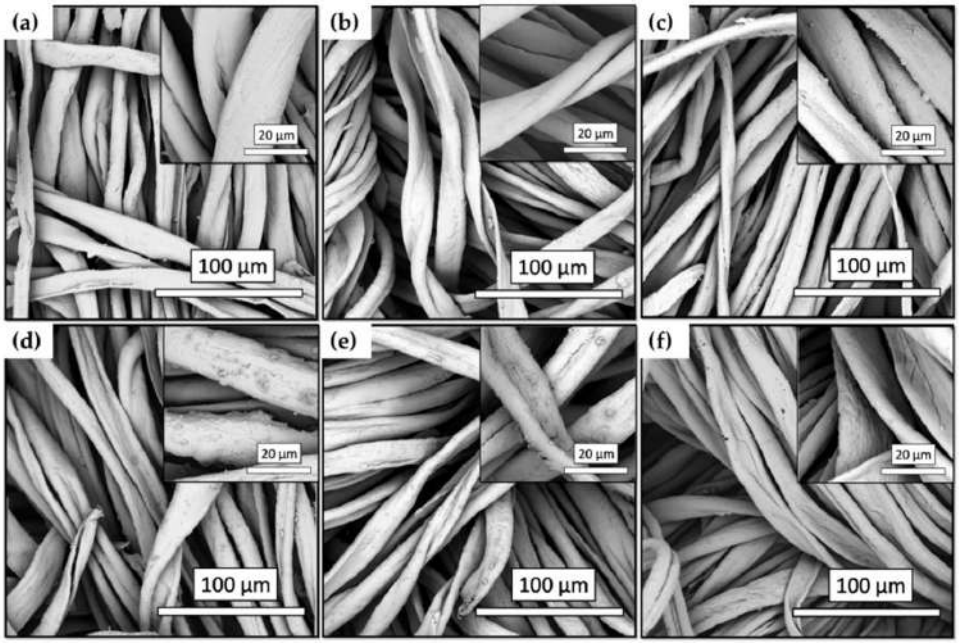

Figure 14. SEM images of untreated cotton (**a**) and GC2_C′2-coated, (**b**) GC8_C′8-coated, (**c**) GC16_C′16-coated, (**d**) GC2_C′16-coated, (**e**) GC8_C′16-coated, and (**f**) modified cotton fabrics (the inserts are partially enlarged images).

Surface roughness is a common indicator of product quality and occasionally even included as a technical requirement for obtaining the required fabric surface functionality [97]. In this regard, by comparing Figure 14a–f, it can be concluded that the addition of an alkyl(trialkoxy)silane with a long hydrocarbon chain to the coating films transforms, to some extent, the surface morphology from flat texture to rough surface. In short, the activation process promotes the alkyl(trialkoxy)silane-graft copolymerization reaction and contributes to the almost super hydrophobicity and hydrophobic stability of the cotton fabric. By the addition of a rougher surface nanoarchitecture on the micro-scaled fabric, the structural basis for transforming the extreme hydrophilicity of the cotton fabric into stable almost super hydrophobicity was therefore achieved [98,99].

3.5. Moisture-Adsorption Analysis

The determination of humidity is always of enormous importance when in the production process there is absorption or lack of humidity to and from the products. In numerous quantities of products and finishings, moisture content is both a quality characteristic and an important cost factor [100].

As shown in Table 6, the untreated cotton sample had a water absorption of 4.31%. The thin hydrophilic fabrics can easily absorb water vapor and water can pass to the other face. It is well established that original cotton fabrics exhibit high breathability as well as hygroscopicity. These outstanding properties of such cotton fabrics are attributed to their abundant hydrophilic groups (hydroxyl). This tendency and sensitivity of cellulose fabrics towards moisture, leads to a limit in their use [101]. Therefore, a proper surface modification can greatly affect the moisture adsorption of textiles [102,103].

Table 6. Moisture-adsorption standard test.

Sample Code	Weight (g)	Drying Temperature (°C)	Drying Time (min) [1]	Humidity (%)
Untreated cotton	2.156	130	5–6	4.31
COT + G	2.181	130	2	3.62
COT + GC2_C′2	2.230	130	3	4.44
COT+ GC8_C′8	2.198	130	2	3.55
COT + GC16_C′16	2.209	130	3	4.07
COT + GC2_C′16	2.280	130	2–3	3.90
COT + GC8_C′16	2.206	130	3–4	4.12

[1] Drying time until constant weight.

As a matter of fact, the GPTMS-modified cotton fabrics samples, compared with original ones, had lower WVT values. By applying pure GPTMS-sol, this water absorption was the same because the modified GPTMS-based coating was potentially still hydrophilic. The molecular chain similarly owns abundant hydrophilic groups (i.e., carboxyl, hydroxyl). Thus, the surface of GPTMS-modified cotton fibers still possessed a hydrophilic nature and abundant highly active hydrophilic groups on the fiber surface.

To achieve a significant change in the response to water absorption, these GPTMS-sols must be modified with a strong hydrophobic additive such as hexadecyltriethoxysilane (16 carbon alkyl(trialkoxy) chain). This decrease is consequently accentuated by the addition of the alkyl(trialkoxy)silane monomers, proportionally with the increase in the length of the alkyl(trialkoxy) chain.

3.6. Air-Permeability Measurement

Air permeability is one of the most important properties of a fabric, mainly intended for technical or smart textile applications and it is highly related on its porosity [104]. Additionally, air permeability is a crucial property for fabric applications in order to assess the chances of reducing the physiological strain on the human body and the hazards of heat stress [105]. It is obvious that non-coated fabrics, due to their low thicknesses and high porosities, show higher permeability in comparison to the coated fabrics and therefore, finishings can affect this behavior [106,107].

The breathability and physical properties of pristine cotton fabric and coated cotton fabrics were measured in terms of the air permeability and the obtained results are summarized in Figure 15.

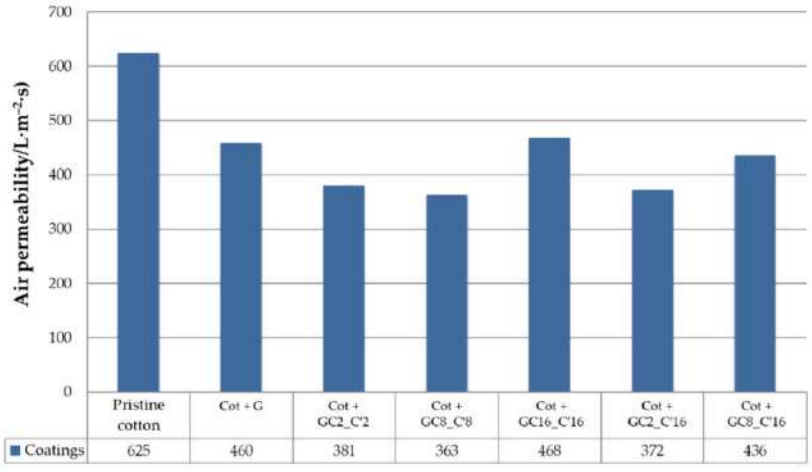

Figure 15. Histogram of the air permeability of the cotton fabrics treated by the nanocomposite sol samples G, GC2_C′2, GC8_C′8, GC16_C′16, GC2_C′16, and GC8_C′16.

Herein, it can be seen that the treatment of fabrics with the hydrophobic alkyl(trialkoxy) silane solutions moderately decreases the air permeability of fabric by a maximum of about 40%. Especially for the Cot + GC16_C'16 and Cot + GC8_C'16 samples, the coating did not highly influence the air permeability of the cotton fabric, assessing an overall good breathability of the textile support, and therefore, making them suitable for applications in a wide range of industrial-related sectors.

4. Conclusions

In this research, functional alkyl(trialkoxy)silane-modified hybrid nanostructured materials were developed and successfully employed as eco-friendly hydrophobic and water-based stain resistant coatings for cotton fabrics the via sol–gel technique and cure/pad applications. In particular, the aim of the present work was to investigate different functional alkyl(trialkoxy)silanes as precursors to obtain efficient and stable hybrid sol–gel GPTMS-based coatings and to further reduce the cotton surface energy, thus improving hydrophobicity and water-based stain resistance properties on textiles in an eco-sustainable way. This method reveals a promising application for the future finishing and functionalization of ordinary fabrics since it is straightforward, affordable, and ecologically friendly.

Morphological characterizations were performed on all the samples by optical microscopy and SEM. This last revealed an improvement on the surface roughness of the treated fabrics.

The investigation of the fabrics hydrophobicity via water contact angle (WCA) measurements showed that the treated fabrics exhibited high static contact angles (up to ca. 150°). Moreover, this was confirmed by a spray test, performed according to the AATCC 22 standard, in order to evaluate the dynamic surface-wettability of the coated samples. The water-based stain resistance of the treated fabric, was also demonstrated towards different tested liquids, solutions, and soil. Therefore, an oil/water separation experiment, was performed revealing, qualitatively, good ability of the GC16_C'16-modified samples, in particular, to retain paraffin oil, representing a valuable approach for possible efficient industrial and long-term oil/water separation approaches.

The quality characteristics of the fabrics were additionally evaluated by moisture-adsorption analysis and air-permeability test, observing with the latter an overall good breathability of the coated cotton fabrics compared to the pristine one.

All experimental findings, indicated that the synergic action of the rough surface structures and their low surface energy, caused by the chosen functional alkyl(trialkoxy)silane in the sol–gel nanohybrid coatings, provided treated cotton fabrics with excellent hydrophobicity and therefore water repellency by an eco-friendly approach.

Thus the results demonstrate the effectiveness of this nanohybrid sol–gel based functional double-coating treatment for cotton fabrics, for the preparation of hydrophobic surfaces that may have applications in different sectors ranging from textile and biomedical to water separation, providing a valuable contribution to eco-friendly hydrophobic surface treatments, with the possibility of being scaled to other types of fabrics.

Author Contributions: Conceptualization, M.R.P., T.T. and S.S.; methodology, T.T. and M.R.P.; validation, S.S.; investigation, M.R.P., T.T., S.S. and G.R.; resources, M.R.P.; data curation, M.R.P., T.L., T.T., A.V., S.S. and G.R.; writing—original draft preparation, M.R.P., T.T., S.S. and G.R.; writing—review and editing M.R.P., T.T., A.V. and S.S.; supervision, M.R.P. and T.T. All authors have read and agreed to the published version of the manuscript.

Funding: The research is supported by "Technology and materials for safe low consumption and low life-cycle cost vessels and crafts" project (PON MUR 2014–2020; CUP ARS01_00293). Area of specialization "BLUE GROWTH".

Institutional Review Board Statement: Not applicable.

Informed Consent Statement: Not applicable.

Data Availability Statement: Not applicable.

Acknowledgments: All authors wish to thank S. Romeo, G. Napoli, and F. Giordano for the informatic and technical assistance in all instrumentation set-up and subsequent data-fitting. This work was also performed within the framework of the PhD program of S.S., as financed by Confindustria (Noxosorkem Group S.r.l.) and CNR, and G.R., as financed by PON-MUR "Ricerca e Innovazione 2014–2020" RESTART project; MUR, Confindustria and CNR are gratefully acknowledged.

Conflicts of Interest: The authors declare no conflict of interest.

References

1. Toprak, T.; Anis, P. Textile industry's environmental effects and approaching cleaner production and sustainability, an overview. *J. Text. Eng. Fash. Technol.* **2017**, *2*, 429–442. [CrossRef]
2. Schindler, W.D.; Hauser, P.J. *Chemical Finishing of Textiles*; Woodhead Publishing: Cambridge, UK, 2004.
3. Hasanbeigi, A.; Price, L. A technical review of emerging technologies for energy and water efficiency and pollution reduction in the textile industry. *J. Clean. Prod.* **2015**, *95*, 30–44. [CrossRef]
4. Trovato, V.; Sfameni, S.; Rando, G.; Rosace, G.; Libertino, S.; Ferri, A.; Plutino, M.R. A review on stimuli-responsive smart materials for wearable health technology: Retrospective, perspective and prospective. *Molecules* **2022**, *27*, 5709. [CrossRef]
5. Sobha, K.; Surendranath, K.; Meena, V.; Jwala, T.K.; Swetha, N.; Latha, K.S.M. Emerging trends in nanobiotechnology. *Biotechnol. Mol. Biol. Rev.* **2010**, *5*, 1–12.
6. Ahmad, S.; Fatma, A.; Manal, E.; Ghada, A.M. Applications of Nanotechnology and Advancements in Smart Wearable Textiles: An Overview. *Egypt. J. Chem.* **2020**, *63*, 2177–2184.
7. Sanchez, C.; Julián, B.; Belleville, P.; Popall, M. Applications of hybrid organic–inorganic nanocomposites. *J. Mater. Chem.* **2005**, *15*, 3559. [CrossRef]
8. Wang, Z.; Lan, T.; Pinnavaia, T. Hybrid organic-inorganic nanocomposites formed from an epoxy polymer and a layered silicic acid (magadiite). *Chem. Mater.* **1996**, *8*, 2200–2204.
9. Mahltig, B.; Textor, T. *Nanosols and Textiles*; World Scientific: Singapore, 2008; ISBN 978-981-283-350-1.
10. Mahltig, B.; Haufe, H.; Böttcher, H. Functionalisation of textiles by inorganic sol–gel coatings. *J. Mater. Chem.* **2005**, *15*, 4385. [CrossRef]
11. Ismail, W.N.W. Sol–gel technology for innovative fabric finishing—A Review. *J. Sol-Gel Sci. Technol.* **2016**, *78*, 698–707. [CrossRef]
12. Ielo, I.; Giacobello, F.; Sfameni, S.; Rando, G.; Galletta, M.; Trovato, V.; Rosace, G.; Plutino, M.R. Nanostructured Surface Finishing and Coatings: Functional Properties and Applications. *Materials* **2021**, *14*, 2733. [CrossRef]
13. Trovato, V.; Rosace, G.; Colleoni, C.; Sfameni, S.; Migani, V.; Plutino, M.R. Sol-gel based coatings for the protection of cultural heritage textiles. *IOP Conf. Ser. Mater. Sci. Eng.* **2020**, *777*, 12007. [CrossRef]
14. Giacobello, F.; Ielo, I.; Belhamdi, H.; Plutino, M.R. Geopolymers and Functionalization Strategies for the Development of Sustainable Materials in Construction Industry and Cultural Heritage Applications: A Review. *Materials* **2022**, *15*, 1725. [CrossRef]
15. Trovato, V.; Mezzi, A.; Brucale, M.; Abdeh, H.; Drommi, D.; Rosace, G.; Plutino, M.R. Sol-Gel Assisted Immobilization of Alizarin Red S on Polyester Fabrics for Developing Stimuli-Responsive Wearable Sensors. *Polymers* **2022**, *14*, 2788. [CrossRef]
16. Filipic, J.; Glazar, D.; Jerebic, S.; Kenda, D.; Modic, A.; Roskar, B.; Vrhovski, I.; Stular, D.; Golja, B.; Smolej, S.; et al. Tailoring of antibacterial and UV protective cotton fabric by an in-situ synthesis of silver particles in the presence of a sol–gel matrix and sumac leaf extract. *Tekstilec* **2020**, *63*, 4–13. [CrossRef]
17. Puoci, F.; Saturnino, C.; Trovato, V.; Iacopetta, D.; Piperopoulos, E.; Triolo, C.; Bonomo, M.G.; Drommi, D.; Parisi, O.I.; Milone, C.; et al. Sol–Gel Treatment of Textiles for the Entrapping of an Antioxidant/Anti-Inflammatory Molecule: Functional Coating Morphological Characterization and Drug Release Evaluation. *Appl. Sci.* **2020**, *10*, 2287. [CrossRef]
18. Zhang, Y.Y.; Xu, Q.B.; Fu, F.Y.; Liu, X.D. Durable antimicrobial cotton textiles modified with inorganic nanoparticles. *Cellulose* **2016**, *23*, 2791–2808. [CrossRef]
19. Cuk, N.; Sala, M.; Gorjanc, M. Development of antibacterial and UV protective cotton fabrics using plant food waste and alien invasive plant extracts as reducing agents for the in-situ synthesis of silver nanoparticles. *Cellulose* **2021**, *28*, 3215–3233. [CrossRef]
20. Ielo, I.; Giacobello, F.; Castellano, A.; Sfameni, S.; Rando, G.; Plutino, M.R. Development of Antibacterial and Antifouling Innovative and Eco-Sustainable Sol–Gel Based Materials: From Marine Areas Protection to Healthcare Applications. *Gels* **2022**, *8*, 26. [CrossRef]
21. Saleemi, S.; Naveed, T.; Riaz, T.; Memon, H.; Awan, J.A.; Siyal, M.I.; Xu, F.; Bae, J. Surface Functionalization of Cotton and PC Fabrics Using SiO_2 and ZnO Nanoparticles for Durable Flame Retardant Properties. *Coatings* **2020**, *10*, 124. [CrossRef]
22. Ibrahim, H.M.; Zaghloul, S.; Hashem, M.; El-Shafei, A. A green approach to improve the antibacterial properties of cellulosebased fabrics using Moringa oleifera extract presence of silver nanoparticles. *Cellulose* **2021**, *28*, 549–564. [CrossRef]
23. Colleoni, C.; Massafra, M.R.; Rosace, G. Photocatalytic properties and optical characterization of cotton fabric coated via sol–gel with non-crystalline TiO_2 modified with poly(ethylene glycol). *Surf. Coat. Technol.* **2012**, *207*, 79–88. [CrossRef]
24. Colleoni, C.; Guido, E.; Migani, V.; Rosace, G. Hydrophobic behaviour of non fluorinated sol-gel based cotton and polyester fabric coatings. *J. Ind. Text.* **2015**, *44*, 815–834. [CrossRef]

25. Sfameni, S.; Rando, G.; Galletta, M.; Ielo, I.; Brucale, M.; De Leo, F.; Cardiano, P.; Cappello, S.; Visco, A.; Trovato, V.; et al. Design and Development of Fluorinated and Biocide-Free Sol–Gel Based Hybrid Functional Coatings for Anti-Biofouling/Foul-Release Activity. *Gels* **2022**, *8*, 538. [CrossRef]
26. Textor, T.; Mahltig, B. A sol–gel based surface treatment for preparation of water repellent antistatic textiles. *Appl. Surf. Sci.* **2010**, *256*, 1668–1674. [CrossRef]
27. Alongi, J.; Colleoni, C.; Rosace, G.; Malucelli, G. The role of pre-hydrolysis on multi step sol-gel processes for enhancing the flame retardancy of cotton. *Cellulose* **2013**, *20*, 525–535. [CrossRef]
28. Ahmed, M.; Morshed, M.; Farjana, S.; Ana, S. Fabrication of new multifunctional cotton–modal–recycled aramid blended protective textiles through deposition of a 3D-polymer coating: High fire retardant, water repellent and antibacterial properties. *New J. Chem.* **2020**, *44*, 12122–12133. [CrossRef]
29. Castellano, A.; Colleoni, C.; Iacono, G.; Mezzi, A.; Plutino, M.R.; Malucelli, G.; Rosace, G. Synthesis and characterization of a phosphorous/nitrogen based sol-gel coating as a novel halogen- and formaldehyde-free flame retardant finishing for cotton fabric. *Polym. Degrad. Stab.* **2019**, *162*, 148–159. [CrossRef]
30. Caldara, M.; Colleoni, C.; Guido, E.; Rosace, G. Optical sensor development for smart textiles. In Proceedings of the 12th World Textile Conference AUTEX, Zadar, Croatia, 13–15 June 2012; pp. 1149–1452.
31. Caldara, M.; Colleoni, C.; Guido, E.; Re, V.; Rosace, G. Optical monitoring of sweat pH by a textile fabric wearable sensor based on covalently bonded litmus-3-glycidoxypropyltrimethoxysilane coating. *Sens. Actuators B Chem.* **2016**, *222*, 213–220. [CrossRef]
32. Trovato, V.; Rosace, G.; Colleoni, C.; Plutino, M.R. Synthesis and characterization of halochromic hybrid sol-gel for the development of a pH sensor fabric. *IOP Conf. Ser. Mater. Sci. Eng.* **2017**, *254*, 72027. [CrossRef]
33. Ielo, I.; Rando, G.; Giacobello, F.; Sfameni, S.; Castellano, A.; Galletta, M.; Drommi, D.; Rosace, G.; Plutino, M.R. Synthesis, Chemical–Physical Characterization, and Biomedical Applications of Functional Gold Nanoparticles: A Review. *Molecules* **2021**, *26*, 5823. [CrossRef]
34. Mahltig, B.; Textor, T. Combination of silica sol and dyes on textiles. *J. Sol-Gel Sci. Technol.* **2006**, *39*, 111–118. [CrossRef]
35. AbouElmaaty, T.; Abdeldayem, S.; Ramadan, S.; Sayed-Ahmed, K.; Plutino, M. Coloration and Multi-Functionalization of Polypropylene Fabrics with Selenium Nanoparticles. *Polymers* **2021**, *13*, 2483. [CrossRef]
36. Ibrahim, N.; Eid, B.; Abd El-Aziz, E.; AbouElmaaty, T.; Ramadan, S. Loading of chitosan Nano metal oxide hybrids ontocotton/polyester fabrics to impart permanent and effective multifunctions. *Int. J. Biol. Macromol.* **2017**, *105*, 769–776. [CrossRef]
37. Aya, R.; Abdel Rahim, A.; Amr, H.; El-Amir, M. Improving Performance and Functional Properties of Different Cotton Fabrics by Silicon Dioxide Nanoparticles. *J. Eng. Sci.* **2019**, *4*, 1–17.
38. AbouElmaaty, T.; Elsisi, H.G.; Elsayad, G.M.; Elhadad, H.H.; Sayed-Ahmed, K.; Plutino, M.R. Fabrication of New Multifunctional Cotton/Lycra Composites Protective Textiles through Deposition of Nano Silica Coating. *Polymers* **2021**, *13*, 2888. [CrossRef]
39. Trovato, V.; Vitale, A.; Bongiovanni, R.; Ferri, A.; Rosace, G.; Plutino, M.R. Development of a Nitrazine Yellow-glycidyl methacrylate coating onto cotton fabric through thermal-induced radical polymerization reactions: A simple approach towards wearable pH sensors applications. *Cellulose* **2021**, *28*, 3847–3868. [CrossRef]
40. Li, X.M.; Reinhoudt, D.; Crego, C.M. What do we need for a superhydrophobic surface? A review on the recent progress in the preparation of superhydrophobic surfaces. *Chem. Soc. Rev.* **2007**, *36*, 1350–1368. [CrossRef]
41. Richard, E.; Lakshmi, R.V.; Aruna, S.T.; Basu, B.J. A simple cost-effective and eco-friendly wet chemical process for the fabrication of superhydrophobic cotton fabrics. *Appl. Surf. Sci.* **2013**, *277*, 302–309. [CrossRef]
42. Xu, B.; Cai, Z.; Wang, W.; Ge, F. Preparation of superhydrophobic cotton fabrics based on SiO2 nanoparticles and ZnO nanorod arrays with subsequent hydrophobic modification. *Surf. Coat. Technol.* **2010**, *204*, 1556–1561. [CrossRef]
43. Zhang, X.; Shi, F.; Niu, J.; Jiang, Y.; Wang, Z. Superhydrophobic surfaces: From structural control to functional application. *J. Mater. Chem* **2008**, *18*, 621. [CrossRef]
44. Patankar, N.A. Mimicking the Lotus Effect: Influence of Double Roughness Structures and Slender Pillars. *Langmuir* **2004**, *20*, 8209–8213. [CrossRef]
45. Cassie, A.B.D.; Baxter, S. Wettability of porous surfaces. *Trans. Faraday Soc.* **1944**, *40*, 546–551. [CrossRef]
46. Balani, K.; Batista, R.G.; Lahiri, D.; Agarwal, A. The hydrophobicity of a lotus leaf: A nanomechanical and computational approach. *Nanotechnology* **2009**, *20*, 305707. [CrossRef]
47. Heiman-Burstein, D.; Dotan, A.; Dodiuk, H.; Kenig, S. Hybrid Sol-Gel Superhydrophobic Coatings Based on Alkyl Silane-Modified Nanosilica. *Polymers* **2021**, *13*, 539. [CrossRef]
48. Xue, C.H.; Jia, S.T.; Zhang, J.; Ma, J.Z. Large-area fabrication of superhydrophobic surfaces for practical applications: An overview. *Sci. Technol. Adv. Mater.* **2010**, *11*, 033002. [CrossRef]
49. Zhang, M.; Wang, S.; Wang, C.; Li, J. A facile method to fabric at superhydrophobic cotton fabrics. *Appl. Surf. Sci.* **2012**, *261*, 561. [CrossRef]
50. Huang, W.Q.; Xing, Y.J.; Yu, Y.; Shang, S.M.; Dai, J.J. Enhanced washing durability of hydrophobic coating on cellulose fabric using polycarboxylic acids. *Appl. Surf. Sci.* **2011**, *257*, 4443. [CrossRef]
51. Rando, G.; Sfameni, S.; Galletta, M.; Drommi, D.; Cappello, S.; Plutino, M.R. Functional Nanohybrids and Nanocomposites Development for the Removal of Environmental Pollutants and Bioremediation. *Molecules* **2022**, *27*, 4856. [CrossRef]

52. Bae, G.Y.; Jeong, Y.G.; Min, B.G. Superhydrophobic PET fabrics achieved bysilica nanoparticles and water-repellent agent. *Fibers Polym.* **2010**, *11*, 976. [CrossRef]
53. Bae, G.Y.; Geun, Y.; Min, B.G.; Jeong, Y.G.; Lee, S.C.; Jang, J.H.; Koo, G.H. Superhydrophobicity of cotton fabrics treated with silica nanoparticles and water-repellent agent. *J. Colloid Interface Sci.* **2009**, *337*, 170–175. [CrossRef]
54. Lehocky, M.; Amaral, P.F.F.; St'ahel, P.; Coelho, M.A.Z.; Timmons, A.M.; Coutinho, J.A.P. Preparation and characterization of organosilicon thin films for selective adhesion of yarrowialipolytica yeast cells. *J. Chem. Technol. Biotechnol.* **2007**, *366*, 360–366. [CrossRef]
55. Lakshmi, R.V.; Bera, P.; Anandan, C.; Basu, B. Effect of the size of silica nanoparticles on wettability and surface chemistry of sol–gel superhydrophobic and oleophobic nanocomposite coatings. *J. Appl. Surf. Sci.* **2014**, *320*, 780. [CrossRef]
56. Huang, W.H.; Lin, C.S. Robust superhydrophobic transparent coatings fabricated by a low-temperature sol–gel process. *Appl. Surf. Sci.* **2014**, *305*, 702. [CrossRef]
57. Shang, Q.; Zhou, Y.; Xiao, G. A simple method for the fabrication of silica-based superhydrophobic surfaces. *Coat. Technol. Res.* **2014**, *11*, 509. [CrossRef]
58. Ramezani, M.; Vaezi, M.R.; Kazemzadeh, A. Preparation of silane-functionalized silica films via two-step dip coating sol–gel and evaluation of their superhydrophobic properties. *Appl. Surf. Sci.* **2014**, *317*, 147. [CrossRef]
59. Zou, H.; Lin, S.; Tu, Y.; Liu, G.; Hu, J.; Li, F.; Miao, L.; Zhang, G.; Luo, H.; Liu, F.; et al. Simple approach towards fabrication of highly durable and robust superhydrophobic cotton fabric from functional di block copolymer. *J. Mat. Chem. A* **2013**, *1*, 11246. [CrossRef]
60. Gao, Y.; Huang, Y.G.; Feng, S.J.; Gu, G.T.; Qing, F.L. Novel superhydrophobic and highly oleophobic PFPE-modified silica nanocomposite. *J. Mater. Sci.* **2010**, *45*, 460. [CrossRef]
61. Guido, E.; Colleoni, C.; De Clerck, K.; Plutino, M.R.; Rosace, G. Influence of catalyst in the synthesis of a cellulose-based sensor: Kinetic study of 3-glycidoxypropyltrimethoxysilane epoxy ring opening by Lewis acid. *Sens. Actuators B Chem.* **2014**, *203*, 213–222. [CrossRef]
62. Trovato, V.; Colleoni, C.; Castellano, A.; Plutino, M.R. The key role of 3-glycidoxypropyltrimethoxysilane sol–gel precursor in the development of wearable sensors for health monitoring. *J. Sol-Gel Sci. Technol.* **2018**, *87*, 27–40. [CrossRef]
63. Plutino, M.R.; Guido, E.; Colleoni, C.; Rosace, G. Effect of GPTMS functionalization on the improvement of the pH-sensitive methyl red photostability. *Sens. Actuators B* **2017**, *238*, 281–291. [CrossRef]
64. Rosace, G.; Guido, E.; Colleoni, C.; Brucale, M.; Piperopoulos, E.; Milone, C.; Plutino, M.R. Halochromic resorufin-GPTMS hybrid sol-gel: Chemical-physical properties and use as pH sensor fabric coating. *Sens. Actuators B Chem.* **2017**, *241*, 85–95. [CrossRef]
65. Plutino, M.R.; Colleoni, C.; Donelli, I.; Freddi, G.; Guido, E.; Maschi, O.; Mezzi, A.; Rosace, G. Sol-gel 3-glycidoxypropyltriethoxysilane finishing on different fabrics: The role of precursor concentration and catalyst on the textile performances and cytotoxic activity. *J. Colloid Interface Sci.* **2017**, *506*, 504–517. [CrossRef]
66. Ielo, I.; Galletta, M.; Rando, G.; Sfameni, S.; Cardiano, P.; Sabatino, G.; Drommi, D.; Rosace, G.; Plutino, M.R. Design, synthesis and characterization of hybrid coatings suitable for geopolymeric-based supports for the restoration of cultural heritage. *IOP Conf. Ser. Mater. Sci. Eng.* **2020**, *777*, 012003. [CrossRef]
67. Sfameni, S.; Rando, G.; Marchetta, A.; Scolaro, C.; Cappello, S.; Urzì, C.; Visco, A.; Plutino, M.R. Development of eco-friendly hydrophobic and fouling-release coatings for blue-growth environmental applications: Synthesis, mechanical characterization and biological activity. *Gels* **2022**, *8*, 528. [CrossRef]
68. Zhu, D.; Hu, N.; Schaefer, D.W. *Chapter 1—Water-Based Sol–Gel Coatings for Military Coating Applications*; Elsevier: Amsterdam, The Netherlands, 2020; pp. 1–27.
69. Khatri, M.; Qureshi, U.A.; Ahmed, F.; Khatri, Z.; Kim, I.S. Dyeing of Electrospun Nanofibers BT. In *Handbook of Nanofibers*; Barhoum, A., Bechelany, M., Makhlouf, A.S.H., Eds.; Springer International Publishing: Cham, Switzerland, 2019; pp. 373–388, ISBN 978-3-319-53655-2.
70. El-Ghazali, S.; Khatri, M.; Kobayashi, S.; Kim, I.S. 1—An overview of medical textile materials. In *Medical Textiles from Natural Resources*; The Textile Institute Book, Series; Mondal, M.I.H., Ed.; Woodhead Publishing: Sawston, UK, 2022; pp. 3–42, ISBN 978-0-323-90479-7.
71. Basak, S.; Samanta, K.K.; Chattopadhyay, S.K. Fire retardant property of cotton fabric treated with herbal extract. *J. Text. Inst.* **2015**, *106*, 1338–1347. [CrossRef]
72. Lin, T.-C.; Lee, D.-J. Cotton fabrics modified for use in oil/water separation: A perspective review. *Cellulose* **2021**, *28*, 4575–4594. [CrossRef]
73. Hu, B.; Pu, H.; Sun, D.-W. Multifunctional cellulose based substrates for SERS smart sensing: Principles, applications and emerging trends for food safety detection. *Trends Food Sci. Technol.* **2021**, *110*, 304–320. [CrossRef]
74. Malshe, P.; Mazloumpour, M.; El-Shafei, A.; Hauser, P. Multi-functional military textile: Plasma-induced graft polymerization of a C6 fluorocarbon for repellent treatment on nylon–cotton blend fabric. *Surf. Coat. Technol.* **2013**, *217*, 112–118. [CrossRef]
75. Marmur, A.A. Guide to the Equilibrium Contact Angles Maze. In *Contact angle, Wettability and Adhesion*; CRC Press: Boca Raton, FL, USA, 2009; pp. 1–18.
76. Ubuo, E.E.; Udoetok, I.A.; Tyowua, A.T.; Ekwere, I.O.; Al-Shehri, H.S. The Direct Cause of Amplified Wettability: Roughness or Surface Chemistry? *J. Compos. Sci.* **2021**, *5*, 213. [CrossRef]

77. Wenzel, R.N. Resistance of solid surfaces to wetting by water. *Ind. Eng. Chem.* **1936**, *28*, 988–994. [CrossRef]
78. Glosz, K.; Stolarczyk, A.; Jarosz, T. Siloxanes—Versatile Materials for Surface Functionalisation and Graft Copolymers. *Int. J. Mol. Sci.* **2020**, *21*, 6387. [CrossRef]
79. Han, Y.; Hu, J.; Xin, Z. In-Situ Incorporation of Alkyl-Grafted Silica into Waterborne Polyurethane with High Solid Content for Enhanced Physical Properties of Coatings. *Polymers* **2018**, *10*, 514. [CrossRef]
80. Sánchez-Milla, M.; Gómez, R.; Pérez-Serrano, J.; Sánchez-Nieves, J.; de la Mata, F.J. Functionalization of silica with amine and ammonium alkyl chains, dendrons and dendrimers: Synthesis and antibacterial properties. *Mater. Sci. Eng. C* **2020**, *109*, 110526. [CrossRef]
81. Radhakrishnan, B.; Ranjan, R.; Brittain, W.J. Surface initiated polymerizations from silica nanoparticles. *Soft Matter* **2006**, *2*, 386–396. [CrossRef]
82. Donnini, J.; Corinaldesi, V.; Nanni, A. Mechanical properties of FRCM using carbon fabrics with different coating treatments. *Compos. Part B Eng.* **2016**, *88*, 220–228. [CrossRef]
83. Koo, K.; Park, Y. Characteristics of double-layer coated fabrics with and without phase change materials and nano-particles. *Fibers Polym.* **2014**, *15*, 1641–1647. [CrossRef]
84. Mazzon, G.; Zahid, M.; Heredia-Guerrero, J.A.; Balliana, E.; Zendri, E.; Athanassiou, A.; Bayer, I.S. Hydrophobic treatment of woven cotton fabrics with polyurethane modified aminosilicone emulsions. *Appl. Surf. Sci.* **2019**, *490*, 331–342. [CrossRef]
85. Lin, H.; Rosu, C.; Jiang, L.; Sundar, V.A.; Breedveld, V.; Hess, D.W. Nonfluorinated Superhydrophobic Chemical Coatings on Polyester Fabric Prepared with Kinetically Controlled Hydrolyzed Methyltrimethoxysilane. *Ind. Eng. Chem. Res.* **2019**, *58*, 15368–15378. [CrossRef]
86. Pavlidou, S.; Paul, R. 3—Soil repellency and stain resistance through hydrophobic and oleophobic treatments. In *Waterproof and Water Repellent Textiles and Clothing*; The Textile Institute Book, Series; Williams, J., Ed.; Woodhead Publishing: Sawston, UK, 2018; pp. 73–88. ISBN 978-0-08-101212-3.
87. Peran, J.; Ercegović Ražić, S. Application of atmospheric pressure plasma technology for textile surface modification. *Text. Res. J.* **2019**, *90*, 1174–1197. [CrossRef]
88. Liu, Y.; Xin, J.H.; Choi, C.-H. Cotton Fabrics with Single-Faced Superhydrophobicity. *Langmuir* **2012**, *28*, 17426–17434. [CrossRef]
89. Li, Y.; Yu, Q.; Yin, X.; Xu, J.; Cai, Y.; Han, L.; Huang, H.; Zhou, Y.; Tan, Y.; Wang, L.; et al. Fabrication of superhydrophobic and superoleophilic polybenzoxazine-based cotton fabric for oil–water separation. *Cellulose* **2018**, *25*, 6691–6704. [CrossRef]
90. He, Y.; Wan, M.; Wang, Z.; Zhang, X.; Zhao, Y.; Sun, L. Fabrication and characterization of degradable and durable fluoride-free super-hydrophobic cotton fabrics for oil/water separation. *Surf. Coat. Technol.* **2019**, *378*, 125079. [CrossRef]
91. Tang, H.; Fu, Y.; Yang, C.; Zhu, D.; Yang, J. A UV-driven superhydrophilic/superoleophobic polyelectrolyte multilayer film on fabric and its application in oil/water separation. *RSC Adv.* **2016**, *6*, 91301–91307. [CrossRef]
92. Wang, J.; Chen, Y. Oil–water separation capability of superhydrophobic fabrics fabricated via combining polydopamine adhesion with lotus-leaf-like structure. *J. Appl. Polym. Sci.* **2015**, *132*. [CrossRef]
93. Zhao, Y.; Liu, E.; Fan, J.; Chen, B.; Hu, X.; He, Y.; He, C. Superhydrophobic PDMS/wax coated polyester textiles with self-healing ability via inlaying method. *Prog. Org. Coat.* **2019**, *132*, 100–107. [CrossRef]
94. Huang, G.; Huo, L.; Jin, Y.; Yuan, S.; Zhao, R.; Zhao, J.; Li, Z.; Li, Y. Fluorine-free superhydrophobic PET fabric with high oil flux for oil–water separation. *Prog. Org. Coat.* **2022**, *163*, 106671. [CrossRef]
95. Canal, L.P.; González, C.; Molina-Aldareguía, J.M.; Segurado, J.; LLorca, J. Application of digital image correlation at the microscale in fiber-reinforced composites. *Compos. Part A Appl. Sci. Manuf.* **2012**, *43*, 1630–1638. [CrossRef]
96. Ghaffari, S.; Yousefzadeh, M.; Mousazadegan, F. Investigation of thermal comfort in nanofibrous three-layer fabric for cold weather protective clothing. *Polym. Eng. Sci.* **2019**, *59*, 2032–2040. [CrossRef]
97. Wan, T.; Stylios, G.K. Effects of coating process on the surface roughness of coated fabrics. *J. Text. Inst.* **2017**, *108*, 712–719. [CrossRef]
98. Hsieh, C.-T.; Chen, W.-Y.; Wu, F.-L. Fabrication and superhydrophobicity of fluorinated carbon fabrics with micro/nanoscaled two-tier roughness. *Carbon* **2008**, *46*, 1218–1224. [CrossRef]
99. Park, S.; Kim, J.; Park, C.H. Influence of micro and nano-scale roughness on hydrophobicity of a plasma-treated woven fabric. *Text. Res. J.* **2016**, *87*, 193–207. [CrossRef]
100. Zarrinabadi, E.; Abghari, R.; Nazari, A.; Mirjalili, M. Environmental effects of enhancement of mechanical and hydrophobic properties of polyester fabrics using silica/kaolinite/silver nanocomposite: A facile technique for synthesis and RSM optimization. *Eurasian J. Biosci.* **2018**, *12*, 1–14.
101. Forsman, N.; Lozhechnikova, A.; Khakalo, A.; Johansson, L.-S.; Vartiainen, J.; Österberg, M. Layer-by-layer assembled hydrophobic coatings for cellulose nanofibril films and textiles, made of polylysine and natural wax particles. *Carbohydr. Polym.* **2017**, *173*, 392–402. [CrossRef]
102. Glampedaki, P.; Jocic, D.; Warmoeskerken, M.M.C.G. Moisture absorption capacity of polyamide 6,6 fabrics surface functionalised by chitosan-based hydrogel finishes. *Prog. Org. Coat.* **2011**, *72*, 562–571. [CrossRef]
103. Tissera, N.D.; Wijesena, R.N.; Perera, J.R.; de Silva, K.M.N.; Amaratunge, G.A.J. Hydrophobic cotton textile surfaces using an amphiphilic graphene oxide (GO) coating. *Appl. Surf. Sci.* **2015**, *324*, 455–463. [CrossRef]

104. Zupin, Ž.; Hladnik, A.; Dimitrovski, K. Prediction of one-layer woven fabrics air permeability using porosity parameters. *Text. Res. J.* **2011**, *82*, 117–128. [CrossRef]
105. Liu, R.; Li, J.; Li, M.; Zhang, Q.; Shi, G.; Li, Y.; Hou, C.; Wang, H. MXene-Coated Air-Permeable Pressure-Sensing Fabric for Smart Wear. *ACS Appl. Mater. Interfaces* **2020**, *12*, 46446–46454. [CrossRef]
106. Jiang, J.; Shen, Y.; Yu, D.; Yang, T.; Wu, M.; Yang, L.; Petru, M. Porous Film Coating Enabled by Polyvinyl Pyrrolidone (PVP) for Enhanced Air Permeability of Fabrics: The Effect of PVP Molecule Weight and Dosage. *Polymers* **2020**, *12*, 2961. [CrossRef]
107. Oh, J.-H.; Ko, T.-J.; Moon, M.-W.; Park, C.H. Nanostructured fabric with robust superhydrophobicity induced by a thermal hydrophobic ageing process. *RSC Adv.* **2017**, *7*, 25597–25604. [CrossRef]

MDPI
St. Alban-Anlage 66
4052 Basel
Switzerland
Tel. +41 61 683 77 34
Fax +41 61 302 89 18
www.mdpi.com

Nanomaterials Editorial Office
E-mail: nanomaterials@mdpi.com
www.mdpi.com/journal/nanomaterials

MDPI
St. Alban-Anlage 66
4052 Basel
Switzerland

Tel: +41 61 683 77 34

www.mdpi.com

ISBN 978-3-0365-7536-0